

PROBING PROTON STRUCTURE THROUGH SINGLE
POLARISATION OBSERVABLES OF COMPTON SCATTERING
AND π^0 PHOTOPRODUCTION WITHIN THE $\Delta(1232)$ REGION

by

Cristina Collicott

Submitted in partial fulfillment of the
requirements for the degree of
Doctor of Philosophy

at

Dalhousie University
Halifax, Nova Scotia
April 2015

© Copyright by Cristina Collicott, 2015

Table of Contents

List of Tables	vii
List of Figures	viii
Abstract	xi
List of Abbreviations and Symbols Used	xii
Acknowledgements	xvi
Chapter 1 Introduction	1
Chapter 2 Theoretical Review	5
2.1 Nucleon Compton scattering	5
2.1.1 Compton scattering amplitudes	5
2.1.1.1 First order expansion: Born terms	5
2.1.1.2 Second order expansion: Scalar Polarisabilities	6
2.1.1.3 Third order expansion: Spin Polarisabilities	7
2.1.2 Low-energy expansion	10
2.1.3 Dispersion relations at fixed- t	10
2.2 Sum Rules	15
2.2.1 Baldin sum rule	15
2.2.2 BEFT sum rule	16
2.2.3 GDH γ_0 sum rule	17
2.2.4 LN γ_π sum rule	17
2.3 Polarised Compton scattering	18
2.3.1 Stokes parameters	18
2.3.2 Asymmetries	19
2.3.2.1 Defined by the polarised cross section	19
2.3.2.2 Defined by the scattering amplitudes	20
2.3.2.3 Sensitivity to spin polarisabilities	23
2.4 π^0 photoproduction	27
Chapter 3 Studies of the Proton Polarisabilities	28
3.1 Baldin sum rule	28
3.2 Scalar Polarisabilities	29

3.3	Forward spin polarisability	31
3.4	Backward spin polarisability	31
3.5	Spin Polarisabilities	33
3.5.1	Theoretical predictions	33
3.5.2	Experimental studies	36
Chapter 4	Experiment	40
4.1	Linearly polarised photon beam	40
4.1.1	MAMI electron accelerator	41
4.1.2	Bremsstrahlung production	44
4.1.2.1	Incoherent Bremsstrahlung production	44
4.1.2.2	Coherent Bremsstrahlung production	45
4.1.2.3	Degree of linear polarisation	47
4.1.2.4	Diamond orientation: The Stonehenge Technique	48
4.1.2.5	Collimation	50
4.1.3	Glasgow Tagged Photon Spectrometer	50
4.2	Liquid hydrogen target	53
4.3	Event detection	54
4.3.1	Crystal Ball Photon Spectrometer	54
4.3.1.1	Multiwire proportional chambers	55
4.3.1.2	Particle Identification Detector	55
4.3.2	TAPS	57
4.3.2.1	Veto wall	58
4.3.3	Detector summary	58
4.3.4	Event readout	59
4.3.4.1	Trigger system	59
4.3.4.2	Scalers	60
4.3.4.3	Data acquisition software: Acqu	61
Chapter 5	Event Reconstruction	62
5.1	Software	62
5.1.1	AcquRoot	62
5.1.1.1	Decode Hits	63
5.1.1.2	Cluster Hits	63
5.1.1.3	Particle tracks	65
5.1.1.4	TA2GoAT - Output to ROOT trees	67
5.1.2	GoAT	67
5.1.2.1	Particle identification	68
5.1.2.2	Meson reconstruction	68
5.1.2.3	Data sorting	70

5.2	Detector Calibrations	71
5.2.1	a2CaLib	71
5.2.2	ADC pedestals and TDC offsets	71
5.2.3	Time calibrations	72
5.2.4	Energy calibrations	74
5.3	Determination of photon polarisation	76
Chapter 6	Analysis	86
6.1	Overview	86
6.2	π^0 photoproduction	88
6.2.1	Event selection	88
6.2.2	Empty target contribution	92
6.2.3	Example calculation	93
6.2.4	Determination of the polarisation offset, ϕ_o	93
6.2.5	Results	97
6.2.6	Discussion	102
6.3	Compton scattering	103
6.3.1	Event Selection	103
6.3.1.1	Kinematic cuts	103
6.3.2	Missing Mass Cuts	107
6.3.3	Empty target contribution	118
6.3.4	Example calculation	119
6.3.5	Results	122
6.3.6	Discussion	122
Chapter 7	Discussion	127
7.1	Outlook	130
Appendix A	Σ_3 results for π^0 photoproduction	133
Bibliography	145

List of Tables

3.1	Theoretical predictions of the proton spin polarisabilities	35
4.1	Main parameters of the MAMI electron accelerator	42
4.2	Main parameters of the CB-TAPS detector system	58
5.1	Example set of ADC and TDC parameters for a BaF ₂ crystal	64
6.1	Missing mass cuts for Compton scattering	115
6.2	Σ_3 for incident photon energies 277.1 ± 10.1 MeV	125
6.3	Σ_3 for incident photon energies 297.0 ± 10.1 MeV	126
7.1	Spin polarisabilities determined from experimental data	129
A.1	Σ_{π_0} for incident photon energies 213.52 ± 3.90 MeV	133
A.2	Σ_{π_0} for incident photon energies 220.95 ± 3.92 MeV	134
A.3	Σ_{π_0} for incident photon energies 225.92 ± 3.91 MeV	135
A.4	Σ_{π_0} for incident photon energies 235.89 ± 3.89 MeV	136
A.5	Σ_{π_0} for incident photon energies 243.40 ± 3.90 MeV	137
A.6	Σ_{π_0} for incident photon energies 250.85 ± 3.92 MeV	138
A.7	Σ_{π_0} for incident photon energies 257.09 ± 2.66 MeV	139
A.8	Σ_{π_0} for incident photon energies 272.09 ± 5.15 MeV	140
A.9	Σ_{π_0} for incident photon energies 280.80 ± 3.92 MeV	141
A.10	Σ_{π_0} for incident photon energies 288.29 ± 3.90 MeV	142
A.11	Σ_{π_0} for incident photon energies 295.78 ± 3.88 MeV	143
A.12	Σ_{π_0} for incident photon energies 303.30 ± 3.89 MeV	144

List of Figures

2.1	Compton scattering cross section considering only Born terms, the low-energy expansion, and fixed- t dispersion relations . . .	11
2.2	Sensitivity of Σ_{2z} asymmetry to the proton spin polarisabilities	24
2.3	Sensitivity of Σ_{2x} asymmetry to the proton spin polarisabilities	25
2.4	Sensitivity of Σ_3 asymmetry to the proton spin polarisabilities	26
3.1	Scalar polarisabilities determined from a dispersion relation analysis of low-energy Compton scattering data	30
3.2	Backward spin polarisability determined from a dispersion relation analysis of Compton scattering data	32
3.3	Σ_{2x} Compton scattering asymmetry for ω from 273 MeV to 303 MeV	38
4.1	MAMI racetrack microtron system	42
4.2	Layout of the MAMI electron accelerator	43
4.3	Example enhancement spectrum for coherent bremsstrahlung .	48
4.4	An example Stonehenge plot	49
4.5	Glasgow Tagged photon spectrometer	51
4.6	Example distribution of electrons within the Glasgow Tagged photon spectrometer	52
4.7	Liquid hydrogen target	53
4.8	Simulated geometry of the CB-TAPS system.	54
4.9	An example $\Delta E/E$ histogram	56
4.10	$\Delta E/E$ histogram comparison for run period	60
5.1	Cluster structure of the Crystal Ball and TAPS	64
5.2	Angular distribution between PID hits, MWPC hits, and NaI clusters	66
5.3	Example set of ADC and TDC distributions for a BaF ₂ crystal	72

5.4	Example timing distributions of NaI clusters, PID hits, BaF ₂ clusters, and Veto hits	73
5.5	Timing calibration for the CB-TAPS detector system	74
5.6	Example invariant mass distributions of NaI clusters	75
5.7	Tagging efficiency for amorphous and diamond radiators	78
5.8	Coherent Bremsstrahlung enhancement distributions	79
5.9	Fitting of polarisation enhancement distributions	79
5.10	Coherent Bremsstrahlung polarisation distributions	80
5.11	Polarisation distributions at coherent edge positions 300 MeV and 320 MeV	82
5.12	Distribution of coherent edge positions from active fitting	83
5.13	Polarisation errors from edge fitting	85
6.1	Invariant mass distribution of π^0 mesons	88
6.2	Time signature distribution of π^0 mesons	89
6.3	Example missing mass distribution of π^0 mesons	91
6.4	Example missing mass distribution with empty target subtraction	92
6.5	Example ϕ -distribution of π^0 mesons	94
6.6	Determination of correction factor, F	95
6.7	Example asymmetry distribution with empty target subtraction	95
6.8	Polarisation offset parameters	96
6.9	Available π^0 photoproduction statistics	97
6.10	Σ_3 Asymmetry, $\theta = 60$ to 65 degrees	99
6.11	Σ_3 Asymmetry, $\theta = 90$ to 95 degrees	99
6.12	Asymmetry fits, $\theta = 60$ to 65 degrees	100
6.13	Asymmetry fits, $\theta = 90$ to 95 degrees	101
6.14	Σ_3 Asymmetry, $E_\gamma = 297.0 \pm 5.1$ MeV	102
6.15	Coplanarity and opening angle distributions	104
6.16	Simulated coplanarity and opening angle distributions	106

6.17	Example missing mass distribution of Compton photons . . .	108
6.18	Simulated and experimental data: π^0 photoproduction	109
6.19	Simulated and experimental data: Compton scattering at E = 277.1 ± 10.1 MeV	110
6.20	Simulated and experimental data: Compton scattering at E = 297.0 ± 10.1 MeV	111
6.21	Simulated and experimental data: Low energy recoil protons .	112
6.22	Asymmetry calculated as a function of missing mass cut . . .	114
6.23	Logic steps of missing mass algorithm	115
6.24	Missing mass algorithm results: E = 277.1 ± 10.1 MeV	116
6.25	Missing mass algorithm results: E = 297.0 ± 10.1 MeV	117
6.26	Empty target missing mass distributions for Compton photons	118
6.27	Example ϕ -distribution for Compton photons	120
6.28	Determination of correction factor, F	121
6.29	Example asymmetry distribution of Compton photons	121
6.30	Asymmetry distribution results: E = 277.1 ± 10.1 MeV	123
6.31	Asymmetry distribution results: E = 297.0 ± 10.1 MeV	124
6.32	Σ_3 asymmetry results: E = 277.1 ± 10.1 MeV	125
6.33	Σ_3 asymmetry results: E = 297.0 ± 10.1 MeV	126
7.1	Σ_3 asymmetry results with new spin polarisability values . . .	131

Abstract

Nucleon polarisabilities are fundamental structure observables, like the nucleon mass or charge, which are sensitive to the internal quark dynamics of the nucleon. Polarised Compton scattering off the proton can be used to study the polarisabilities of the proton, thus probing the internal structure of the proton. Spin dependent terms of the nucleon polarisabilities quantify the response of the proton's spin to an applied electromagnetic field. The leading order polarisabilities, denoted by $\bar{\gamma}_{E1E1}$, $\bar{\gamma}_{M1M1}$, $\bar{\gamma}_{E1M2}$, and $\bar{\gamma}_{M1E2}$, quantify the spin response to electric and magnetic dipole and quadrupole interactions.

Single polarization observables for Compton scattering, which are sensitive to these polarisabilities, were measured along with single polarization observables π^0 photoproduction within the $\Delta(1232)$ resonance region. Σ_3 is a single polarisation observable which connects the polarised and unpolarised cross sections for linearly polarised photons incident upon unpolarised protons. Within this work, the execution and analysis of an experiment completed at the MAMI tagged photon facility in Mainz, Germany, is presented. Σ_3 was measured for π^0 photoproduction for incident photon energies of 210 MeV up to 307 MeV (just below two-pion threshold). Σ_3 was measured for Compton scattering for incident photon energies of 267 MeV to 307 MeV.

A new extraction of the leading order spin polarisabilities of the proton is presented. This extraction used Σ_3 results for Compton scattering from this work, and Σ_{2x} results from previous measurements at the MAMI tagged photon facility. Through this analysis, the spin polarisabilities of the proton were determined to be $\bar{\gamma}_{E1E1} = -5.0 \pm 1.5$, $\bar{\gamma}_{M1M1} = 3.13 \pm 0.88$, $\bar{\gamma}_{E1M2} = 1.7 \pm 1.7$, and $\bar{\gamma}_{M1E2} = 1.26 \pm 0.43$, in units of 10^{-4} fm^4 . These experimentally determined spin polarisabilities are in good agreement with dispersion theory, K-matrix theory, and Heavy Baryon chiral perturbation theory calculations.

List of Abbreviations and Symbols Used

α_e	Electromagnetic coupling constant
α_{E1}	electric dipole scalar polarisability
α_{E2}	electric quadrupole scalar polarisability
\mathbf{a}_i	Low-energy constants of dispersion relations
\mathbf{A}_i	Scattering amplitudes of dispersion relations
ADC	Analog-to-digital converter
β_{M1}	magnetic dipole scalar polarisability
β_{M2}	magnetic quadrupole scalar polarisability
BaF ₂	Barium fluoride,
CB	Crystal Ball Photon Spectrometer
CM	Center of mass
DAQ	Data acquisition
DR	Dispersion relation
E	Electric field
ϵ_{Tagg}	Tagging efficiency
EFT	Effective field theory
EM	Electromagnetic
$F_{\gamma\perp}$	Photon flux for polarisation orientation “perp”
$F_{\gamma\parallel}$	Photon flux for polarisation orientation “para”
F	Ratio of photon fluxes (“perp”/“para”)
FPGA	Field-programmable gate array
FWHM	Full width at half maximum
γ_{E1E1}	electric dipole-dipole spin polarisability

γ_{M1M1}	magnetic dipole-dipole spin polarisability
γ_{E1M2}	electric dipole magnetic quadrupole spin polarisability
γ_{M1E2}	magnetic dipole electric quadrupole spin polarisability
γ_0	forward spin polarisability
γ_π	backward spin polarisability
GoAT	Generation of Analysis Trees
H	Magnetic field
H_{eff}	Effective Hamiltonian
HBχPT	Heavy Baryon χ PT
HDSM	Harmonic double-sided microtron
IM	Invariant mass
κ	Anomalous magnetic moment
LEX	Low energy expansion
LH₂	Liquid hydrogen
LINAC	Linear accelerator
M	Mass of the nucleon
MAMI	Mainzer Microtron
MM	Missing mass
MWPC	Multiwire proportional chambers
ν	Mandelstam variable, ν
NaI	Sodium iodide
NB	Non-Born
Ω_{OA}	Opening angle
OA	Opening angle
p_γ	Degree of linear polarisation

ϕ	Azimuthal angle
ϕ_o	Polarisation offset
ϕ_{cop}	Coplanarity angle
PbWO₄	Lead tungstate
PDG	Particle Data Group
PID	Particle identification detector
PMT	Photomultiplier tube
PSA	Pulse shape analysis
QCD	Quantum chromodynamics
QED	Quantum electrodynamics
R	Enhancement of linear polarisation
RTM	Racetrack microtron
s	Mandelstam variable, s
σ_{\perp}	Differential cross section for polarisation orientation “perp”
σ_{\parallel}	Differential cross section for polarisation orientation “para”
Σ_{2x}	Double polarisation observable connected to circularly polarised photons and transversely (x-axis) polarised protons
Σ_{2z}	Double polarisation observable connected to circularly polarised photons and longitudinally (z-axis) polarised protons
Σ_3	Single polarisation observable connected to linearly polarised photons and unpolarised protons
SSE	Small scale expansion
t	Mandelstam variable, t
θ	Polar angle
TAPS	Two armed photon spectrometer

TDC	Time-to-digital converter
TOF	Time of flight
u	Mandelstam variable, u
VME	Versa Module Europa
ω	Incident photon energy
ω'	Scattered photon energy
χPT	Chiral perturbation theory

Acknowledgements

Achievements and accomplishments in science are rarely a singular effort. Nowhere is that more true than the field of experimental physics. The reality is, the community of people who have supported me is too large for personal acknowledgements in each case. However, I am grateful for their support.

First, and foremost, I would like to thank my supervisor. Dr. Adam Sarty. You've been everything I could wish for in a supervisor, and more. You've given me so many opportunities over the years, and I really can't put in to words what you've done for me. Thank you. To my committee, and my external Dr. Henry Weller, thank you for your time, your corrections, and your tough questions. A special thankyou to Dr. Dave Hornidge. You've always been there for me as a supervisor and a mentor while in Germany. To the rest of Team Compton, especially Phil and Evie, thanks for all the support and good times. To Oli, thank you for late night portal games, and morning coffees, and for keeping me sane while finishing my thesis. And finally, thank you to my parents and my family who encouraged me to take on new challenges and risks in life, and made me the person I am today.

*The beam is on
our hopes won't be shattered,
Our photons, however
will be tagged then scattered.*

Chapter 1

Introduction

Quantum electrodynamics (QED) is a quantum field theory describing the electromagnetic (EM) force, where the EM force is mediated by the photon. Electromagnetic interactions with charged point-like particles are well described by QED. However, when describing the interactions of non point-like particles, like the proton, a model of the internal structure is required to describe the charge and magnetic distributions being probed by the QED photon. Quantum chromodynamics (QCD) is a quantum field theory describing the strong force, which is mediated by gluons. At scales close to a femtometre, the strong force is responsible for binding quarks together to form hadronic particles. A residual strong force remains at slightly larger scales, up to about 3 fm, which is responsible for binding protons and neutrons together inside the nucleus. While the Lagrangian for this QCD interaction is well known at very high energies, it quickly becomes difficult to solve as the energy scale decreases (corresponding to distance scale increases). For this reason, structure observables of the hadron (e.g. size, shape, polarisability) cannot be obtained from QCD directly. However, QCD inspired models of the effective quark interactions have been developed and a common goal of modern hadronic structure studies is to make connections between the results of these QCD-inspired models and experimental results. This thesis represents one such venture to provide measurement of some unique nucleon structure properties that are hoped to provide particular sensitivity to disentangle model properties, and models themselves, in pursuit of identifying the best QCD-inspired models.

QCD has two main properties: confinement and asymptotic freedom. Confinement requires that a force exists between quarks which increases with distance. Because of this increasing force, as the two quarks separate, it becomes more energetically favourable to create a new quark/anti-quark pair before the quarks separate and become unbound from each other. The second property of QCD, asymptotic freedom,

requires that quarks interact weakly as energy increases (or distance decreases). QCD is therefore dominated by confinement at low-energies and dominated by asymptotic freedom at high-energies. Perturbative QCD provides a limited but powerful approach to produce testable predictions within the framework of QCD. By restricting oneself to the region of QCD dominated by asymptotic freedom, namely high-energy interactions, the strong force coupling constant, α_s , is small. In this region, many terms can be simplified allowing for perturbative QCD predictions. However, as the energy scale decreases, or distance scale increases, the coupling constant becomes so large that perturbative QCD is no longer useful. For this reason, structure observables of hadrons (eg. size, shape) cannot be directly obtained through perturbative QCD. Non-perturbative approaches to QCD exists, most notably lattice QCD. Lattice QCD is a lattice gauge theory, which means spacetime is discretized into a lattice of points. Quark fields are defined at the lattice points and gluon fields are defined on the links between lattice points. As the lattice size grows to infinity, and the lattice spacing, a , goes to zero, a complete description of spacetime is recovered. However, computationally this is difficult to realise and results from lattice QCD are often derived from an extrapolation to $a = 0$.

This thesis focuses on structure observables for the proton called polarizabilities, which are accessible through the nuclear Compton scattering process. Nuclear Compton scattering is a two-body elastic scattering process of a photon off the nucleus. In the case of nuclear Compton scattering with hydrogen, ^1H , the photon scatters off an individual proton,

$$\gamma + p \rightarrow \gamma' + p'. \quad (1.1)$$

A proton is a composite system made of three valence quarks (uud). At photon energies below ≈ 100 MeV, scattering cross sections for photons incident on the proton depend on the protons charge, mass, and magnetic moment as well as on two fundamental structure constants - the electric and magnetic scalar (spin-independent) polarizabilities, α_{E1} and β_{M1} respectively. These scalar polarizabilities quantify the response of the protons structure to an electric or magnetic field and can be thought of as the electric “stretchability” and the magnetic “align-ability” of the proton. At incident photon energies above 100 MeV, higher order terms must be included in the calculation of the scattering cross sections (thus creating a dependence on structure

quantities beyond those listed previously). In particular, the four spin polarizabilities (γ_{E1E1} , γ_{M1M1} , γ_{E1M2} , and γ_{M1E2}) are the next leading order terms. While the spin-dependent polarizabilities have no classical analog, they are often analogized to the “stiffness” of the nucleon against electromagnetic deformations. These polarisabilities describe the proton’s internal response to electromagnetic interactions. As stated earlier, a primary goal of modern hadronic structure studies is to make connections between the results of QCD-inspired models and lattice QCD calculations to the results of experiment- and nuclear Compton scattering provides a powerful interaction with which QCD-inspired structure models can be tested and constrained. Nucleon polarizabilities, fundamental structure observables sensitive to the internal quark dynamics of the nucleon, provide an ideal testing ground for the validity of QCD-inspired structure models.

Although the leading order scalar polarisabilities, α_{E1} and β_{M1} , have been studied for the proton and the neutron, very few experiments have attempted to study the spin-dependent polarizabilities (γ_{E1E1} , γ_{M1M1} , γ_{E1M2} , and γ_{M1E2}), and no experiment to date has separated all four leading spin polarisability terms. The scattering behaviour of Compton scattering is sensitive to the polarisabilities, and therefore can be used to access the nucleon polarisabilities. Although experimental and theoretical interest in Compton scattering has existed for decades, modern experiments using polarised photon beams and targets provide access to new internal structure observables. A series of polarised Compton scattering experiments have been proposed to run at the MAMI tagged photon facility in Mainz, Germany. These experiments would each measure a single or double polarisation asymmetry (Σ_3 , Σ_{2x} , and Σ_{2z}) for Compton scattering off the proton. Each asymmetry quantifies a change in the scattering behaviour, or cross section, due to a change in polarisation, and each exhibits a unique sensitivity to the individual spin polarisabilities. A global study of the asymmetries will allow for the first extraction of the four leading order spin polarisabilities of the proton for the first time ever. A measurement of the proton spin polarisabilities is meaningful for two main reasons, (1) the spin polarisabilities are fundamental structure constants of the proton, just like the radius, charge, mass and magnetic moment, which have not been measured before and (2) the spin polarisabilities are an ideal test for exploring the validity of QCD-inspired structure models.

A detailed overview of the nucleon polarisabilities from the viewpoint of the full, formal theoretical physics standpoint will be presented in Chapter 2. This theoretical overview will detail the connection between nucleon polarisabilities and Compton scattering, a discussion of sum rules related to the polarisabilities, and finally the relation between measurable asymmetries and the polarisabilities. In Chapter 3, a review of previous experimental and theoretical studies specifically for the proton polarisabilities is presented. Chapters 4 through 6 outline the execution and analysis of my experiment at the MAMI tagged photon facility to measure the Σ_3 asymmetry, a single polarisation observable, which connects the polarised and unpolarised cross sections for linearly polarised photons incident upon unpolarised protons. My detailed measurements of Σ_3 within the $\Delta(1232)$ resonance region will be presented for both Compton scattering (the main thesis focus) and π^0 photoproduction (a reaction measured simultaneously with the Compton scattering reaction, providing important experimental systematic checks as well as useful complementary data). Results for the Σ_3 asymmetry will be compared to previous measurements in Chapter 6. Finally, a preliminary extraction of the proton's spin polarisabilities is provided in Chapter 7. This final extraction combines Σ_3 results derived from this work and a previous measurement from our MAMI collaboration by Martel [1] of Σ_{2x} for Compton scattering, a double polarisation observable, which connects the polarised and unpolarised cross sections for circularly polarised photons incident upon a transversely polarised proton target. The analysis by Martel was the first measurement of a double polarisation observable for Compton scattering, and allowed for a very preliminary extraction of γ_{E1E1} of $(-4.5 \pm 1.5) \times 10^{-4} \text{ fm}^4$. A more recent analysis by Martel [2] combined earlier Σ_3 results from the LEGS collaboration [3][4] with Σ_{2x} results from Martel to determine a preliminary extraction of the proton's spin polarisabilities. In Chapter 7, a comparison of two spin polarisability extractions is given as the highlight result of this thesis: the previous extraction combining the earlier LEGS and Martel measurements is compared to a new extraction obtained by combining Martel's Σ_{2x} results with this work's Σ_3 measurements.

Chapter 2

Theoretical Review

2.1 Nucleon Compton scattering

Nuclear Compton scattering, specifically Compton scattering from protons and neutrons, provides important insight into the internal structure of nucleons. Nuclear Compton scattering experiments can probe the internal structure of nucleons and act as a test of quantum field theories describing the electromagnetic properties of the nucleus, and their constituent nucleons. Although experimental and theoretical interest in Compton scattering has existed for decades, modern experiments using polarised photon beams and targets provide access to new internal structure observables.

2.1.1 Compton scattering amplitudes

The scattering amplitude for nucleon Compton scattering,

$$\gamma + N \rightarrow \gamma' + N', \quad (2.1)$$

can be expanded in terms of the energy of the incident photon, ω . To first order in the incident photon energy, ω^1 , the scattering amplitude is consistent with scattering from a point-like particle. However, at higher orders (ω^2 and above), degrees of freedom related to the internal structure and spin of the nucleus will enter the scattering amplitudes.

2.1.1.1 First order expansion: Born terms

The zeroth and first order terms, known together as the Born terms, depend solely on the nucleon's charge, mass, and magnetic moment. Following the derivation given by Levchuk and L'vov [5], the zeroth term of the effective Hamiltonian has the form,

$$H_{\text{eff}}^{(0)} = eZ\phi + \frac{\pi^2}{2M}, \quad (2.2)$$

where eZ is the nucleon's electric charge, ϕ is the scalar potential, M is the nucleon's mass, and where $\boldsymbol{\pi}$ is a covariant momentum defined as,

$$\boldsymbol{\pi} = \mathbf{p} - eZ\mathbf{A}, \quad (2.3)$$

where \mathbf{p} is the momentum and \mathbf{A} is the external vector potential. At first order, the effective Hamiltonian is also dependent on the anomalous magnetic moment, κ , and has the form,

$$H_{\text{eff}}^{(1)} = -\frac{e(Z + \kappa)}{2M} \boldsymbol{\sigma} \cdot \mathbf{H} - \frac{e(Z + 2\kappa)}{8M^2} \boldsymbol{\sigma} \cdot (\mathbf{E} \times \boldsymbol{\pi} - \boldsymbol{\pi} \times \mathbf{E}), \quad (2.4)$$

where \mathbf{E} and \mathbf{H} are the electric and magnetic field, respectively, and $\boldsymbol{\sigma}$ is the proton's Pauli spin matrices. In the case of Compton scattering off a proton, the electric charge is simply equal to e and the Born terms of the Compton scattering amplitude can be written,

$$\begin{aligned} H_{\text{eff}}^{(0)} &= e\phi + \frac{(\mathbf{p} - e\mathbf{A})^2}{2M}, \\ H_{\text{eff}}^{(1)} &= -\frac{e(1 + \kappa)}{2M} \boldsymbol{\sigma} \cdot \mathbf{H} - \frac{e(1 + 2\kappa)}{8M^2} \boldsymbol{\sigma} \cdot (\mathbf{E} \times \boldsymbol{\pi} - \boldsymbol{\pi} \times \mathbf{E}). \end{aligned} \quad (2.5)$$

2.1.1.2 Second order expansion: Scalar Polarisabilities

The first order effective Hamiltonian, given for Compton scattering off the proton in Equation (2.5), is valid as $\omega \rightarrow 0$. However, as ω increases, the nucleon's internal degrees of freedom must be included in the scattering amplitudes. At second order, the effective Hamiltonian (given in the Heaviside unit system) has the form,

$$H_{\text{eff}}^{(2)} = -\frac{1}{2} [4\pi\alpha_{E1}\mathbf{E}^2 + 4\pi\beta_{M1}\mathbf{H}^2], \quad (2.6)$$

with two new terms, $\alpha_{E1}(\omega)$ and $\beta_{M1}(\omega)$, which are the electric and magnetic scalar dipole polarisabilities respectively [6]. These scalar dipole polarisabilities, functions of ω , describe the response of the nucleon's structure to an electric or magnetic field. They can be understood by thinking of the nucleon as a composite system formed by its quark core surrounded by a charged virtual pion cloud. This pion charge

cloud, often referred to as the sea quarks, arises due to the nucleon's emission and subsequent absorption of virtual pions. Similar to an atomic polarisability, where an atom within an electric field acquires a dipole moment associated with an electron cloud surrounding the nucleus, the nucleon itself acquires an electric dipole moment associated with its pion charge cloud. This induced electric dipole moment, \mathbf{p} , is proportional to the electric field, \mathbf{E} , through the electric dipole polarisability, α_{E1} ,

$$\mathbf{p} = 4\pi\alpha_{E1}\mathbf{E}. \quad (2.7)$$

Similarly, a nucleon in a magnetic field will obtain a magnetic dipole moment, \mathbf{m} , proportional to the magnetic field, \mathbf{B} , through the magnetic dipole polarisability, β_{M1} ,

$$\mathbf{m} = 4\pi\beta_{M1}\mathbf{B}. \quad (2.8)$$

α_{E1} is often referred to as the ‘‘electric stretchability’’ which can be related to a stretching of the pion charge cloud within the electric field. There are two competing processes which contribute to the magnetic scalar polarisability. The core quarks exhibit paramagnetism while the pion charge cloud exhibits both paramagnetism and diamagnetism. The paramagnetism is, however, the stronger of the two and the overall dipole moments align with the magnetic field. For this reason, β_{M1} is often referred to as the ‘‘magnetic align-ability’’. While α_{E1} and β_{M1} are functions of ω , a set of static scalar polarisabilities can be determined as $\omega \rightarrow 0$. These static scalar polarisabilities are denoted by $\bar{\alpha}_{E1}$ and $\bar{\beta}_{M1}$.

Higher order scalar polarisabilities, related to electric or magnetic quadrupole moments and higher, can be defined in a similar fashion. However, these terms do not appear in the scattering amplitudes below fourth order. The quadrupole terms for the electric and magnetic scalar polarisabilities are denoted by α_{E2} and β_{M2} . Similarly, the quadrupole terms of the static scalar polarisabilities are denoted by $\bar{\alpha}_{E2}$ and $\bar{\beta}_{M2}$.

2.1.1.3 Third order expansion: Spin Polarisabilities

Degrees of freedom related to the nucleon's spin appear in the third order (ω^3) effective Hamiltonian, given by,

$$H_{\text{eff}}^{(3)} = -\frac{1}{2} \left[4\pi\gamma_{E1E1}\boldsymbol{\sigma} \cdot (\mathbf{E} \times \dot{\mathbf{E}}) + 4\pi\gamma_{M1M1}\boldsymbol{\sigma} \cdot (\mathbf{H} \times \dot{\mathbf{H}}) \right] \\ + 4\pi \left[\gamma_{E1M2}H_{ij}\sigma_i E_j - \gamma_{M1E2}E_{ij}\sigma_i H_j \right], \quad (2.9)$$

where $\dot{\mathbf{E}}$ and E_{ij} are partial derivatives with respect to time and space, defined respectively as $\dot{\mathbf{E}} = \partial_t \mathbf{E}$ and $E_{ij} = \frac{1}{2}(\nabla_i E_j + \nabla_j E_i)$. $\dot{\mathbf{H}}$ and H_{ij} are defined in a similar fashion. The new terms appearing in the third order effective Hamiltonian - γ_{E1E1} , γ_{M1M1} , γ_{E1M2} and γ_{M1E2} - are the leading order spin polarisabilities and they quantify the spin dependent response of the proton to an electromagnetic interaction. Although it is difficult to establish a classical analog for the spin polarisabilities, they can be understood as an induced precession of the nucleon spin. Using this understanding, the frequency of this precession is proportional to the magnitude of the spin polarisabilities and the direction of precession is connected to the sign. Each polarisability quantifies a unique spin response term and the nomenclature of the spin polarisability terms can be related to the multipole fields associated with the electromagnetic interaction. In terms of the Compton scattering interaction, each term corresponds to the specific combination of total angular momenta and parities of the incident and scattered photons. If the total angular momentum of a photon is denoted by L , an electric or magnetic multipole field is denoted by EL or ML respectively. The parity is then given by:

$$\pi_L = (-1)^L, \quad (2.10)$$

for an electric multipole field, and:

$$\pi_L = (-1)^{L+1}, \quad (2.11)$$

for a magnetic multipole field. The γ_{M1E2} polarisability, for example, can thus be described in terms of the incident and scattered photon properties: the incident and scattered photons carry total angular momentum and parity given by 2^+ and 1^+ respectively. Due to parity and angular momentum conservation rules, the photon properties place corresponding restrictions on the allowed initial and final states of the proton. To form a complete picture, we can again relate this to the γ_{M1E2} spin polarisability. Since the Compton scattering interaction involves a $\frac{1}{2}^+$ proton in its initial and final states, it is straightforward to show that one possible intermediate state could be the excitation of the proton to the $\frac{3}{2}^+$ state (the excitation of a Δ^+) through the absorption of an E2 photon. This can be followed by the emission of an M1 photon and de-excitation of the proton back to the $\frac{1}{2}^+$ state:

$$\gamma(2^+) + p(\frac{1}{2}^+) \rightarrow \Delta^+(\frac{3}{2}^+) \rightarrow \gamma(1^+) + p(\frac{1}{2}^+). \quad (2.12)$$

Higher order spin polarisabilities, beyond the dipole-dipole ($\gamma_{E1E1}, \gamma_{M1M1}$) and dipole-quadrupole ($\gamma_{E1M2}, \gamma_{M1E2}$) terms, appear in the higher order effective Hamiltonians.

Similar to the scalar polarisabilities, the spin polarisabilities are also functions of ω and a set of static spin polarisabilities can be determined as $\omega \rightarrow 0$ where the leading order terms are denoted by $\bar{\gamma}_{E1E1}, \bar{\gamma}_{M1M1}, \bar{\gamma}_{E1M2},$ and $\bar{\gamma}_{M1E2}$. Two linear combinations of the static spin polarisabilities, $\bar{\gamma}_{E1E1}, \bar{\gamma}_{M1M1}, \bar{\gamma}_{E1M2},$ and $\bar{\gamma}_{M1E2},$ can be defined. These are known as the forward spin polarisability, given by,

$$\gamma_0 = -\bar{\gamma}_{E1E1} - \bar{\gamma}_{M1M1} - \bar{\gamma}_{E1M2} - \bar{\gamma}_{M1E2}, \quad (2.13)$$

and the backward spin polarisability, given by,

$$\gamma_\pi = -\bar{\gamma}_{E1E1} + \bar{\gamma}_{M1M1} - \bar{\gamma}_{E1M2} + \bar{\gamma}_{M1E2}. \quad (2.14)$$

The forward and backward polarisabilities appear directly in the Compton scattering cross section at $\theta_{\gamma'} = 0^\circ$ or 180° respectively. For example, the differential cross section for Compton scattering off the proton at forward angles is given in the lab frame by [7],

$$\begin{aligned} \left(\frac{d\sigma}{d\Omega}\right)_{(\theta=0)} &= \left[\frac{e^2}{4\pi M} - \omega^2 (\bar{\alpha}_{E1} + \bar{\beta}_{M1}) \right]^2 + \frac{e^4 \kappa^4 \omega^2}{64\pi^2 M^3} - \frac{e^2 \omega^4}{2\pi M} \\ &\quad - \frac{e^2 \omega^4}{24\pi M} (12\bar{\alpha}_{E\nu} + 12\bar{\beta}_{M\nu} + \bar{\alpha}_{E2} + \bar{\beta}_{M2}) - \frac{e^4 \kappa^2 \omega^4}{4\pi M} \gamma_0 + \mathcal{O}(\omega^6), \end{aligned} \quad (2.15)$$

where γ_0 appears directly in the last term of the cross section equation.

In equation 2.15, additional terms appear which are related to expansions of the scattering amplitude beyond third order. The Compton scattering amplitude can be extended to even higher orders in ω , resulting in additional terms in the effective Hamiltonian. A fourth order expansion is given by Babusci, Giordano, L'vov, Matone, and Nathan [7],

$$H_{\text{eff}}^{(4)} = -\frac{1}{2} \left[4\pi\alpha_{E\nu} \dot{\mathbf{E}}^2 + 4\pi\beta_{M\nu} \dot{\mathbf{H}}^2 \right] - \frac{1}{12} \left[4\pi\alpha_{E2} E_{ij}^2 + 4\pi\beta_{M2} H_{ij}^2 \right]. \quad (2.16)$$

As discussed previously, $\bar{\alpha}_{E2}$ and $\bar{\beta}_{M2}$ are the quadrupole terms of the electric and magnetic scalar polarisabilities. Two additional terms, $\bar{\alpha}_{E\nu}$ and $\bar{\beta}_{M\nu}$, known as the dispersion polarisabilities also appear. These dispersion polarisabilities, which appeared in equation 2.15, can be thought of as correction factors to the scalar dipole polarisabilities, related to the ω -dependence of the dipole polarisabilities [8].

2.1.2 Low-energy expansion

The low-energy expansion, developed by Petrun'kin [9][10], calculated the Compton scattering amplitude to order ω^2 . This expansion gives an expression for the differential cross section, given in Gaussian units, as,

$$\left(\frac{d\sigma}{d\Omega}\right) = \left(\frac{d\sigma}{d\Omega}\right)_{\text{Born}} + \left(\frac{d\sigma}{d\Omega}\right)_{\text{NB}}$$

where,

$$\left(\frac{d\sigma}{d\Omega}\right)_{\text{NB}} = -\omega\omega' \left(\frac{\omega'}{\omega}\right)^2 \frac{e^2}{M} \left[\frac{\bar{\alpha}_{E1} + \bar{\beta}_{M1}}{2} (1+z)^2 + \frac{\bar{\alpha}_{E1} - \bar{\beta}_{M1}}{2} (1-z)^2 \right], \quad (2.17)$$

where $z = \cos \theta_{\gamma'}$ and ω' is the energy of the scattered photon, given by,

$$\omega' = \frac{\omega}{1 + (\omega/M)(1+z)} \quad (2.18)$$

The Born term, as described in Section 2.1.1.1, describes Compton scattering off a point-like particle. The non-Born (NB) term includes the structure related terms α_{E1} and β_{M1} . Since the Petrun'kin low-energy expansion only includes up to order ω^2 , the spin polarisabilities do not appear in equation (2.17). The low-energy expansion was further developed by Guiasu, Pomponiu and Radescu to include terms up to the fourth order [11].

2.1.3 Dispersion relations at fixed- t

An expansion of the Compton scattering amplitude in terms of ω provides powerful insight into the scattering dependencies. However, as ω increases, the low-energy expansions can not be applied. Dispersion relations (DRs), which are partially constrained by experimental data, can provide a more powerful approach to study the Compton scattering amplitudes in these higher energy regions (eg. Δ -resonance region). Figure 2.1 shows the comparison of fixed- t dispersion relations to the low-energy expansion (LEX) and scattering from a point-like proton (Born terms). Above ≈ 20 MeV, the Born terms no longer agree with LEX and DR theory curves. LEX and DRs begin to diverge at $\omega \approx 100$ MeV. A comparison of DRs to low energy Compton scattering experiments shows that data were in agreement with DRs (not LEX) above $\omega \approx 100$ MeV, showing the importance of theories beyond the low-energy expansion.

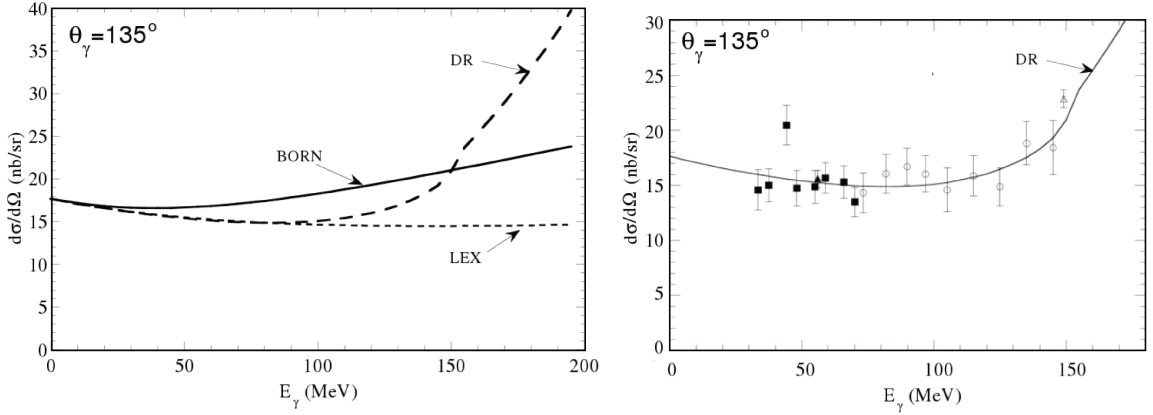


Figure 2.1: **Left:** Theoretical cross sections for Compton scattering at $\theta_{\gamma'} = 135^\circ$ are shown for Born terms alone, the low-energy (LEX) expansion, and fixed- t dispersion relations (DR) [12]. **Right:** Experimental cross sections measured for Compton scattering at $\theta_{\gamma'} = 135^\circ$ along with fixed- t dispersion relations (DR). Reproduced from [12].

A set of Lorentz invariant Mandelstam variables can be defined in the center of mass frame as,

$$s = (k + p)^2, \quad u = (k - k')^2, \quad t = (k - p')^2, \quad \nu = (s - u)/4M, \quad (2.19)$$

where k and k' are the four-momenta of the incident and scattered photon and p and p' are the four-momenta of the target and recoil nucleon. The sum of the Mandelstam variables is related to the nucleon mass, M , by,

$$s + u + t = 2M^2. \quad (2.20)$$

The differential cross section can be expressed as a function of the scattering T-matrix,

$$\left(\frac{d\sigma}{d\Omega} \right) = \frac{|T_{fi}|^2}{64\pi^2 s}. \quad (2.21)$$

The T-matrix can be defined by six independent scattering amplitudes, $A_i(\nu, t)$, first introduced by L'vov, Petrun'kin, and Schumacher [13], which are functions of the Mandelstam variables ν and t . In the lab frame, ν and t can be expressed in terms of the incident and scattered photon energy and angle,

$$\nu = (\omega + \omega')/2, \quad t = -2\omega\omega'(1 - z). \quad (2.22)$$

The T-matrix for the Compton scattering amplitude is expressed in the lab frame as,

$$\begin{aligned}
N(t)T_{fi} = & \left[\left(1 - \frac{t}{4M^2}\right) (-A_1 - A_3) - \frac{\nu^2}{M^2}A_5 - A_6 \right] 2m\omega\omega' \mathbf{e}'^* \cdot \mathbf{e} \\
& + \left[\left(1 - \frac{t}{4M^2}\right) (A_1 - A_3) + \frac{\nu^2}{M^2}A_5 - A_6 \right] 2m\omega\omega' \mathbf{h}'^* \cdot \mathbf{h} \\
& + \left[A_2 + \left(1 - \frac{\omega'}{M}\right) A_4 + \frac{\nu}{M}A_5 + A_6 \right] i\omega^2\omega' \boldsymbol{\sigma} \cdot \hat{\mathbf{k}}\mathbf{h}'^* \cdot \mathbf{e} \\
& - \left[A_2 - \left(1 + \frac{\omega}{M}\right) A_4 - \frac{\nu}{M}A_5 - A_6 \right] i\omega\omega'^2 \boldsymbol{\sigma} \cdot \hat{\mathbf{k}}'\mathbf{h}'^* \cdot \mathbf{e} \\
& + \left[A_2 + \left(1 + \frac{\omega'}{M}\right) A_4 + \frac{\nu}{M}A_5 - A_6 \right] i\omega^2\omega' \boldsymbol{\sigma} \cdot \hat{\mathbf{k}}\mathbf{e}'^* \cdot \mathbf{h} \\
& - \left[A_2 - \left(1 - \frac{\omega}{M}\right) A_4 - \frac{\nu}{M}A_5 + A_6 \right] i\omega\omega'^2 \boldsymbol{\sigma} \cdot \hat{\mathbf{k}}'\mathbf{e}'^* \cdot \mathbf{h} \\
& + \left[A_5 - A_6 \right] 2i\nu\omega\omega' \boldsymbol{\sigma} \cdot \mathbf{h}'^* \times \mathbf{h} \\
& - \left[A_5 + A_6 \right] 2i\nu\omega\omega' \boldsymbol{\sigma} \cdot \mathbf{e}'^* \times \mathbf{e}
\end{aligned} \tag{2.23}$$

where \mathbf{e} and \mathbf{e}' are the polarization vectors of the incident and scattered photons, \mathbf{h} and \mathbf{h}' are given by,

$$\mathbf{h} = \hat{\mathbf{k}} \times \mathbf{e}, \quad \mathbf{h}' = \hat{\mathbf{k}}' \times \mathbf{e}', \tag{2.24}$$

and $N(t)$ is a function of the Mandelstam variable, t , given by,

$$N(t) = \sqrt{1 - \frac{t}{4M^2}}. \tag{2.25}$$

The scattering amplitudes can be separated into Born and non-Born terms, given by,

$$A_i(\nu, t) = A_i^{\text{Born}}(\nu, t) + A_i^{\text{NB}}(\nu, t). \tag{2.26}$$

Dispersion relations have been used to study the scattering amplitudes, for example, see Pasquini, Drechsel, and Vanderhaeghen [14][15]. The real part of the scattering amplitudes, $\text{Re}A_i(\nu, t)$, can be related to their imaginary parts through dispersion relations at fixed- t :

$$\text{Re}A_i(\nu, t) = A_i^{\text{Born}}(\nu, t) + \frac{2}{\pi} \mathcal{P} \int_{\nu_{th}}^{\infty} \frac{\text{Im}_s A_i(\nu', t)}{\nu'^2 - \nu^2} d\nu', \tag{2.27}$$

where \mathcal{P} denotes the Cauchy principal value and $\text{Im}_s A_i$ are discontinuities in the s-channel of the Compton scattering process. In nuclear Compton scattering, s-channel

processes require that the photon and nucleon join to form an intermediate state. The integrand is integrated from the pion photoproduction threshold, ν_{thr} , where

$$\nu_{thr} = m_\pi + \frac{2m_\pi^2 + t}{4M}. \quad (2.28)$$

As ν goes to ∞ , the integral term of the dispersion relation does not converge for scattering amplitudes A_1 and A_2 . To ensure that all terms converge, dispersion relations are calculated at fixed- t , subtracting the case at $\nu = 0$. In this case, the subtracted dispersion relations are given by,

$$\text{Re}A_i(\nu, t) = A_i^{\text{Born}}(\nu, t) + [A_i(0, t) - A_i^{\text{Born}}(0, t)] + \frac{2}{\pi} \nu^2 \mathcal{P} \int_{\nu_{th}}^{\infty} \frac{\text{Im}_s A_i(\nu', t)}{\nu'(\nu'^2 - \nu^2)} d\nu'. \quad (2.29)$$

This process, of subtracting the case at $\nu = 0$, results in a class of dispersion relations known as once-subtracted fixed- t dispersion relations. Equation (2.26) can be rearranged to isolate the non-Born scattering amplitudes,

$$A_i^{\text{NB}}(\nu, t) = A_i(\nu, t) - A_i^{\text{Born}}(\nu, t), \quad (2.30)$$

and a set of low-energy constants can be defined as,

$$a_i = A_i^{\text{NB}}(0, 0), \quad a_{i,t} = \left(\frac{\partial A_i^{\text{NB}}}{\partial t} \right)_{\nu=t=0}. \quad (2.31)$$

The scalar and spin polarisabilities can be directly connected to these low-energy constants allowing the polarisabilities to be expressed in terms of a_i and $a_{i,t}$. The leading order scalar and spin polarisabilities (these are the polarisabilities which appear in the second and third order effective Hamiltonian for Compton scattering), can be expressed in terms of the low-energy constants, a_i . These are shown in the left column of equation (2.32). It is also possible to express higher order polarisabilities in terms of the low-energy constants. The next to leading order polarisabilities, can be expressed in terms of the low-energy constants, $a_{i,t}$. These are shown in the right column of equation (2.32).

$$\begin{aligned}
\bar{\alpha}_{E1} &= -\frac{1}{4\pi}(a_1 + a_3 + a_6), & \bar{\alpha}_{E2} &= -\frac{3}{\pi}(a_{1,t} + a_{3,t} + a_{6,t}), \\
\bar{\beta}_{M1} &= \frac{1}{4\pi}(a_1 - a_3 - a_6), & \bar{\beta}_{M2} &= \frac{3}{\pi}(a_{1,t} - a_{3,t} - a_{6,t}), \\
\bar{\gamma}_{E1E1} &= \frac{1}{8\pi M}(a_2 - a_4 + 2a_5 + a_6), & \bar{\gamma}_{E2E2} &= \frac{1}{24\pi M}(a_{2,t} - a_{4,t} + 3a_{5,t} + 2a_{6,t}), \\
\bar{\gamma}_{M1M1} &= \frac{-1}{8\pi M}(a_2 + a_4 + 2a_5 - a_6), & \bar{\gamma}_{M2M2} &= \frac{-1}{24\pi M}(a_{2,t} + a_{4,t} + 3a_{5,t} - 2a_{6,t}), \\
\bar{\gamma}_{E1M2} &= \frac{1}{8\pi M}(a_2 - a_4 - a_6), & \bar{\gamma}_{E2M3} &= \frac{1}{12\pi M}(a_{2,t} - a_{4,t} - a_6), \\
\bar{\gamma}_{M1E2} &= \frac{-1}{8\pi M}(a_2 + a_4 + a_6), & \bar{\gamma}_{M2E3} &= \frac{-1}{12\pi M}(a_{2,t} + a_{4,t} + a_{6,t}). \quad (2.32)
\end{aligned}$$

The forward and backward polarisabilities, described in equations (2.13) and (2.14), can also be expressed in terms of the low-energy constants, a_i ,

$$\begin{aligned}
\gamma_0 &= -\bar{\gamma}_{E1E1} - \bar{\gamma}_{M1M1} - \bar{\gamma}_{E1M2} - \bar{\gamma}_{M1E2} = \frac{1}{2\pi M} a_4, \\
\gamma_\pi &= -\bar{\gamma}_{E1E1} + \bar{\gamma}_{M1M1} - \bar{\gamma}_{E1M2} + \bar{\gamma}_{M1E2} = -\frac{1}{2\pi M}(a_2 + a_5). \quad (2.33)
\end{aligned}$$

Similarly, the sum of the scalar dipole polarisabilities is given by,

$$\bar{\alpha}_{E1} + \bar{\beta}_{M1} = -\frac{1}{2\pi}(a_3 + a_6), \quad (2.34)$$

and the difference of the scalar dipole polarisabilities is given by,

$$\bar{\alpha}_{E1} - \bar{\beta}_{M1} = -\frac{1}{2\pi} a_1. \quad (2.35)$$

2.2 Sum Rules

Four quantities were described in equations (2.33), (2.34) and (2.35): (1) $\bar{\alpha}_{E1} + \bar{\beta}_{M1}$ and (2) $\bar{\alpha}_{E1} - \bar{\beta}_{M1}$, the sum and difference between the scalar dipole polarisabilities respectively, and (3) γ_0 and (4) γ_π , the forward and backward polarisability respectively. A set of sum rules relate these quantities to the total photoabsorption cross section.

2.2.1 Baldin sum rule

The sum of the static ($\omega = 0$) dipole scalar polarisabilities, denoted by $\bar{\alpha}_{E1}$ and $\bar{\beta}_{M1}$, can be constrained by the Baldin sum rule [16], given by,

$$\bar{\alpha}_{E1} + \bar{\beta}_{M1} = \frac{1}{2\pi^2} \int_{\omega_{th}}^{\infty} \frac{\sigma_{tot}(\omega)}{\omega^2} d\omega, \quad (2.36)$$

where $\sigma_{tot}(\omega)$ is the total cross section. The lower limit of the integrand is ω_{th} , the threshold energy for photon-nucleon interactions. When considering the contribution from meson photoproduction to the total cross section (ex. $\gamma N \rightarrow \pi N$), the threshold energy corresponds to the minimum energy required to produce a pion, the lightest meson, which is $\omega_{th} \approx 140$ MeV. There are, however, contributions to the total cross section from electromagnetic interactions (ex. Compton scattering or pair production) with thresholds much lower than 140 MeV. Compared to the strong interaction of meson photoproduction, electromagnetic interactions will have very small cross sections. This is due to the relatively small EM coupling constant ($\alpha_e \approx 1/137$) which appears in the scattering amplitude of EM interactions. Considering only strong interactions in the Baldin sum rule ($\omega_{th} \approx 140$ MeV), neglecting the contribution to the total cross section from electromagnetic interactions, only results in an error on the order of $1/137 \approx 1\%$.

Physics related to the Δ -resonance region (single pion photoproduction) will dominate the integrand for two main reasons: (1) the integrand in equation (2.36) is weighted by ω^2 , making the contribution from lower energies dominant, and (2) the single pion photoproduction cross section is the largest contribution to the total photoabsorption cross section.

2.2.2 BEFT sum rule

The difference between the static dipole scalar polarisabilities can be constrained by the BEFT sum rule. First developed by Bernabeu, Ericson, Ferro Fontan, and Tarrach [17], the BEFT sum rule is given by,

$$\bar{\alpha}_{E1} - \bar{\beta}_{M1} = (\bar{\alpha}_{E1} - \bar{\beta}_{M1})_s + (\bar{\alpha}_{E1} - \bar{\beta}_{M1})_t, \quad (2.37)$$

where the s-channel contribution is given by,

$$(\bar{\alpha}_{E1} - \bar{\beta}_{M1})_s = \frac{1}{2\pi^2} \int_{\omega_{th}}^{\infty} \left(1 + \frac{2\omega}{M}\right)^{\frac{1}{2}} \frac{\sigma_{tot}(\omega)_P - \sigma_{tot}(\omega)_{NP}}{\omega^2} d\omega, \quad (2.38)$$

where $\sigma_{tot}(\omega)_P$ and $\sigma_{tot}(\omega)_{NP}$ are the total photoabsorption cross sections for interactions where there is a parity change between intermediate state and nucleon, and where there is no parity change, respectively. Recalling equations (2.10) and (2.11), the parity of an electric (EL) or magnetic (ML) multipole were given as $(-1)^L$ and $(-1)^{L+1}$ respectively. Consider a photon (EL or ML) incident upon a proton with $J^\pi = \frac{1}{2}^+$. Conservation of parity requires a parity change in the intermediate state for multipoles E1, M2, E3, *etc.* Similarly, conservation of parity requires no parity change in the intermediate state for multipoles M1, E2, M3, *etc.*

The t-channel contribution is given by,

$$(\bar{\alpha}_{E1} - \bar{\beta}_{M1})_t = \frac{1}{16\pi^2} \int_{4m_\pi^2}^{\infty} \left(\frac{16}{4M^2 - t}\right) \left(\frac{t - 4m_\pi^2}{t}\right)^{\frac{1}{2}} \left[f_+^0(t) F_0^{0*}(t) - \left(M^2 \frac{t}{4}\right) \left(\frac{t}{4} - m_\pi^2\right) f_+^2(t) F_0^{2*}(t) + \dots \right], \quad (2.39)$$

where $f_+^J(t)$ and $F_0^J(t)$ are the partial wave helicity amplitudes of $N\bar{N} \rightarrow \pi\pi$ and $\pi\pi \rightarrow \gamma\gamma$ processes. An evaluation by Schumacher [18] gives a rather simple evaluation assuming the dominance of the S-wave σ -meson contribution. In this case, the t-channel contribution is approximated as,

$$(\bar{\alpha}_{E1} - \bar{\beta}_{M1})_t = \frac{g_{\sigma NN} F_{\sigma\gamma\gamma}}{2m_\sigma^2}, \quad (2.40)$$

where $g_{\sigma NN}$ is the σ -nucleon coupling constant, $F_{\sigma\gamma\gamma}$ is the two-photon σ decay amplitude and m_σ is the mass of the σ -meson.

2.2.3 GDH γ_0 sum rule

A sum rule can be determined for the forward spin polarisability [19], given by,

$$\gamma_0 = -\frac{1}{4\pi^2} \int_{\omega_{th}}^{\infty} \frac{\sigma_{3/2}(\omega) - \sigma_{1/2}(\omega)}{\omega^3} d\omega, \quad (2.41)$$

where $\sigma_n(\omega)$ is the total photoabsorption cross section for circularly polarised photons and longitudinally polarised protons. The cases $n=3/2$ and $n=1/2$ are determined from photoabsorption where the helicity of the photon beam and polarisation of the proton target are parallel and anti-parallel respectively. A similar relation, known as the Gerasimov-Drell-Hearn (GDH) sum rule [20][21], relates the polarised total photoabsorption cross sections to the static structure properties of the nucleon which appear in the Born terms of the Compton scattering amplitude. This relation is given by,

$$\frac{\alpha_e \kappa^2}{2M^2} = \frac{1}{4\pi^2} \int_{\omega_{th}}^{\infty} \frac{\sigma_{3/2}(\omega) - \sigma_{1/2}(\omega)}{\omega} d\omega, \quad (2.42)$$

where α_e is the electromagnetic coupling constant and, as before, M and κ are the nucleon's mass and anomalous magnetic moment respectively.

2.2.4 LN γ_π sum rule

A sum rule for the backward spin polarisability, γ_π , has been defined by L'vov and Nathan.

$$\gamma_\pi = \gamma_\pi^s + \gamma_\pi^t, \quad (2.43)$$

Similar to the GDH γ_0 sum rule, the LN sum rule relates the backward polarisability to the total photoabsorption cross section for circularly polarised photons and longitudinally polarised protons. The s-channel contribution is given by,

$$\gamma_\pi^s = \frac{1}{4\pi^2} \int_{\omega_{th}}^{\infty} \left(1 + \frac{\omega}{M}\right) \left(1 + \frac{2\omega}{M}\right)^{\frac{1}{2}} \sum_n P_n \frac{\sigma_{3/2}^n(\omega) - \sigma_{1/2}^n(\omega)}{\omega^3} d\omega, \quad (2.44)$$

where P_n is +1 for cases where there is no parity change in the s-channel intermediate state, and P_n is -1 for cases where there is a parity change. As discussed in Section 2.2.2, multipoles E1, M2, E3, *etc.* lead to parity changes ($P_n = -1$) in the intermediate state, while multipoles M1, E2, M3, *etc.* have no parity change ($P_n = +1$).

The t-channel contribution is given by,

$$\gamma_\pi^t = \left[\frac{g_{\pi NN} F_{\pi^0 \gamma \gamma}}{2m_{\pi^0}^2} \tau_3 + \frac{g_{\eta NN} F_{\eta \gamma \gamma}}{2m_\eta^2} + \frac{g_{\eta' NN} F_{\eta' \gamma \gamma}}{2m_{\eta'}^2} \right]. \quad (2.45)$$

This t-channel term is a sum of contributions from the t-channel exchange of a π , η and η' meson. For each meson, g_{xNN} is the meson-nucleon coupling constant, $F_{x\gamma\gamma}$ is the two-photon decay amplitude, m_x is the meson mass, and τ_3 is equal to 1 or -1 for the proton or neutron, respectively.

2.3 Polarised Compton scattering

Single and double polarisation observables can be measured for nuclear Compton scattering involving polarised photons or nucleons. These polarisation observables, known as asymmetries, quantify the effect of polarisation on the scattering process.

2.3.1 Stokes parameters

Stokes parameters, denoted by ξ_i ($i = 1, 2, 3$), characterise the photon polarisation. They are constrained by the relation,

$$\sqrt{\xi_1^2 + \xi_2^2 + \xi_3^2} \leq 1 \quad (2.46)$$

While the Stokes parameters are frame dependent, the ξ_2 component and the quantity,

$$\xi_L = \sqrt{\xi_1^2 + \xi_3^2}. \quad (2.47)$$

are Lorentz invariant. The degree of circular polarisation of a photon is characterised by ξ_2 , where ξ_2 of 1 and -1 correspond to right and left helicity cases respectively. The degree of linear polarisation of a photon is characterised by ξ_1 and ξ_3 . Assuming a photon has its momentum along the z-axis, the angle between the electric field and x-z plane, φ , is given by,

$$\cos(2\varphi) = \frac{\xi_3}{\xi_L}, \quad \sin(2\varphi) = \frac{\xi_1}{\xi_L}. \quad (2.48)$$

ξ_3 of 1 and -1 corresponds to linearly polarised photons polarised parallel and perpendicular, $\varphi = 0$ and $\frac{\pi}{2}$, to the scattering plane. $\xi_1 = \pm 1$ corresponds to linearly polarised photons polarised with an angle $\varphi = \pm \frac{\pi}{4}$.

2.3.2 Asymmetries

A set of polarisation observables, known as asymmetries, can be defined which quantify the change in the cross section due to a specific polarisation orientation. Single polarisation asymmetries, where either the photon or nucleon is polarised, are denoted by Σ_i or Σ_j . For polarised photons, the subscript $i = (1,2,3)$ indicates which of the photon's Stokes parameter is equal to ± 1 . For polarised nucleons, the subscript $j = (x,y,z)$ indicates the polarisation axis of the nucleon. Double polarisation asymmetries, where both the photon and nucleon are polarised, are denoted similarly by Σ_{ij} .

Many asymmetries can be defined, which are either single or double polarisation asymmetries. For example, Σ_y is a single polarisation asymmetry where the photon is unpolarised and the nucleon is polarised along the $\pm y$ axis. Similarly, Σ_{3y} is a double polarisation asymmetry where the photon is polarised either parallel or perpendicular to the scattering plane.

2.3.2.1 Defined by the polarised cross section

Each Σ can be defined by its connection to the polarised cross section. As an example, the Σ_3 asymmetry is a single polarisation observable where the nucleon is unpolarised, and the photon is linearly polarised either parallel or perpendicular to the scattering plane ($\xi_3 = \pm 1$). In this case, the polarised cross section can be related to the unpolarised cross section by,

$$\left(\frac{d\vec{\sigma}}{d\Omega}(\theta, \phi) \right) = \left(\frac{d\sigma}{d\Omega}(\theta) \right) [1 + p_\gamma \Sigma_3 \cos(2\phi)], \quad (2.49)$$

where p_γ is the degree of linear polarisation. It is straight forward to show that the Σ_3 asymmetry can be expressed in terms of the polarised cross section with a flip in the polarisation axis. Using $d\sigma^\parallel$ and $d\sigma^\perp$ to denote the polarised differential cross section where the photon polarisation is parallel ($\xi_3 = 1$) or perpendicular ($\xi_3 = -1$) to the scattering plane, the Σ_3 asymmetry can be expressed,

$$\Sigma_3 = \frac{d\sigma^\parallel - d\sigma^\perp}{d\sigma^\parallel + d\sigma^\perp}. \quad (2.50)$$

This definition of the asymmetries can be extended to the other possible single and double polarisation asymmetries. For nucleons polarised along the $\pm y$ -axis, two asymmetries can be defined: Σ_y and Σ_{3y} . For Σ_y , the photons are unpolarised. For Σ_{3y} , the photons are polarised parallel or perpendicular to the scattering plane ($\xi_3 \pm 1$).

$$\Sigma_y = \frac{d\sigma_y - d\sigma_{-y}}{d\sigma_y + d\sigma_{-y}}, \quad \Sigma_{3y} = \frac{(d\sigma^\parallel - d\sigma^\perp)_y - (d\sigma^\parallel - d\sigma^\perp)_{-y}}{(d\sigma^\parallel + d\sigma^\perp)_y + (d\sigma^\parallel + d\sigma^\perp)_{-y}} \quad (2.51)$$

For linearly polarised photons, with $\varphi = \pm \frac{\pi}{4}$ ($\xi_1 = \pm 1$), two asymmetries can be defined, Σ_{1x} and Σ_{1z} , which have nucleons polarised along the x- and z-axis respectively.

$$\Sigma_{1x} = \frac{d\sigma_x^{\pi/4} - d\sigma_x^{-\pi/4}}{d\sigma_x^{\pi/4} + d\sigma_x^{-\pi/4}}, \quad \Sigma_{1z} = \frac{d\sigma_z^{\pi/4} - d\sigma_z^{-\pi/4}}{d\sigma_z^{\pi/4} + d\sigma_z^{-\pi/4}}, \quad (2.52)$$

Finally, for circularly polarised photons with right (R) and left (L) helicity ($\xi_2 = \pm 1$), two asymmetries can be defined, Σ_{2x} and Σ_{2z} , which have nucleons polarised along the x- and z-axis respectively.

$$\Sigma_{2x} = \frac{d\sigma_x^R - d\sigma_x^L}{d\sigma_x^R + d\sigma_x^L}, \quad \Sigma_{2z} = \frac{d\sigma_z^R - d\sigma_z^L}{d\sigma_z^R + d\sigma_z^L}, \quad (2.53)$$

2.3.2.2 Defined by the scattering amplitudes

It is possible to define the asymmetries in terms of the scattering amplitudes, A_i , which were discussed in detail in Section 2.1.3. It was shown in equation (2.21) that the differential cross section can be expressed as a function of the scattering T-matrix. This T-matrix can be expressed as a function independent functions, denoted by W_{ij} .

In the case of polarised Compton scattering, we can express the T-matrix in the following way,

$$|T_{fi}(\vec{\gamma} \vec{N} \rightarrow \gamma N)|^2 = W_{00} + W_{03}\xi_3 + \mathbf{N} \cdot \mathbf{S}(W_{30} + W_{33}^+\xi_3) \\ + \mathbf{K} \cdot \mathbf{S}(W_{11}^+\xi_1 + W_{12}^+\xi_2) + \mathbf{Q} \cdot \mathbf{S}(W_{21}^+\xi_1 + W_{22}^+\xi_2), \quad (2.54)$$

where \mathbf{N} , \mathbf{Q} , and \mathbf{K} are orthogonal four-vectors, \mathbf{S} is the nucleon polarisation four-vector which is orthogonal to the nucleon four-momentum, and ξ_i are the Stokes parameters. In cases where the photon and nucleon are unpolarised ($\xi_i = \mathbf{S} = 0$), only the W_{00} term survives in the T-matrix. In cases where the photon is polarised, but the nucleon is unpolarised ($\mathbf{S} = 0$), only the W_{00} and W_{03} terms survive.

It was shown in equation (2.23) that the T-matrix can be expressed as a function of the independent amplitudes, A_i . W_{ij} can also be defined in terms of A_i , however many of these W_{ij} will be imaginary. The W_{30} term, for example, can be expressed,

$$W_{30} = -8\nu \text{Im}(tA_1A_5^* + \nu A_3A_5^*). \quad (2.55)$$

At energies below the pion photoproduction threshold the T-matrix, and the amplitudes A_i , are real [15], and therefore not all W_{ij} terms contribute below threshold. Only six amplitudes, W_{00} , W_{03} , W_{12}^\pm , and W_{22}^\pm , are non-zero below pion photoproduction threshold. The W_{00} term is directly proportional to the unpolarised cross section by,

$$\left(\frac{d\sigma}{d\Omega}\right) = \frac{1}{64\pi^2s}W_{00}, \quad (2.56)$$

where the W_{00} function is given by,

$$W_{00} = \frac{1}{4}(4M^2 - t)(t^2|A_1|^2 + \nu^2|A_3|^2) - \frac{1}{4}(t^3|A_2|^2 + \nu^3|A_4|^2) \\ - \nu^2t(t + 8\nu^2)|A_5|^2 + \frac{\nu}{2}(t^2 + 2M^2\nu^2)|A_6|^2 \\ + \text{Re} \left[2\nu^2t^2(A_1 + A_2)A_5^* + \frac{\nu^2}{2}(4M^2A_3 + tA_4)A_6^* \right]. \quad (2.57)$$

The remaining terms which are non-zero below pion production threshold, W_{03} , W_{12}^\pm , W_{22}^\pm , are given by,

$$\begin{aligned}
W_{03} &= \frac{\nu t}{2} \text{Re} \left[((4M^2 - t)A_1 + 4\nu^2 A_5) A_3^* + 4M^2 A_1 A_6^* \right], \\
W_{22}^\pm &= 2 \text{Re} \left[-Mt (tA_2 - 4\nu^2 A_5) A_1^* \mp \nu \eta A_3 (\eta A_4^* + tA_6^*) \right], \\
W_{12}^\pm &= \text{Re} \left[-\frac{\nu}{2M} ((4M^2 - t)A_3 + 4M^2 A_6) (\nu A_4^* + tA_6^*) \right] \\
&\quad \pm 2\nu t (tA_2 - 4\nu^2 A_5) A_5^*,
\end{aligned} \tag{2.58}$$

where,

$$\eta = (4\nu^2 + t - t^2/4M^2). \tag{2.59}$$

Each asymmetry can also be defined in terms of W_{ij} , and therefore in terms of the scattering amplitudes, A_i . However, of the asymmetries defined in Section 2.3.2.1, only three asymmetries can be written in terms of the six amplitudes (W_{00} , W_{03} , W_{12}^\pm , and W_{22}^\pm) which are non-zero below pion production threshold. These asymmetries are given by,

$$\Sigma_3 = \frac{d\sigma^\parallel - d\sigma^\perp}{d\sigma^\parallel + d\sigma^\perp} = \frac{W_{03}}{W_{00}}, \tag{2.60}$$

$$\Sigma_{2x} = \frac{d\sigma_x^R - d\sigma_x^L}{d\sigma_x^R + d\sigma_x^L} = \frac{C_x W_{12}^+ + C_x W_{22}^+}{W_{00}}, \quad \text{where: } C_x = -\frac{\omega'}{2} \sin \theta, \tag{2.61}$$

$$\Sigma_{2z} = \frac{d\sigma_z^R - d\sigma_z^L}{d\sigma_z^R + d\sigma_z^L} = \frac{C_z^- W_{12}^+ + C_z^+ W_{22}^+}{W_{00}}, \quad \text{where: } C_z^\pm = -\frac{1}{2}(\pm\omega - \omega' \cos \theta), \tag{2.62}$$

where C_x , and C_z^\pm are defined in terms of the lab frame photon energies, ω and ω' .

2.3.2.3 Sensitivity to spin polarisabilities

A detailed sensitivity study was completed by Martel [1] based on the dispersion relations of Pasquini, Drechsel and Vanderhaeghen [14][15]. These studies investigated the sensitivity of the Σ_3 , Σ_{2x} , and Σ_{2z} asymmetries to the spin polarisabilities.

The fixed- t dispersion relation calculation of Pasquini, Drechsel, and Vanderhaeghen [14][15] was used to study the sensitivity of the asymmetries. This code, along with other theoretical predictions, will be discussed in chapter 3. The DR analysis of Pasquini *et al.* predicts nominal values of the spin polarisabilities given by,

$$\begin{aligned}
 \bar{\gamma}_{E1E1} &= -4.3 \times 10^{-4} \text{ fm}^4 \\
 \bar{\gamma}_{M1M1} &= 2.9 \times 10^{-4} \text{ fm}^4 \\
 \bar{\gamma}_{E1M2} &= -0.01 \times 10^{-4} \text{ fm}^4 \\
 \bar{\gamma}_{M1E2} &= 2.1 \times 10^{-4} \text{ fm}^4
 \end{aligned} \tag{2.63}$$

It should be noted, however, that the nominal values predicted by the DRs should not be considered important when discussing the sensitivity of the asymmetries to the spin polarisabilities. Using the Pasquini DR analysis, it is possible to produce a set of asymmetry predictions for Σ_3 , Σ_{2x} , and Σ_{2z} based on these nominal values. As a simple sensitivity test, asymmetries are produced first using nominal values and then again varying each spin polarisability individually by $\pm 1.0 \times 10^{-4} \text{ fm}^4$. The results of these studies are reproduced here for Σ_{2z} in Figure 2.2, for Σ_{2x} in Figure 2.3, and for Σ_3 in Figure 2.4. The asymmetries are each shown for a low energy region, corresponding to an incident photon energy of 240 MeV, and a high energy region, corresponding to an incident photon energy of 280 MeV. Within these energy regions, Σ_{2x} is most sensitive to variations in $\bar{\gamma}_{E1E1}$, Σ_{2z} is most sensitive to variations in $\bar{\gamma}_{M1M1}$, and Σ_3 is most sensitive to variations in $\bar{\gamma}_{M1M1}$ and $\bar{\gamma}_{M1E2}$. More rigorous sensitivity tests, varying multiple spin polarisabilities at once, showed the same sensitivity dependence of the asymmetries.

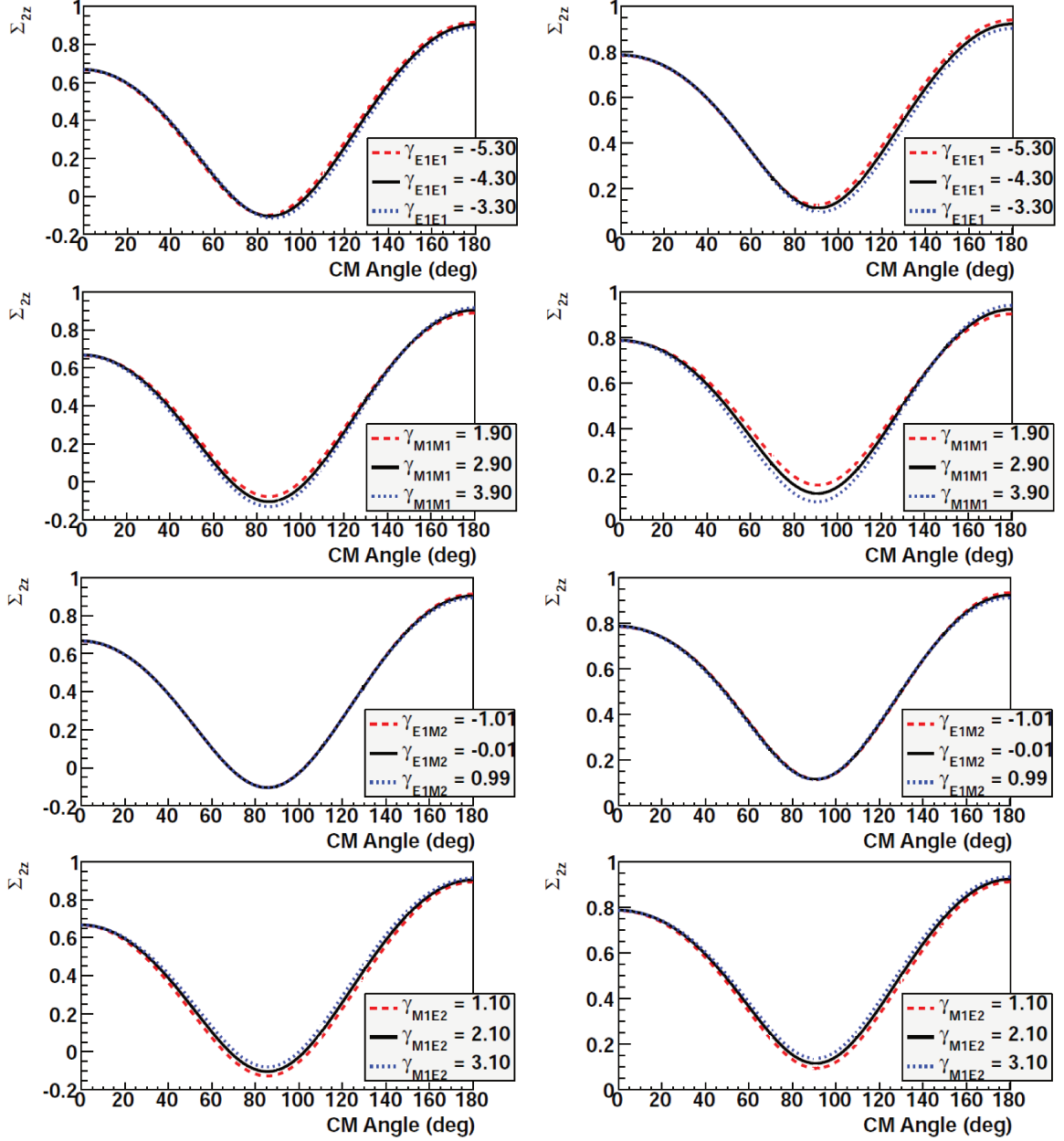


Figure 2.2: Sensitivities of the Σ_{2z} asymmetry to variations in a single polarisability. Polarisabilities are varied from the nominal values given in equation (2.63). Asymmetries shown for $E_\gamma = 240$ MeV (left) and 280 MeV (right), varying either $\bar{\gamma}_{E1E1}$ (first row), $\bar{\gamma}_{M1M1}$ (second row), $\bar{\gamma}_{E1M2}$ (third row), or $\bar{\gamma}_{M1E2}$ (fourth row). Reproduced from [1].

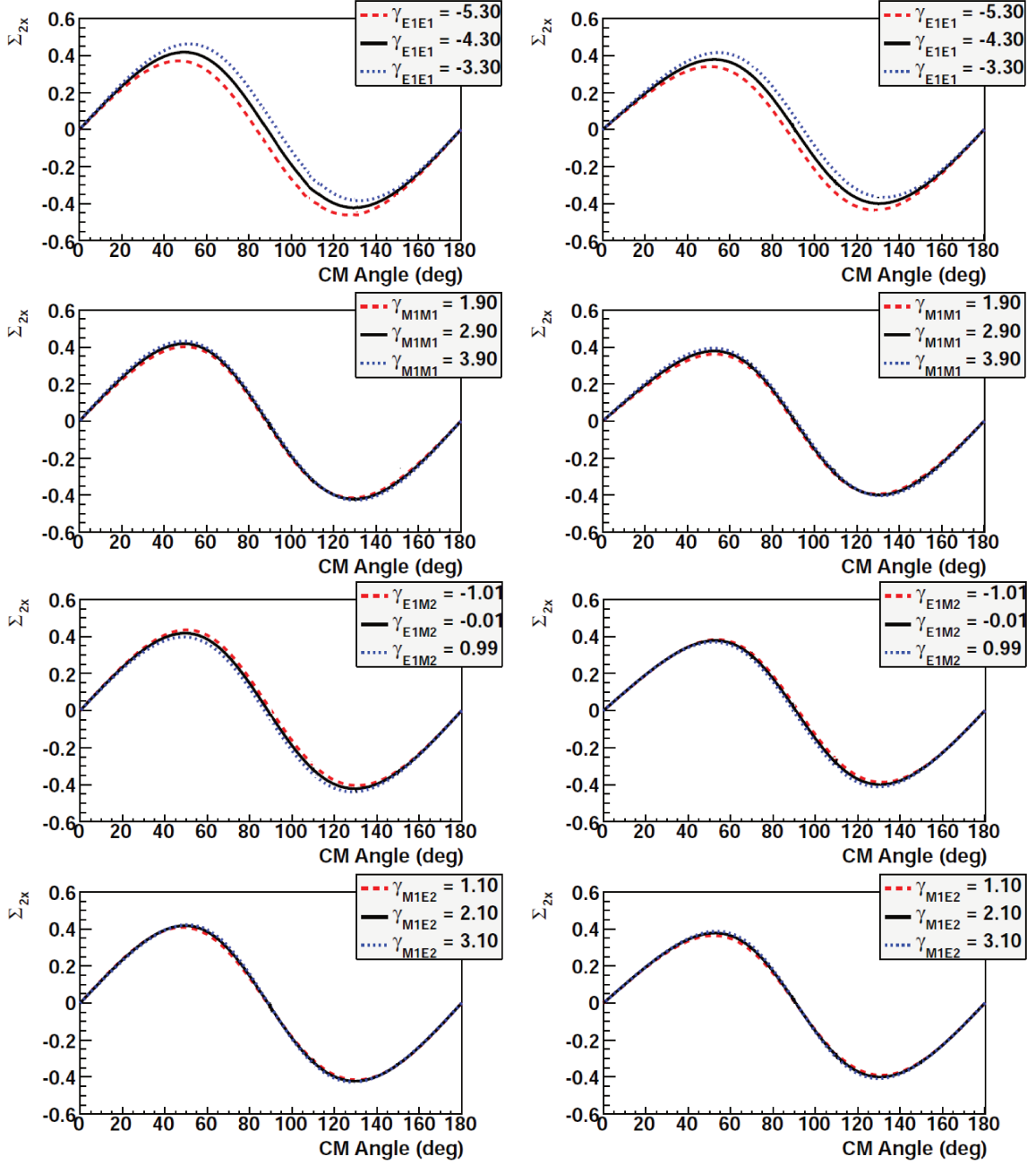


Figure 2.3: Sensitivities of the Σ_{2x} asymmetry to variations in a single polarisability. Polarisabilities are varied from the nominal values given in equation (2.63). Asymmetries shown for $E_\gamma = 240$ MeV (left) and 280 MeV (right), varying either $\bar{\gamma}_{E1E1}$ (first row), $\bar{\gamma}_{M1M1}$ (second row), $\bar{\gamma}_{E1M2}$ (third row), or $\bar{\gamma}_{M1E2}$ (fourth row). Reproduced from [1].

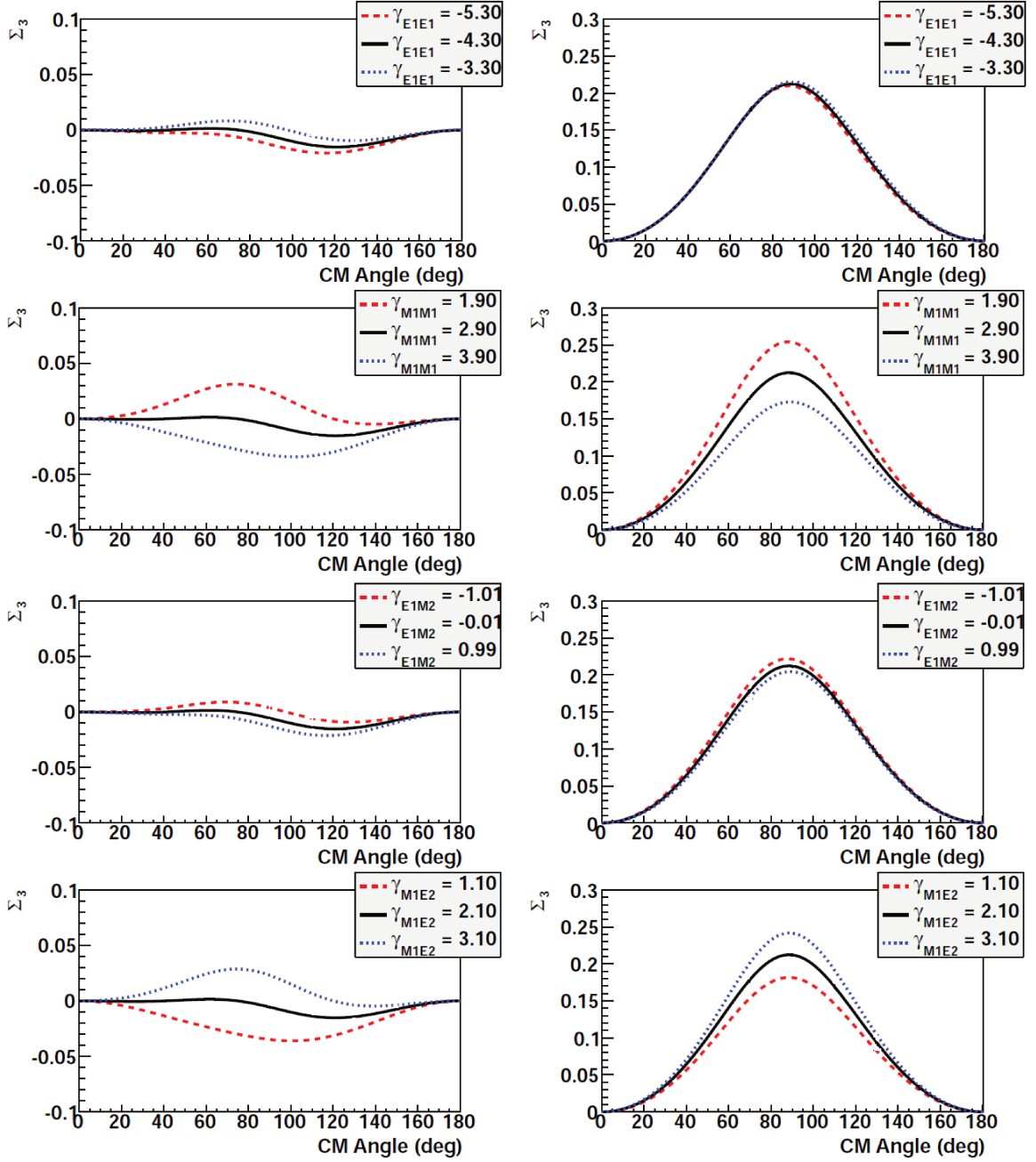


Figure 2.4: Sensitivities of the Σ_3 asymmetry to variations in a single polarisability. Polarisabilities are varied from the nominal values given in equation (2.63). Asymmetries shown for $E_\gamma = 240$ MeV (left) and 280 MeV (right), varying either $\bar{\gamma}_{E1E1}$ (first row), $\bar{\gamma}_{M1M1}$ (second row), $\bar{\gamma}_{E1M2}$ (third row), or $\bar{\gamma}_{M1E2}$ (fourth row). Reproduced from [1].

2.4 π^0 photoproduction

For photons impinging on a proton target, Compton scattering is only one of many interactions which can occur. Equation (2.12) showed that the γ_{M1E2} spin polarisability could be understood by an s-channel process which excited a Δ as an intermediate state. Although not the only contribution to Compton scattering, within the Δ -resonance region, the excitation of a Δ intermediate state is a dominant channel. However, the de-excitation of the Δ back into a photon-proton pair, as depicted in equation (2.12), is not the dominant decay channel. The branching ratios of $\Delta \rightarrow \gamma p$ and $\Delta \rightarrow \pi N$ are given by,

$$\frac{\Gamma_{\Delta \rightarrow \gamma p}}{\Gamma} \approx 0.6 \%, \quad \frac{\Gamma_{\Delta \rightarrow \pi N}}{\Gamma} > 99 \%. \quad (2.64)$$

Decays into a pion-nucleon pair are much more likely. Within the Δ -resonance region, the dominant reaction is neutral pion photoproduction, given by,

$$\gamma + p \rightarrow \pi^0 + p'. \quad (2.65)$$

The dominant decay channel of the π^0 is an electromagnetic decay into a photon-photon pair, $\pi^0 \rightarrow 2\gamma$, with a branching ratio given by,

$$\frac{\Gamma_{\pi^0 \rightarrow \gamma\gamma}}{\Gamma} > 99 \%. \quad (2.66)$$

The final state of π^0 photoproduction is then almost exclusively $\gamma p \rightarrow \pi^0 p \rightarrow \gamma\gamma p$. Experimentally, due to the similarity in final states, π^0 photoproduction can be a challenging background process to separate from Compton scattering. In cases where one of the decay photons is undetected, the final detected state appears identical to Compton scattering.

Despite the challenge π^0 photoproduction poses to Compton scattering experiments, it can also serve as a useful reaction for systematic tests of experimental detection systems. Due to our equipment's ability to reconstruct the decay photons, and by imposing a requirement that the invariant mass of the two-photon system be close to the pion mass, π^0 photoproduction is a relatively background-free reaction with our experimental setup. Therefore, along with a detailed study of Compton scattering, a detailed study of π^0 photoproduction will be presented. Additionally, where appropriate, π^0 photoproduction will be used to constrain parameters in the analysis of Compton scattering.

Chapter 3

Studies of the Proton Polarisabilities

As introduced in chapter 1, expanding the Compton scattering amplitude in terms of incident photon energy, ω , to third order results in six leading order scalar and spin polarisability terms:

- α_{E1}, β_{M1} - scalar electric and magnetic dipole polarisability terms,
- $\gamma_{E1E1}, \gamma_{M1M1}$ - dipole-dipole spin polarisability terms,
- $\gamma_{E1M2}, \gamma_{M1E2}$ - dipole-quadrupole spin polarisability terms.

The static polarisabilities, $\omega = 0$, are related to the total photoabsorption cross section through sum rules given in equations (2.36) and (2.41).

3.1 Baldin sum rule

Experimental evaluations of the Baldin sum rule, from photoabsorption experiments on the proton, date back over 40 years. An evaluation by Damashek and Gilman [22] extracted a value for the Baldin sum rule from experimental data measured at SLAC and DESY in the late 1960s. Damashek and Gilman determined the Baldin sum rule for the proton to be,

$$(\bar{\alpha}_{E1} + \bar{\beta}_{M1})_p = (14.2 \pm 0.3) \times 10^{-4} \text{ fm}^3 \quad (3.1)$$

Modern extractions have re-evaluated the Baldin sum rule in light of additional experimental data. An experiment by Armstrong *et al.* [23] at the Daresbury Nuclear Physics Lab measured the photoabsorption cross section in hydrogen over the energy range $\omega=265\text{-}4215$ MeV. This comprehensive dataset is complimented by precise data taken by MacCormick *et al.* [24] at the tagged photon beam facility of the MAMI accelerator in Mainz, which cover an energy range $\omega=200\text{-}800$ MeV. Although these datasets agree quite well, there is a small discrepancy within the Δ -resonance region.

Partial wave analyses show good agreement with the Mainz data within this region of discrepancy.

An evaluation of the Baldin sum rule was performed by Babusci, Giordano, and Matone [25] using the Daresbury and Mainz datasets. In their analysis, the experimental data were fitted to obtain a function which represented the data well. The total photoabsorption cross sections were determined using the SAID partial wave analysis [26] (solution SP97K). Babusci, Giordano, and Matone determined the Baldin sum rule for the proton to be,

$$(\bar{\alpha}_{E1} + \bar{\beta}_{M1})_p = (13.69 \pm 0.14) \times 10^{-4} \text{ fm}^3 \quad (3.2)$$

A re-evaluation, using the same datasets, was performed by Olmos de Leòn *et al.* [27]. In this case, no fitting function was used and the total photoabsorption cross sections were determined using partial wave analysis. Near the threshold region (below 200 MeV), multiple solutions of the partial wave analysis by Arndt, Strakovsky, and Workman [28] were used and the average value was adopted. Above this energy, the SAID partial wave analysis [26] (solution SM99K) was used. The Baldin sum rule for the proton was determined by Olmos de Leòn *et al.* as,

$$(\bar{\alpha}_{E1} + \bar{\beta}_{M1})_p = (13.8 \pm 0.4) \times 10^{-4} \text{ fm}^3 \quad (3.3)$$

3.2 Scalar Polarisabilities

Low-energy Compton scattering experiments were performed by Olmos de Leòn *et al.* [27] to extract values for the scalar dipole polarisabilities, $\bar{\alpha}_{E1}$ and $\bar{\beta}_{M1}$. Differential cross sections for Compton scattering were measured using the TAPS setup at the MAMI tagged photon facility for incident photon energies, ω , from 55 MeV to 165 MeV. The data set of Olmos de Leòn *et al.* was combined with three other low-energy Compton scattering experiments [27]:

1. MacGibbon *et al.* - 70 MeV to 100 MeV [12],
2. Federspiel *et al.* - 32 MeV to 72 MeV [29], and
3. Zieger *et al.* - 98 MeV to 132 MeV (backward angles) [30].

The dispersion relation approach of L'vov, Petrun'kin and Schumacher [13] was used to extract $\bar{\alpha}_{E1}$ and $\bar{\beta}_{M1}$ from the combined data set, as well as from each data set alone [27]. Shown in Figure 3.1 are the values for $\bar{\alpha}_{E1}$ and $\bar{\beta}_{M1}$ extracted from each data set. In this case, $\bar{\alpha}_{E1}$ and $\bar{\beta}_{M1}$ were free parameters, not constrained by the Baldin sum rule.

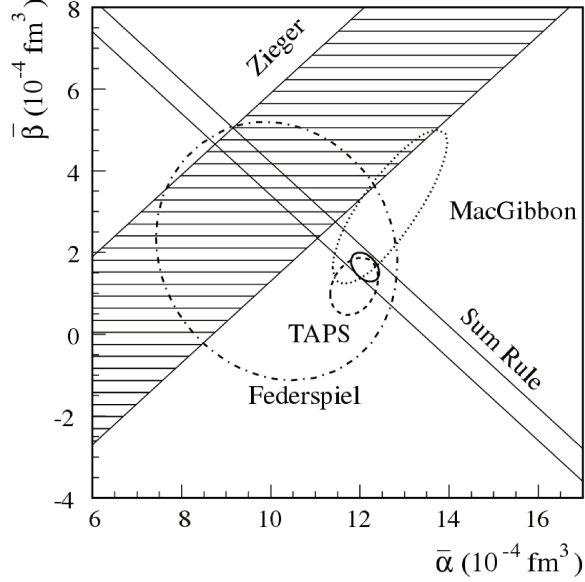


Figure 3.1: $\bar{\alpha}_{E1}$ and $\bar{\beta}_{M1}$ determined from a dispersion relation analysis of low-energy Compton scattering data sets: TAPS [27], MacGibbon [12], Federspiel [29]. A constraint in $\bar{\alpha}_{E1} - \bar{\beta}_{M1}$ from Zieger [30] is shown, along with the Baldin sum rule determined by Olmos [27]. Reproduced from [27].

A global fit to the combined data sets with and without the Baldin sum rule as a constraint was performed. With no constraint on the sum of the scalar polarisabilities, $\bar{\alpha}_{E1}$ and $\bar{\beta}_{M1}$ for the proton were determined to be,

$$\begin{aligned} (\bar{\alpha}_{E1})_p &= (11.9 \pm 0.5_{\text{stat.}} \mp 0.5_{\text{sys.}}) \times 10^{-4} \text{ fm}^3 \\ (\bar{\beta}_{M1})_p &= (1.5 \pm 0.6_{\text{stat.}} \pm 0.2_{\text{sys.}}) \times 10^{-4} \text{ fm}^3. \end{aligned} \quad (3.4)$$

Applying the Baldin sum rule as a constraint, using the result given in equation (3.3), $\bar{\alpha}_{E1}$ and $\bar{\beta}_{M1}$ for the proton were determined to be,

$$\begin{aligned} (\bar{\alpha}_{E1})_p &= (12.1 \pm 0.3_{\text{stat.}} \mp 0.4_{\text{sys.}}) \times 10^{-4} \text{ fm}^3 \\ (\bar{\beta}_{M1})_p &= (1.6 \pm 0.4_{\text{stat.}} \pm 0.4_{\text{sys.}}) \times 10^{-4} \text{ fm}^3. \end{aligned} \quad (3.5)$$

Until recently, the scalar dipole polarisabilities given in equation (3.5) were accepted by the particle data group, PDG. However, recently the PDG values for the scalar dipole polarisabilities were re-evaluated considering new χ PT calculations by Lensky and Pascalutsa [31] and McGovern, Phillips, and Grißhammer [32]. In both cases, the magnetic scalar polarisability was determined to be greater than $3 \times 10^{-4} \text{ fm}^3$. After re-evaluation, $\bar{\alpha}_{E1}$ and $\bar{\beta}_{M1}$ for the proton were determined to be,

$$\begin{aligned} (\bar{\alpha}_{E1})_p &= (11.2 \pm 0.4) \times 10^{-4} \text{ fm}^3 \\ (\bar{\beta}_{M1})_p &= (2.5 \pm 0.4) \times 10^{-4} \text{ fm}^3. \end{aligned} \quad (3.6)$$

Although this more recent evaluation results in an increased value for $\bar{\beta}_{M1}$, in all cases $\bar{\beta}_{M1}$ is determined to be much smaller than $\bar{\alpha}_{E1}$. This can be connected to the competing paramagnetic and diamagnetic contributions to the magnetic polarisability cancelling, resulting in a small value for $\bar{\beta}_{M1}$.

3.3 Forward spin polarisability

The forward spin polarisability, γ_0 , given in equation (2.13), is a linear combination of the four leading order spin polarisabilities. A sum rule, relating γ_0 to the total photoabsorption cross section for circularly polarised photons and longitudinally polarised protons, is given in equation (2.41). Additionally, in equation (2.33), the forward spin polarisability is shown to depend only on the a_4 low-energy constant.

The forward spin polarisability sum rule was evaluated from data taken at the tagged photon facilities at MAMI and ELSA. The MAMI data set covered a range of incident photon energies, ω , from 200 MeV to 800 MeV [19] while the ELSA data set covered energies from 700 MeV to 1800 MeV [33]. Within this analysis, the forward spin polarisability was determined to be,

$$\gamma_0 = (-1.00 \pm 0.08_{\text{stat.}} \mp 0.10_{\text{sys.}}) \times 10^{-4} \text{ fm}^4. \quad (3.7)$$

3.4 Backward spin polarisability

The backward spin polarisability, γ_π , given in equation (2.14), is also a linear combination of the four leading order spin polarisabilities. Experiments at the tagged

photon facility at MAMI [34] measured Compton scattering for incident photon energies, ω , from 200 MeV to 470 MeV. These data were measured with a single large NaI detector at $\theta_{\gamma'} = 136^\circ$ (lab frame), along with the Gottingen SENECA detector as a forward wall detector. A dispersion relation analysis was applied to the MAMI data set, along with data sets from Saskatoon [35], LARA [36][37], and LEGS [3][4]. The LEGS data set shows a large discrepancy from all other data sets, (see Figure 3.2).

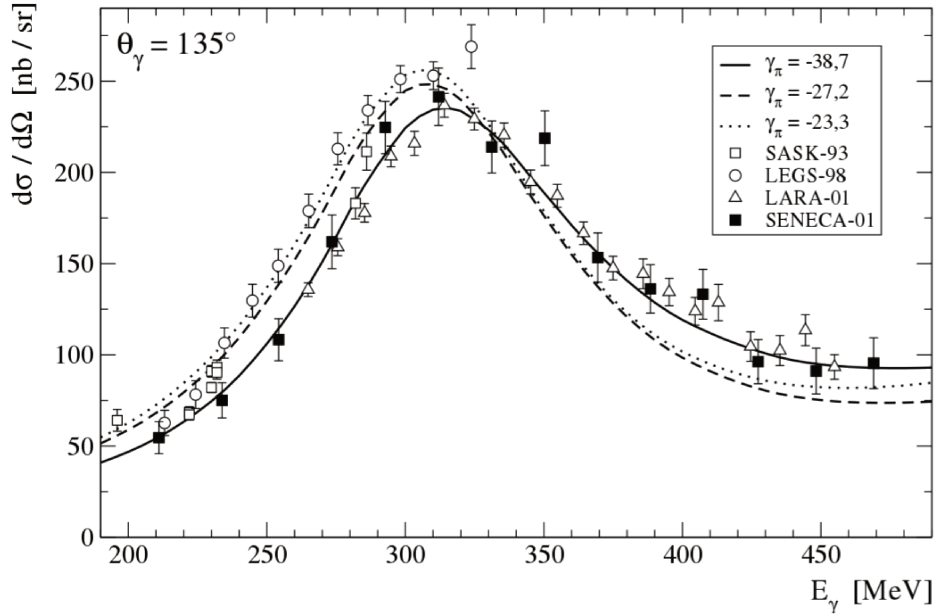


Figure 3.2: Differential cross sections for Compton scattering measured with the SENECA detector at MAMI at $\theta_{\gamma'} = 135^\circ$ (lab frame). Data from experiments at Saskatoon, LARA, and LEGS are shown along with a dispersion relation curves with γ_π of -38.7 , -27.2 , and -23.3 , in standard spin polarisability units of 10^{-4} fm^4). Reproduced from [34].

Due to the discrepancies of the LEGS data, a γ_π value was extracted for the LEGS data set separately. The backward spin polarisability, determined from the LEGS data set alone, is determined to be $\gamma_\pi = -23.3 \times 10^{-4} \text{ fm}^4$. A γ_π determination, fitting to the MAMI, LARA, and Saskatoon data sets, gives the backward spin polarisability as,

$$\gamma_\pi = (-38.7 \pm 1.8) \times 10^{-4} \text{ fm}^4. \quad (3.8)$$

The large backward spin polarisability is dominated by a π^0 -pole term, the t-channel emission of a virtual π^0 . The contribution of this term was evaluated by Schumacher [6] and found to be $\gamma_\pi^{\pi^0\text{-pole}} = -46.7 \times 10^{-4} \text{ fm}^4$. This term can be separated from the

backward spin polarisability, leaving a “dispersive” term given by,

$$\gamma_{\pi}^{\text{disp}} = (8.0 \pm 1.8) \times 10^{-4} \text{ fm}^4. \quad (3.9)$$

The π^0 -pole term contributes only to the A_2 scattering amplitude, and therefore only to the a_2 low-energy constant. While the a_2 term contributes to all four leading order spin polarisabilities, it cancels in γ_0 leading to a very small forward spin polarisability in comparison to the backward polarisability.

3.5 Spin Polarisabilities

The spin polarisabilities of the proton have only been studied experimentally through the forward and backward polarisabilities, discussed in Sections 3.3 and 3.4. A series of polarised Compton scattering experiments have been proposed to determine the proton spin polarisabilities experimentally. This experimental program, which is the focus of this dissertation, is discussed in Section 3.5.2. Despite the lack of experimental measurements, theoretical interest has resulted in a large set of theoretical predictions, in particular from dispersion relations calculations and from chiral perturbation calculations. In Section 3.5.1, theoretical predictions of the proton spin polarisabilities are discussed.

3.5.1 Theoretical predictions

Significant theoretical interest in the nucleon polarisabilities has resulted in numerous theoretical predictions for the spin polarisabilities of the proton. Table 3.1 outlines a subset of these theoretical predictions. These predictions come from a variety of theoretical frameworks including dispersion relation calculations, chiral perturbation theory calculations, and a “dressed” K-matrix model based upon K-matrix formalism combined with dispersion relations.

Fixed- t dispersion relations (DRs), discussed previously in Section 2.1.3, produce a set of low-energy constants which are directly connected to the scalar and spin polarisabilities. Within dispersion relations, the real part of the scattering amplitudes, A_i can be related to their imaginary parts through DRs, given previously in equation (2.27). However, not all scattering amplitudes converge, and a set of once-subtracted fixed- t dispersion relations can be defined (subtracting off the case of $\nu = 0$), given

previously in equation (2.29). The low-energy constants of these fixed- t dispersion relations were previously defined in equation (2.31). Fixed- t DRs are calculated with a fixed Mandelstam variable t . Similarly, it is also possible to define dispersion relations for fixed-angle, rather than fixed- t . These DRs are known as fixed-angle dispersion relations or hyperbolic dispersion relations. Due to the convergence behaviour of the DR scattering amplitudes, A_i , fixed- t DRs are best applied to small values of t (corresponding to forward angles, $\theta_{lab} = 0^\circ$). Similarly, fixed-angle DRs are best applied at backward angles [15]. Table 3.1 shows proton spin polarisabilities from two dispersion relation calculations: (1) HDPV, a once-subtracted fixed- t DR [8], and (2) DPV, a fixed-angle (hyperbolic) DR [15] calculated at $\theta_{lab} = 180^\circ$.

Chiral perturbation theory (χ PT) is an effective field theory (EFT) which can be used to study the low-energy region of QCD. As discussed in Chapter 1, as the energy scale decreases, or distance increases, perturbative QCD is no longer useful. In this low-energy regime, QCD is dominated by confinement, and therefore QCD-inspired models that incorporate hadronic degrees of freedom are used instead of the quarks and gluons. In other words, at low energies, pions and nucleons appear as the degrees of freedom, rather than the more fundamental quarks and gluons. EFTs can be used to calculate physical quantities, such as the polarisabilities. As the QCD Lagrangian cannot be directly solved, and perturbative QCD is not useful in the low-energy regime, an effective Lagrangian is constructed which, as stated by Stephen Weinberg, is “the most general possible Lagrangian, including all terms consistent with assumed symmetry principles” [38]. However, the resulting effective Lagrangian consists of an infinite number of terms. Thus, calculating physical quantities using χ PT requires a power counting scheme which allows terms in the effective Lagrangian to be organised in terms of importance. A power counting scheme allows a χ PT calculation to be considered up to a given order, with higher order terms being neglected. The effective Lagrangian terms carry coefficients, known as coupling constants or low-energy constants, which are typically treated as free parameters and determined and constrained by fitting to experimental data. Power counting schemes, and degrees of freedom applied vary between χ PT calculations. Table 3.1 shows proton spin polarisabilities from five chiral perturbation calculations: (1-2) $\mathcal{O}(p^4)_a$ and $\mathcal{O}(p^4)_b$, two fourth order (p-expansion) calculations [39][40], (3) $\mathcal{O}(\epsilon^3)$, a small scale (ϵ -expansion)

calculation [41], (4) HB χ PT, a heavy baryon chiral perturbation calculation [32], and (5) B χ PT, a covariant baryon chiral perturbation calculation [42]. Calculations (3) through (5) have $\Delta(1232)$ degrees of freedom.

In addition to calculations based upon dispersion relations and chiral perturbation theory, K-matrix formalism has been applied to Compton scattering (for a review of K-matrix formalism, see Ref. [43]). In the dressed K-matrix formalism of Ref. [44], traditional K-matrix formalism (satisfying unitarity) is combined with dispersion relations (satisfying analyticity). Within this framework, the imaginary parts of the scattering amplitudes are generated under the K-matrix formalism, and a requirement that the real parts of the amplitudes satisfy DRs is imposed. Table 3.1 shows proton spin polarisabilities obtained from the the dressed K-matrix model calculations of Ref. [44].

	HDPV	DPV	$\mathcal{O}(p^4)_a$	$\mathcal{O}(p^4)_b$	$\mathcal{O}(\epsilon^3)$	HB χ PT	B χ PT	K-matrix
$\bar{\gamma}_{E1E1}$	-4.3	-3.8	-5.4	1.3	-1.9	-1.1 ± 1.8	-3.3	-4.8
$\bar{\gamma}_{M1M1}$	2.9	2.9	1.4	3.3	0.4*	2.2 ± 1.2	3.0	3.5
$\bar{\gamma}_{E1M2}$	-0.02	0.5	1.0	0.2	0.7	-0.4 ± 0.4	0.2	-1.8
$\bar{\gamma}_{M1E2}$	2.2	1.6	1.0	1.8	1.9	1.9 ± 0.4	1.1	1.1
γ_0	-0.8	-1.1	1.9	-3.9	-1.1	-2.6	-1.0	2.0
γ_π	9.4	7.8	6.8	6.1	3.5	5.6	7.2	11.2

Table 3.1: Theoretical predictions of the proton spin polarisabilities are shown for various theoretical frameworks. HDPV is a once-subtracted fixed- t dispersion relation calculation [8]. DPV is a fixed-angle (hyperbolic) dispersion relation calculation [15] calculated at $\theta_{\text{lab}} = 180^\circ$. $\mathcal{O}(p^4)_a$ and $\mathcal{O}(p^4)_b$ are both fourth order (p-expansion) calculations [39][40]. $\mathcal{O}(\epsilon^3)$ is a small scale (ϵ -expansion) calculation [41]. HB χ PT is a heavy baryon chiral perturbation calculation [32]. B χ PT is a covariant baryon chiral perturbation calculation [42]. Finally, K-matrix is a dressed K-matrix model [44], based on K-matrix formalism and dispersion relations. All polarisabilities are given in units of 10^{-4} fm^4 with the $\gamma_\pi^{\pi^0\text{-pole}}$ removed.

*Note: Ref. [45] suggests the $\bar{\gamma}_{M1M1}$ determined by Ref. [41], $\mathcal{O}(\epsilon^3)$ small scale calculation, should be adjusted by +2.5 due to a missing Δ -pole contribution.

Table 3.1 shows a subset of all theoretical calculations of the proton spin polarisabilities. It is interesting to note that HDPV, DPV, B χ PT, and K-matrix calculations all produce similar spin polarisability predictions. The only exception being the large (negative) $\bar{\gamma}_{E1M2}$ predicted by the K-matrix calculation. These predictions however seem to be quite different from the remaining chiral perturbation calculations, which

themselves produce a variety of different spin polarisabilities predictions. Given that the forward and backward polarisabilities have been measured experimentally, it is interesting to directly compare the different theoretical predictions for γ_0 and γ_π . DPV produces a γ_π very close to the experimental value of 8.0 ± 1.8 . This is not surprising as DPV is a fixed-angle DR, calculated at $\theta_{\text{lab}} = 180^\circ$. Many of the calculations produce values of γ_0 and γ_π significantly different from the experimental values. It is interesting to note that only the DPV and B χ PT calculations show agreement to experiment for both the forward and backward polarisabilities. Given the wide range of values for each spin polarisability term, an experiment to measure the spin polarisabilities could be a useful test and constraint of the various theories.

3.5.2 Experimental studies

A series of experiments has been proposed to extract the spin polarisabilities of the proton from single and double polarisation asymmetries for Compton scattering off the proton. This experimental program, which is the focus of this dissertation, is currently ongoing at the MAMI tagged photon facility in Mainz, Germany. In total, three asymmetries will be measured within the Δ -resonance region, $\omega \approx 300$ MeV:

1. **Beam Asymmetry - Σ_3**

Linearly polarised photons ($\xi_3 \pm 1$) and unpolarised protons.

Σ_3 is defined in terms of the polarised cross section in equation (2.60).

2. **Beam-target Asymmetry - Σ_{2x}**

Circularly polarised photons ($\xi_2 \pm 1$) and transversely ($\pm x$) polarised protons.

Σ_{2x} is defined in terms of the polarised cross section in equation (2.61).

3. **Beam-target Asymmetry - Σ_{2z}**

Circularly polarised photons ($\xi_2 \pm 1$) and longitudinally ($\pm z$) polarised protons.

Σ_z is defined in terms of the polarised cross section in equation (2.62).

The choice to measure these specific asymmetries was motivated by their sensitivity to the underlying spin polarisabilities. In each case, an experimental measurement of the asymmetry results in a statistical accuracy sufficient to provide reasonable constraints on the spin polarisability values, within a reasonable amount of beamtime.

Additionally, these asymmetries have a varying sensitivity to the different polarisabilities with Σ_{2x} most sensitive to variations in $\bar{\gamma}_{E1E1}$, Σ_{2z} most sensitive to variations in $\bar{\gamma}_{M1M1}$, and Σ_3 sensitive to variations in $\bar{\gamma}_{M1M1}$ and $\bar{\gamma}_{M1E2}$. These sensitivities were presented in Section 2.3.2.3. Along with constraints from the Baldin sum rule, γ_0 , and γ_π , a global fit to all experimental measurements of the Compton scattering asymmetries can be used to extract the spin polarisabilities.

As part of the current experimental program, data for the beam-target asymmetry, Σ_{2x} , were measured at the MAMI tagged photon facility and analysed by Martel [1]. The spin polarisabilities of the proton were extracted using the once-subtracted fixed- t dispersion relation approach of Holstein, Drechsel, Pasquini and Vanderhaeghen [8], previously discussed in Section 3.5.1 as HDPV. Figure 3.3 shows Σ_{2x} measured for incident photon energies, ω , from 273 MeV to 303 MeV along with dispersion relation calculations for varied values of $\bar{\gamma}_{E1E1}$. Data were fit using the HDPV calculations, allowing $(\bar{\alpha} + \bar{\beta})$, $(\bar{\alpha} - \bar{\beta})$, $\bar{\gamma}_{E1E1}$, γ_0 and γ_π , to vary. The fitting routine assumed a fixed value of $\bar{\gamma}_{M1M1}$ of 2.9 (the nominal prediction of HDPV in Table 3.1). An extraction of $\bar{\gamma}_{E1E1}$ from this [1] analysis gives,

$$\bar{\gamma}_{E1E1} = (-4.5 \pm 1.5) \times 10^{-4} \text{ fm}^4. \quad (3.10)$$

The analysis of Σ_{2x} by Martel was not only the first measurement of a double polarisation observable for Compton scattering, but also allowed for the first experimental determination of $\bar{\gamma}_{E1E1}$ for the proton. A comparison of this result to the theoretical predictions in Table 3.1 shows that, despite the relatively large error, it is already possible to identify some disagreement between theoretical predictions and experiments for the $\bar{\gamma}_{E1E1}$ spin polarisability term.

A more recent analysis by Martel [2] determined the four leading order terms of the proton's spin polarisabilities, combining Σ_3 results from the LEGS collaboration [4] and Σ_{2x} results from the MAMI tagged photon facility. Data taken by the LEGS collaboration measured the beam asymmetry, Σ_3 , for Compton scattering off the proton for incident energies from 213 MeV to 333 MeV and an angular range of $\theta_{\gamma'}$ from 70° to 130° (CM frame)[3]. As before, data were fit using the HDPV calculations. However, in this case $\bar{\gamma}_{M1M1}$ was no longer fixed, but allowed to vary along with $(\bar{\alpha} + \bar{\beta})$, $(\bar{\alpha} - \bar{\beta})$, $\bar{\gamma}_{E1E1}$, γ_0 and γ_π .

An extraction of all four spin polarisabilities, combining the LEGS data set and Martel Σ_{2x} results, gives the result,

$$\begin{aligned}
 \bar{\gamma}_{E1E1} &= (-3.5 \pm 1.2) \times 10^{-4} \text{ fm}^4, \\
 \bar{\gamma}_{M1M1} &= (3.16 \pm 0.85) \times 10^{-4} \text{ fm}^4, \\
 \bar{\gamma}_{E1M2} &= (-0.7 \pm 1.2) \times 10^{-4} \text{ fm}^4, \\
 \bar{\gamma}_{M1E2} &= (1.99 \pm 0.29) \times 10^{-4} \text{ fm}^4,
 \end{aligned}
 \tag{3.11}$$

which are in good agreement with the dispersion theory, K-matrix theory, and Heavy Baryon chiral perturbation theory calculations shown in Table 3.1.

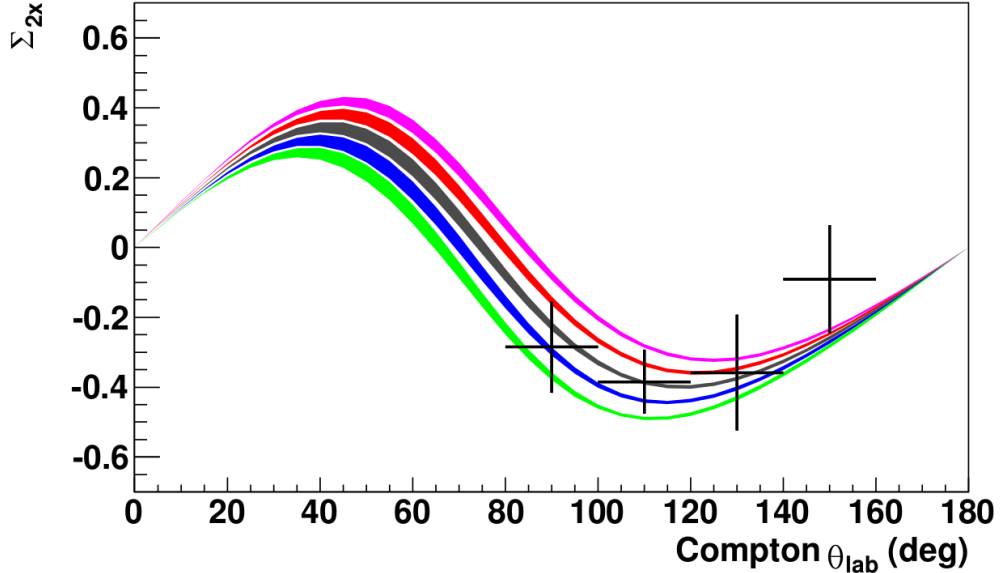


Figure 3.3: Σ_{2x} measured for incident photon energies from 273 MeV to 303 MeV. Also shown are dispersion relation calculations for values of $\bar{\gamma}_{E1E1}$ holding other spin polarisabilities fixed to the nominal values given in Table 3.1 (HDPV). DR curves are shown in coloured bands for values of $\bar{\gamma}_{E1E1}$, from top to bottom, of -2.3, -3.3, -4.3, -5.3, and -6.3, in standard spin polarisability units of 10^{-4} fm^4). Reproduced from [1].

The LEGS data set measured the Σ_3 asymmetry for Compton scattering over a very wide range of energies and angles. Such a large data set is ideal for fitting and extracting the spin polarisabilities. However, the validity of this comprehensive data set has been questioned. In Figure 3.2, the Compton scattering cross sections showed a significant discrepancy between data taken at Mainz, LARA, and Saskatoon. Although

it is possible that a discrepancy exists only in cross sections, and not in asymmetries, a discrepancy so large motivates a cross check of the LEGS data set. For this reason, in addition to the beam-target asymmetries, the Σ_3 asymmetry was remeasured at the MAMI tagged photon facility. Once complete, a global fit to all asymmetry results can be performed to extract the leading order spin polarisabilities of the proton. Results from the Σ_3 experiment at MAMI are presented in the following chapters.

Chapter 4

Experiment

The following chapter outlines the execution of an experiment during a run period in December 2012 at the MAMI tagged photon facility in Mainz, Germany. To study the Σ_3 asymmetry for Compton scattering and π^0 photoproduction, a source of linearly polarised photons and unpolarised protons is required. Electrons, accelerated using the Mainz Microtron electron accelerator, were incident upon a diamond radiator to create a source of linearly polarised photons via a coherent bremsstrahlung process. The energy of the incident photon was inferred by a momentum analysis of the bremsstrahlung electrons using the Glasgow Tagged Photon Spectrometer. The photon beam was then collimated and impinged upon a 10 cm liquid hydrogen, LH_2 , unpolarised proton target. Detection of final state particles was accomplished using the Crystal Ball and TAPS detectors, a detector system with a roughly 4π angular coverage. Each of these detector systems is comprised of a highly segmented photon calorimeter, coupled with additional detectors to detect and identify charged particles. The CB-TAPS detector system provides excellent energy and angular resolution for studying Compton scattering and the large angular acceptance helps to identify and reject background reactions.

4.1 Linearly polarised photon beam

During the run period, a linearly polarised photon beam was produced at the MAMI tagged photon facility via a coherent bremsstrahlung process. Coherent bremsstrahlung is produced by high-energy electrons incident upon a crystalline radiator, typically a thin diamond crystal. A 30 μm diamond radiator was used during the run period. This radiator was aligned within the electron beam, using the Stonehenge technique [46]. Using this technique, along with collimation of the photon beam, a linearly polarised photon beam with a high degree of polarisation was produced.

4.1.1 MAMI electron accelerator

The Mainz Microtron, MAMI, is a continuous wave (100% duty factor) electron accelerator capable of providing electrons with energies up to 1.6 GeV. Acceleration of electrons is accomplished in three distinct stages: (1) electron injector linear accelerator, LINAC, (2) a cascade of three racetrack microtrons, RTMs, and (3) the Harmonic Double Sided Microtron, HDSM [47].

Electrons are first boiled off a 100 keV electron gun via thermionic emission. After this, they are accelerated via an injector LINAC. The electrons are ejected from the injector LINAC with a total energy of 4.1 MeV. After this stage, the electrons enter a cascade of racetrack microtrons, RTMs. Each RTM is composed of a LINAC section coupled with two large dipole bending magnets. After being accelerated through a LINAC, the electron is bent by 180° via a large dipole magnet and passed through focusing devices. A second dipole magnet is then used to bend the electron back into the LINAC section, further accelerating the electron. With each successive turn, the electron gains energy and the radius of curvature through the bending magnet increases. The increase of path length per turn, Δs , is related to the increase in energy per turn, ΔT_{RTM} , by [48],

$$\Delta s = 2\pi \frac{\Delta T_{\text{RTM}}}{e\beta cB} \quad (4.1)$$

where B is the strength of the dipole magnet field. For relativistic electrons, $\beta \approx 1$. After the initial injector LINAC, the electron is accelerated through three successive racetrack microtrons with a final ejection energies of 15.3 MeV, 185.9 MeV, and 883.1 MeV for each RTM respectively. By recirculating the electron through the linear accelerating section, the racetrack microtron design creates a relatively compact electron accelerator. As the energy increases, larger dipole magnets are required to bend the electron beam. By RTM 3, the combined weight of the dipole bending magnets exceeds 900 metric tons, making the Mainz Microtron the world's largest racetrack microtron system. A diagram of the injector LINAC leading into a racetrack microtron system is shown in Figure 4.1.

For energies beyond 883 MeV, an additional racetrack microtron is not feasible due to the increased size of the dipole magnets. For this reason, energies up to 1.6 GeV are provided by the Harmonic Double Sided Microtron, HDSM. The HDSM is

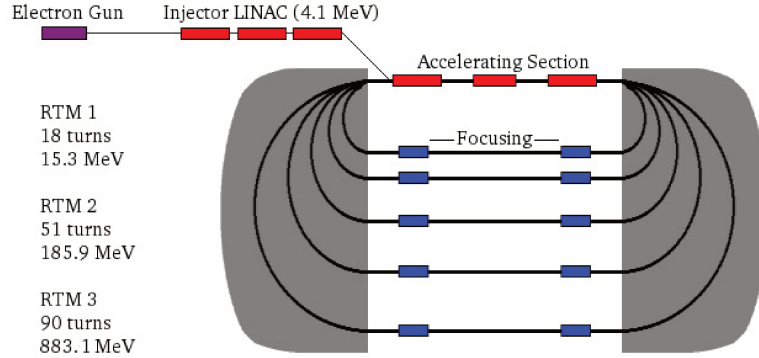


Figure 4.1: Initial stages of MAMI electron accelerator including electron injection and three racetrack microtrons. Total energies are shown for each stage with a maximum energy of 883.1 MeV reached after RTM 3.

similar in concept to the racetrack microtron, however four bending magnets are used along with two LINAC sections. Since each magnet only needs to bend the electron by 90° , the size of the individual magnets can be reduced. Data taken for this dissertation did not make use of the HDSM stage of the Mainz Microtron. A table of the main parameters of the MAMI electron accelerator is given in Table 4.1.

	Units	Injector	RTM 1	RTM 2	RTM 3
General					
Injection Energy	[MeV]	0.511	4.1	15.3	185.9
Ejection Energy	[MeV]	4.1	15.3	185.9	883.1
Number of cycles		-	18	51	90
LINAC System					
ΔT_{RTM} per cycle	[MeV]	-	0.62	3.35	7.75
LINAC length	[m]	4.93	0.80	3.55	8.87
Magnet System					
Magnetic Field	[T]	-	0.106	0.572	1.323
Fe/Cu weight of magnets	10^3 [kg]	-	4/0.2	90/2.3	900/11.6

Table 4.1: Main parameters of the MAMI electron accelerator (December 2012) [47].

During the run period, electrons were accelerated to relativistic energies using the accelerator system up to RTM3. Two precise measurements of the total electron beam energy were performed during the run period. Each measurement determined the total electron energy to be $E_o = 883.15 \pm 0.16$ MeV.

An overview of the entire MAMI electron accelerator is shown in Figure 4.2. During the run period, electrons were accelerated through a series of racetrack microtrons. The three racetrack microtrons are pictured, along with the HDSM which was not used during the run period. Also shown in Figure 4.2 are four experimental halls (A1, A2, A4, and X1). The experiment outlined within this work took place in the A2 experimental hall. Once an electron is accelerated through the cascade of racetrack microtrons, it is guided into the A2 experimental hall using a series of bending and focusing magnets.

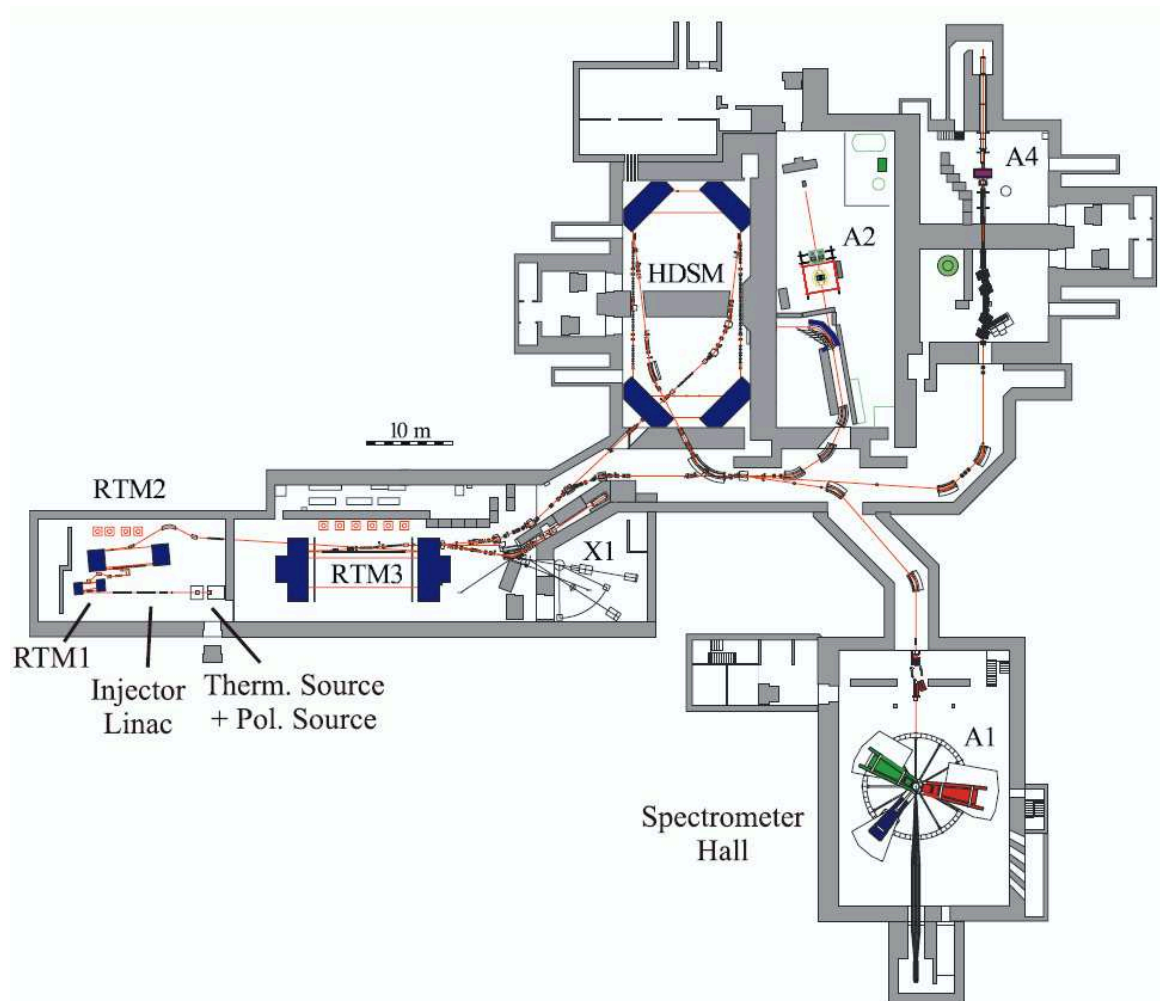


Figure 4.2: An overview of the entire MAMI electron accelerator is shown. The MAMI electron accelerator comprises three racetrack microtrons, along with the Harmonic Double Sided Microtron, which can accelerate electrons up to 1.6 GeV. Four experimental halls are also pictured (A1, A2, A4, and X1). Reproduced from [47].

4.1.2 Bremsstrahlung production

Bremsstrahlung radiation occurs when a high-energy electron interacts with an electromagnetic field, transfers a small amount of momentum to the field's source, and creates a bremsstrahlung photon in this process. For an incident electron with initial state (E_o, \mathbf{p}_o) and final state (E, \mathbf{p}) , with a produced photon (k, \mathbf{k}) and momentum transfer \mathbf{q} , energy and momentum conservation requires,

$$E_o = E + k, \quad (4.2)$$

$$\mathbf{p}_o = \mathbf{p} + \mathbf{k} + \mathbf{q}. \quad (4.3)$$

The set of all allowed momentum transfers is restricted both by kinematics, which set a lower limit on q , and the fact that the bremsstrahlung cross section falls off rapidly with increasing values of q , setting an effective upper limit. One can define the set of allowed \mathbf{q} , defined relative to the incoming electron momentum vector, \mathbf{p}_o , in terms of transverse (q_T) and longitudinal (q_L) components [49],

$$\begin{aligned} 0 &\leq q_T \lesssim 2x, \\ \delta(x) &\leq q_L \lesssim 2\delta(x), \end{aligned} \quad (4.4)$$

where x is the fractional photon energy, given by,

$$x = \frac{k}{E_o}, \quad (4.5)$$

and $\delta(x)$, defined as the minimum q_L allowed, is given by,

$$\delta(x) = \frac{x}{2E_o(1-x)}. \quad (4.6)$$

The allowed momentum transfer region is referred to as the pancake region since the transverse component extends across a much larger region than that of the longitudinal component. This gives rise to a pancake centered on, and normal to, \mathbf{p}_o .

4.1.2.1 Incoherent Bremsstrahlung production

Electrons incident upon an amorphous radiator produce incoherent bremsstrahlung. In this case, the incident electron interacts with the Coulomb field of an atomic nucleus. The cross section for incoherent bremsstrahlung, σ^{in} , is a Bethe-Heitler spectrum which decreases quickly as photon energy increases (roughly $\frac{1}{k}$). The momentum

transfer, \mathbf{q} , for incoherent bremsstrahlung can lie anywhere within the pancake region. This produces a uniform azimuthal distribution in the polarisation vector of the photon, thus producing an unpolarised photon beam.

4.1.2.2 Coherent Bremsstrahlung production

Electrons incident upon a crystalline radiator produce incoherent bremsstrahlung. In this case, the incident electron interacts with, and transfers momentum to, the crystal as a whole (as opposed to individual nuclei). Instead of the smooth (roughly $\frac{1}{k}$) distribution of incoherent bremsstrahlung, coherent bremsstrahlung shows a cross section with structure related to the lattice structure of the crystal.

A crystalline radiator, as used in the production of linearly polarised photons, is a material which has a structure composed of a regularly repeating pattern of atoms. This base pattern, often referred to as the crystal's unit cell, repeats at a point known as a lattice point and these lattice points combine to form the direct crystal lattice. The axes of the unit cell are described by three primitive lattice vectors, \mathbf{a}_1 , \mathbf{a}_2 , and \mathbf{a}_3 . From this direct crystal lattice, it is possible to define the reciprocal crystal lattice. Similar to the direct lattice, we can define a set of primitive reciprocal lattice vectors, \mathbf{b}_1 , \mathbf{b}_2 , and \mathbf{b}_3 . These can be expressed in terms of \mathbf{a}_i by [50],

$$\begin{aligned}\mathbf{b}_1 &= 2\pi \frac{(\mathbf{a}_2 \times \mathbf{a}_3)}{(\mathbf{a}_1 \times \mathbf{a}_2) \cdot \mathbf{a}_3}, \\ \mathbf{b}_2 &= 2\pi \frac{(\mathbf{a}_3 \times \mathbf{a}_1)}{(\mathbf{a}_1 \times \mathbf{a}_2) \cdot \mathbf{a}_3}, \\ \mathbf{b}_3 &= 2\pi \frac{(\mathbf{a}_1 \times \mathbf{a}_2)}{(\mathbf{a}_1 \times \mathbf{a}_2) \cdot \mathbf{a}_3}.\end{aligned}\tag{4.7}$$

Planes and vectors in the lattice can be described using a set of indices, the Miller indices [51], g_1, g_2, g_3 . A reciprocal lattice vector, \mathbf{g} , can then be defined in terms of its Miller indices by,

$$\mathbf{g} = g_1\mathbf{b}_1 + g_2\mathbf{b}_2 + g_3\mathbf{b}_3.\tag{4.8}$$

Planes orthogonal to \mathbf{g} are denoted by $(g_1g_2g_3)$ and negative indices are denoted \bar{g}_i .

While the momentum transfer, \mathbf{q} , is still constrained by the pancake region, the coherent bremsstrahlung process places an additional constraint upon \mathbf{q} . Namely, in

the coherent case, \mathbf{q} must simultaneously lie within the pancake region and coincide with a reciprocal lattice vector of the crystal. Recalling that the reciprocal lattice is defined by the primitive reciprocal lattice vectors, \mathbf{b}_i , one can define two important angles, θ and α . The angle θ is defined as the angle between the \mathbf{p}_o and \mathbf{b}_1 vectors while α is defined as the angle between the $(\mathbf{p}_o, \mathbf{b}_1)$ and $(\mathbf{b}_2, \mathbf{b}_3)$ planes. The longitudinal and transverse components of the reciprocal lattice vector are [49],

$$\begin{aligned} g_T &\approx \sqrt{(g_2)^2 + (g_3)^2}, \\ g_L &\approx g_1 + \theta(g_2 \cos \alpha + g_3 \sin \alpha). \end{aligned} \quad (4.9)$$

When the condition $g_L = \delta(x)$, the lower limit of the pancake region (defined in Equation 4.4) is satisfied, the coherent bremsstrahlung spectrum shows a sharp discontinuity. As the fractional photon energy crosses over the discontinuity, the coherent bremsstrahlung cross section falls off. The fractional photon energy at this discontinuity point, x_d , is given by,

$$x_d = \frac{2E_o g_L}{1 + 2E_o g_L}. \quad (4.10)$$

The orientation of the crystal relative to the incident electron determines the set of reciprocal vectors within the pancake region. As the momentum transfer, \mathbf{q} , must align with a reciprocal vector, the orientation of the crystal also determines the set of allowed momentum transfers. In contrast to incoherent bremsstrahlung, the constraint on the momentum transfer in coherent bremsstrahlung results in a constraint upon the polarization vector of the produced photon.

In addition to the coherent contribution, the total cross section for electron scattering off a crystalline radiator includes an incoherent contribution arising from lattice vibrations, or phonons. The total cross section for a crystal can be expressed,

$$\sigma^{crystal} = \sigma^{co} + \sigma^{in}. \quad (4.11)$$

The incoherent contribution for a crystalline radiator is still well approximated by the Bethe-Heitler distribution. For diamond, the incoherent cross section for a crystalline radiator is approximately 15% less than the incoherent cross section for an amorphous carbon radiator of the same thickness [52].

4.1.2.3 Degree of linear polarisation

A linearly polarised photon beam can be produced by bringing an electron beam incident upon a crystalline radiator. The enhancement, R , in the cross section due to coherent bremsstrahlung production can be given by,

$$R = \frac{\sigma^{crystal}}{\sigma^{in}}. \quad (4.12)$$

A plot of the enhancement as a function of photon energy will show sharp drops at photon energies associated with discontinuity points, x_d . The sharp decrease in the spectrum is known as a coherent edge. In cases where more than one reciprocal lattice vector lies within the pancake region, the enhancement spectrum will show multiple peaks. An example enhancement spectrum from the December 2012 run period is shown in Figure 4.3 for coherent bremsstrahlung on a 30 μm diamond radiator. This enhancement spectra was determined by measuring the distributions of retarded electrons as a function of energy. This is accomplished using the Glasgow Tagged Photon Spectrometer, discussed in Section 4.1.3. The incoherent contribution is approximated by measuring the same electron distribution using an amorphous radiator. The enhancement distribution is then simply produced by dividing the two distributions. The primary peak, with a coherent edge positioned near 300 MeV, corresponds to coherent bremsstrahlung production off the [022] reciprocal lattice vector. The bremsstrahlung distribution from the diamond radiator was divided by a distribution from an amorphous 10 μm Copper radiator to model the incoherent contribution. Although Copper itself has a lattice structure, standard copper is made of grains, each a few microns in size. Each grain has a lattice structure, but since they are all randomly orientated, the total distribution is effectively amorphous.

To describe the resulting degree of polarisation in the photon beam, it is useful to define a reference frame. If one defines the horizontal plane of the lab frame as $(\mathbf{p}_o, \mathbf{e}_x)$ then the plane which describes the polarization reference frame can be described by $(\mathbf{b}_1, \mathbf{e}_x)$. The coherent component of $\sigma^{crystal}$ can then be expressed in terms of the perpendicular and parallel components,

$$\sigma^{co} = \sigma^\perp + \sigma^\parallel, \quad (4.13)$$

where σ^\perp (σ^\parallel) has a photon polarisation vector perpendicular (parallel) to the polarisation reference frame $(\mathbf{b}_1, \mathbf{e}_x)$. The degree of linear polarisation of the photon beam,

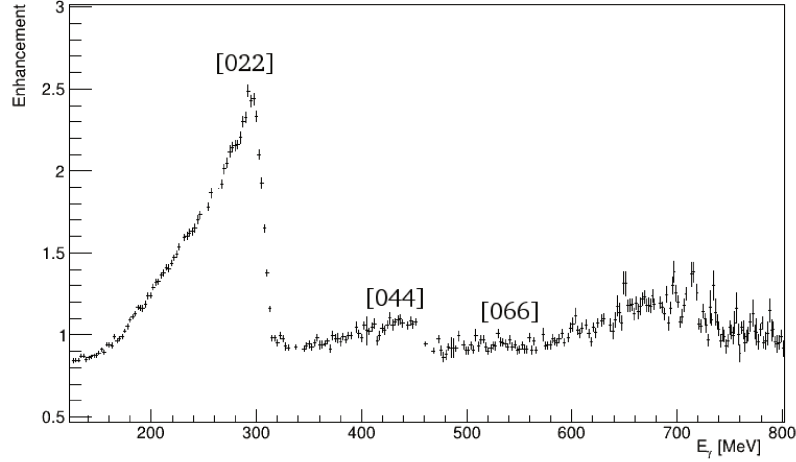


Figure 4.3: Example enhancement spectrum, produced during the run period, for coherent bremsstrahlung off a $30 \mu\text{m}$ diamond crystal. The incoherent contribution was approximated with an amorphous $10 \mu\text{m}$ Copper radiator. The three primary peaks are labelled with the Miller indices of their reciprocal lattice vectors.

P , produced from a crystalline radiator, is then given by [53],

$$P = \frac{\sigma^\perp - \sigma^\parallel}{\sigma^{crystal}}. \quad (4.14)$$

The degree of polarisation can also be expressed in terms of the enhancement, R ,

$$P = \frac{(R - 1)(\sigma^\perp - \sigma^\parallel)}{R(\sigma^\perp + \sigma^\parallel)}, \quad (4.15)$$

where large enhancements correspond to high degrees of linear polarisation.

4.1.2.4 Diamond orientation: The Stonehenge Technique

As discussed in Section 4.1.2.2, the coherent bremsstrahlung spectrum is determined by the set of reciprocal lattice vectors which lie within the allowed momentum pancake region. By controlling the orientation of the crystal within the incident electron beam, the characteristics of the coherent bremsstrahlung spectrum can be controlled. As an example, equations (4.9) and (4.10) show the connection between the crystal orientation and the coherent edge position.

To properly align the crystal within the electron beam, it is mounted on a five-axis goniometer capable of adjusting the crystal orientation. The Stonehenge technique

[46], developed by Ken Livingston (MAMI A2 collaborator, from University of Glasgow), was used to align the diamond radiator at the beginning of the run period. Alignment of the crystal is achieved by rotating the crystal about its vertical and horizontal axes, θ_v and θ_h . A bremsstrahlung enhancement spectrum is taken for each point and the intensity can be plotted as a function of photon energy and the vertical and horizontal stepping function coordinates. An example Stonehenge plot, produced during the run period, is shown in Figure 4.4. Colour intensity in the Stonehenge plot is used to show the level of enhancement. By examining the intensity pattern of the Stonehenge plot, one can produce a complete set of alignment coordinates for the crystal. For complete details of the Stonehenge technique and the interpretation of Stonehenge plots, see ref. [46].

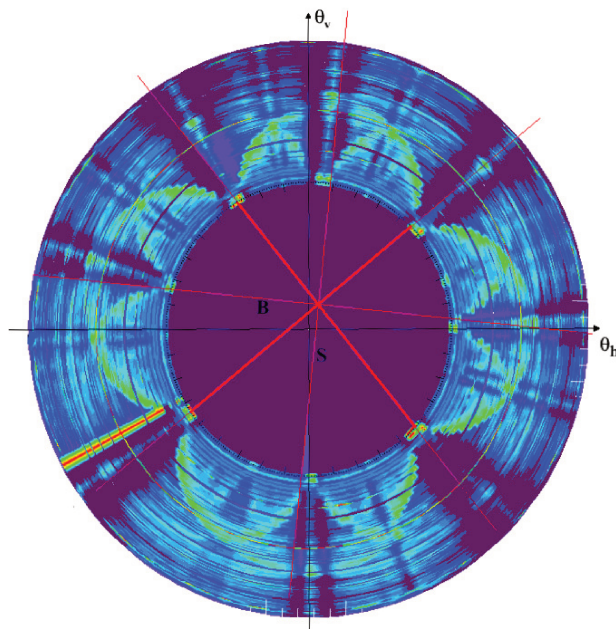


Figure 4.4: Example Stonehenge plot produced during the alignment process of the run period. Stonehenge plots are produced by rotating the diamond about a vertical and horizontal axis, θ_v and θ_h , to calculate a series of enhancement spectra. The enhancement spectra are shown, where the radial axis corresponds to the energy of the bremsstrahlung photon, and the intensity corresponds to the degree of enhancement.

During the run period, the diamond was aligned within the electron beam to produce two polarisation settings, p_{\perp} and p_{\parallel} , with photon polarisation vectors separated by 90° . The diamond was aligned using the Stonehenge technique such that the dominant $[022]$ reciprocal lattice vector produced a primary coherent edge at 310 MeV.

4.1.2.5 Collimation

Collimation of the produced photon beam can be used to increase the degree of linear polarisation. This effect arises due to differences within the angular distributions of incoherent and coherent bremsstrahlung. In the case of incoherent bremsstrahlung, photons are emitted in a cone around \mathbf{p}_o with a characteristic angle given by [54],

$$\theta_\gamma = \frac{m_e c^2}{E_o}. \quad (4.16)$$

Thus, for incoherent bremsstrahlung, this distribution depends only on the incident electron energy and is independent of the photon energy. Therefore, collimation of the incoherent bremsstrahlung photons will reject a roughly even distribution of photons over the photon energy. However, in the case of coherent bremsstrahlung, the angular distribution of the emitted photon does depend on the photon energy. For each peak in the bremsstrahlung enhancement spectrum, the emission angle of the photon becomes smaller (more forward) as the photon energy approaches each x_d , the coherent edges. Collimation of the coherent bremsstrahlung photons will therefore preferentially remove photons from the lower-energy region of the peak. This reduces the polarisation (by rejecting polarised photons) in these low-energy regions, thus narrowing the peaks of the bremsstrahlung enhancement spectrum. However, by accepting the forward emitted coherent photons, while simultaneously rejecting incoherent photons of the same energy, one increases the degree of polarisation in this higher-energy regions of each peak. During the run period, the photon beam was collimated using a 3 mm lead collimator situated 2.5 m downstream of the radiator.

4.1.3 Glasgow Tagged Photon Spectrometer

The energy of the photon was inferred from a momentum analysis of the bremsstrahlung electron using the Glasgow Tagged Photon Spectrometer. The incident electron energy, E_o , is well known and re-arranging equation (4.2), the photon energy can be given by,

$$k = E_o - E. \quad (4.17)$$

The process of inferring the photon energy by detecting the bremsstrahlung electron is known as tagging. The Glasgow Tagged Photon Spectrometer, or Tagger, uses a

large dipole magnet to bend the path of the electron. The radius of curvature of a charged particle within a magnetic field is given by,

$$r = \frac{p}{qB}. \quad (4.18)$$

A focal plane detector, comprised of 353 plastic scintillators, is used to momentum analyse the electrons. For a given magnetic field, B , the radius of curvature will depend directly on the momentum, p , of the particle. Thus, the position along the focal plane detector can be used to determine the energy of the bremsstrahlung electron. The magnetic field strength, B , is chosen such that electrons which did not interact within the radiator are bent into a beam dump. Figure 4.5 shows the tagging process using the Glasgow Tagged Photon Spectrometer.

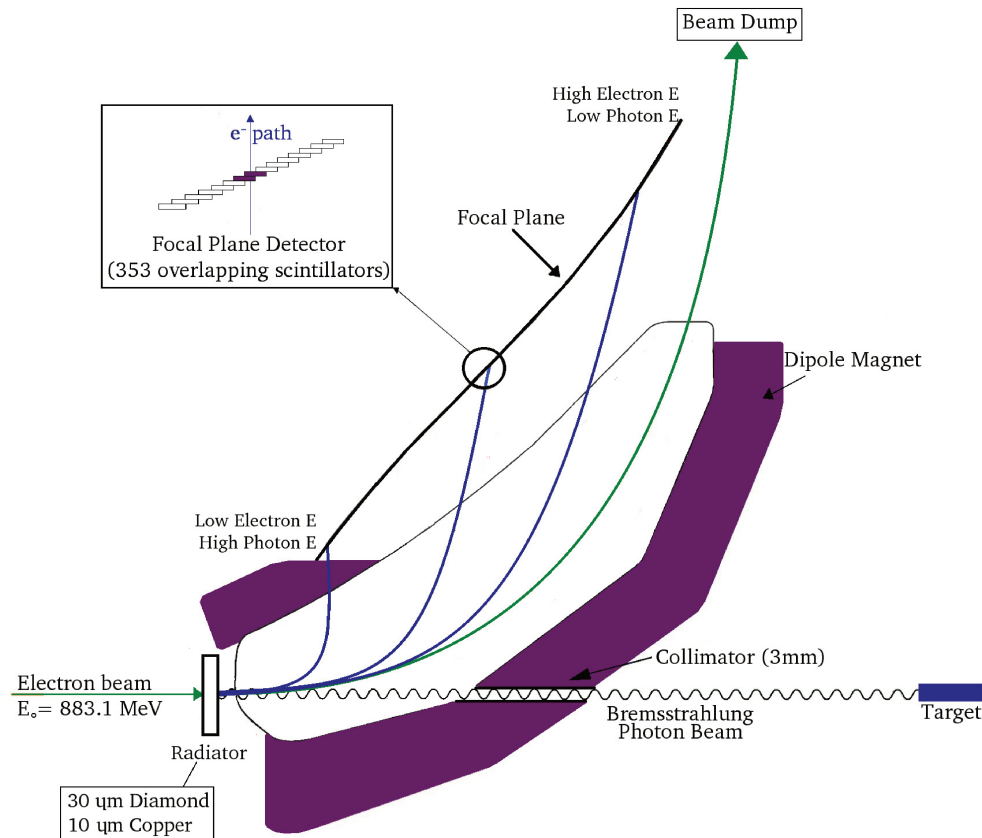


Figure 4.5: Glasgow Tagged photon spectrometer. Relativistic electrons are incident upon a radiator to produce bremsstrahlung photons. The photons are collimated and continue to the target. The electrons are momentum analysed with the Tagger to determine the photon energy.

Each scintillator is roughly $2 \text{ cm} \times 8 \text{ cm} \times 2 \text{ mm}$ and is coupled to a photomultiplier tube, PMT. Additionally, each scintillator overlaps with the neighbouring scintillators by roughly 50%. To identify electron signals, a “hit” is formed in the focal plane detector when there is a coincidence between two overlapping scintillators. The requirement of a coincidence between two scintillators results in 352 tagger channels. Bremsstrahlung photons are tagged by making a time coincidence between detected reaction particles and the electron’s time signal. An example distribution of the tagger channel hits, produced during the run period, is shown in Figure 4.6. The corresponding distribution of photon energies is also shown. The incoherent Bethe-Heitler distribution is clearly visible, along with an enhancement associated with the primary polarisation near 310 MeV.

During the run period, a maximum rate of 10^6 electrons per second per active scintillator was maintained to preserve the lifetime of the PMTs. Tagger channels above 320 were not used to increase the electron rate in the region of interest. This resulted in a range of tagged photon energies between 125 and 820 MeV. The current of the incident electron beam was 30 nA for coherent bremsstrahlung produced with the $30 \mu\text{m}$ diamond radiator and 10 nA for incoherent bremsstrahlung produced with the $10 \mu\text{m}$ copper radiator.

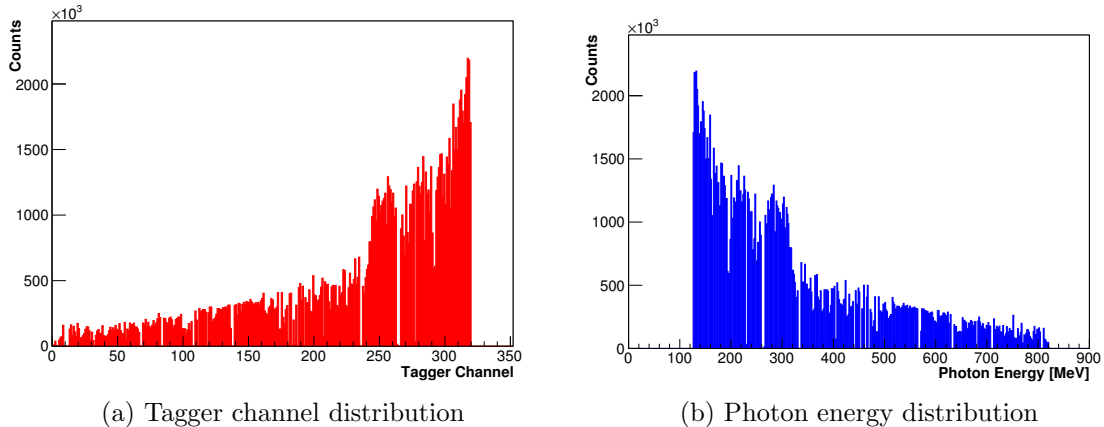


Figure 4.6: Example distribution of electrons within the Glasgow Tagged photon spectrometer (left) and the associated photon energies (right).

To measure the flux of electrons, N_{e^-} , a discriminated signal from each tagger channel was sent to a scaler module and counted. Due to the collimation of the bremsstrahlung photon beam, the flux of photons incident upon the target cannot be

directly inferred from the measured electron flux, and therefore dedicated measurements must be made to relate the electron flux to the photon flux on target. For such dedicated measurements, a lead glass detector, $20\text{ cm} \times 20\text{ cm} \times 20\text{ cm}$, was placed in the beam line, 15 m downstream from the radiator. The Pb-glass was assumed to have 100% efficiency and a time coincidence between the lead glass and a signal in a tagger channel was counted as a tagged photon, N_{Tagg} . The tagging efficiency for a given channel, i , is then given by,

$$\epsilon_{\text{Tagg}}(i) = \frac{N_{\text{Tagg}}(i)}{N_{e^-}(i)}, \quad (4.19)$$

which allows the direct relation between measured electron flux the resulting flux of photons on target. During the run period, ten tagging efficiency measurements were performed. The current of the incident electron beam was reduced such that the rate of photons on the Pb-glass detector was 10^5 photons per second. A full analysis of the tagging efficiency measurements is discussed later in Section 5.3.

4.2 Liquid hydrogen target

During the run period, linearly polarised photons were incident upon an unpolarised liquid hydrogen, LH_2 , target. A cylindrical target cell, made of $125\text{ }\mu\text{m}$ Kapton, was filled with LH_2 at 1080 mb pressure. Additional layers of insulating material were wrapped around the target cell. The target cell length was $100.0 \pm 1.0\text{ mm}$, with a density of 4.249×10^{23} protons/ cm^2 [55]. The LH_2 target cell is shown in Figure 4.7.



Figure 4.7: Inner Kapton cell of the liquid hydrogen, LH_2 , target. The length of the target cell was $100.0 \pm 1.0\text{ mm}$, with a density of 4.249×10^{23} protons/ cm^2 . Reproduced from [55].

4.3 Event detection

For photons which underwent an interaction within the target, the CB-TAPS detector system was used to detect and identify the final state reaction particles. The components of the CB-TAPS system are shown in Figure 4.8 and will be discussed in the following section.

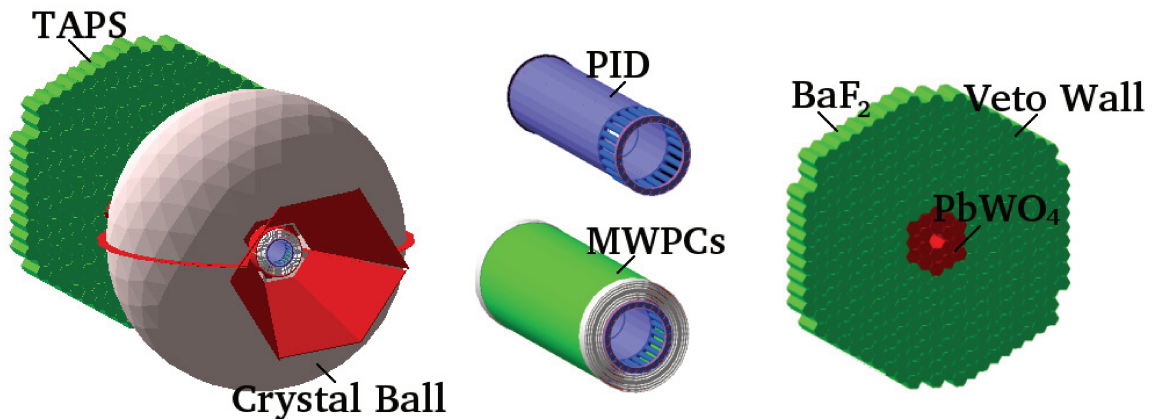


Figure 4.8: Simulated geometry of the CB-TAPS system. The Crystal Ball and TAPS detectors are shown along with their composite detectors. The Crystal Ball is composed of NaI detectors and the PID and MWPCs are detectors interior to the Crystal Ball, surrounding the target. TAPS is composed of BaF₂ and PbWO₄ detectors. The Veto wall, shown in dark green, is situated in front of the main TAPS calorimeter.

4.3.1 Crystal Ball Photon Spectrometer

The Crystal Ball, CB, is a highly segmented photon calorimeter. Roughly spherical, the CB comprises 672 sodium iodide, NaI(Tl), crystals. Each crystal, a truncated pyramid with a length of 40.6 cm, is coupled to an individual PMT. The signal from each PMT is then fed into an analog-to-digital converter, ADC, and a time-to-digital converter, TDC. The CB surrounds the target and provides 94% coverage of the 4π solid angle range. The Crystal Ball was originally designed for colliding beam experiments at the Stanford Linear Accelerator and participated in the early J/ψ experiments in the 1970s. To accommodate colliding beams, the Crystal Ball has a large gap in the forward and backward region. Each missing section of the CB covers an area equivalent to 24 NaI crystals. The CB covers a polar angle of 21° to 159° .

Photons deposit energy within the CB via the development of electromagnetic showers, predominantly through pair production. Since pair production scales with Z^2 , the high density and atomic number of sodium iodide make it an ideal material for photon detectors. Additionally, the high light output of NaI helps to ensure a good energy resolution over a wide range of photon energies. As photons typically deposit energy within a large number of crystals, a weighted energy algorithm is used to determine the position of the photon. This is similar to a center of gravity calculation. For the CB, this weighted energy determination gives an angular resolution better than the crystal size. By comparison, hadrons tend to deposit their energy within only one or two crystals. This results in an angular resolution in the NaI which is worse for hadrons than photons.

4.3.1.1 Multiwire proportional chambers

To improve the angular resolution of charged particles, two coaxial multiwire proportional chambers sit within the CB, surrounding the target. Each chamber is constructed from three layers of wound wire. The wires of the inner and outer layer are wound at $\pm 45^\circ$ and act as a cathode. The wires of the middle layer run parallel to the beam axis and act as an anode. An ionizing gas mixture of 66% Argon, 28.5% Ethane, 5% Ethanol, and 0.5% Freon was used within the MWPCs and a voltage of 2400V was applied to each wire chamber. The information from all six layers can be combined to provide much better tracking and position information for charged particles than possible from the CB alone.

4.3.1.2 Particle Identification Detector

The inner radius of the Crystal Ball is 25.3 cm. The timing resolution of the CB is not sufficient enough to perform particle identification using time of flight methods because of the short distance between target and detectors. An additional detector, the Particle Identification Detector, was designed to work with the existing Crystal Ball and MWPCs detectors and provide particle identification of charged particles. The PID detector is composed of 24 thin plastic scintillators, each 1.5 cm \times 50 cm \times 4 mm, forming a barrel around the target. Due to spatial constraints, the PID was installed between the target and the MWPCs. With the PID surrounding the target,

reaction products pass through the PID before the MWPCs. This causes a reduced resolution in the tracking of charged particles, however, the scintillators so thin and the effect is not large.

Particle identification is accomplished using a $\Delta E/E$ method which involves correlating a sample of the particle's differential energy loss in a thin detector with its total energy as measured in a calorimeter. As charged particles pass through a PID scintillator, they deposit a small fraction of their energy. For electrons and charged pions, the energy deposit is roughly constant at 1-2 MeV. Protons, however, will deposit energy proportional to their total energy with slower protons depositing a higher fraction of their total energy. The total energy of the particle is measured in the CB. If a charged particle is not stopped in the CB, the $\Delta E/E$ method will not work well. The CB is capable of stopping protons up to 425 MeV and charged pions up to 250 MeV. A two dimensional histogram of the differential energy loss, ΔE , measured in the PID, and the energy, E , measured in the CB, results in distinct bands associated with the different particle types. Two dimensional cuts can be used to identify protons, electrons and charged pions using this $\Delta E/E$ method. An example $\Delta E/E$ histogram is shown in Figure 4.9 and the particle bands have been identified.

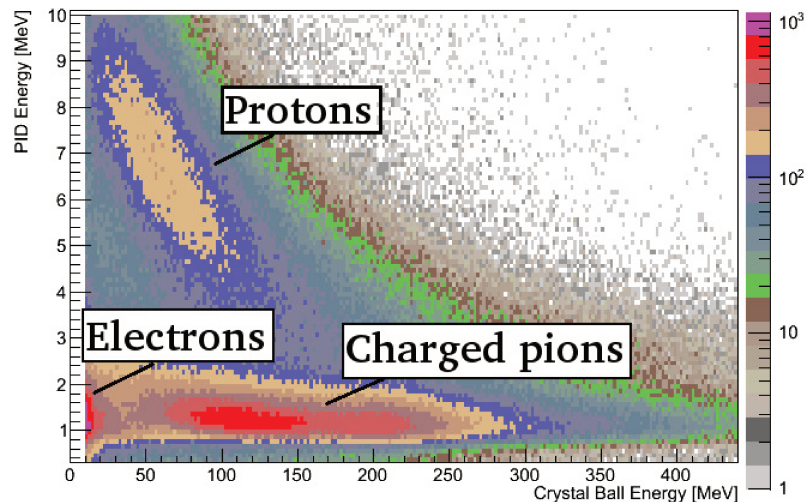


Figure 4.9: An example $\Delta E/E$ histogram. The differential energy loss, ΔE , in the PID and the energy, E , measured in the CB, will result in distinct bands associated with the different particle types. A two dimensional cut can be used to identify protons, electrons and charged pions using the $\Delta E/E$ method.

4.3.2 TAPS

The Crystal Ball was originally designed for colliding beam experiments. However, for a fixed target experiment, reaction products are Lorentz boosted forward introducing a need for an additional detector in the forward region. The TAPS detector, Two-Armed Photon Spectrometer, was introduced to provide detection in the forward polar region not covered by the Crystal Ball.

TAPS, a highly segmented photon calorimeter, comprises 366 barium fluoride, BaF_2 , crystals and 72 lead tungstate, PbWO_4 , crystals. Each BaF_2 crystal is shaped as a hexagonal prism with a length of 22.5 cm. The crystals are arranged in a honeycomb pattern to form a solid hexagonal wall downstream of the Crystal Ball detector, approximately 145 cm from the target. The PbWO_4 crystals are shaped such that four crystals combine to have the same shape and size as a BaF_2 crystal. The PbWO_4 crystals form the two inner rings of the TAPS detector and are used to handle the high rates expected near the beam. Each BaF_2 and PbWO_4 crystal is coupled to a PMT. The signal from each PMT is then fed into an ADC and TDC. Similar to the Crystal Ball, photons will deposit their energy in many TAPS crystals through electromagnetic showers. An energy weighted position, similar to a center of gravity calculation, is also applied to determine the position. The coverage of the polar angle from the BaF_2 crystals is 4° to 20° . The PbWO_4 crystals extend the polar angle coverage of TAPS to be 2° to 20° . During the run period, many of the PMTs connected to PbWO_4 crystals were broken. Additionally, the readout electronics were not completely implemented. For these reasons, the PbWO_4 are not considered for this analysis.

The distance from the target to TAPS, along with the excellent timing resolution of BaF_2 crystals, make particle identification using time of flight methods possible. A two dimensional plot of the time of a particle detected within TAPS, t , and the energy deposit in TAPS, E , will produce distinct bands associated with different particle masses (similar to the PID). Particle identification is also possible using pulse shape analysis, PSA. BaF_2 crystals produce two light components with a fast and slow relaxation time. The relative intensity of the fast and slow components is inversely related to the ionizing power of the incoming particle. Hadrons, for example, have a high ionizing power for the rate of energy loss and therefore a small fast/slow ratio.

4.3.2.1 Veto wall

An additional detector, the Veto wall, provides a third method for particle identification. The Veto wall is composed of 384 thin plastic scintillators, each 5mm thick and hexagonally shaped to match a BaF₂ crystal. Each BaF₂ crystal, and each group of four PbWO₄ crystals, has a dedicated Veto scintillator which is coupled to a PMT via a wavelength shifting fiber. Similar to the PID, the fractional energy deposition in a Veto wall scintillator, ΔE , can be matched to the total energy deposition in TAPS, E . A two dimensional histogram, similar to the one shown in Figure 4.9, can be created for charged particle identification.

4.3.3 Detector summary

The main parameters of the CB-TAPS detector system are given in Table 4.2. An estimate of the angular and energy resolutions is given for both the Crystal Ball and TAPS detector systems for photons and charged particles within the energy region of interest. Only an estimate is given as the resolution of charged particles and photons can differ, and the full resolution is a function of energy and polar angle.

	Crystal Ball	TAPS
Main Spectrometer Design	672 NaI(Tl)	72 PbWO ₄ and 366 BaF ₂
Additional Detectors	PID MWPCs	Veto wall
Polar (θ) coverage	21° to 159°	2° to 20°
Azimuthal (ϕ) coverage	0° to 360°	0° to 360°
Polar (θ) resolution	2°	1°
Azimuthal (ϕ) resolution	2°	1°
FWHM γ Energy resolution	2%	3%
Charged Particle Detection	PID - dE/E method 2 MWPCs - tracking	Veto - dE/E method Pulse shape analysis Time of flight

Table 4.2: Main parameters of the CB-TAPS detector system.

4.3.4 Event readout

4.3.4.1 Trigger system

The total energy deposited in the Crystal Ball is used to form a trigger condition for event readout. The trigger condition, known as the Energy Sum trigger, is designed to be the sum of all energy deposits in the NaI crystals of the Crystal Ball. To accomplish this trigger, each NaI crystal is coupled to a dedicated PMT and the analog signals from all PMTs are summed together giving an analog signal which is the total energy in the Crystal Ball. This summed analog signal is then duplicated and passed through one discriminator with a low threshold and one discriminator with a high threshold. The low threshold forms a first level trigger condition which initiates a trigger signal and inhibits the system to future signals. The high threshold forms the final experimental trigger. If the energy sum signal passes both the low and high thresholds, the information from all ADCs and TDCs in the detector system are read out and stored and the system is un-inhibited. The information associated with a single readout of the detector system is referred to as an event. In cases where the energy sum signal passes the low threshold but not the high threshold, a “fast clear” signal is passed to all ADCs and TDCs. This resets the hardware and un-inhibits the system. The two-tiered discriminator setup is used, rather than a single high threshold discriminator, to give a better timing resolution to the trigger.

During the run period, the Energy Sum trigger was used for event readout. The low threshold setting was 45mV and the high threshold setting was 180mV, corresponding to an energy deposit of roughly 20 MeV and 80 MeV respectively. The rate of fast clear signals - which passed the low threshold setting, but not the high threshold setting - was roughly 6 kHz. The rate of trigger signals - which passed both the low and high threshold settings - was roughly 2 kHz. Due to a faulty wire connection, the fast clear signal was not delivered to the PID. Thus, in cases where the Energy Sum signal passed the low threshold discriminator, but not the high threshold discriminator, the ADC and TDC information in the PID was not cleared. When an Energy Sum signal does finally pass the high threshold, and the entire event information is read out, it is possible that the PID information is from an earlier time. While it is expected that this error would result in a severe reduction in the PID efficiency,

it is relatively unlikely that the PID information from an earlier time would coincide with a future event. Thus, when an energy deposition in the PID is connected to an energy deposition in the MWPCs or Crystal Ball it can likely be used. In Figure 4.9, an example $\Delta E/E$ histogram was shown. Figure 4.10 shows a comparison of this example to one produced during the run period. Although some differences can be seen, in general the typical $\Delta E/E$ structure is seen clearly suggesting that PID energy deposition is not often miscorrelated with an energy deposition in the Crystal Ball.

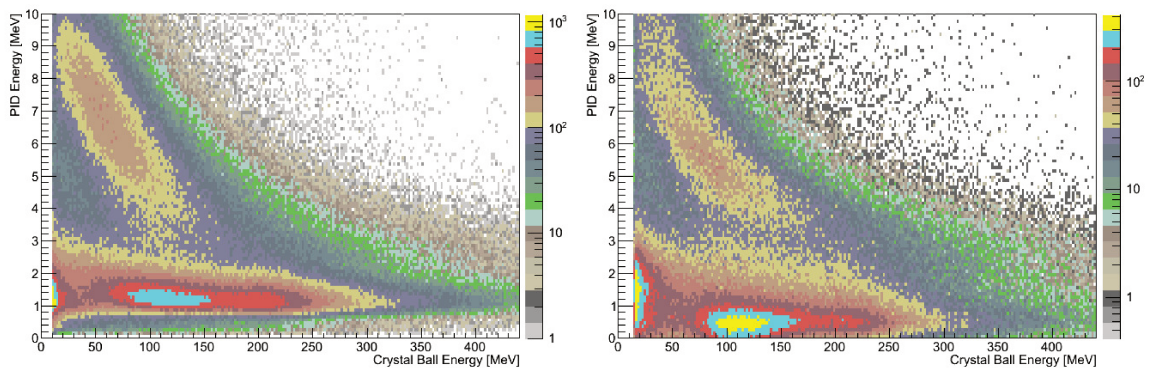


Figure 4.10: Left: A typical $\Delta E/E$ histogram, shown in Figure 4.9, is shown. Right: An example $\Delta E/E$ histogram, produced during the run period, is shown. Despite the faulty fast clear connection to the PID, the characteristic bands associated with the different particle types are clear.

4.3.4.2 Scalers

A set of scalers are read out once every 1000 events. These scalers store information related to all aspects of the experiment. As discussed in Section 4.1.3, a set of scalers are used to measure the incident electron flux. Additional scalers are used to record the livetime of the detector system. As discussed in 4.3.4.1, during event readout, the data acquisition system is inhibited once a trigger signal passes the low threshold Energy Sum trigger. The system remains inhibited until either a fast clear signal is delivered or the trigger passes the experimental trigger threshold and the event is read out. The percentage of time which the system is open to signals is known as livetime. To determine the livetime, a 1 MHz pulse generator signal is used. The signal is duplicated and one signal is passed into a free running scaler which counts the generated pulses. A copy is sent into a second scaler, which is inhibited whenever

the data acquisition system is inhibited. In this way, the ratio of the inhibited scaler and free running scaler determines the livetime.

4.3.4.3 Data acquisition software: Acqu

Acqu is a C++ based data acquisition framework, developed by John Annand (MAMI A2 collaborator, from University of Glasgow), which is used to control event readout for the CB-TAPS detector system. It comprises two main components, AcquDAQ and AcquRoot. When a trigger condition is satisfied, the ADC and TDC information of all detector elements is read out. To accomplish this, AcquDAQ uses a large network of slave VME CPUs to control data acquisition of sub-components of the CB-TAPS system. A single computer, running AcquRoot, collects and merges multiple data streams across a network connection. During data taking, AcquRoot is responsible for the data merging. Post data taking, AcquRoot can also unpack and analyse data offline.

Chapter 5

Event Reconstruction

The following chapter outlines the event reconstruction applied for this analysis. Section 5.1 outlines the two pieces of software used for event reconstruction, (1) AcqRoot, which decodes raw ADC and TDC information into particle tracks, and (2) GoAT, which performs particle identification and data sorting. Section 5.2 outlines the calibration process, necessary to convert raw ADC and TDC information into energy and time. Finally, section 5.3 outlines the process of determining the degree of photon polarisation.

5.1 Software

When an event passes the trigger condition, the ADC and TDC information from each component of the detector system is read out and stored for offline analysis. AcqRoot, part of the Acqu analysis framework designed by John Annand, unpacks raw data into particle tracks which can be analysed. An extension to the standard Acqu framework, known as GoAT, was developed for this analysis. GoAT provides particle identification, event selection, and also provides an option to perform physics reconstructions. Although GoAT was developed (by the author) for this analysis, it provides comprehensive particle reconstruction up to 1.6 GeV and has been adopted as the standard method for analysis using the CB-TAPS detector system.

5.1.1 AcqRoot

AcqRoot is a C++ based analysis framework which analyses data from the CB-TAPS detector system. AcqRoot is built upon ROOT, an object-oriented framework developed at CERN which has become a standard for experimental physics analyses. AcqRoot contains a hierarchy of classes which first decode the ADC and TDC information of the CB-TAPS detector system to form *hits* in the individual detector elements. These hits contain the energy and timing information associated with an

element of the detector system. A clustering algorithm is applied to the hits within the NaI and BaF₂ detectors. The cluster information, and the hit information from the Veto wall, the PID, and the MWPCs are then linked to form particle tracks. A special C++ class, TA2GoAT, was designed to store the output from AcqRoot into ROOT trees, a useful storage format which retains event-by-event information. This output is used as the input for GoAT.

5.1.1.1 Decode Hits

As discussed in Section 4.3, the individual detector elements of the CB-TAPS detector system are each coupled to an individual PMT. The signal from each PMT is then fed into an analog-to-digital converter, ADC, and a time-to-digital converter, TDC. An ADC and TDC stores a digital value proportional to the energy and time of the analog signal respectively. These digital values are discretized into ADC or TDC channels. An ADC or TDC channel can be converted by,

$$E = \mathbf{a}_E(C - P), \quad T = \mathbf{a}_T(C - O), \quad (5.1)$$

where C is the digital ADC or TDC channel, P is the pedestal channel of the ADC, and O is the offset channel of the TDC. A linear energy and time gain factor, \mathbf{a}_E and \mathbf{a}_T respectively, are needed to convert the digital values into energy and time. These gain factors, as well as the pedestal or offset channel, must be determined through calibrations, discussed in Section 5.2. For each ADC and TDC, a low and high software threshold is applied. A hit is formed when both the ADC and TDC for a detector element pass the thresholds simultaneously. Shown in Table 5.1 is an example set of parameters for a single BaF₂ crystal in TAPS. The ADC and TDC distributions for the example channel are shown in Figure 5.3.

5.1.1.2 Cluster Hits

Both the Crystal Ball and TAPS are highly segmented detectors. Due to this segmentation, particles — especially photons, which deposit energy via electromagnetic showers — will tend to deposit energy across multiple crystals. For this reason, a clustering algorithm is applied to the hits pattern. Clusters are formed by first searching for the hit with the highest deposited energy. This hit becomes the central crystal of

ADC	ADC gain, \mathbf{a}_E	[MeV/channel]	0.3120
	ADC pedestal	[channel]	102.15
	Low software threshold	[MeV]	4.0
	High software threshold	[MeV]	2000.0
TDC	TDC gain, \mathbf{a}_T	[ns/channel]	0.10091
	TDC offset	[channel]	2957.27
	Low software threshold	[ns]	-200.0
	High software threshold	[ns]	200.0

Table 5.1: Example set of ADC and TDC parameters for a single BaF₂ crystal in the TAPS detector. An ADC gain and pedestal channel convert a digital ADC channel to MeV. Similarly, a TDC gain and offset channel convert a digital TDC channel to ns. A software threshold is then applied to both the energy and time to form a hit in the BaF₂ crystal.

the cluster. Hits within the surrounding crystals, which are the nearest neighbours to the central crystal, are then incorporated into the cluster. The search is then repeated using hits which have not yet been included into a cluster. This continues until all hits have been accounted for. The cluster structure for both the Crystal Ball and TAPS is shown in Figure 5.1. A typical crystal has 12 neighbours for the Crystal Ball and 6 neighbours for TAPS. Some crystals, specifically those near the edges of the detectors, can have fewer neighbours.

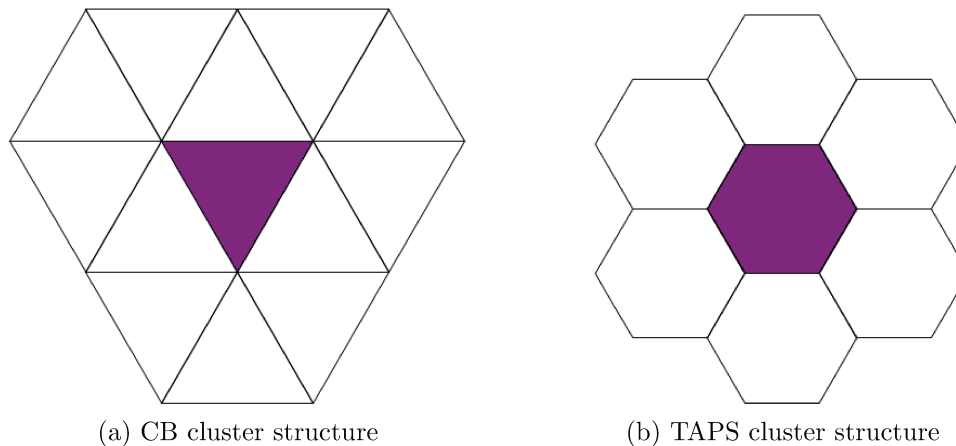


Figure 5.1: The cluster structure of (a) the Crystal Ball and (b) TAPS is shown. A clustering algorithm is applied to the hits in each detector. Beginning with the crystal with the highest energy, neighbouring crystals are grouped together to form clusters within each detector. [1]

A cluster can be characterised by its size, which is determined by the number of hits included into the cluster. A maximum cluster size of 13 is possible for the

CB and 7 for TAPS. A cluster energy is determined by summing the energies of the composite crystals. A cluster threshold is then applied to all clusters such that any clusters which fall below a minimum energy deposition are discarded. For both the Crystal Ball and TAPS, a 15 MeV cluster threshold has been applied.

5.1.1.3 Particle tracks

Particle tracks are formed by linking cluster information, from either CB or TAPS, to hits detected in the charged particle detectors. In the case of the Crystal Ball, hits in the PID or MWPC are linked with clusters in the NaI. In the case of TAPS, hits in the Veto wall are linked with clusters in the BaF₂.

For the Crystal Ball, angular cuts are used to form particle tracks. The PID detector only provides information about the azimuthal scattering angle (ϕ) of particle tracks. Therefore, a ϕ -difference is used to link hits in the PID and clusters in the NaI, or hits in the PID and MWPCs. The resulting distributions are shown in Figure 5.2a and 5.2b respectively. For this analysis, angular cuts of $\Delta\phi_{\text{PID} - \text{NaI}} = [-20^\circ, 20^\circ]$ and $\Delta\phi_{\text{PID} - \text{MWPC}} = [-50^\circ, 50^\circ]$ were applied. As the MWPCs can provide information about the particle's azimuthal (ϕ) and polar (θ) scattering angles, a vector-angle is calculated between hits in the MWPCs and clusters in the CB. The resulting distribution is shown in Figure 5.2c. For this analysis, an angular cut of $\angle_{\text{MWPC} - \text{NaI}} = [0^\circ, 20^\circ]$ was applied. By linking the MWPCs and PID, it is possible to form particle tracks which do not involve a cluster in the NaI. This can provide significant improvement in the detection of low-energy charged particles which may not be detected by the CB.

For TAPS, linking between the BaF₂ clusters and hits in the Veto wall is comparatively easier than the Crystal Ball. As discussed in Section 4.3.2.1, each BaF₂ crystal has a dedicated Veto scintillator shaped to match a BaF₂ crystal. To form particle tracks, hits in Veto scintillators directly in front of a BaF₂ cluster are linked together.

Once particle tracks have been formed, the particles are added to a particle class in AcqRoot. The energy of the particle track is taken to be the cluster energy, which

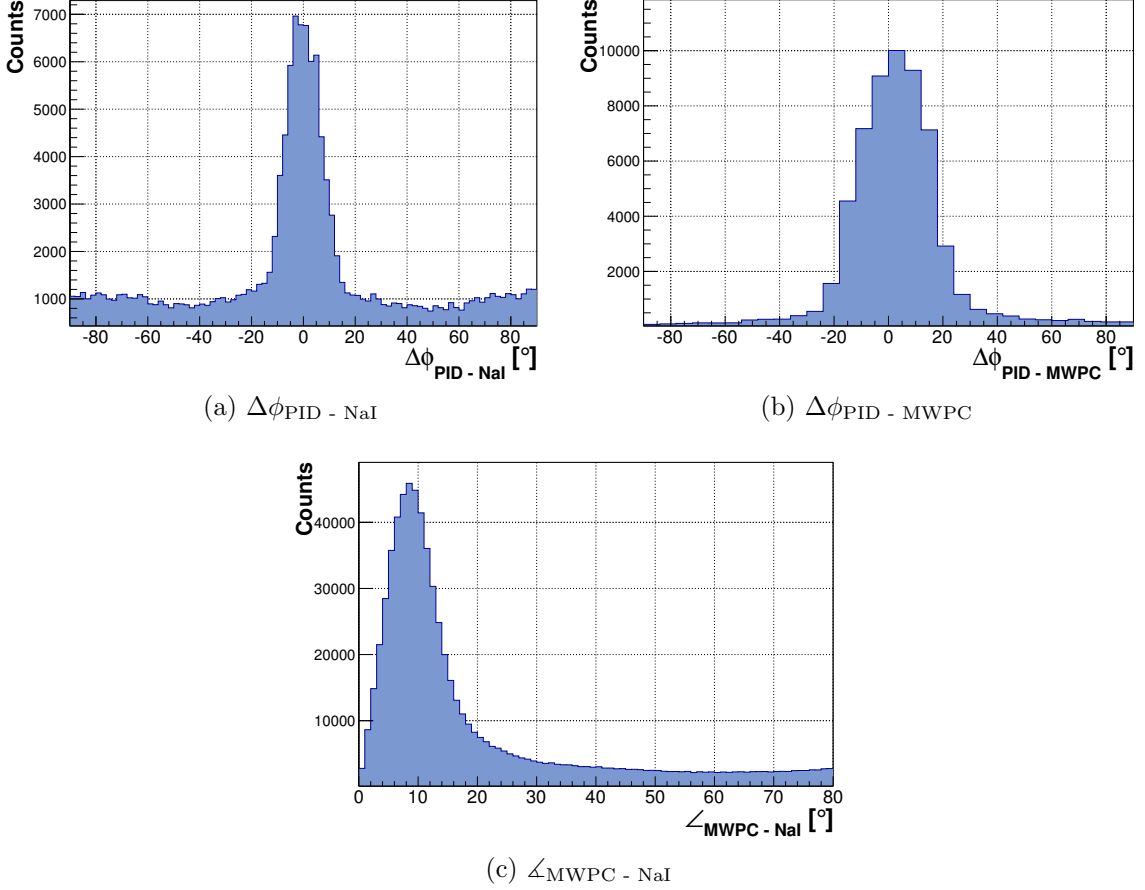


Figure 5.2: The angular distributions between PID hits, MWPC hits, and NaI clusters are shown. Angular cuts are used to determine which detector information is linked to form particle tracks. For this analysis, angular cuts of $\Delta\phi_{\text{PID} - \text{NaI}} = [-20^\circ, 20^\circ]$, $\Delta\phi_{\text{PID} - \text{MWPC}} = [-50^\circ, 50^\circ]$, and $\angle_{\text{MWPC} - \text{NaI}} = [0^\circ, 20^\circ]$ were applied.

was determined as the sum of the individual hit energies,

$$E_{\text{track}} = \sum_{\text{hits}} E_i. \quad (5.2)$$

For particle tracks which do not involve a cluster — only possible for PID-MWPC combinations — a zero energy is stored. The time is taken to be the time of the central crystal of the cluster. Again, in cases which do not involve a cluster, a zero time is stored. An energy weighted algorithm determines the angle of the particle track. The position of each NaI or BaF₂ crystal, \vec{r}_i , is well known and a weighted track vector, \vec{r}_{track} , is determined by,

$$\vec{r}_{\text{track}} = \sum_{\text{hits}} \vec{r}_i \sqrt{E_i}. \quad (5.3)$$

The angular position, θ and ϕ , of the particle track are taken from the weighted track vector. Determining the particle track's position using an energy weighted position, it is possible to achieve an angular resolution better than a single crystal size. For particle tracks which do not involve a cluster, at least one MWPC must be involved. In these cases, θ and ϕ are taken from the MWPC track information.

5.1.1.4 TA2GoAT - Output to ROOT trees

Historically, within the MAMI A2-Collaboration, AcquRoot has been used as a complete physics analysis program. Users could implement a C++ based physics class which had access to all event information, including particle tracks. Within this physics class, particle identification and meson reconstruction would be completed followed by a physics analysis. Although functional, this method was relatively inflexible.

Rather than perform a complete physics analysis within AcquRoot, AcquRoot stores the event information as a ROOT tree to be further analysed. A C++ class, TA2GoAT, was designed for this purpose. Particle tracks are collected from the Crystal Ball and TAPS. Parameters for each particle track — including energy, time, and angular information — are stored. Additionally, event information related to the trigger, detector hits, Tagger, and photon polarisation is stored. This output is used as the input for GoAT.

5.1.2 GoAT

GoAT — Generation of Analysis Trees — is a C++ based analysis framework which is an extension of AcquRoot. ROOT trees, output by AcquRoot, containing full event-by-event information are used as input. Using these trees, GoAT provides methods for particle identification, meson reconstruction, and data sorting. Within GoAT, particle identification is done in two stages: first, individual particle tracks are identified, and second, particle tracks are combined to reconstruct mesons. Finally, data can be sorted to select specific particles and energy ranges and event information is stored in ROOT trees designed for physics analysis.

5.1.2.1 Particle identification

As a first step to particle identification, individual particle tracks are identified. As discussed in Section 4.3, the CB-TAPS detector system provides a multitude of different methods for charged particle identification. A $\Delta E/E$ cut, discussed in detail in Section 4.3.1.2, can be used to identify protons, electrons and charged pions for both the Crystal Ball and TAPS. Alternate methods, such as time of flight (TOF) or pulse shape analysis (PSA) can also be used for TAPS. Neutral particles (photons and neutrons) can be identified by their lack of energy deposition in any charged particle detector. Separation of photons and neutrons can be accomplished through PSA and TOF for TAPS. Separation of photons and neutrons is considerably more difficult for the Crystal Ball, which cannot make use of PSA or TOF. One possible method of separation is a cut on the cluster size of the particle track. Photons will tend to deposit energy across multiple crystals, resulting in a higher cluster size. Neutrons however will tend to deposit their energy within a few crystals. Thus, a cut placed on the cluster size can act as tool to separate photons and neutrons.

Although complex particle identification is possible within GoAT, a simplified approach was adopted for this analysis. Rather than particle identification, all particle tracks were categorised as either charged or neutral. An energy deposition in any charged particle detector — PID, MWPC, or Veto — was used to mark a particle track as charged. A pseudo particle, known as a rootino, was used to label and store these unidentified charged tracks. All other tracks, those without any energy deposition in charged particle detectors, were marked as neutral and stored as photons.

5.1.2.2 Meson reconstruction

All mesons are unstable and decay within a very short time, much too fast to be detected directly within the Crystal Ball or TAPS. Instead, their presence must be inferred by examining the decay products which are detected. Once individual particle tracks have been identified, GoAT provides a method to reconstruct meson decays. Below 1.6 GeV, the maximum incident photon energy possible with the MAMI electron accelerator, meson production is dominated by three mesons: π^0 , η , and η' mesons. Therefore, meson reconstruction within GoAT focuses on these three mesons.

Although not directly detected, a meson can be inferred by determining the invariant mass of the sum of the detected decay particles. For a particle with an energy, E , and momentum, \vec{p} , the invariant mass, m , is given by,

$$m = \sqrt{E^2 - \vec{p}^2}, \quad (5.4)$$

Similarly, an invariant mass can be determined for a system of particles,

$$m = \sqrt{(E_1 + E_2 + \dots + E_n)^2 - (\vec{p}_1 + \vec{p}_2 + \dots + \vec{p}_n)^2}, \quad (5.5)$$

To deal with complicated meson decays, two different invariant masses are calculated, $m_{\pi\text{-test}}$ and $m_{\eta\text{-test}}$, given by,

$$m = \sqrt{\left(\sum_{\text{tracks}} E_i\right)^2 - \left(\sum_{\text{tracks}} \vec{p}_i\right)^2}, \quad (5.6)$$

$$\text{where, } \left\{ \begin{array}{l} m_{\pi\text{-test}} : i \neq \text{proton, neutron, charged pion, electron} \\ m_{\eta\text{-test}} : i \neq \text{proton, neutron} \end{array} \right\}.$$

For $m_{\pi\text{-test}}$, designed to test for pion decays, particle tracks identified as protons or neutrons are ignored as they are assumed to be target recoils. Additionally, particle tracks identified as charged pions or electrons are ignored as π^0 decays involving charged particles are extremely uncommon. As charged meson decay is common for η and η' mesons, only protons and neutrons are ignored when calculating $m_{\eta\text{-test}}$. A weighted invariant mass, \bar{m} , is then calculated for each meson using a unique weighting factor. This is given by,

$$\bar{m}_{\pi^0} = \frac{|m_{\pi\text{-test}} - m_{\pi^0}|}{\omega_{\pi^0}}, \quad \bar{m}_{\eta} = \frac{|m_{\eta\text{-test}} - m_{\eta}|}{\omega_{\eta}}, \quad \bar{m}_{\eta'} = \frac{|m_{\eta\text{-test}} - m_{\eta'}|}{\omega_{\eta'}}. \quad (5.7)$$

For this analysis, the following weighting factors were adopted,

$$\omega_{\pi^0} = 20 \text{ MeV}, \quad \omega_{\eta} = 44 \text{ MeV}, \quad \omega_{\eta'} = 66 \text{ MeV}. \quad (5.8)$$

Finally, a cut is placed on each weighted invariant mass, requiring,

$$\bar{m}_{\text{meson}} \leq 1. \quad (5.9)$$

This cut essentially acts as an invariant mass cut, requiring that \bar{m}_{meson} is within a window defined by $m_{\text{meson}} \pm \omega_{\text{meson}}$. If two weighted invariant masses pass this

condition simultaneously, the smallest of the two is accepted. If these conditions are met, a meson is reconstructed and stored.

If no meson is reconstructed, a secondary meson reconstruction is possible. Due to the dominance of 2γ decay modes for π^0 and η mesons, a two particle invariant mass is constructed. For two particles, i and j , the invariant mass can be written,

$$m_{ij} = \sqrt{(E_i + E_j)^2 - (\vec{p}_i + \vec{p}_j)^2}, \quad (i \neq j), \quad (5.10)$$

$$\text{where, } \left\{ \begin{array}{l} i \neq \text{proton, neutron, charged pion, electron} \\ j \neq \text{proton, neutron, charged pion, electron} \end{array} \right\}.$$

A two particle invariant mass is computed for all possible i, j pairs. Again, a weighted invariant mass is computed as outlined in Equation 5.7 and a weighting factor is applied as in Equation 5.8. A cut on the weighted invariant mass is applied, as in Equation 5.9. If more than one particle pair satisfies this cut, the list of accepted pairs is sorted by their weighted invariant mass values. Iterating through the list, pairs with the smallest weighted invariant mass are accepted first. However, each particle index is included only once. If these conditions are met, a meson is reconstructed and stored.

As mesons are reconstructed from multiple particle tracks, the meson information, such as energy, and angle, is a combination of the particle tracks. The energy, E , and momentum, \vec{p} , of a reconstructed meson are given by,

$$E_{\text{meson}} = \sum_{\text{tracks}} E_i, \quad \vec{p}_{\text{meson}} = \sum_{\text{tracks}} \vec{p}_i. \quad (5.11)$$

The angular position, θ and ϕ , of the meson are taken from the meson momentum vector. Finally, the time associated with the meson is taken as the average time of all particle tracks.

5.1.2.3 Data sorting

Once particle identification and meson reconstruction is complete, event-by-event information is stored into ROOT trees. These ROOT trees are designed to be used for a physics-based analysis, and contain full event information. This data sorting, if used, acts as a preliminary event selection. For this analysis, two unique sorting conditions

were applied. A first sorting criteria was applied to select Compton Scattering events. Under this first selection criteria, events were accepted if there was exactly 1 photon and 1 rootino reconstructed, with no other particles or mesons reconstructed in the same event. A second sorting criteria was applied to select π^0 -photoproduction events. Under this second selection criteria, events were accepted if there was exactly 1 π^0 , and either 0 or 1 rootino reconstructed, with no other particles or mesons reconstructed in the same event. Events passing these conditions were stored in ROOT files to be analysed.

5.2 Detector Calibrations

As discussed in Section 5.1.1.1, an ADC and TDC stores a digital value proportional to the energy and time of the analog signal respectively. As outlined in equation 5.1, a gain factor and an offset, or pedestal, are needed to convert the digital values into energy and time. These gain factors, as well as the pedestal and offset channel, must be determined through calibrations.

5.2.1 a2CaLib

A program developed by the University of Basel, a2CaLib, is used to calibrate data for the CB-TAPS detector system. AcqRoot, previously discussed in Section 5.1.1, first decodes hits, clusters hits together, and creates particle tracks. As calibration parameters are needed to decode the raw hit information, an initial set of calibration parameters is used. Within AcqRoot, a C++ based physics class, TA2MyCaLib, collects particle track information and creates a set of calibration histograms. These histograms are then used by a2CaLib to determine a new set of calibration parameters. For some calibrations, parameters are determined from the analysis of many detector elements at once. Because of this, the calibration process is sometimes iterative.

5.2.2 ADC pedestals and TDC offsets

For each ADC and TDC, a pedestal and offset channel must be calibrated. These calibrations are done by fitting the raw ADC and TDC distributions. Shown in Figure 5.3 are example ADC and TDC distributions for a single BaF₂ crystal. The

distributions shown correspond to the ADC and TDC discussed in Table 5.1. The ADC pedestal channel appears as a sharp peak below the main signal and the TDC offset channel is fitted such that the timing peak would be centered on zero. For the example channel shown below, the ADC pedestal channel and TDC offset channel were determined to be 102.15 and 2957.27 respectively.

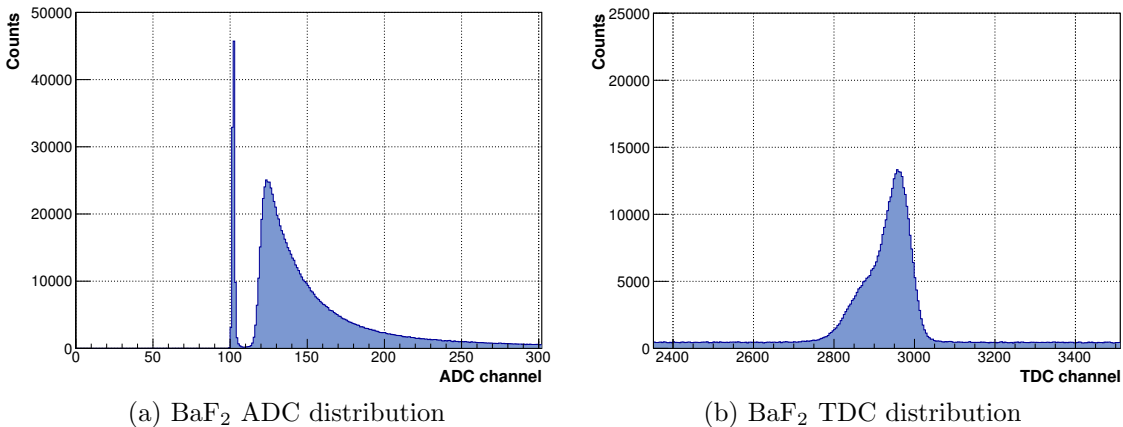


Figure 5.3: Example set of ADC and TDC distributions for a single BaF₂ crystal in the TAPS detector. An ADC pedestal channel and TDC offset channel were determined to be 102.15 and 2957.27 respectively. The example BaF₂ crystal shown here corresponds to the same example crystal used in Table 5.1.

Fitting of the ADC pedestals and TDC offsets must be done for each BaF₂ crystal, Veto element, and PID scintillator. However, for NaI crystals in the Crystal Ball, ADC pedestals are not calibrated. Instead, sampling ADCs are used in the place of conventional ADCs. Along with providing a digital measurement of the signal region, sampling ADCs provide a measurement of the pedestal region simultaneously. Using this approach, the pedestals are actively measured and need not be calibrated. As the pedestal has already been subtracted, the pedestal channel, P , of each NaI crystal is assumed to be zero in equation 5.1.

5.2.3 Time calibrations

Time calibrations were performed to align the time signatures of each detector element of the NaI, PID, BaF₂, and Veto wall. For the PID and Veto wall, the time of each hit was plotted for each detector element. For the NaI and BaF₂, the times for

each detector were extracted from all reconstructed clusters. As discussed in Section 5.1.1.3, the cluster time is equal to the central crystal of a cluster. Thus, for the NaI and BaF₂, the cluster time was plotted as a function of the central crystal.

Figure 5.4 shows example time distributions for a single detector element in the NaI, PID, BaF₂, and Veto wall. Two-dimensional histograms, shown in Fig. 5.5, show the distribution for all detector elements. In all cases, the gain factors and TDC offsets were calibrated such that the peak of the time distribution is centered upon zero.

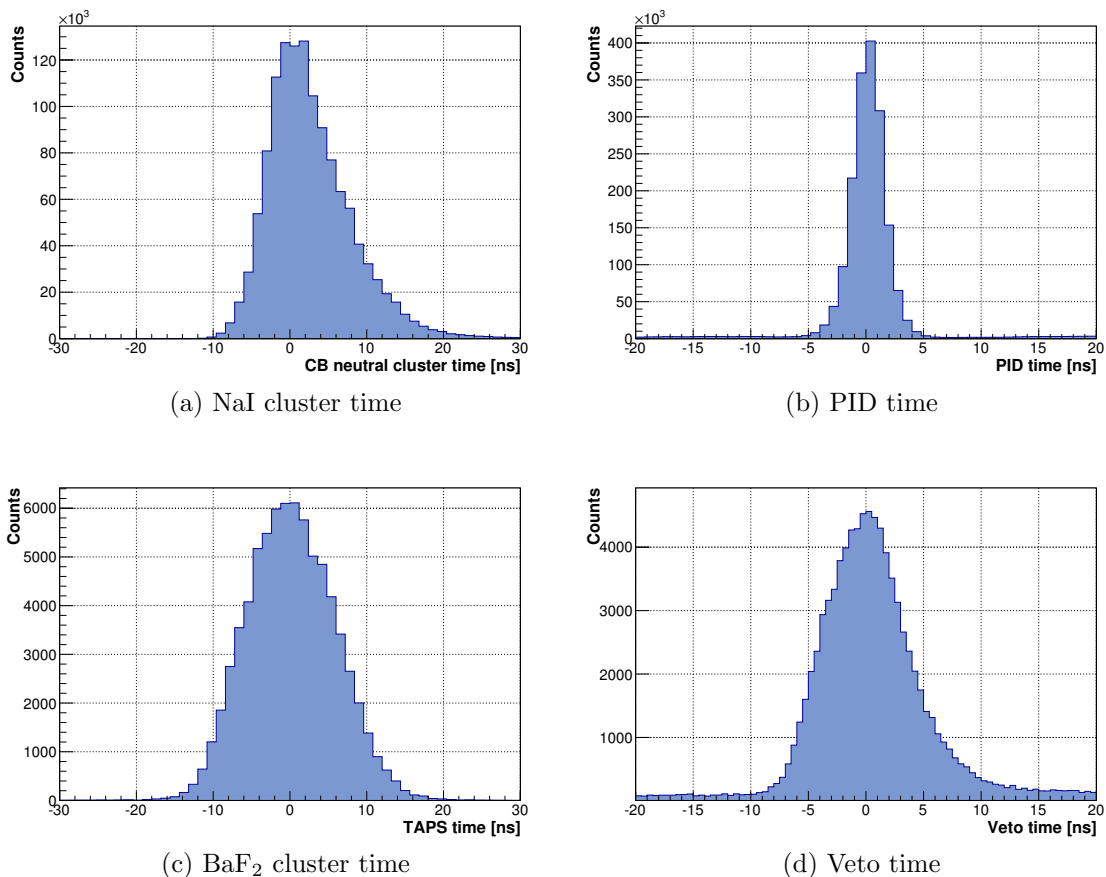


Figure 5.4: The timing distributions of NaI clusters, PID hits, BaF₂ clusters, and Veto hits are each shown for an example detector element. Each distribution is calibrated such that the peak is aligned to zero.

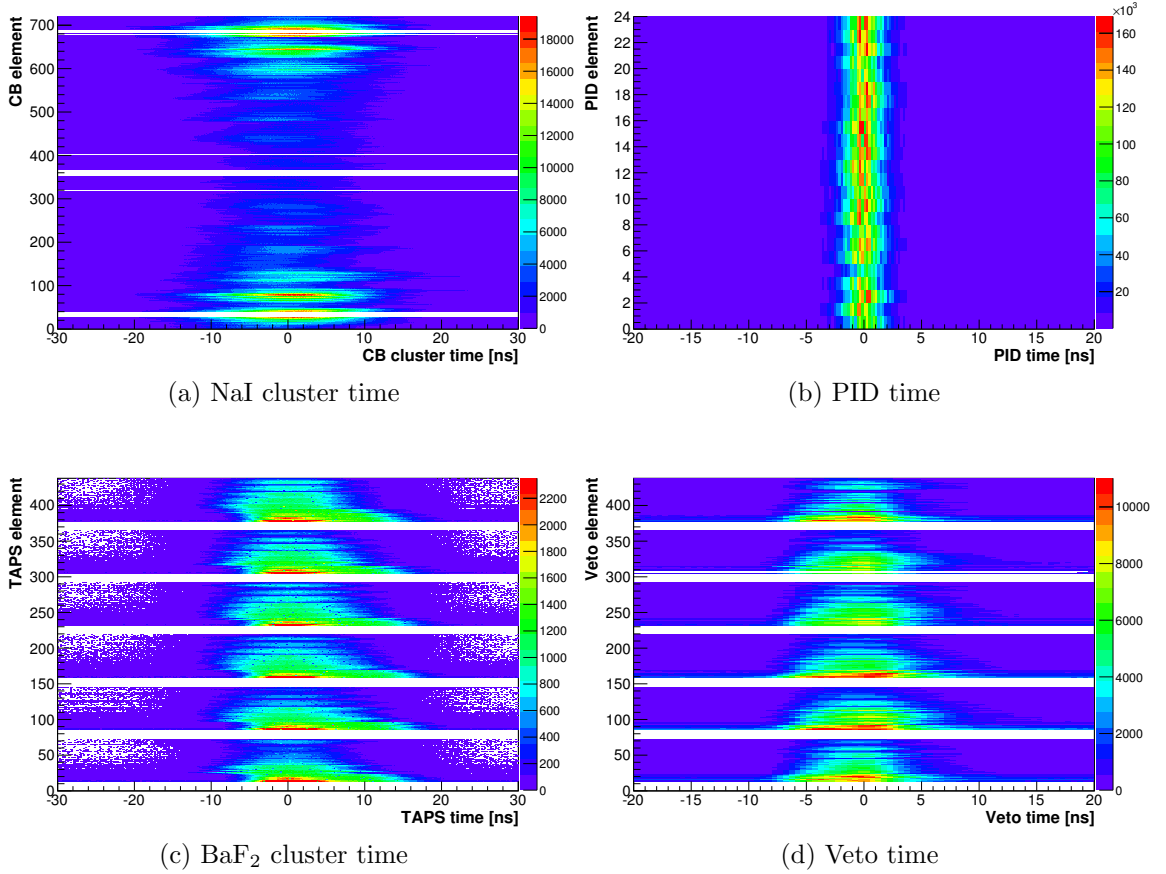


Figure 5.5: The timing distributions of NaI clusters, PID hits, BaF₂ clusters, and Veto hits are each shown as a function of detector element. After calibration, all timing distributions are aligned to zero.

5.2.4 Energy calibrations

Energy calibrations were performed to ensure that the energy response of all crystals in the Crystal Ball and TAPS was uniform. A two particle invariant mass, m_{ij} , is calculated from all particle track pairs, given by,

$$m_{ij} = \sqrt{(E_i + E_j)^2 - (\vec{p}_i + \vec{p}_j)^2}, \quad (i \neq j). \quad (5.12)$$

Due to the dominance of single π^0 photoproduction, the two-particle invariant mass will show a distinctive peak near the π^0 rest mass, at roughly 135 MeV. Calibration of the NaI energies was done using particle pairs where both particle tracks were detected in the Crystal Ball. The energy gain of both central crystals was calibrated such that the peak of the invariant mass distribution would be 135 MeV, or m_{π^0} . As the invariant mass involves two particle tracks, each of which involves NaI crystals

beyond the central crystal, this approach requires many iterations to calibrate the energy. After each successive calibration, the peak position of the invariant mass converges closer to the expected π^0 mass. In total, 20 iterations of the CB energy calibration were completed. Figure 5.6a shows an example invariant mass distribution for a single detector element in the NaI. A two-dimensional histogram, shown in 5.6b, shows the distribution for all NaI crystals. For all crystals, the gain factors were calibrated such that the peak of the invariant mass distribution is centered upon the pion mass, m_{π^0} . After the calibration of all NaI crystals, the energy of BaF₂ crystals was calibrated using the same method. For BaF₂ crystals, calibration was done using particle pairs where one particle track was detected in the Crystal Ball and the other was detected in TAPS. Invariant mass distributions for a single BaF₂ crystal, and all BaF₂ crystals, are shown in Figures 5.6c and 5.6d respectively.

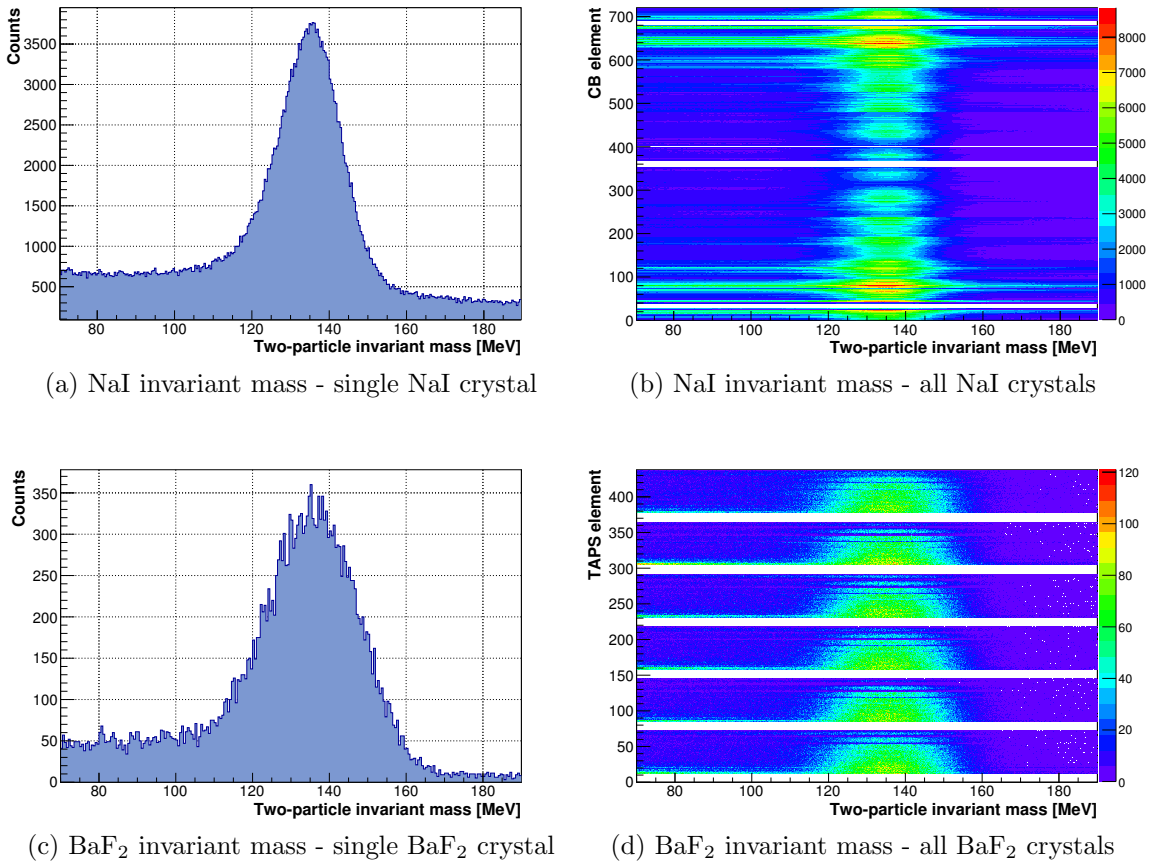


Figure 5.6: The invariant mass distribution of NaI and BaF₂ clusters is shown. A two particle invariant mass is used to calibrated the energy crystals. Each crystal is calibrated such that the invariant mass peak is aligned to the pion mass, m_{π^0} .

5.3 Determination of photon polarisation

A polarised photon beam was produced via coherent bremsstrahlung production on a diamond radiator. This linearly polarised photon beam was polarised in two polarisation settings, referred to as “para” or “perp”, with polarisation planes separated by 90° . This process was described in detail in Section 4.1.2.2. For photons produced through coherent Bremsstrahlung production, the degree of polarisation is a relatively complex function of the diamond’s lattice structure and the bremsstrahlung photon’s energy. A fitting routine, designed by Ken Livingston (MAMI A2 collaborator, from University of Glasgow), was used to determine the degree of photon polarisation.

The degree of photon polarisation was determined from daily tagging efficiency measurements. During these measurements, the current of the incident electron beam was reduced such that the rate of photons on the Pb-glass detector was 10^5 photons per second. For each tagging efficiency, a background measurement was made at the beginning and end of the tagging efficiency set. During these background measurements, no electron beam was incident upon the radiators. While this contribution was small, the background measurements are still subtracted from the tagging efficiency runs. A 30 minute tagging efficiency run was performed for each polarisation orientation using the $30\ \mu\text{m}$ diamond radiator and an amorphous run was performed using the $10\ \mu\text{m}$ Copper radiator. A tagging efficiency, previously given in equation 4.19, can be calculated for each Tagger channel by,

$$\epsilon_{\text{Tagg}}(i) = \frac{N_{\text{Tagg}}(i)}{N_{e^-}(i)},$$

where, N_{e^-} is measured from free running scalers attached to each tagger channel, and N_{Tagg} is the number of electrons measured from each tagger channel triggered by the lead glass detector. In total ten tagging efficiency measurements were taken. The unpolarised tagging efficiency, measured using the Copper radiator, is shown in Figure 5.7a. A roughly uniform tagging efficiency of 30% was measured for all tagging efficiency channels, and all tagging efficiency sets. The polarised tagging efficiencies, measured using the diamond radiator, are shown for each polarisation orientation in Figures 5.7b and 5.7c. A clear enhancement in the tagging efficiency, which is most predominant in the energy region between 200 MeV and 300 MeV, is expected. This occurs in regions of increased photon polarisation due to the characteristic angle of

the coherent bremsstrahlung distribution, which is more forward peaked for highly polarised photons.

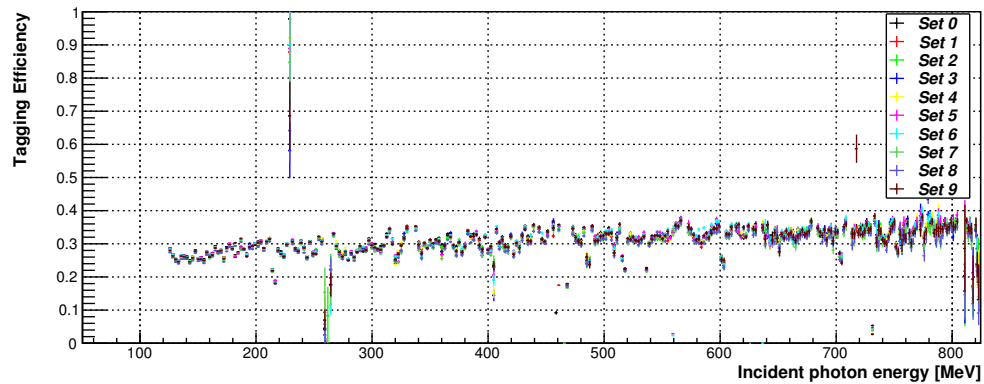
An enhancement, R , can be calculated for each Tagger channel by,

$$R(i) = \frac{N_{\text{Tagg}}(i)_{\text{coherent}}}{N_{\text{Tagg}}(i)_{\text{incoherent}}}, \quad (5.13)$$

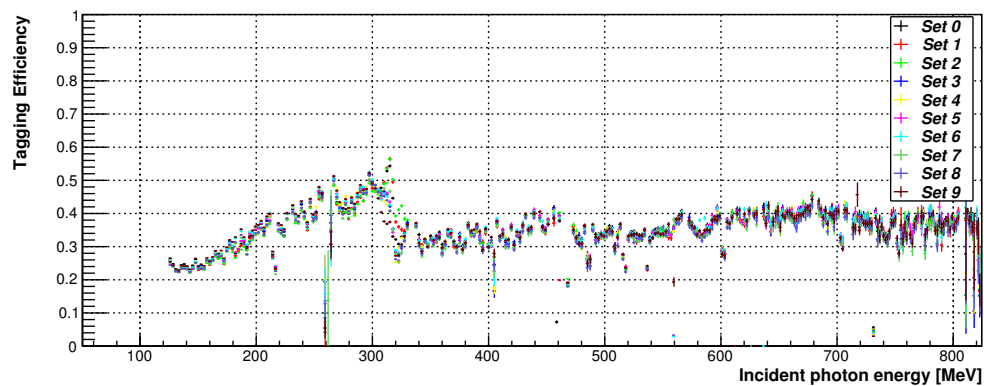
where $N_{\text{Tagg}}(i)_{\text{coherent}}$ and $N_{\text{Tagg}}(i)_{\text{incoherent}}$ are the number of electrons measured in a tagger channel using the diamond and copper radiator respectively. An enhancement was determined for each polarisation orientation, “para” and “perp”. The resulting enhancements are shown in Figure 5.8. All ten measurements are in general agreement with one another, however a close-up view of the energy range between 270 MeV and 350 MeV shows a significant spread in the reconstructed enhancements. This effect is directly related to the position of the coherent edge, which varies slightly for each tagging efficiency measurement. The coherent edge, given previously in equation 4.10, is highly sensitive to slight variations in the orientation of the diamond’s lattice structure within the electron beam.

A fitting routine, designed by Ken Livingston, has been developed to model the coherent bremsstrahlung distribution. A complete discussion of the fitting algorithm is presented in [56]. The fitting routine attempts to model the coherent contribution from the two primary reciprocal lattice vectors, [022] and [[044]]. Experimental parameters which can be fixed, such as the incident electron energy and collimator diameter, are fixed for the fitting routine. The enhancement distributions are first normalised to 1 at the lowest photon energy. After this, the fitting routine uses a MINUIT minimization function to fit the enhancement distribution. A gaussian smearing accounts for parameters which cannot be measured, including beam divergence and the effect of multiple scattering in the radiator. The parameters of the gaussian smear is determined by fitting to data.

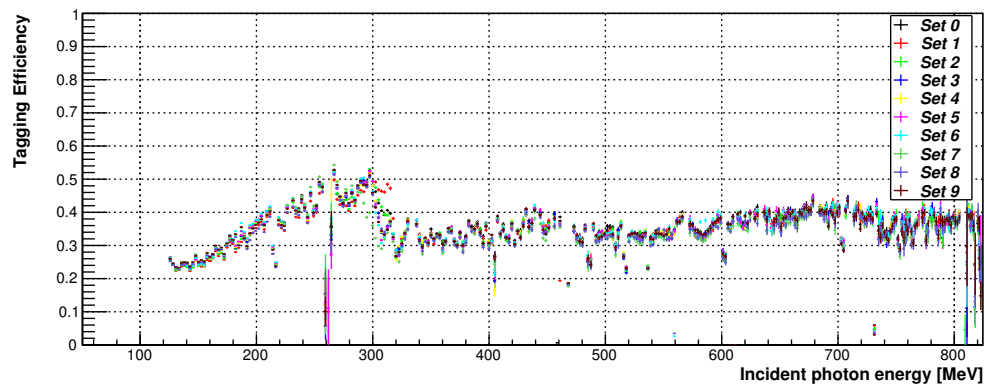
The enhancements and resulting fits, for a single tagging efficiency measurement, are shown in Figure 5.9. For both polarisation orientations, “para” and “perp”, the fitting routine provides good reconstruction of the enhancement distribution up to roughly 450 MeV. Beyond this energy, higher order reciprocal lattice vectors, [066] and higher, would need to be included in the MINUIT fit. However, the contribution of higher order lattice vectors to the primary polarisation peak is negligible and therefore they have not been included.



(a) Tagging efficiency - Unpolarised Copper radiator

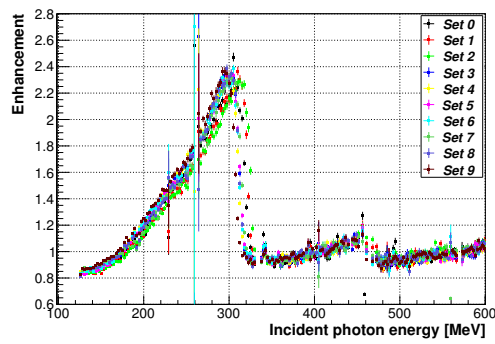


(b) Tagging efficiency - Polarised Diamond radiator (para)

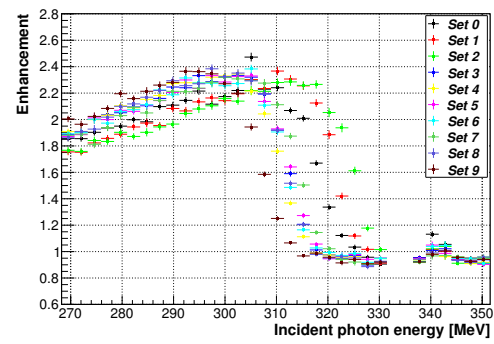


(c) Tagging efficiency - Polarised Diamond radiator (perp)

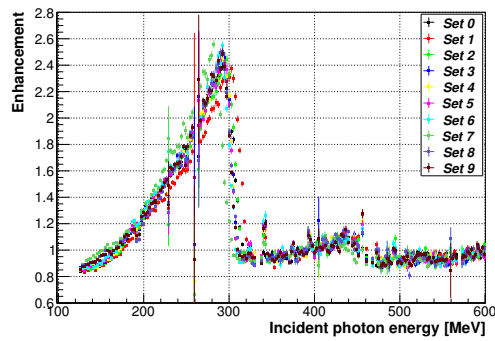
Figure 5.7: Unpolarised and polarised tagging efficiencies are shown for ten tagging efficiency measurements taken during the run period. For unpolarised photons, a tagging efficiency of roughly 30 % was measured. For polarised photons, an enhancement in the tagging efficiency is observed in regions of high photon polarisation. Low efficiency regions reflect the location of a few damaged PMTs of the Tagger.



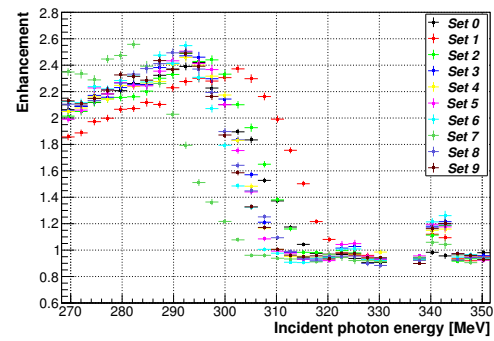
(a) Enhancement (para)



(b) Enhancement (para): (270-350) MeV

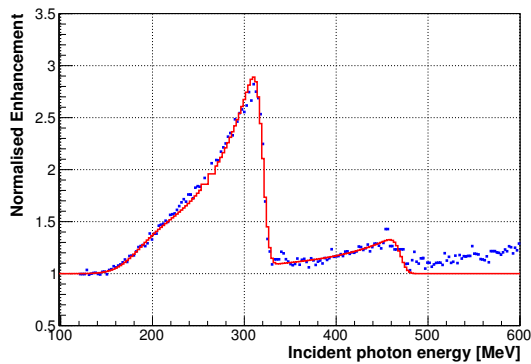


(c) Enhancement (perp)

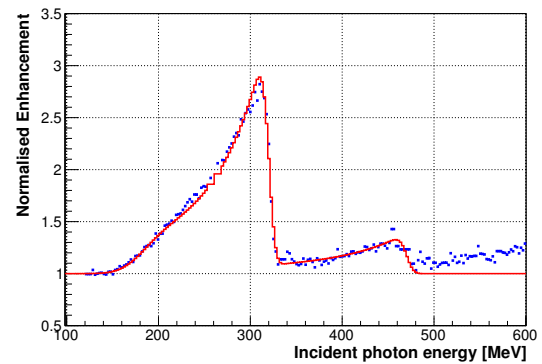


(d) Enhancement (perp): (270-350) MeV

Figure 5.8: Polarisation enhancements are shown for ten daily tagging efficiency measurements. An enhancement distribution, along with a close-up view of the energy range 270 MeV to 350 MeV, is shown for each polarisation orientation, para and perp.



(a) Enhancement and fit (para)



(b) Enhancement and fit (perp)

Figure 5.9: Polarisation enhancements and the resulting fits are shown for a single tagging efficiency measurement, set 0. The fit line, shown in red, shows good agreement with the enhancement distribution up to 450 MeV.

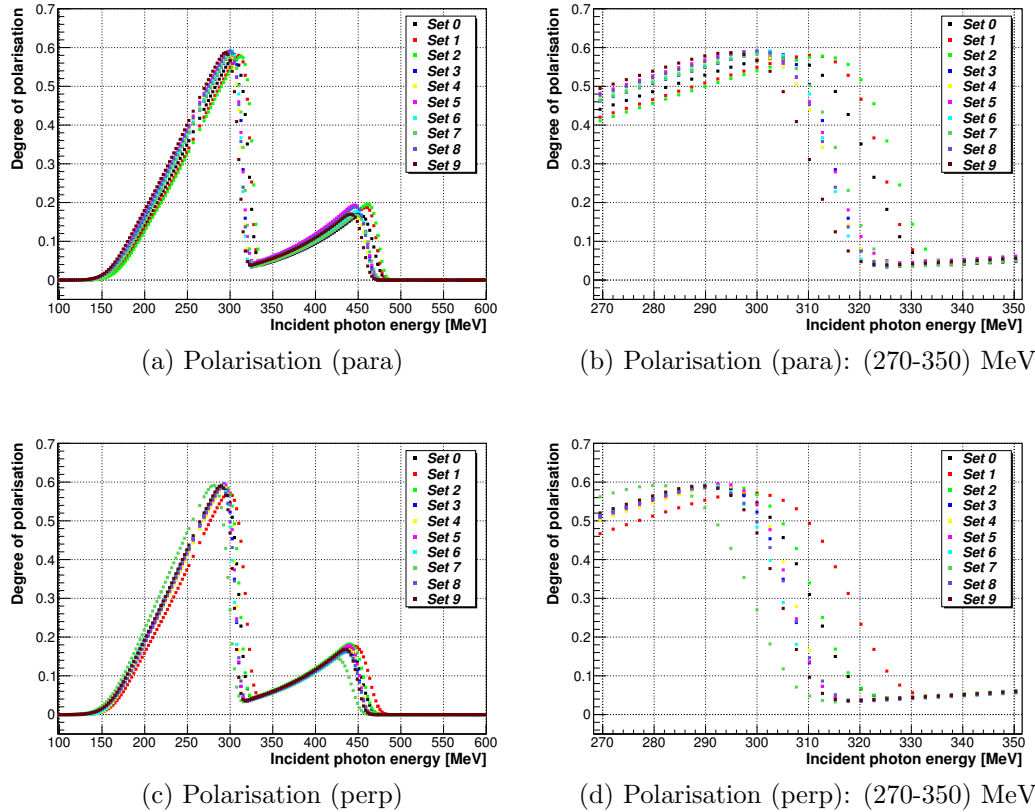


Figure 5.10: Polarisation distributions, determined from fitting the enhancement distributions, are shown for ten daily tagging efficiency measurements. A polarisation distribution, along with a close-up view of the energy range 270 MeV to 350 MeV, is shown for each polarisation orientation, para and perp.

Once an enhancement distribution has been fit, a model of the coherent bremsstrahlung distribution can be used to determine the degree of polarisation (see equation 4.15). The fitting routine is repeated for each tagging efficiency set and the resulting degree of polarisation for each set is shown in Figure 5.10.

Similar to the enhancement distributions, the polarisations derived from the fitting algorithm for each tagging efficiency measurement are in general agreement with one another. However a close-up view of the energy range between 270 MeV and 350 MeV shows a significant spread in the reconstructed polarisations. Again, this effect is directly related to the position of the coherent edge, which varies slightly for each tagging efficiency measurement. For energies below roughly 300 MeV, the spread in the polarisations from each tagging efficiency set is approximately 10%. However, as the polarisation drops off rapidly at the coherent edge position, the

polarisation predicted by each tagging efficiency set differs by up to 60% in the region near 310 MeV.

In Figure 5.10, the polarisation distributions show a significant spread related to the position of the coherent edge during each tagging efficiency measurement. Once an enhancement distribution has been fit, however, it is possible to produce a polarisation distribution for any coherent edge position. Figure 5.11 shows the resulting polarisation distributions generated for two edge positions, 300 MeV and 320 MeV. For a specific coherent edge, the spread in the polarisations from each tagging efficiency set is less than 1% within the primary polarisation peak. Thus, a polarisation distribution — produced for a known coherent edge position — is relatively independent of the tagging efficiency set used. The spread in polarisation values is still significant in the secondary polarisation peak. Modelling the contribution of the [066] and [088] reciprocal lattice vectors would improve the reconstructed polarisation for this higher energy region.

During the run period, a nominal coherent edge position of 310 MeV was set. However, the edge position is highly sensitive to small changes in the orientation of the crystal lattice. These changes can occur if the diamond radiator shifts, and can also occur due to normal drifting of the electron beam. It is, therefore, normal for the coherent edge position to drift with time. To determine the degree of polarisation with a high degree of accuracy, an active determination of the edge position is necessary. Every 1000 events, an enhancement distribution is calculated and the position of the coherent edge is determined. The enhancement, given previously in equation 5.13, requires the incoherent contribution to be known. During the run period, 60 minutes of unpolarised data were taken daily with the 10 μm Copper radiator and used to model this incoherent contribution. Figures 5.12a and 5.12c show an example of the edge position for 2 million events, which corresponds to roughly 30 minutes, for each polarisation orientation. Figures 5.12b and 5.12d show the reconstructed edge position for all data taken during the run period.

Without such an active edge determination, the uncertainty in the degree of polarisation would be at least 10%, as demonstrated in Figure 5.10. However, for active edge fitting, estimating the true uncertainty in the polarisation is relatively difficult.

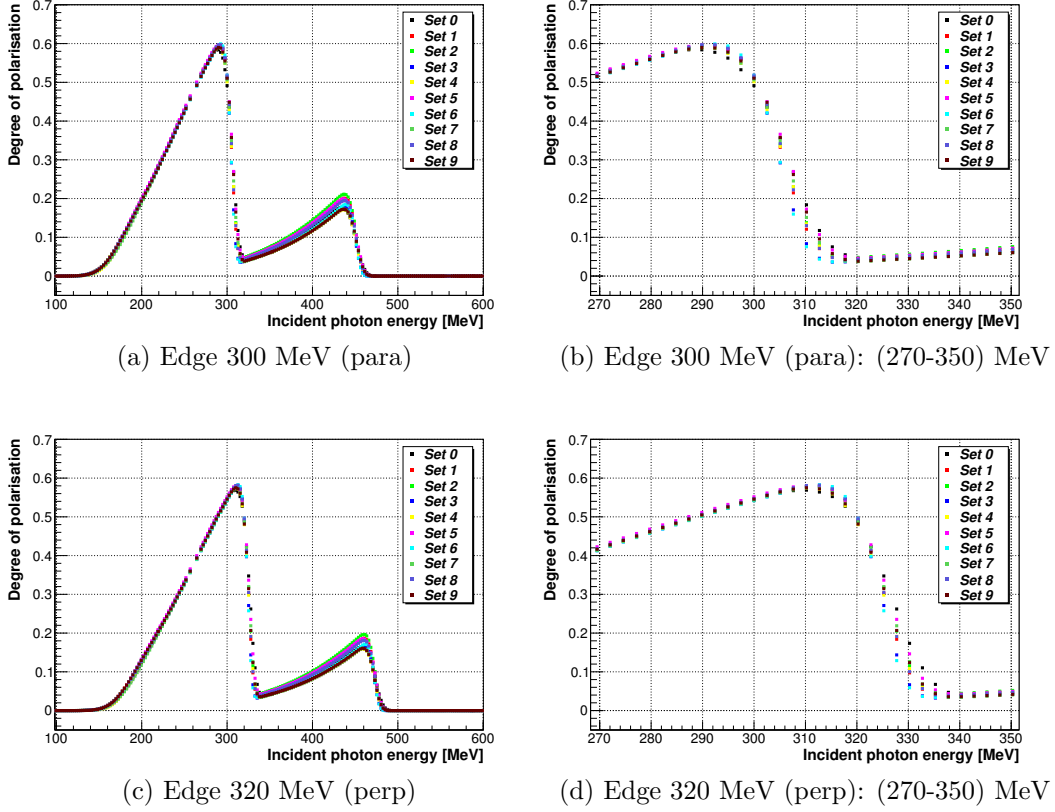


Figure 5.11: Polarisation distributions, determined from fitting the enhancement distributions, are shown for two coherent edge positions, 300 MeV and 320 MeV. A polarisation distribution, along with a close-up view of the energy range 270 MeV to 350 MeV, is shown for each coherent edge position.

For active edge fitting, there are three main sources of error: (1) errors in the enhancement fitting routine, (2) errors resulting from the choice of the tagging efficiency set used to model the coherent bremsstrahlung distribution, and (3) the error in the coherent edge position. First, an error in the enhancement fitting routine will propagate through to become an error in the final degree of polarisation. In Figure 5.9, it was shown that the fitting algorithm produces a very good representation of the enhancement data. In general, errors in the enhancement are roughly 1%. The relationship between an error in the enhancement, ε , and an error in the polarisation, P , is given by [56],

$$\frac{\Delta P}{P} = \frac{1}{(\varepsilon - 1)} \times \frac{\Delta \varepsilon}{\varepsilon} \quad (5.14)$$

According to equation 5.14, a 1% error in an enhancement, with an enhancement value of 2.5, results in an error below 1%. Second, a single tagging efficiency measurement

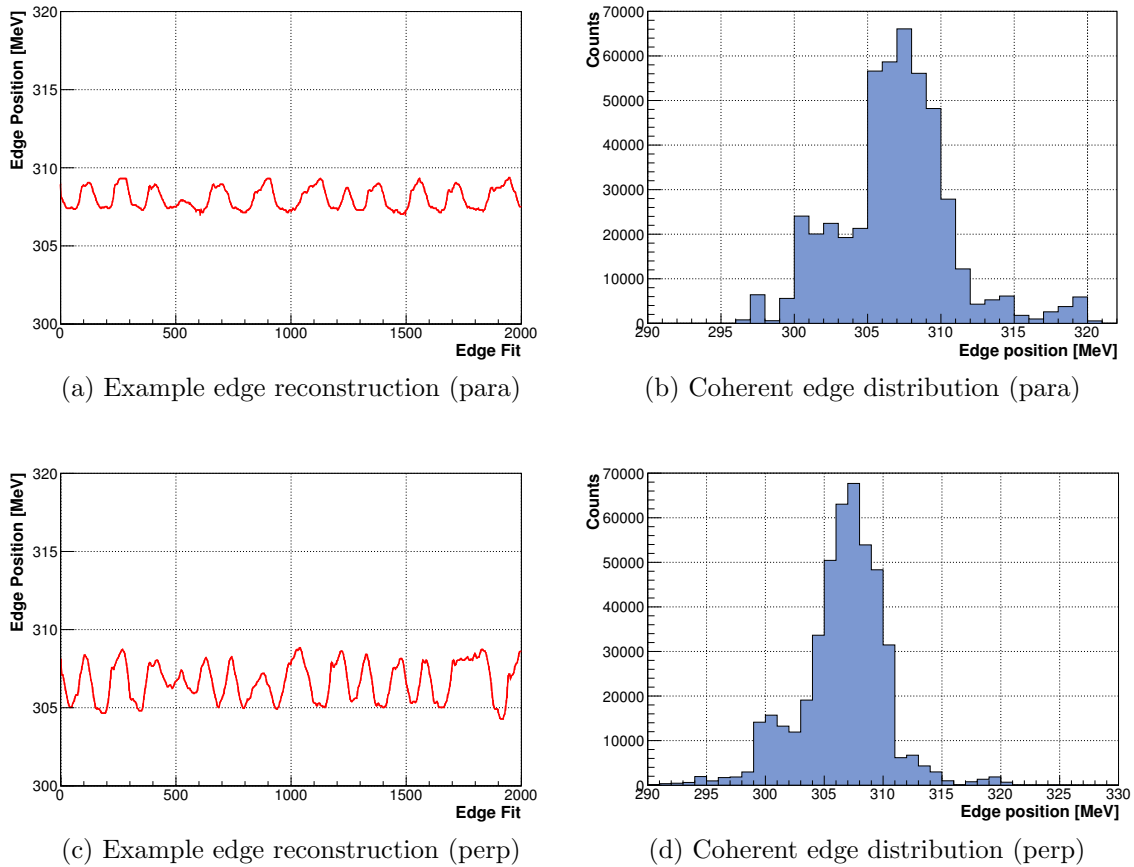


Figure 5.12: The distribution of coherent edge positions from active fitting is shown. The edge position for 2 million events, along with the reconstructed edge position for all data taken during the run period, is shown for both polarisation settings.

is used to model the coherent bremsstrahlung distribution. An error can be defined which estimates the dependence of the final polarisation on the tagging efficiency measurement. However, in Figure 5.11, it was shown that the polarisation is relatively independent of the tagging efficiency set used, resulting in an error less than 1% within the primary polarisation peak. Finally, the third source of error in the polarisation is the fitting of the coherent edge position. Unfortunately, it is relatively difficult to assign an uncertainty to the position of the coherent edge. In Figures 5.12a and 5.12c, two examples of the edge reconstruction were shown. If the edge position fitting was not very accurate, one would expect the edge position to experience artificial jumps and edges. However, in both cases, a gradual oscillation of the edge position was observed. Specifically, small changes in the edge position, changes of much less than

1 MeV, are reconstructed smoothly. Figure 5.13 shows the polarisation distributions for a nominal setting of 310 MeV with perturbations of either 1 MeV, 2 MeV or 3 MeV. Assuming the coherent edge could be fit with an uncertainty of 1 MeV, an error in the polarisation of 1% would be expected. This is derived from the spread in the polarisation values. Similarly, an uncertainty in the edge position of 2 MeV or 3 MeV would propagate to give an error in the polarisation of 2% and 3% respectively. Due to the smooth edge reconstruction, which shows oscillations with structure below 1 MeV, an uncertainty in the edge position between 1 MeV and 2 MeV is expected. A maximum uncertainty in the polarisation ($\Delta P/P$), from all three sources of error, can be estimated to be 2-3%.

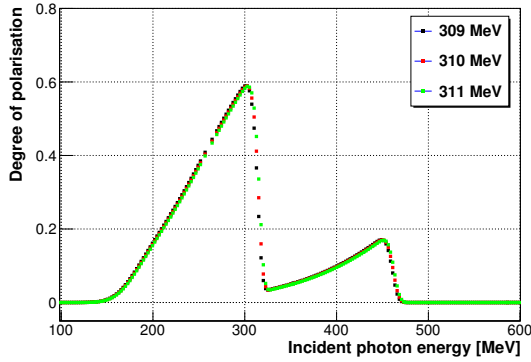
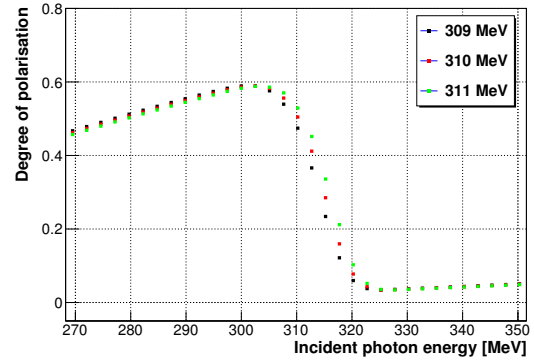
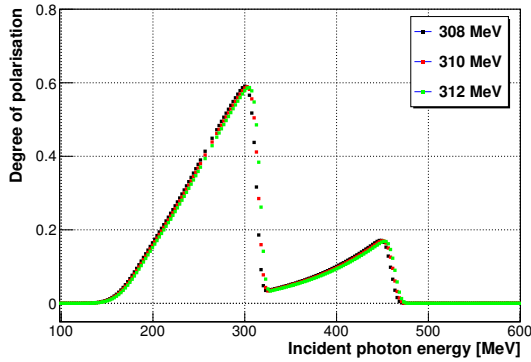
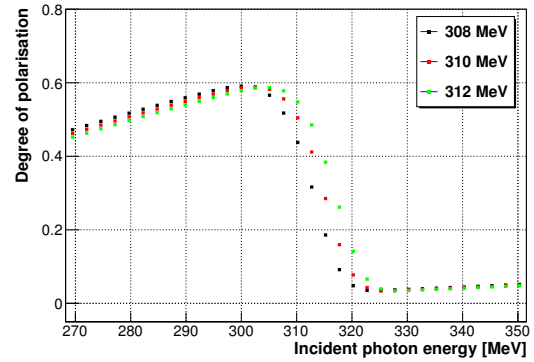
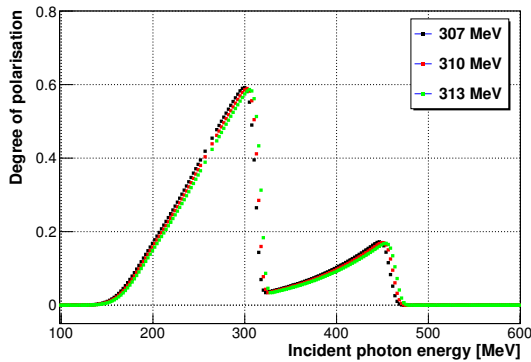
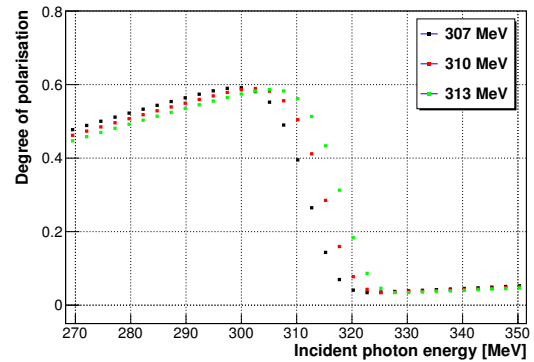
(a) Coherent edge ± 1 MeV(b) Coherent edge ± 1 MeV: (270-350) MeV(c) Coherent edge ± 2 MeV(d) Coherent edge ± 2 MeV: (270-350) MeV(e) Coherent edge ± 3 MeV(f) Coherent edge ± 3 MeV: (270-350) MeV

Figure 5.13: Polarisation distributions are shown at a nominal setting of 310 MeV with perturbations of 1 MeV, 2 MeV or 3 MeV. A close-up view of the energy range 270 MeV to 350 MeV shows a polarisation shift of 1%, 2%, and 3% respectively.

Chapter 6

Analysis

6.1 Overview

In chapter 4, experimental conditions for a December 2012 run period at the MAMI tagged photon facility were presented. This run period will be used to study the beam asymmetry, Σ_3 , for Compton scattering and π^0 photoproduction. The Σ_3 asymmetry is a single polarisation observable which connects the polarised and unpolarised cross sections for linearly polarised photons incident upon unpolarised protons,

$$\frac{d\sigma}{d\Omega}(\theta, \phi, E) = \frac{d\sigma}{d\Omega}(\theta, E)[1 + p_\gamma \Sigma_3 \cos(2\phi + \phi_o)]. \quad (6.1)$$

In the equation above, p_γ is the degree of linear polarisation, and ϕ_o is a polarisation offset related to the orientation of the polarisation plane. If the unpolarised cross section is well known, the beam asymmetry can be determined by fitting a $\cos(2\phi)$ distribution to the polarised cross section. It is possible, however, to determine the beam asymmetry without knowledge of the unpolarised cross section by measuring polarised Compton scattering, or π^0 photoproduction, with two polarisation settings (“para” and “perp”), which have polarisation planes separated by 90° . During the run period, this is accomplished by shifting the orientation of the diamond radiator. Using this approach, the beam asymmetry can be defined by the relation,

$$\Sigma_3(\theta, \phi, E) \cos(2\phi + \phi_o) = \frac{\sigma_\perp(\theta, \phi, E) - \sigma_\parallel(\theta, \phi, E)}{p_{\gamma\perp}\sigma_\perp(\theta, \phi, E) + p_{\gamma\parallel}\sigma_\parallel(\theta, \phi, E)}. \quad (6.2)$$

A fit of the form $A * \cos(2\phi + \phi_o)$ to the asymmetry distribution is used to extract $\Sigma_3(\theta, E)$, where the amplitude of the fit (A) corresponds to $\Sigma_3(\theta, E)$. Using yields, as opposed to complete cross sections, is possible if the incident photon flux is properly accounted for. In general, the photon flux can be given by,

$$F_\gamma = N_{e^-} \times \epsilon_{\text{DAQ}} \times \epsilon_{\text{Tagg}}, \quad (6.3)$$

where N_{e^-} is the incident electron flux, ϵ_{DAQ} is the livetime of the data acquisition system, and ϵ_{Tagg} is the tagging efficiency. In this case, the detection efficiency terms cancel and the beam asymmetry can be defined,

$$\Sigma_3(\theta, \phi, E) \cos(2\phi + \phi_o) = \frac{N_{\perp}(\theta, \phi, E) - F \times N_{\parallel}(\theta, \phi, E)}{p_{\gamma\perp} N_{\perp}(\theta, \phi, E) + F \times p_{\gamma\parallel} N_{\parallel}(\theta, \phi, E)}, \quad (6.4)$$

where F is the ratio of the photon fluxes, ($F_{\gamma\perp}/F_{\gamma\parallel}$). Although the incident electron flux and livetime of the data acquisition system can be accounted for, the tagging efficiency is relatively difficult to incorporate. In Figures 5.7b and 5.7c, the results of ten daily tagging efficiency measurements were shown for each polarisation orientation. Small variations in the tagging efficiency, related to the position of the coherent edge, are seen in the polarised tagging efficiency measurements. Similar to the degree of photon polarisation, drifting of the coherent edge results in a tagging efficiency which is non-constant. The Σ_3 asymmetry, integrated over all ϕ , equals zero. It is therefore possible to determine the correction factor, F , by requiring that the integral of the asymmetry defined in equation 6.4 is equal to zero,

$$\int_{\phi} \Sigma_3(\theta, \phi, E) d\phi = 0 = \int_{\phi} \frac{N_{\perp}(\theta, \phi, E) - F \times N_{\parallel}(\theta, \phi, E)}{p_{\gamma\perp} N_{\perp}(\theta, \phi, E) + F \times p_{\gamma\parallel} N_{\parallel}(\theta, \phi, E)} d\phi, \quad (6.5)$$

In practice, the correction factor F can simply be iterated to find a value of F which produces an asymmetry with an integral of zero. Using this approach, it would not be necessary to have direct knowledge of the photon flux corrections. Rather, a correction factor would be calculated for each energy and theta bin. Assuming the flux of electrons and the position of the average coherent edge is relatively equal for each polarisation setting, the correction factor will be close to 1.

Although the focus of this dissertation is the study of Compton scattering within the $\Delta(1232)$ region, a detailed study of π^0 photoproduction will also be presented. Within the $\Delta(1232)$ energy range, π^0 photoproduction is the dominant source of background for Compton scattering. This large background introduces a significant challenge when studying Compton scattering. However, the relatively large cross section and background-free signal makes π^0 photoproduction a useful reaction for systematic tests of the experimental set-up and constraints upon the analysis. In Section 6.2, Σ_3 results for π^0 photoproduction are shown for an incident photon energy range of 210 MeV to 307 MeV. In Section 6.3, Σ_3 results for Compton scattering are shown for an incident photon energy range of 267 MeV to 307 MeV.

6.2 π^0 photoproduction

6.2.1 Event selection

Sections 5.1.2.1 and 5.1.2.2 outlined the particle and meson reconstruction applied for this analysis. From π^0 mesons identified through this reconstruction, only those produced from two photons are considered for this analysis. In addition to the π^0 , a single charged particle track is allowed but not required. In the context of π^0 photoproduction, this charged particle track would be assumed to be the recoil proton. However, due to energy losses of the proton in the target, it is difficult to detect the proton and therefore it is not required. In Figure 6.1, an example invariant mass distribution for reconstructed π^0 mesons from this run period is shown. The distribution shows a peak position at the mass of the π^0 . The sharp cut-off, seen at 115 MeV and 155 MeV, correspond to the invariant mass cut established by equation 5.7 and 5.8.

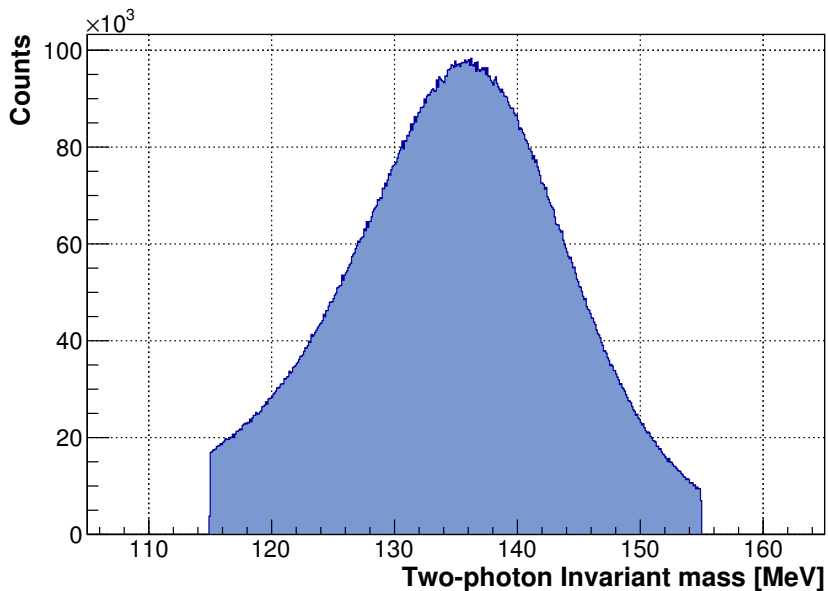


Figure 6.1: An example invariant mass distribution for reconstructed π^0 mesons.

Determination of the incident photon energy is accomplished through the process known as tagging. This process involves measuring the energy of the retarded electron in the Tagger, allowing the energy of the bremsstrahlung photon to be inferred. This process is complicated by the relatively high electron beam current used during the run period, which results in a large number of accidental/random hits in the Tagger.

When a π^0 meson is reconstructed, a time difference is calculated between the π^0 and each hit in the Tagger. An example time distribution, shown in Figure 6.2, shows a sharp time peak near zero along with a flat background distribution. The peak region, known as the prompt peak, is associated with electrons which are in timing coincidence with the reconstructed π^0 . The prompt peak sits on top of a flat background, associated with random electrons. The ratio of the prompt peak to the random background is roughly 6:1 for this run period. To determine the incident photon energy, a cut on the timing coincidence of -20 ns and 15 ns is used to identify prompt electrons. Two large windows, each 450 ns wide, are defined on either side of the prompt peak and can be used to model the accidental/random contribution within the prompt region. In Figure 6.2, the prompt and random time windows are shown in blue and red respectively. For this analysis, time differences which fall outside of the prompt and random windows are ignored.

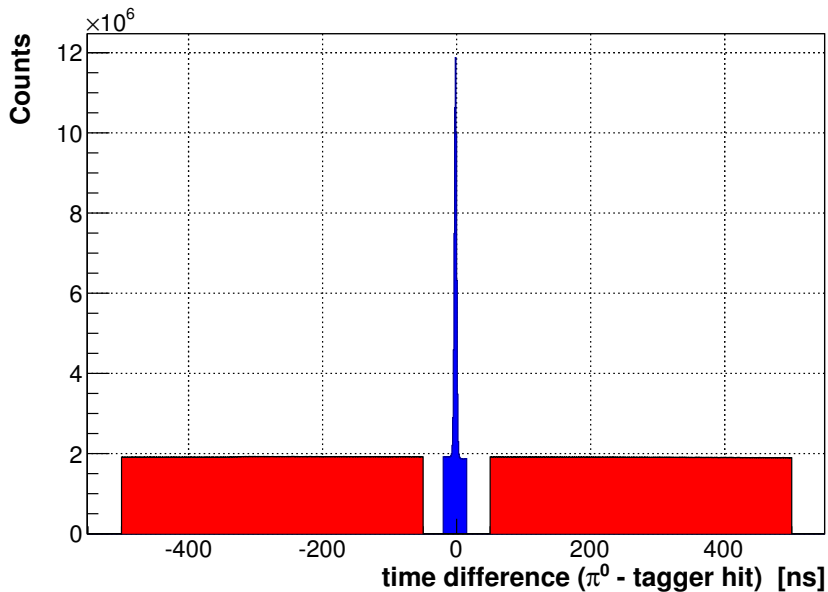


Figure 6.2: An example time distribution for reconstructed π^0 mesons. A time difference between the π^0 and each hit in the tagger is calculated. Cuts on the time difference are used to identify prompt and random electrons. The prompt and random windows are shown in blue and red respectively.

For any particle, a four momentum can be defined as,

$$\vec{P} = (E, p_x, p_y, p_z). \quad (6.6)$$

For π^0 photoproduction, the total energy and momentum of the initial system is

defined as the sum of the incident photon and target proton's four momenta. The total energy and momentum of the final system is defined as the sum of the π^0 and recoil proton's four momenta. Conservation of energy and momentum requires,

$$\vec{P}_{\gamma_{\text{in}}} + \vec{P}_{\text{target}} = \vec{P}_{\pi^0} + \vec{P}_{\text{recoil}} \quad (6.7)$$

By requiring a time coincidence between the π^0 and hit in the tagger, the energy of the incident photon can be determined. Due to the high electron flux, there will typically be many π^0 -tagger hit pairs which need to be considered. If the target proton is assumed to be at rest, the initial system is completely defined. The recoil proton suffers from significant energy loss, and often goes undetected. If the proton is ignored, or even undetected, a missing four momentum can be defined by re-arranging equation 6.7 to solve for the recoil proton,

$$\vec{P}_{\text{miss}} = \vec{P}_{\gamma_{\text{in}}} + \vec{P}_{\text{target}} - \vec{P}_{\pi^0}. \quad (6.8)$$

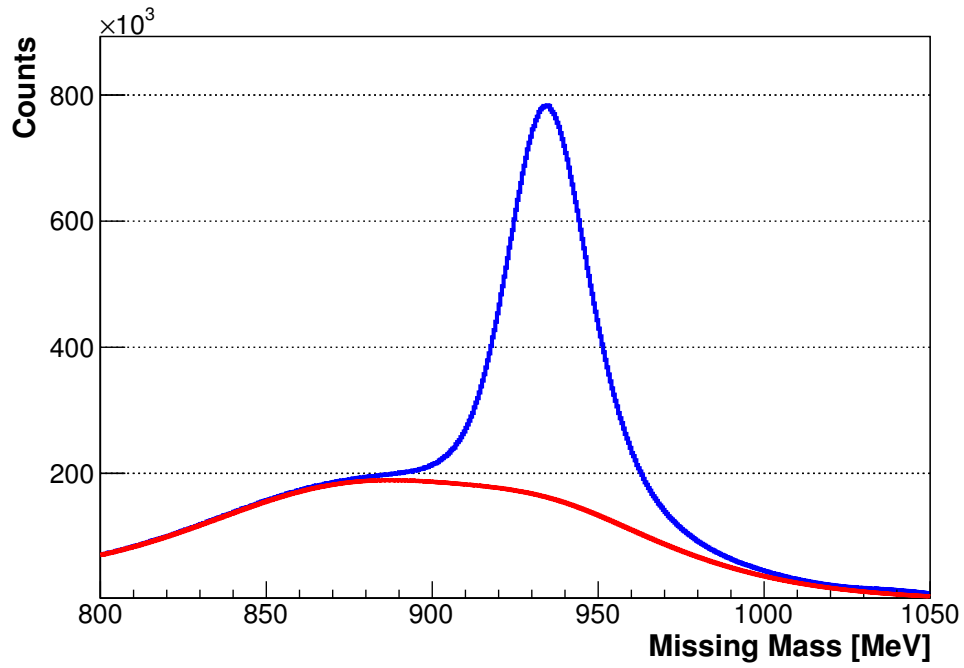
A missing mass can then be defined in terms of the energy and momentum of the missing four momentum by,

$$m_{\text{miss}} = \sqrt{E_{\text{miss}}^2 - \vec{p}_{\text{miss}}^2}. \quad (6.9)$$

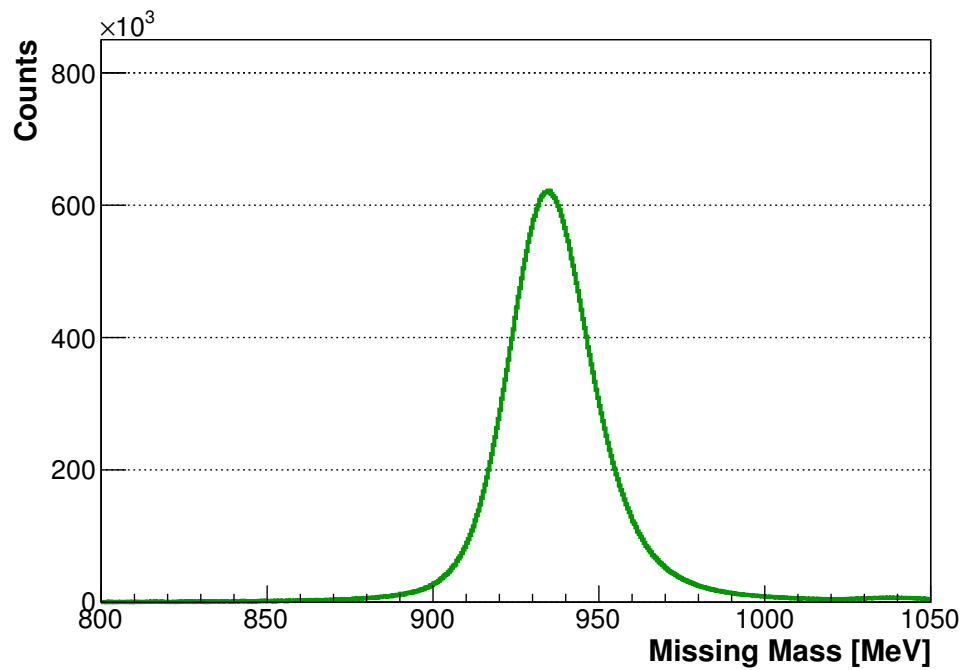
If the missing vector corresponds to the recoil proton, the missing mass should equal the mass of the proton. Due to detector resolution and energy losses, in experimental data, the missing mass will typically produce a gaussian distribution centered upon the proton mass. The missing mass is calculated separately for prompt and random tagger hits and the random contribution to the prompt missing mass can be subtracted by,

$$m_{\text{sub}} = m_{\text{prompt}} - R \times m_{\text{random}}, \quad (6.10)$$

where R is the ratio of the prompt to random window sizes. Figure 6.3a shows an example missing mass distribution for π^0 mesons. The random distribution is shown on top of the prompt distribution, scaled according to R . A subtracted missing mass is shown in 6.3b. After the random subtraction, the missing mass distribution is a roughly gaussian distribution centered upon the proton mass. A final cut is applied to the missing mass and only π^0 -tagger hit pairs with a missing mass between 900 MeV and 1000 MeV are considered.



(a) Missing mass: prompt (blue) and random (red)



(b) Missing mass: prompt-random subtracted

Figure 6.3: Example missing mass distribution of π^0 mesons. In figure (a), the prompt and random distributions are shown together. A prompt-random subtracted missing mass is shown in figure (b).

6.2.2 Empty target contribution

During the run period, photons were incident upon an unpolarised liquid Hydrogen, LH_2 , target. The liquid Hydrogen is contained within a cylindrical target cell, which is surrounded by layers of insulating material. The contribution from all target materials, other than the liquid Hydrogen, can be subtracted using data taken with an empty target cell. During the run period, a small amount of data were collected with an empty target cell. Figure 6.4 shows an example missing mass distribution, including an empty target subtraction. The empty target contribution has been scaled such that the incident electron flux is equal for full and empty target data. Although the empty target contribution is relatively small, the contribution within the region of interest — 900 MeV to 1000 MeV — is non-negligible. Equation 6.4 can be modified to reflect the empty target contribution. In this case, the beam asymmetry can be defined,

$$\Sigma_3(\theta, \phi, E) \cos(2\phi + \phi_o) = \frac{N_{\perp}^*(\theta, \phi, E) - F \times N_{\parallel}^*(\theta, \phi, E)}{p_{\gamma\perp} N_{\perp}^*(\theta, \phi, E) + F \times p_{\gamma\parallel} N_{\parallel}^*(\theta, \phi, E)}, \quad (6.11)$$

where,

$$N^*(\theta, \phi, E) = N(\theta, \phi, E)_{\text{Full target}} - N(\theta, \phi, E)_{\text{Empty target}} \quad (6.12)$$

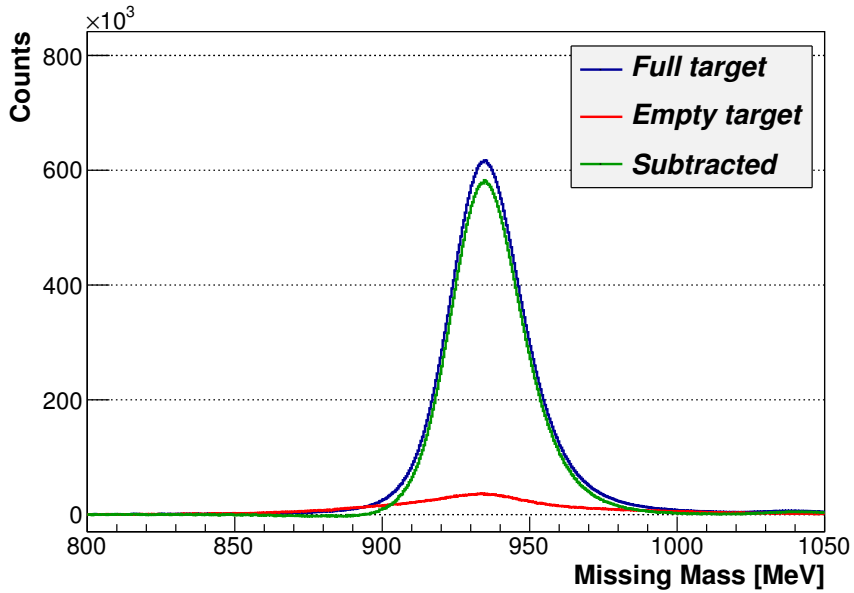


Figure 6.4: Example missing mass distribution of π^0 mesons is shown. The full and empty target missing mass distributions are showed in blue and red respectively, along with an empty target subtracted distribution shown in green.

6.2.3 Example calculation

For a given incident photon energy, E , and π^0 angle, θ , the Σ_3 asymmetry can be determined by fitting ϕ -distributions calculated using equation 6.11. A fit of the form $A * \cos(2\phi + B)$ is applied, where,

$$A = \Sigma_3 \quad B = \phi_o. \quad (6.13)$$

For a given θ and energy range, angular distributions over ϕ can be produced. For each π^0 -tagger hit pair which passes the event selection criteria, outlined in Section 6.2.1, a ϕ -distribution is filled separately for prompt and random electrons. As discussed in Section 6.2.1, a prompt-random subtraction is necessary to eliminate the contribution of accidental tagger hits. Beyond a prompt-random subtraction, it is also necessary to perform an empty target subtraction. Shown in Figure 6.5 is an example ϕ -distribution for each polarisation orientation. The ϕ -distributions shown correspond to a θ range of 90° to 95° , and an energy range of 246.93 MeV to 254.76 MeV. In both cases, a random subtracted ϕ -distribution is shown for full target and empty target data. Finally, the empty target contribution is subtracted from the full target. This ϕ -distribution, including both prompt-random subtraction and empty target subtraction, corresponds to $N^*(\theta, \phi, E)$ given in equation 6.12.

As discussed previously, a correction factor F must be determined to account for the incident photon flux (see equation 6.5). This correction factor forces the integral of the asymmetry, over all ϕ , to be zero. For the ϕ -distributions shown in Figure 6.5, an asymmetry is calculated for a wide range of correction factors. In each case, the integral over all ϕ is calculated. Figure 6.6 shows the integral of the asymmetry as a function of F . In the example shown, an integral of zero corresponds to a correction factor of 0.920. With a correction factor determined, an example asymmetry can be calculated according to equation 6.11. This is shown in Figure 6.7.

6.2.4 Determination of the polarisation offset, ϕ_o

An example calculation of an asymmetry was presented in Section 6.2.3. As mentioned there, an asymmetry distribution can be calculated using equation 6.11 for a given θ and energy range. A fit of the form $A * \cos(2\phi + B)$ can be applied to the asymmetry distribution, where the fit parameter A gives Σ_3 for that θ and energy range. The

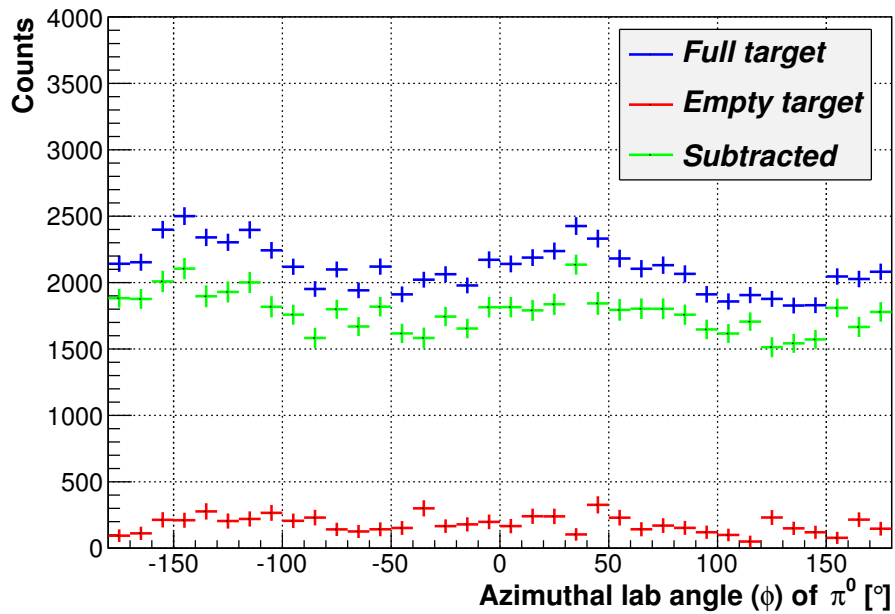
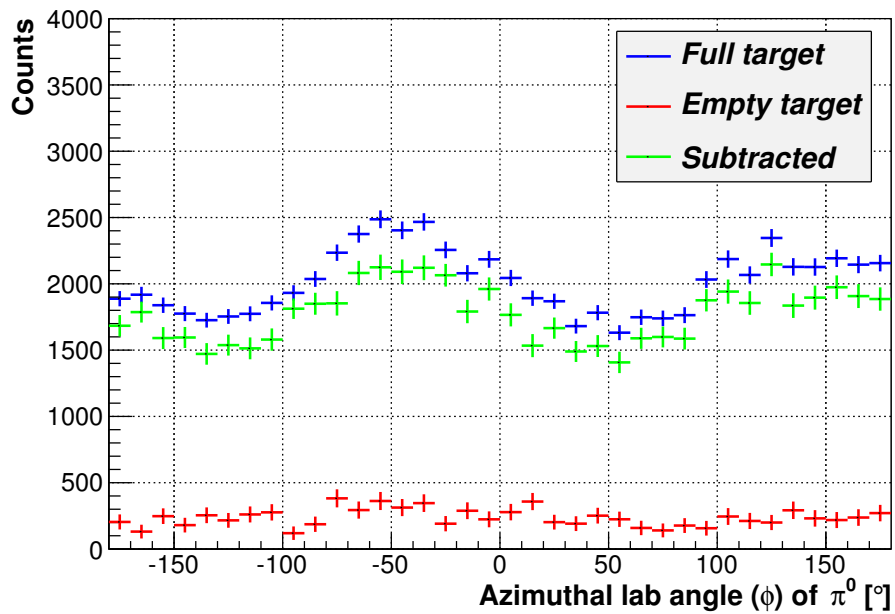
(a) ϕ -distribution: para(b) ϕ -distribution: perp

Figure 6.5: Example ϕ -distribution of π^0 mesons is shown for a θ range of 90° to 95° , and an energy range of 246.93 MeV to 254.76 MeV. A distribution is shown for each polarisation orientation, (a) para, and (b) perp. The full and empty target distributions are showed in blue and red respectively, along with an empty target subtracted distribution shown in green.

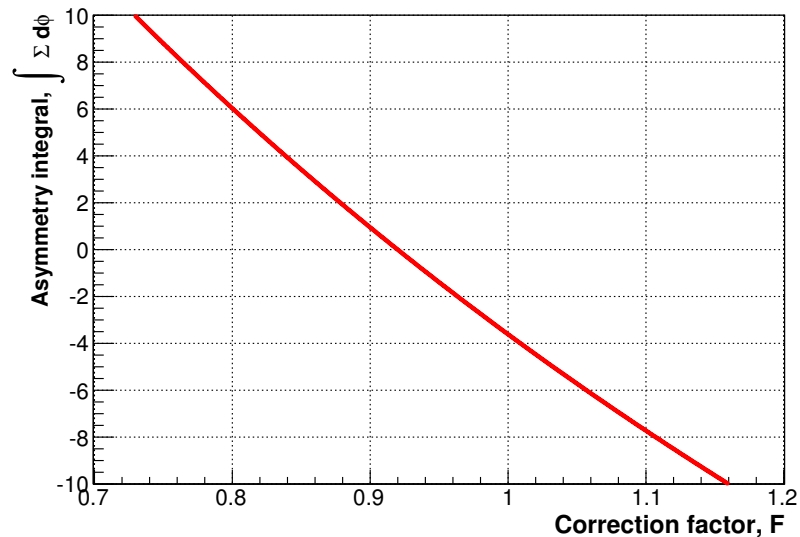


Figure 6.6: The integral of the asymmetry over all phi, $\int \Sigma_3 d\phi$, is shown as a function of the correction factor, F , for a θ range of 90° to 95° , and an energy of 246.93 MeV to 254.76 MeV. The correction factor for this angle and energy range is $F = 0.920$.

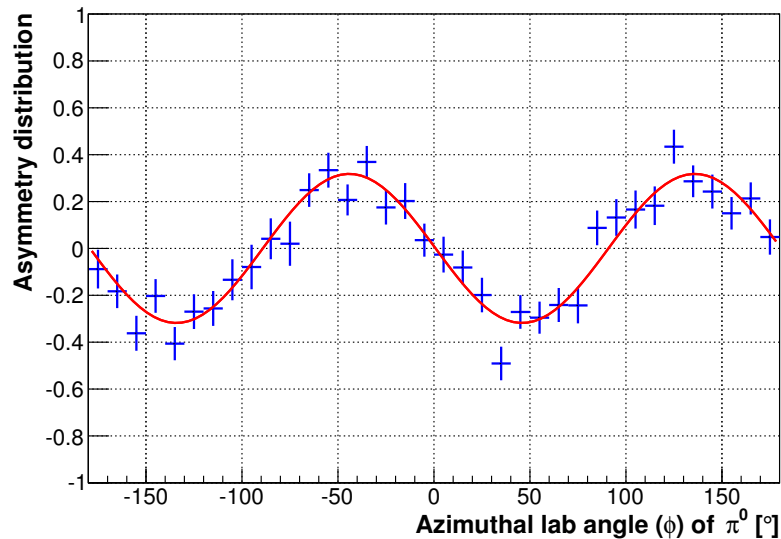


Figure 6.7: Example asymmetry distribution of π^0 mesons is shown for a θ range of 90° to 95° , and an energy of 246.93 MeV to 254.76 MeV. A fit of the form $A \cdot \cos(2\phi + B)$ is applied, shown in red. An extraction of the fit parameter A determines the asymmetry for this θ and energy range to be $\Sigma_3 = 0.318 \pm 0.017$.

fit parameter B , known as the polarisation offset, is related to the orientation of the polarisation planes and should be independent of the theta and energy bin of interest. For this reason, while the polarisation offset needs to be treated as a free parameter for a dataset, it should not be treated as a free parameter for all energy and theta

bins. Rather, a global offset parameter must be determined and then fixed for all asymmetry bins. This is especially important for regions with low statistics, as B can provide a false degree of freedom when not fixed.

Given the high cross section and relatively background-free signal, π^0 photoproduction is the ideal reaction to determine the polarisation offset for this run period. To fix the offset parameter, Σ_3 is calculated for tagger channels 247 to 285. This tagger channel range corresponds to the region of the primary polarisation peak and covers an incident photon energy range of 211.0 MeV to 305.8 MeV. For each tagger channel, an asymmetry distribution is calculated over all θ and fit with a fit of the form $A * \cos(2\phi + B)$, where B is kept as a free parameter. The polarisation offset, B , is then extracted and the resulting offset parameters are shown in Figure 6.8. Finally, a constant line is fit to the offset parameters and a global polarisation offset is determined to be,

$$\phi_o = (1.541 \pm 0.001) \text{ radians} = (88.293 \pm 0.057)^\circ \quad (6.14)$$

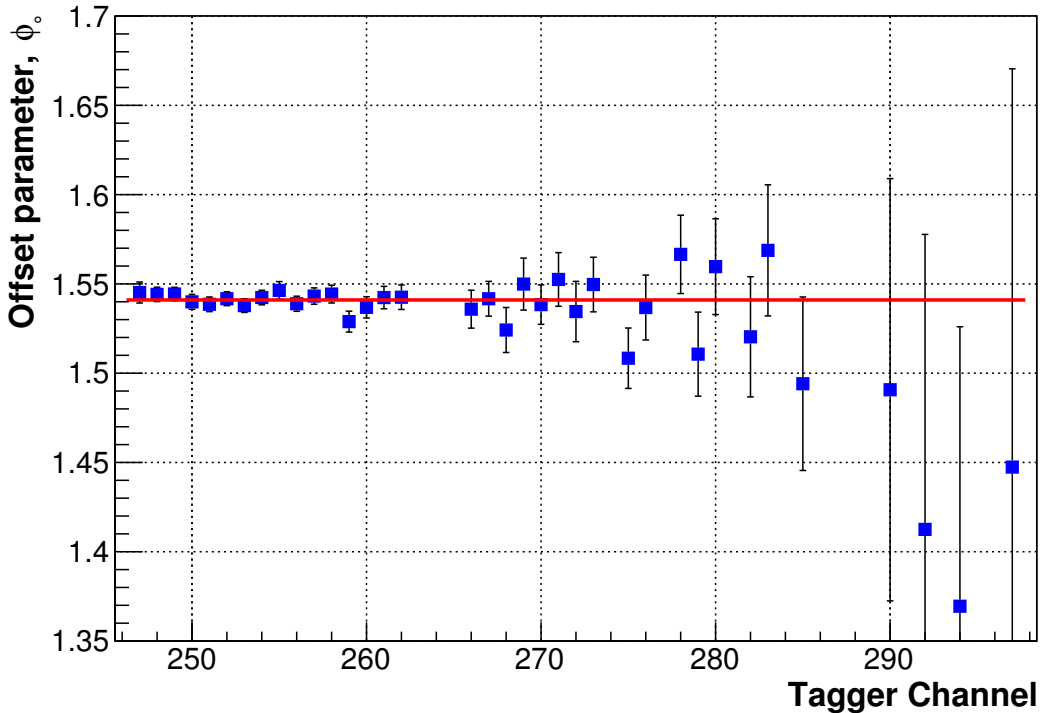


Figure 6.8: Polarisation offset parameters determined for π^0 photoproduction as a function of tagger channel. A constant line is fit to all points to extract a "global" polarisation offset. This fit produces a value of $\phi_o = 1.541$ radians = 88.293° .

6.2.5 Results

The following section outlines the complete analysis of the December 2012 run period to study the Σ_3 asymmetry for π^0 photoproduction within the $\Delta(1232)$ region. Figure 6.9 shows the available statistics in energy and θ . Each distribution, in energy and θ , has had a prompt-random subtraction applied. The incident (tagged) photon energy distribution shows a structure directly related to the polarisation distribution. As discussed previously, regions of high polarisation have a correspondingly high tagging efficiency. In Figure 6.9, the energy distribution appears as discrete bins of energy because only the central energy of each tagger channel is displayed. A gap in the energy distribution appears just above 260 MeV due to a set of broken tagger channels.

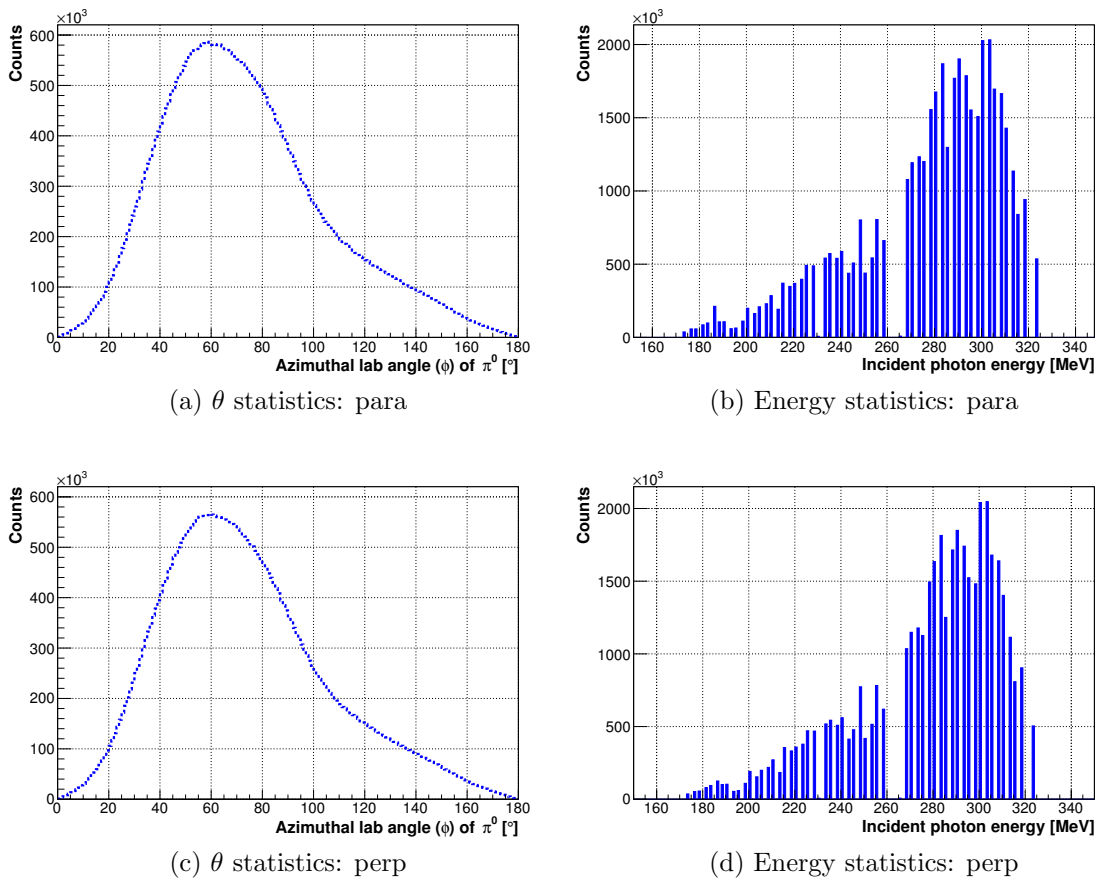


Figure 6.9: Available π^0 photoproduction statistics for the December 2012 run period.

Previous studies of the Σ_3 asymmetry for π^0 photoproduction have been performed - both experimental and theoretical studies. An earlier measurement by Leukel, completed at the MAMI tagged photon facility, studied the Σ_3 asymmetry over an incident photon energy range of 240 MeV to 440 MeV [57]. In addition to studying the Σ_3 for Compton scattering, the LEGS collaboration (discussed previously in chapter 3) measured the Σ_3 asymmetry for π^0 photoproduction over an incident photon energy range of 213 MeV to 333 MeV [4]. Three theoretical models will also be compared, (1) the Dubna-Mainz-Taipai (DMT) model [58], (2) MAID model [59][60], and (3) SAID model (CM12 solution) [26]. The treatment of background terms differs significantly between the models. The MAID model, for example, considers only Born and vector meson exchange terms, combined with nucleon and Delta resonances (no pion loop contribution is considered). By comparison, in the DMT model the pion loop contributions are explicitly calculated. A full discussion of each model is presented in the references cited and a comparison of DMT and MAID is presented in [61].

An example calculation of an asymmetry for a single θ and energy bin was presented in Section 6.2.3. This calculation involved producing an asymmetry distribution including a prompt-random subtraction, empty target subtraction, determination of a photon flux correction factor F , and finally fitting the asymmetry distribution to extract an asymmetry. In the example calculation, the ϕ_o offset was a free parameter, however ϕ_o is now fixed by the result indicated in equation 6.14. For a given θ range, an asymmetry can be extracted as a function of incident photon energy. Figures 6.10 through 6.13 show the resulting asymmetries for two sample theta ranges, (1) 60 to 65 degrees (lab angle), and (2) 90 to 95 degrees (lab angle). In both cases, a comparison to LEGS and Leukel data is shown, as well as to theoretical predictions. Figures 6.10 and 6.11 show the Σ_3 asymmetry as a function of incident photon energy, with a fixed θ range. It is also possible to examine the Σ_3 asymmetry as a function of π^0 scattering angle, for a fixed incident energy range. Figure 6.14 shows the resulting asymmetries for an example incident photon energy range of 297.0 ± 5.1 MeV. A comparison to LEGS and Leukel data is shown, as well as to theoretical predictions from MAID, DMT, and CM12. For each data point, only statistical errors are shown. As discussed in Section 5.3, a total systematic error in the photon polarisation is roughly 2-3%. Since the exact uncertainty is difficult to specify, only statistical errors are shown.

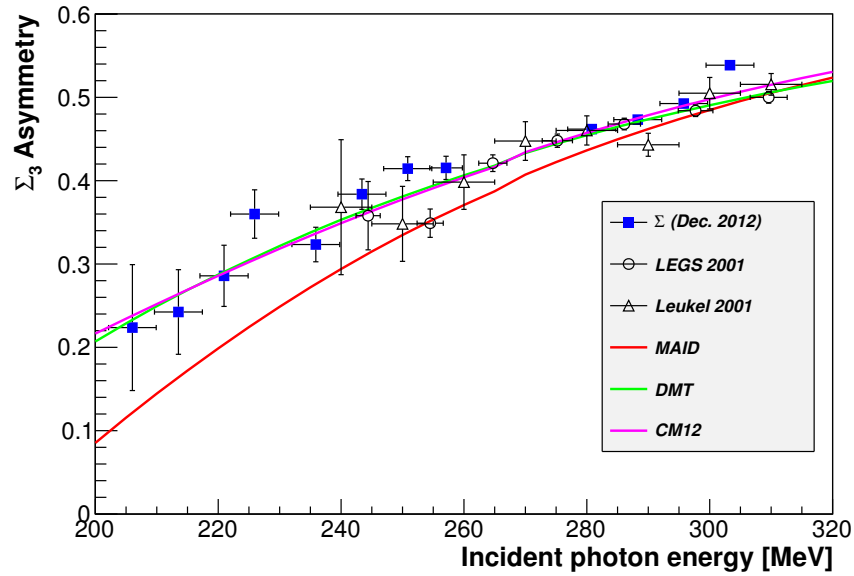


Figure 6.10: Σ_3 asymmetry is shown for θ range of 60 to 65 degrees (lab angle) as a function of incident photon energies. Data covers an energy range of 202.15 MeV to 307.19 MeV. LEGS [4] and Leukel [57] data are shown for comparison. Additionally MAID, DMT, and CM12 model curves are shown. Only statistical errors are shown.

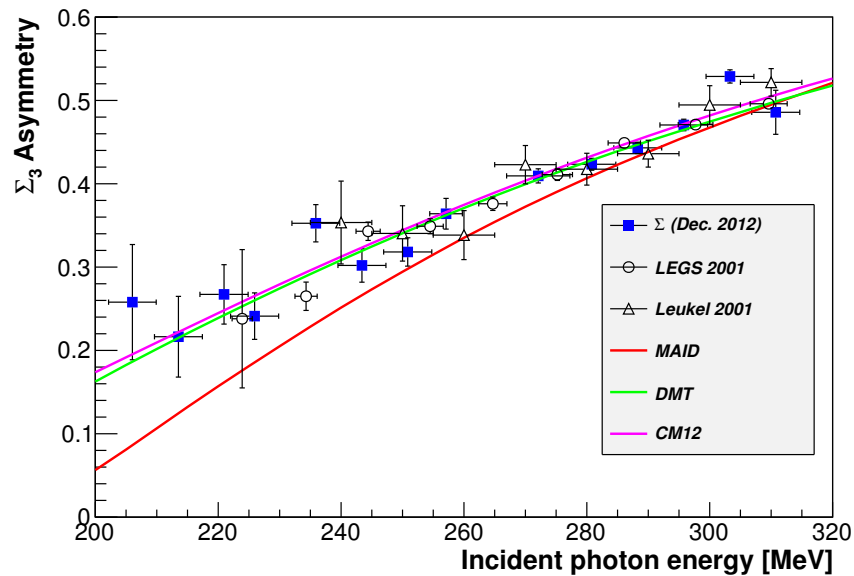


Figure 6.11: Σ_3 asymmetry is shown for θ range of 90 to 95 degrees (lab angle) as a function of incident photon energies. Data covers an energy range of 202.15 MeV to 307.19 MeV. LEGS [4] and Leukel [57] data are shown for comparison. Additionally MAID, DMT, and CM12 model curves are shown. Only statistical errors are shown.

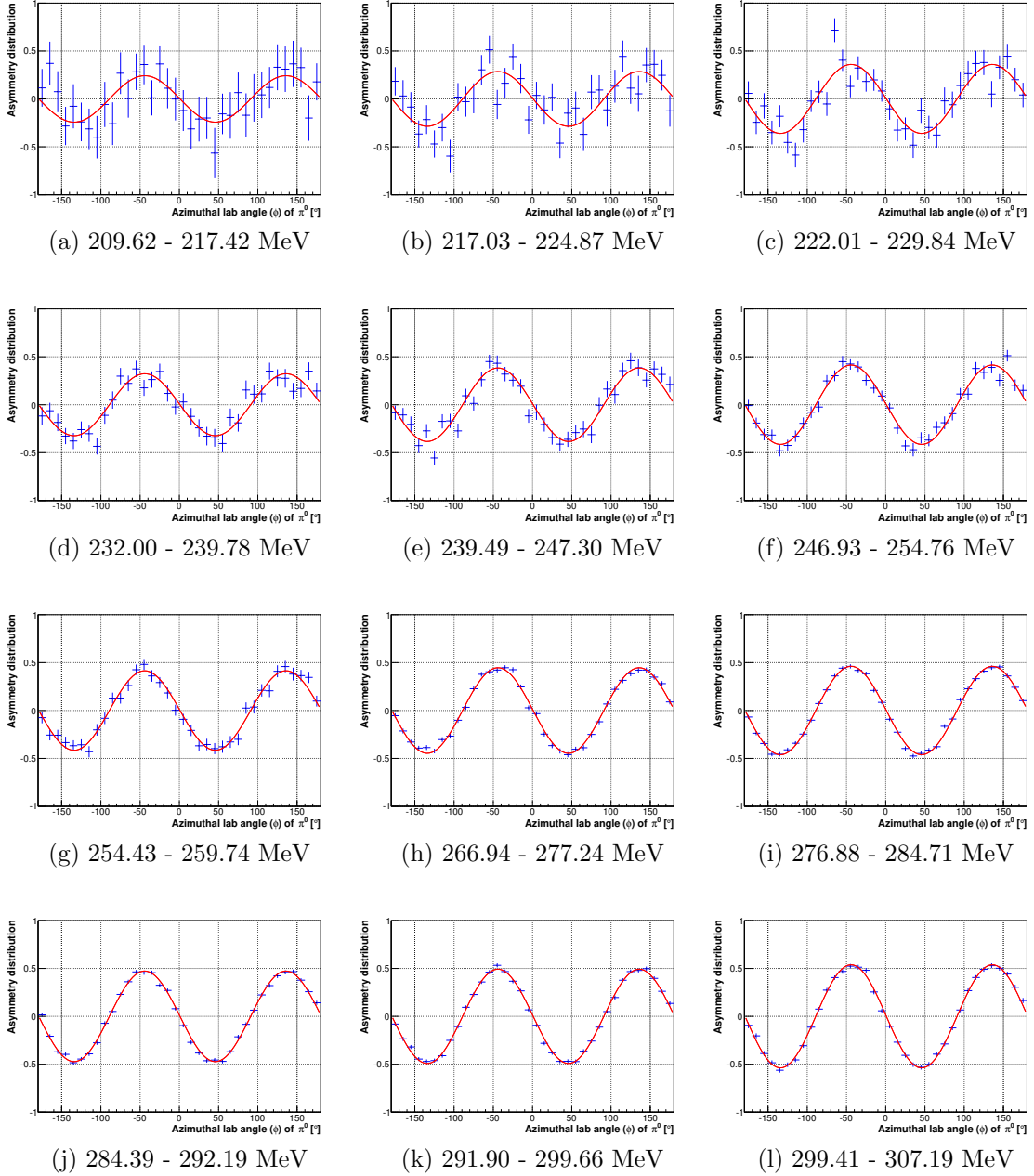


Figure 6.12: Asymmetry distributions are shown for a θ range of 60 to 65 degrees (Lab angle), for a range of incident photon energies. A fit to each asymmetry distribution of the form $A \cos(2\phi + \phi_0)$ is shown in red. The resulting asymmetry as a function of photon energy is shown in Figure 6.11.

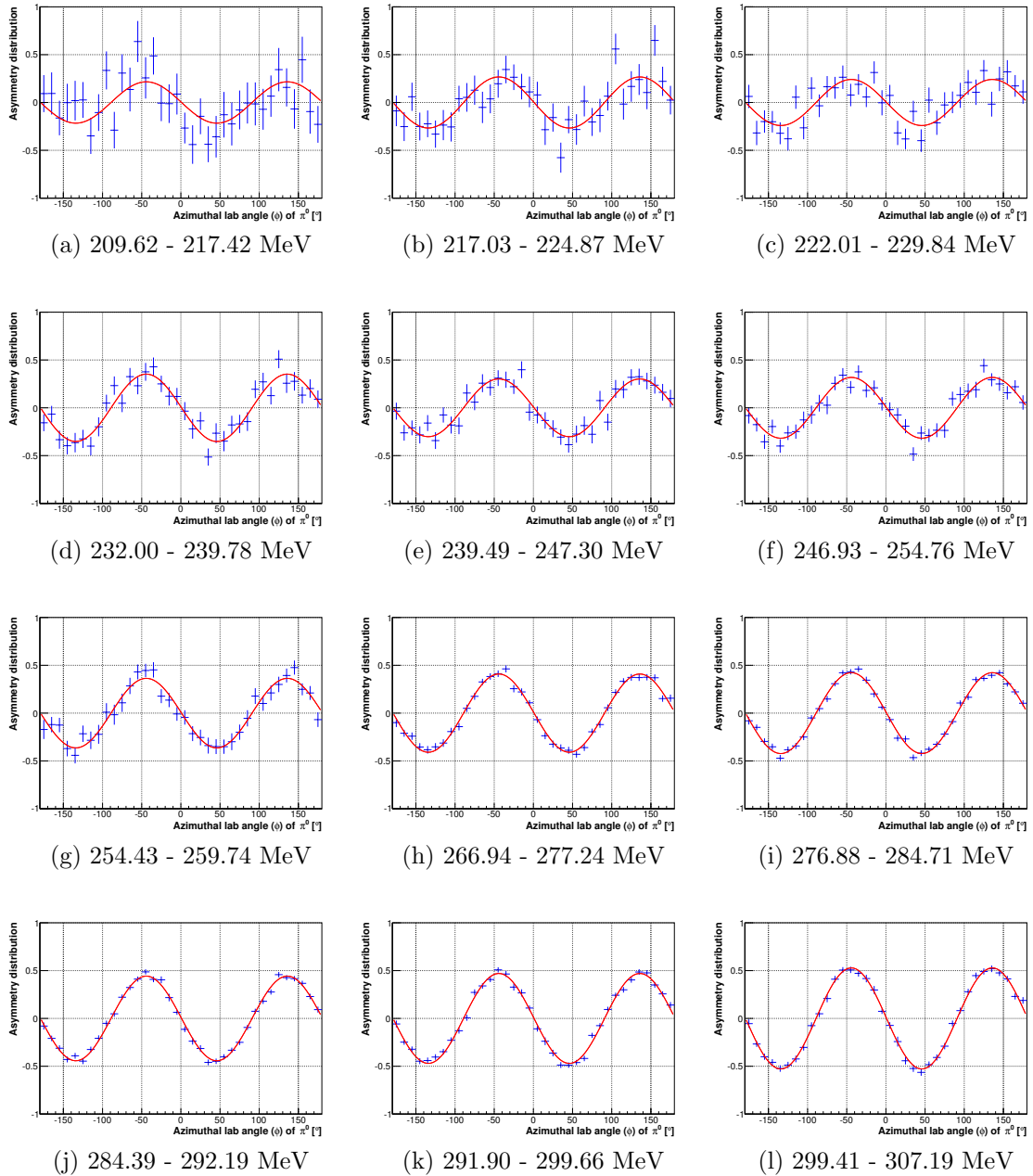


Figure 6.13: Asymmetry distributions are shown for a θ range of 90 to 95 degrees (Lab angle), for a range of incident photon energies. A fit to each asymmetry distribution of the form $A \cos(2\phi + \phi_o)$ is shown in red. The resulting asymmetry as a function of photon energy is shown in Figure 6.10.

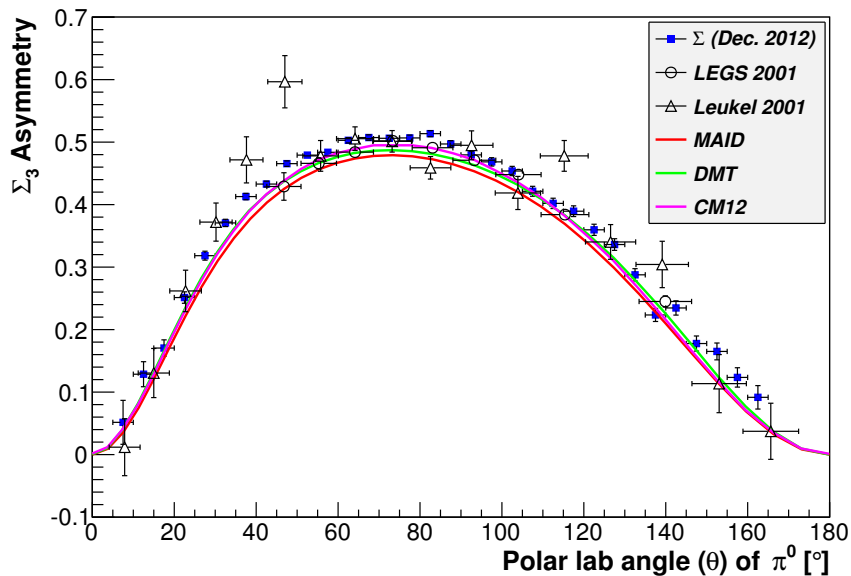


Figure 6.14: Σ_3 asymmetry is shown for incident photon energy of 297.0 ± 5.1 MeV, as a function of π^0 θ angle (lab frame). LEGS [4] and Leukel [57] data are shown for comparison. Additionally MAID, DMT, and CM12 model curves are shown. Only statistical errors are shown.

6.2.6 Discussion

Given the large energy range covered by this run period, combined with full angular coverage, only a small sample of the determined π^0 asymmetries are presented. A complete set of the determined π^0 asymmetries is presented for all angles and energies in Appendix A. In total, over 400 data points have been added to the world database for Σ_3 for π^0 photoproduction. The asymmetry results derived from this work cover the complete angular range, and an incident photon energy range of 210 MeV up to 307 MeV (just below two-pion threshold). A comparison between this work and the LEGS dataset shows very good agreement, an important point considering the discrepancies previously observed in the cross sections of the LEGS dataset. Although the two datasets are in agreement, this work shows a significant improvement over the LEGS dataset, with complete angular coverage and smaller angular bins with similar errors. Additionally, this work shows a significant improvement when compared to the Leukel dataset; not only are the errors significantly reduced, the Leukel data suffers from significant fluctuations which are not observed in this work.

6.3 Compton scattering

6.3.1 Event Selection

Sections 5.1.2.1 and 5.1.2.2 outlined the particle and meson reconstruction applied for this analysis. Only events with a single photon and single charged particle track are considered. As discussed previously, an energy deposition in any charged particle detector — PID, MWPC, or Veto — was used to mark a particle track as charged. Although Compton scattering has a simple final reaction state, event selection within the $\Delta(1232)$ resonance region is complicated by the dominant π^0 photoproduction background. When π^0 photoproduction occurs, the π^0 meson typically decays into two photons. As discussed in Section 6.2, the invariant mass of this two photon system can be used to identify the π^0 meson. However, in cases where a decay photon is undetected, the final state would be a single photon and proton, identical to Compton scattering. Kinematic and angular cuts can be used to reject a portion of this π^0 photoproduction, however if the detected decay photon contains the majority of the original π^0 momentum, the π^0 reaction can be nearly indistinguishable from Compton scattering.

6.3.1.1 Kinematic cuts

Compton scattering is a two-body elastic scattering process. Kinematic cuts can be applied to the reconstructed particles to identify Compton scattering and reject background reactions. For Compton scattering, conservation of energy and momentum require the photon and proton to be coplanar in ϕ within both the center of mass frame and lab frame. A coplanarity angle can be defined by,

$$\phi_{\text{cop}} = |\phi_{\gamma} - \phi_{\text{p}}|. \quad (6.15)$$

For Compton scattering, ϕ_{cop} should be centered around 180° . A second condition can be placed directly on the proton angle. Similar to equation 6.8, a missing four momentum can be calculated for the recoil proton,

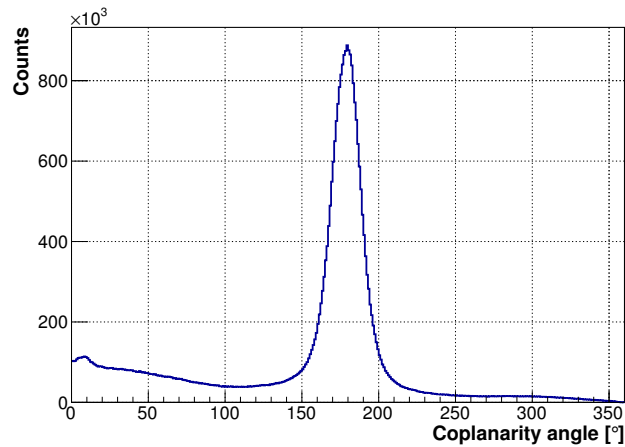
$$\vec{P}_{\text{miss}} = \vec{P}_{\gamma_{\text{in}}} + \vec{P}_{\text{target}} - \vec{P}_{\gamma}. \quad (6.16)$$

For a detected photon, \vec{P}_{miss} corresponds to the predicted energy and momentum of the recoil proton. This missing momentum can be compared to the detected charged

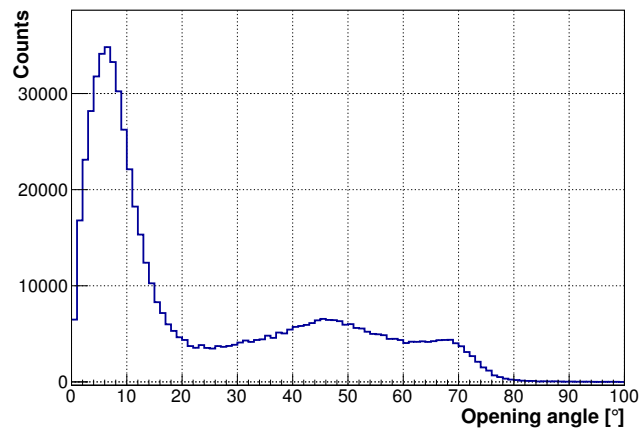
particle to form an additional selection criteria. However, because the proton typically suffers from significant energy losses, only the angle between the missing momentum vector and charged particle is considered. This angle, known as an opening angle, can be defined by,

$$\cos(\Omega_{\text{OA}}) = \frac{\vec{p}_{\text{miss}} \cdot \vec{p}_{\text{recoil}}}{|\vec{p}_{\text{miss}}| \times |\vec{p}_{\text{recoil}}|} . \quad (6.17)$$

Figure 6.15 shows the coplanarity angle, and opening angle, calculated for each photon-charged track pair. The coplanarity distribution shows a sharp peak centered around 180° while the opening angle shows a peak below 10° .



(a) Coplanarity angle, ϕ_{cop}



(b) Opening angle, Ω_{OA}

Figure 6.15: Coplanarity and opening angle distributions are shown for each photon-charged track pair. A prompt-random subtraction has been applied to the opening angle, which includes the incident photon energy.

A coplanarity and opening angle condition can be defined by,

$$|\phi_\gamma - \phi_p| \in 180^\circ \pm X_{\text{cop}}, \quad \Omega_{\text{OA}} \leq X_{\text{OA}}, \quad (6.18)$$

where X_{cop} defines an acceptance window for the coplanarity angle and X_{OA} defines a cut for the opening angle.

A simulation of Compton scattering is used to set optimal coplanarity and opening angle conditions. AcquMC, part of the AcquRoot analysis framework, is an event generator capable of simulating different nuclear reactions. AcquMC was used to produce a simulation of Compton scattering and π^0 photoproduction over an incident photon energy range of 210 MeV to 310 MeV. Simulated events are then analysed using a Geant4 simulation package specifically designed for the A2 collaboration [62]. Geant4 is a simulation toolkit capable of producing realistic models of particle interactions in matter. A2Geant4 is based upon Geant4 and includes an accurate model of the LH₂ proton target and CB-TAPS detector system. The detector simulations shown in Figure 4.8 are produced by the A2Geant4 package. Like real data, the output of this simulation is then analysed using AcquRoot and GoAT. For events with a single photon and single charged particle track reconstructed, a coplanarity angle and opening angle are calculated. Figure 6.16 shows the resulting coplanarity and opening angle distributions. Based on simulation, a coplanarity condition, $X_{\text{cop}} = 15^\circ$, and an opening angle condition, $X_{\text{OA}} = 15^\circ$, accept more than 98% of simulated Compton scattering events.

Interestingly, the simulated π^0 photoproduction distributions closely resemble those from Compton scattering; the coplanarity distribution is centered upon 180° and the opening angle peaks towards 0° . Beyond the primary opening angle peak, a two-peak structure is seen in the opening angle distribution at roughly 45° and 70° . This structure is observed in both real and simulated data and can be related to an acceptance drop which occurs due to the PbWO₄ which are turned off for this analysis. When only a photon and charged track are reconstructed from π^0 photoproduction, this can be considered a mis-identification. The similarity of the simulated distributions can be easily understood when one considers the cause of this mis-identification. This mis-identification arises from three main cases, (1) one decay photon is within an angular region not covered by the detector system, (2) the proton is undetected and a decay photon is mis-identified as charged, or (3) one decay photon carries the

majority of the π^0 momentum. The large angular coverage, and segmented charged particle detectors, of the CB-TAPS detector system significantly reduce the effect of cases 1 and 2. Thus, the predominant source of π^0 mis-identification is due to case 3. In cases where a single decay photon carries the majority of the π^0 momentum, the second decay photon can go undetected. In this case, the high energy decay photon and recoil proton closely mimic the two-body kinematics of Compton scattering. This specific case poses a very difficult challenge when studying Compton scattering, requiring cuts beyond simple kinematic tests. Although a small portion of events from π^0 would be rejected by a 15° coplanarity and opening angle condition, the majority of single photon and single charged particle track events survive these cuts.

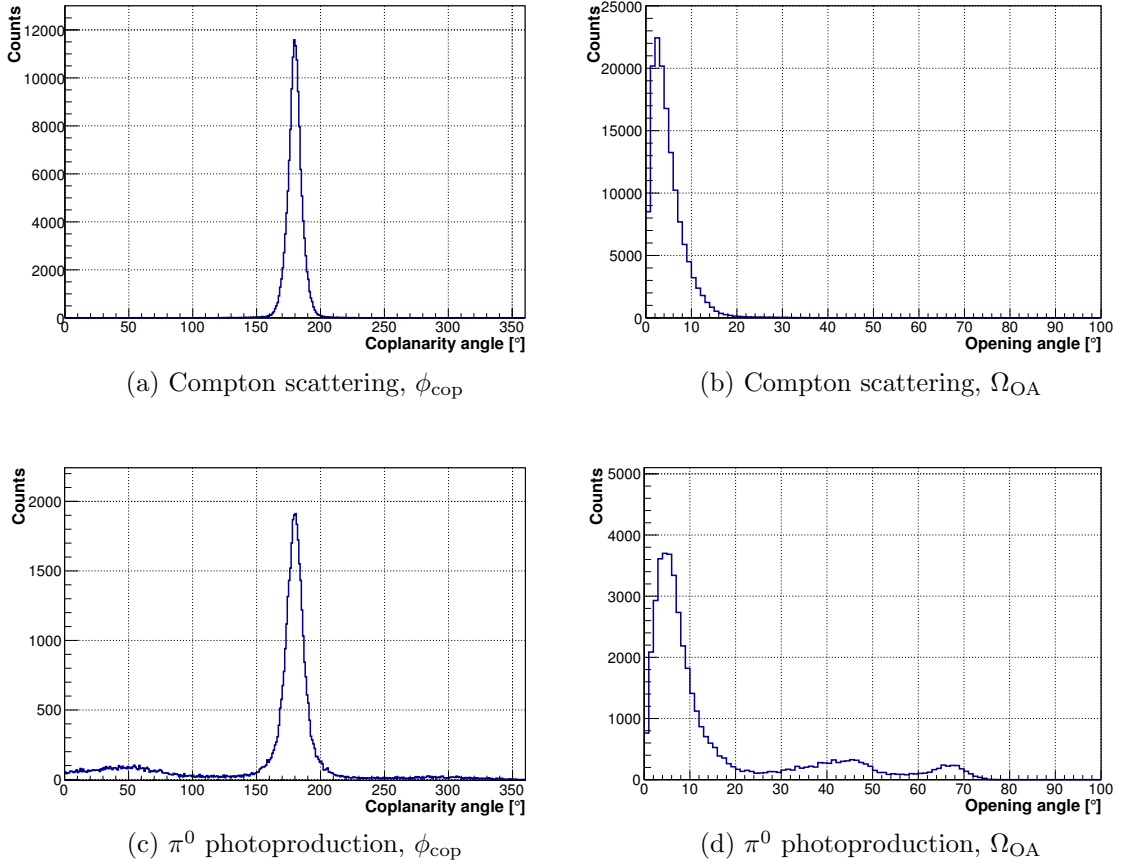
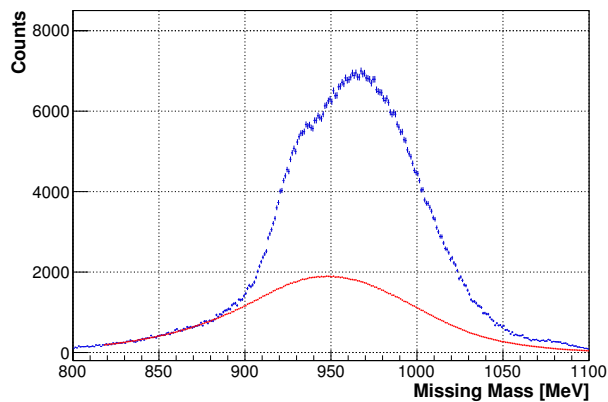


Figure 6.16: Coplanarity and opening angle distributions are shown for simulated Compton scattering and π^0 photoproduction events. Events are simulated using the AcquMC event generator for an incident energy range of 210 to 310 MeV. Realistic detector responses are modelled using A2Geant4.

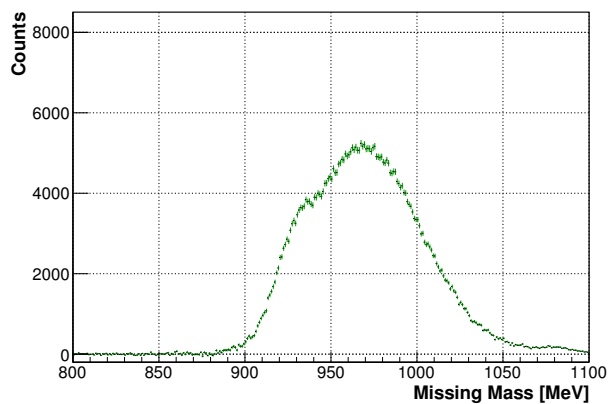
6.3.2 Missing Mass Cuts

A missing mass cut, previously discussed in Section 6.2.1, can be applied to identify Compton scattering events and reject background processes. Equations 6.9 and 6.16 define a missing mass for Compton photons. An example missing mass distribution is shown in Figure 6.17 for events with a single photon and charged track, and a coplanarity and opening angle condition of $\phi_{\text{cop}} = \Omega_{\text{OA}} = 15^\circ$. Although a coplanarity and opening angle condition were applied, no cut on the incident photon energy or angle of the Compton photon were applied. However, the requirement of a detected recoil proton limits the energy and angle ranges which can be reconstructed. A minimum energy is required for the proton to exit the liquid Hydrogen target and be detected in the Crystal Ball or TAPS detectors. This requirement places a minimum threshold on the incident photon energy of roughly 260 MeV. At these energies, recoil protons will be scattered to forward angles, placing a minimum threshold on the Compton photon angle of roughly 65° . Simulation, discussed previously in Section 6.3.1.1, is used to produce a missing mass distribution for comparison. From simulation, a gaussian-like distribution centered upon the proton mass would be expected for Compton scattering events. This gaussian distribution can be seen within the experimental data, however a very large background at missing masses beyond the proton mass is evident.

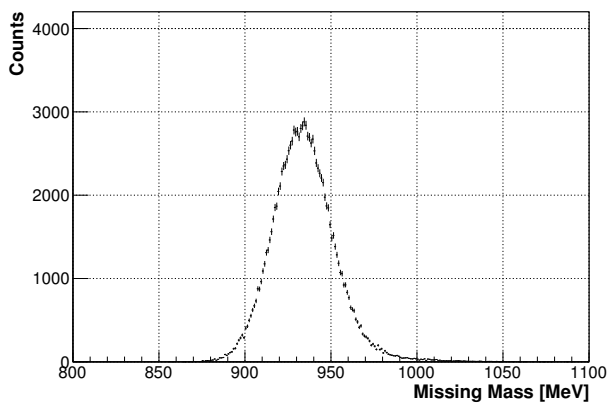
It is necessary to examine the background contributions for specific angle and energy regions as the background can vary significantly across both energy and angle. Two energy bins have been chosen: (1) tagger channels 247 to 254, which corresponds to an incident photon energy of 297.0 ± 10.1 MeV, and (2) tagger channels 255 to 262, which corresponds to an incident photon energy of 277.1 ± 10.1 MeV. The upper and lower limits are based on both experimental and physics limitations. Tagger channel 263 to 265 were broken during the run period, creating a low energy limit. The nominal position of the coherent edge, 310 MeV, results in a drastic drop in polarisation above 310 MeV, creating a higher energy limit. Additionally, to avoid introducing additional background, a high energy limit below the threshold for two π^0 photoproduction is ideal. Six angular bins were chosen: (1) 70° to 80° , (2) 80° to 90° , (3) 90° to 100° , (4) 100° to 115° , (5) 115° to 130° , and (6) 130° to 150° . Angular bins are larger at backwards angles to compensate for reduced statistics.



(a) Missing mass: prompt (blue) and random (red)



(b) Missing mass: prompt-random subtracted



(c) Missing mass: Simulated Compton scattering

Figure 6.17: Example missing mass distribution of (a/b) experimental data and (c) simulated data. Prompt and random missing mass distributions are shown along with a prompt-random subtracted distribution for experimental data. A missing mass calculated from simulated Compton scattering is shown for comparison.

To investigate the background contribution, Compton scattering and π^0 photoproduction were simulated via AcquiMC and A2Geant4. Events with a single photon and charged track are selected and a coplanarity and opening angle condition of $\phi_{\text{cop}} = \Omega_{\text{OA}} = 15^\circ$ are applied. Finally, a single energy and angle bin is selected and a missing mass is calculated for simulated data and experimental data. A fitting routine uses a MINUIT minimization function, scaling the simulated Compton scattering and π^0 photoproduction contributions, to match simulation to real data. An example of this fitting process is shown in Figure 6.18 for incident energy bin 297.0 ± 10.1 MeV, and an angular bin 90° to 100° . Simulated events from Compton scattering and π^0 photoproduction are shown in green and black respectively. The two contributions are summed to create an expected distribution, shown in red. Experimental data, for the same energy and angular region are shown in blue. This fitting method makes a general assumption that no other process contributes to the background distribution. For the example case shown in Figure 6.18, this assumption appears to be valid. Figures 6.20 and 6.19 show missing mass distributions for all energy and angular bins.

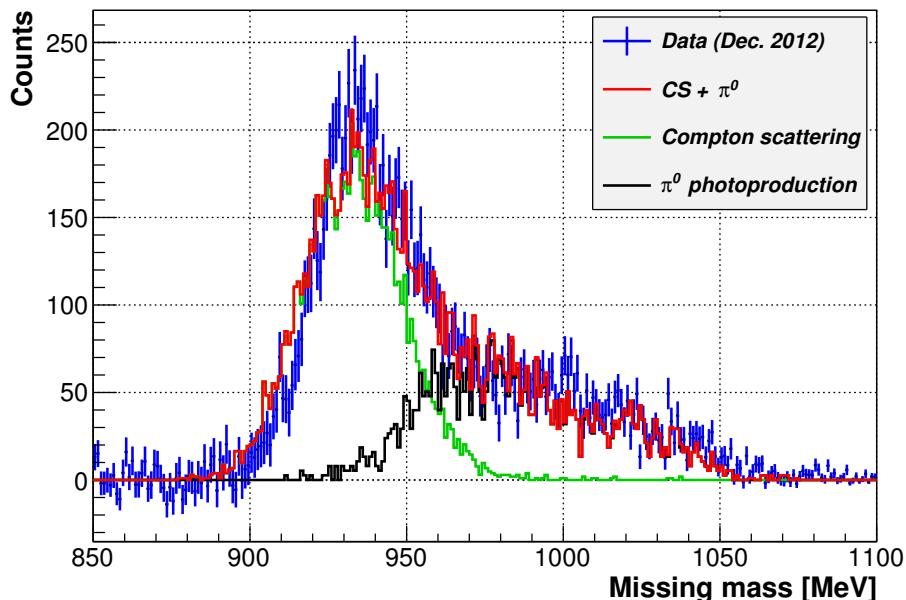


Figure 6.18: A comparison of simulated and experimental data is shown for an incident energy of 277.1 ± 10.1 MeV, and an angular bin 90° to 100° . Simulated events from Compton scattering and π^0 photoproduction are shown in green and black respectively. The two contributions are summed to create an expected distribution, shown in red. Experimental data, shown in blue, show good agreement with the prediction from simulation.

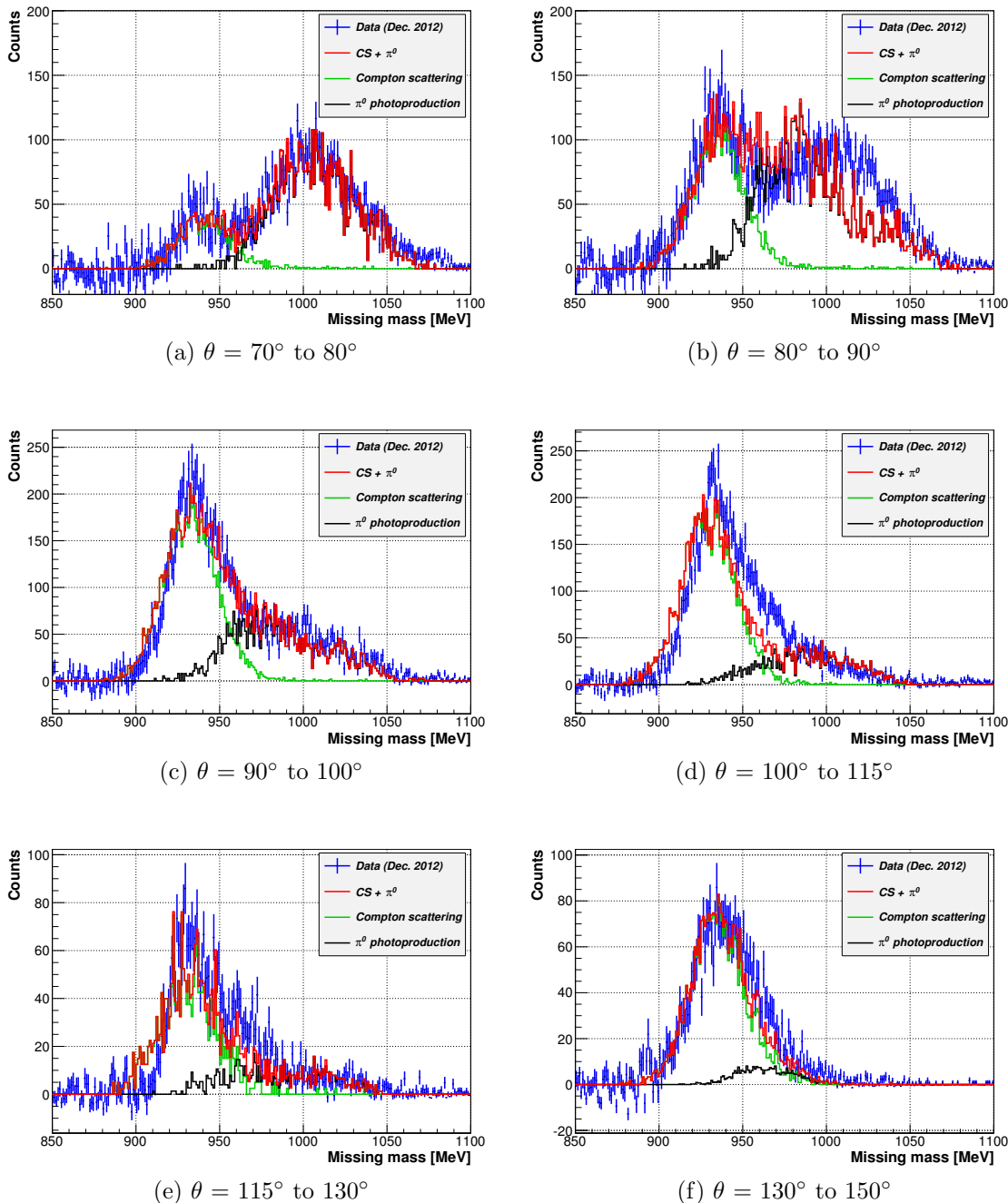


Figure 6.19: A comparison of simulated and experimental data is shown for an incident energy of 277.1 ± 10.1 MeV. Simulated events from Compton scattering and π^0 photoproduction are shown in green and black respectively. The two contributions are summed to create an expected distribution, shown in red. Experimental data are shown in blue.

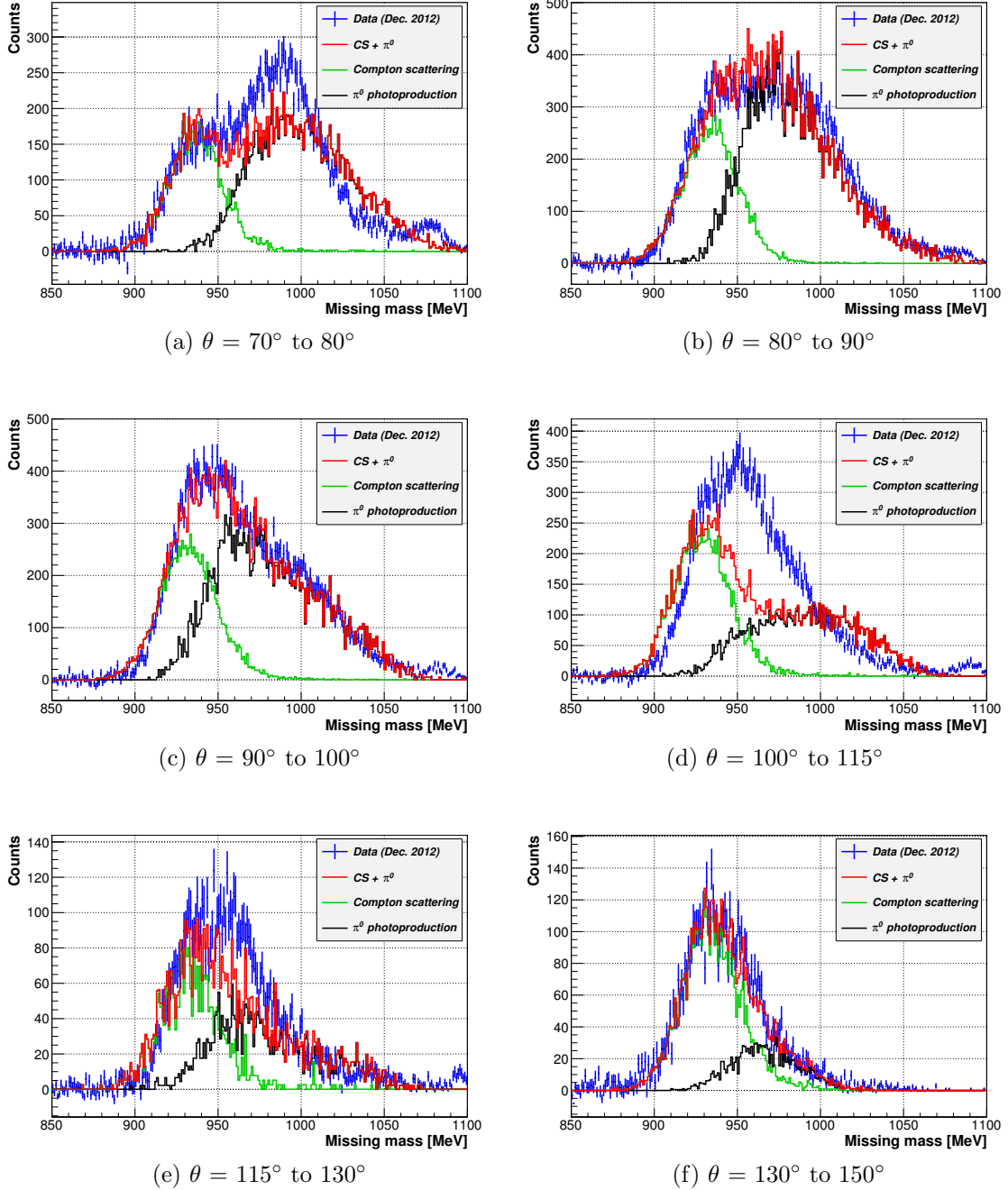


Figure 6.20: A comparison of simulated and experimental data is shown for an incident energy of 297.0 ± 10.1 MeV. Simulated events from Compton scattering and π^0 photoproduction are shown in green and black respectively. The two contributions are summed to create an expected distribution, shown in red. Experimental data are shown in blue.

In some cases, simulation could not replicate the experimental data, Figure 6.20d for example. However, the majority of cases show good agreement to the simulated curves. For Figures 6.20 and 6.19, an event selection was applied, considering only events with a single photon and charged particle detected in either the Crystal Ball or TAPS detector. However, if the recoil proton does not have enough energy to be detected, it is still possible to reconstruct a charged particle track using the PID and MWPCs. This case is only useful for the most forward photon angle bin, 70° to 80° , where the recoil proton has the least energy. Figure 6.21 shows the resulting missing mass distributions for real and simulated data. In the low energy bin, 277.1 ± 10.1 MeV, there is a clear separation between the Compton scattering peak and background distribution. For this analysis, only events reconstructed from recoils which did not deposit energy in the Crystal Ball are considered for the bin $E = 277.1 \pm 10.1$ MeV and $\theta = 70^\circ$ to 80° . For the higher energy bin, these events will not be considered.

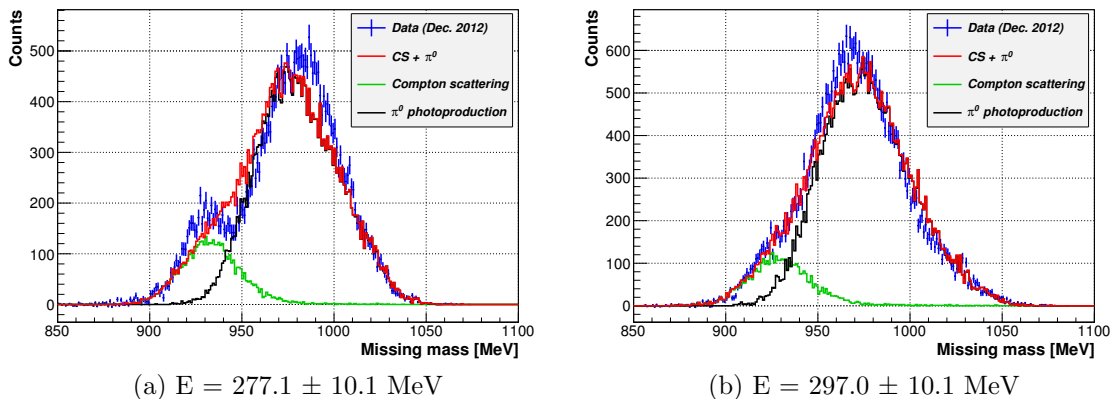


Figure 6.21: A comparison of simulated and experimental data is shown for an angular bin of 70° to 80° . Only events where the charged track is reconstructed from the PID and MWPCs, without a Crystal Ball cluster, are shown. Simulated events from Compton scattering and π^0 photoproduction are shown in green and black respectively. The two contributions are summed to create an expected distribution, shown in red. Experimental data are shown in blue.

In general, simulation and experimental missing mass distributions show very good agreement. In the majority of cases, it is possible to reconstruct the background distributions considering only π^0 photoproduction as a possible source of background. To reject any significant background contamination, it is necessary to set an upper

missing mass limit which coincides with the turn-on-point of π^0 photoproduction. Based on simulation, there is very little background below a missing mass of approximately 930-940 MeV. Although simulation is helpful to inform these missing mass cuts, a more rigorous approach can be applied to determine ideal missing mass cuts. For each energy and angular bin, the asymmetry is recalculated, slowly moving the upper missing mass cut to higher values. As the missing mass cut is moved to higher values, the asymmetry calculations should converge upon the same value with reduced statistical errors. However, as the missing mass cut is moved into a region with background contamination, the asymmetry will begin to diverge. It is important to note that each asymmetry calculation is not uncorrelated. For example, the asymmetry calculated for an upper missing mass cut of 930 MeV uses the same data region as the calculation at 928 MeV, plus a new data region of 928 MeV to 930 MeV. An example of this process is shown in Figure 6.22 for incident energy bin 297.0 ± 10.1 MeV, and an angular bin 70° to 80° . For this example case, the asymmetry is roughly independent of the upper missing mass cut up to values near 940 MeV. Beyond this region, the asymmetry begins to diverge, suggesting a background which appears near 940 MeV.

A missing mass algorithm was developed to determine the maximum upper missing mass cut for each energy and angular bin. The goal of the algorithm is to design a relatively automatic search algorithm which can be applied to all energies and angles. First, a Σ_3 distribution is generated as a function of the upper missing mass cut. Next, a constant line is fit to the Σ_3 distribution, considering only data points below 934 MeV. As these data points are not uncorrelated, the fit value is only used as a guide for the algorithm. Next each possible missing mass cut is considered and two test conditions are evaluated. The primary test, requires that the asymmetry agrees with the fit value within its one-standard deviation statistical uncertainty. A second test, enforced only at missing mass cuts above the proton mass, requires that the asymmetry does not vary by more than 5% by moving to a higher missing mass cut, relative to asymmetry value below the proton missing mass. The second test is a very restrictive test, and is enforced in regions where there is expected to be background contamination from π^0 photoproduction. The logic process of the missing mass algorithm is shown in Figure 6.23. This missing mass algorithm is applied

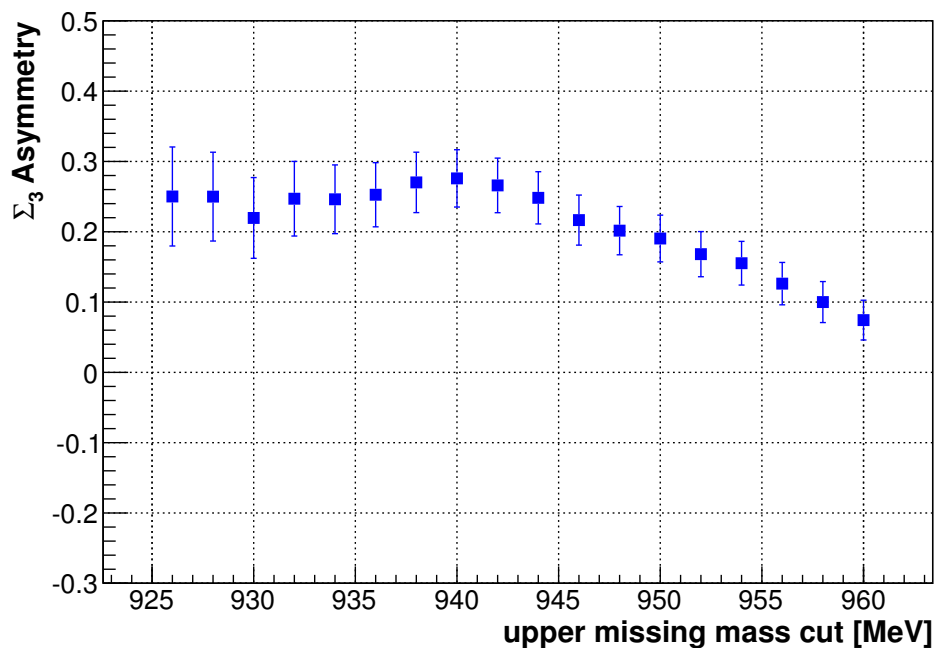


Figure 6.22: An asymmetry is shown as a function of the upper missing mass cut applied. Asymmetries are shown for an incident energy bin 297.0 ± 10.1 MeV, and an angular bin 70° to 80° .

to all energy and angle bins. However, a small adjustment is made for two bins, (1) $E = 277.1 \pm 10.1$ MeV and $\theta = 70^\circ$ to 80° , and (2) $E = 297.0 \pm 10.1$ MeV and $\theta = 100^\circ$ to 115° . In these cases, the same missing mass algorithm is applied, however the fitting range is reduced to consider only data points below a missing mass of 930 MeV. Additionally, the second test condition of the algorithm is applied at 930 MeV, rather than 938 MeV. An adjustment to the algorithm is made for the first bin because, as discussed previously, only events reconstructed from recoils which did not deposit energy in the Crystal Ball are considered. An adjustment to the algorithm is made for the second bin due to the unexplained background distributions shown in Figure 6.20d.

Figures 6.24 and 6.25 show missing mass distributions for all energy and angular bins. The fitting algorithm described here has been applied to determine an optimal missing mass cut for each data set. A horizontal line indicating the fit value is shown for each set, and a vertical dashed line shows the position of the missing mass cut determined from the algorithm. In each case, the algorithm appears to find very reasonable cut positions. At backward angles, where the uncertainties are relatively

large, the second test condition is the dominant reason for the algorithm to exit.

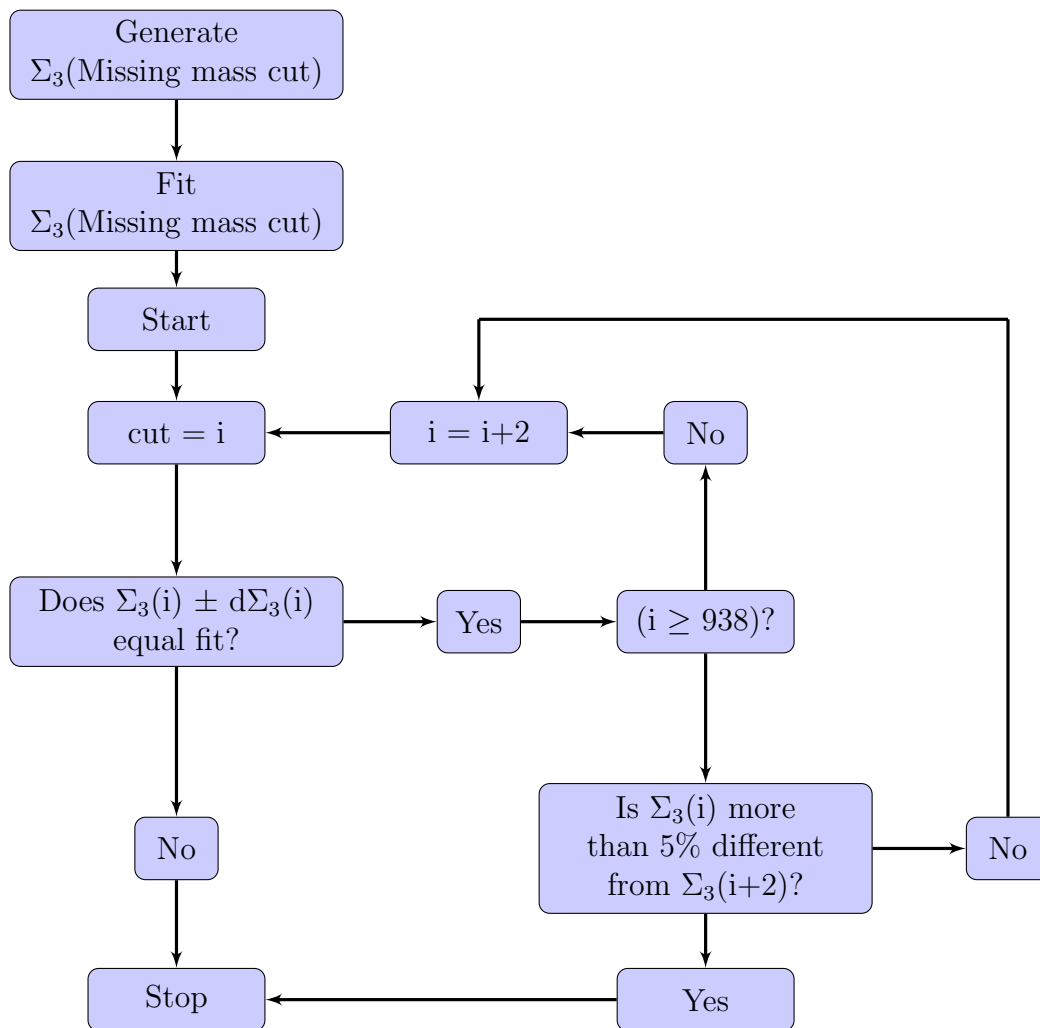


Figure 6.23: Logic steps of missing mass algorithm

Angular bin	Missing Mass cut [MeV] $E = 277.1 \pm 10.1$ MeV	Missing Mass cut [MeV] $E = 297.0 \pm 10.1$ MeV
70° to 80°	930	942
80° to 90°	938	936
90° to 100°	946	934
100° to 115°	940	932
115° to 130°	938	938
130° to 150°	938	938

Table 6.1: Missing mass cuts, determined from a missing mass algorithm, are shown for all energy and angular bins for Compton scattering.

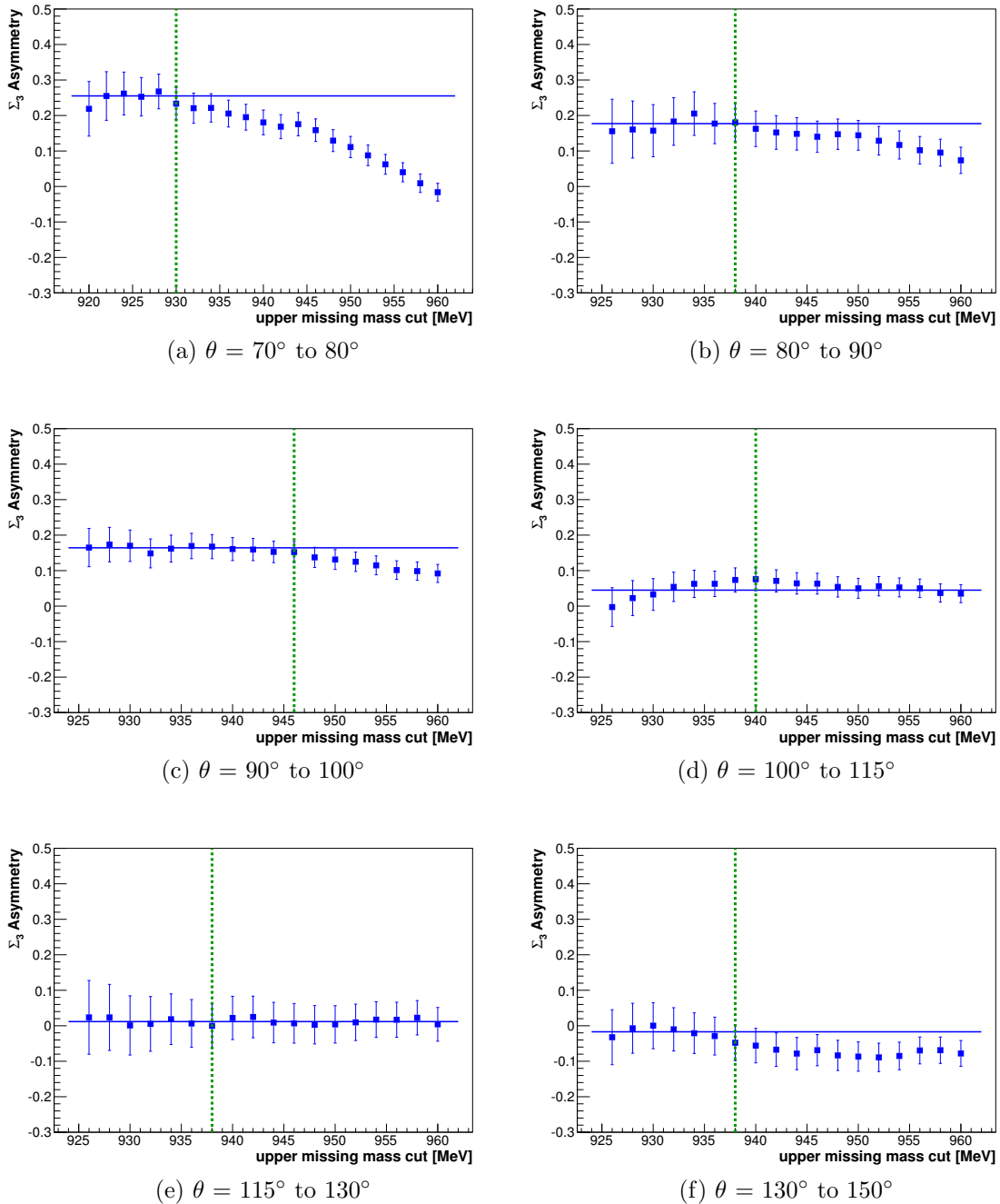


Figure 6.24: An asymmetry is shown as a function of the applied upper missing mass cut. Asymmetries are shown for an incident energy bin 277.1 ± 10.1 MeV. A missing mass algorithm is applied. The horizontal line indicates the algorithm fit value and a vertical dashed line shows the position of the missing mass cut determined from the algorithm.

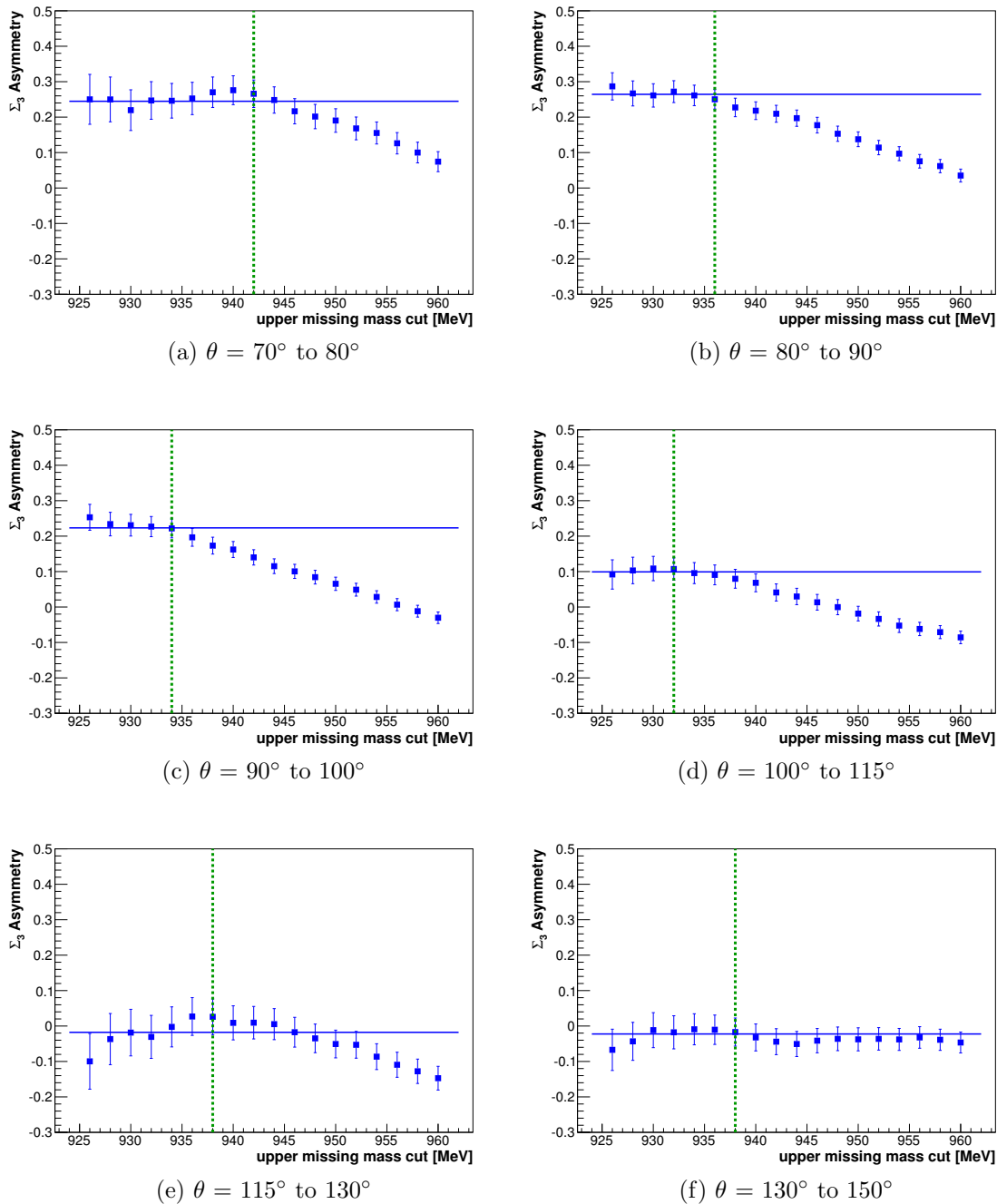
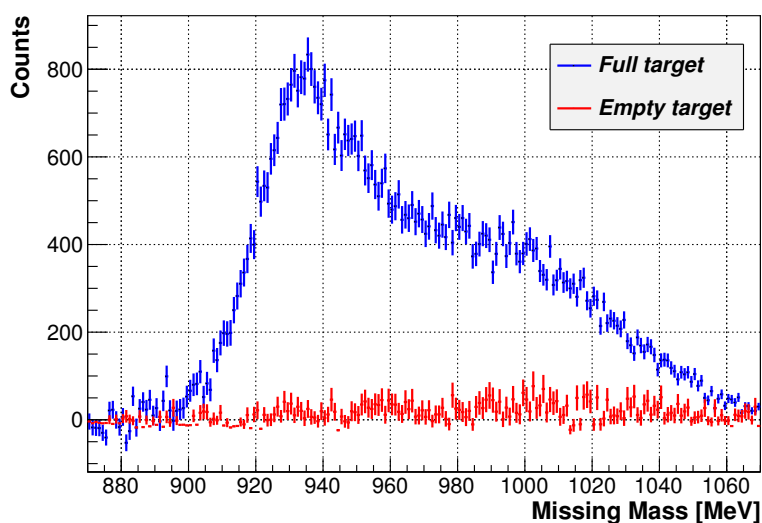


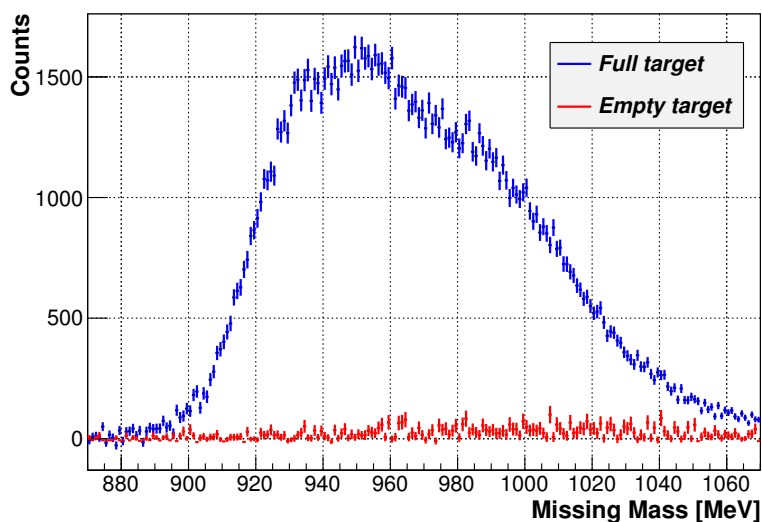
Figure 6.25: An asymmetry is shown as a function of the upper missing mass cut applied. Asymmetries are shown for an incident energy bin 297.0 ± 10.1 MeV. A missing mass algorithm is applied. The horizontal line indicates the algorithm fit value and a vertical dashed line shows the position of the missing mass cut determined from the algorithm.

6.3.3 Empty target contribution

In Section 6.2.2, the empty target contribution was discussed in context of an analysis of π^0 photoproduction. In this case, the empty target contribution was shown to be small, but non-negligible. Figure 6.26 shows the empty target contributions for each energy bin considered in this analysis. For both energy bins, the empty target distributions are small enough that they can be considered to be negligible.



(a) $E = 277.1 \pm 10.1$ MeV



(b) $E = 297.0 \pm 10.1$ MeV

Figure 6.26: Missing mass distributions for events passing a Compton scattering event selection are shown for full and empty target data in blue and red respectively.

6.3.4 Example calculation

For a given incident photon energy, E , and photon angle, θ , the Σ_3 asymmetry can be determined by fitting an asymmetry distribution. As the empty target contribution is negligible for Compton scattering, equation 6.4 can be applied to produce the asymmetry distribution. By convention, there exists a sign change between the definitions of Σ_3 chosen by theorists of either π^0 photoproduction and Compton scattering. To respect this convention, the previous definition of the asymmetry acquires a sign change and the asymmetry is defined by,

$$\Sigma_3(\theta, \phi, E) \cos(2\phi + \phi_o) = - \frac{N_{\perp}(\theta, \phi, E) - F \times N_{\parallel}(\theta, \phi, E)}{p_{\gamma\perp} N_{\perp}(\theta, \phi, E) + F \times p_{\gamma\parallel} N_{\parallel}(\theta, \phi, E)} \quad (6.19)$$

A fit of the form $A * \cos(2\phi + \phi_o)$ is applied, where $A = \Sigma_3$, and ϕ_o was previously determined to be $\phi_o = (1.541 \pm 0.001)$ radians through an analysis of π^0 photoproduction. This determination was presented in Section 6.2.4.

For a given θ and energy range, angular distributions over ϕ can be produced. For Compton photons which pass Compton scattering event selection, outlined in Section 6.3.1, a ϕ -distribution is filled separately for prompt and random electrons. Similar to the example calculation shown in Section 6.2.3, a prompt-random subtraction is applied to the ϕ -distributions. Figure 6.27 shows an example Compton scattering ϕ -distribution for each polarisation orientation, along with an asymmetry distribution shown in Figure 6.29. The ϕ -distributions shown correspond to a θ range of 80° to 90° , and an energy range of 297.0 ± 10.1 MeV.

As discussed previously, a correction factor F must be determined to account for the incident photon flux (see equation 6.5). This correction factor forces the integral of the asymmetry, over all ϕ , to be zero. For the ϕ -distributions shown in Figure 6.27, an asymmetry is calculated for a wide range of correction factors. In each case, the integral over all ϕ is calculated. Figure 6.28 shows the integral of the asymmetry as a function of F . In the example shown, an integral of zero corresponds to a correction factor of 0.983. With a correction factor determined, an example asymmetry can be calculated according to equation 6.19. This is shown in Figure 6.29.

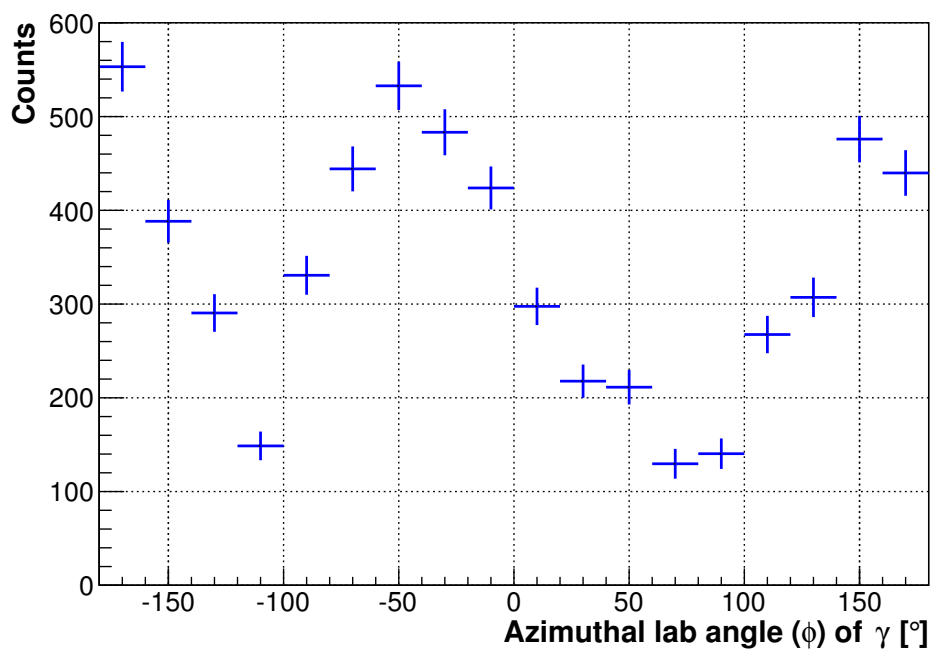
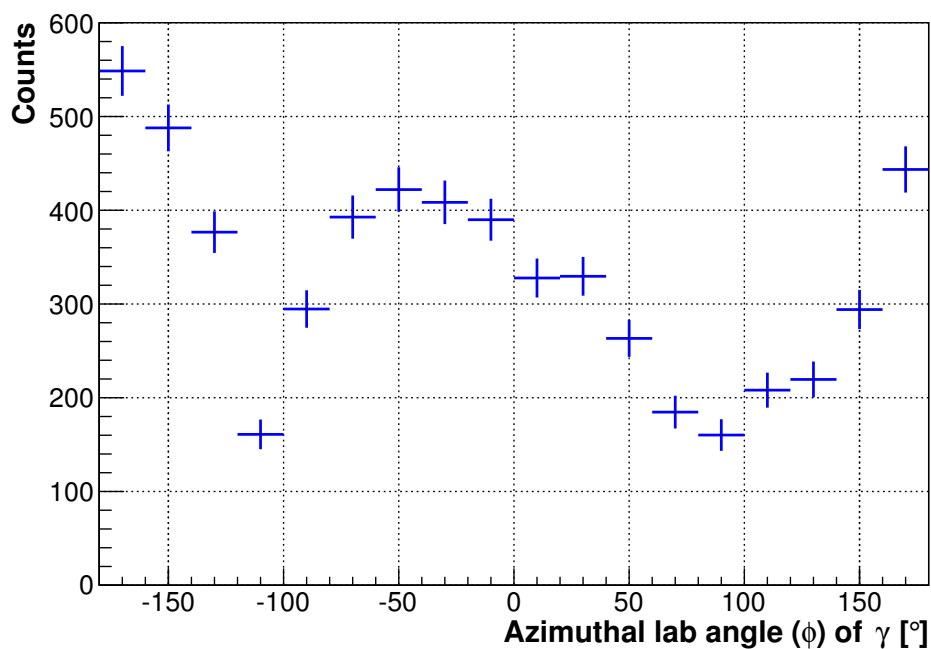
(a) ϕ -distribution: para(b) ϕ -distribution: perp

Figure 6.27: Example ϕ -distribution of Compton photons is shown for a θ range of 80° to 90° , and an energy range of 297.0 ± 10.1 MeV. A distribution is shown for each polarisation orientation, (a) para, and (b) perp.

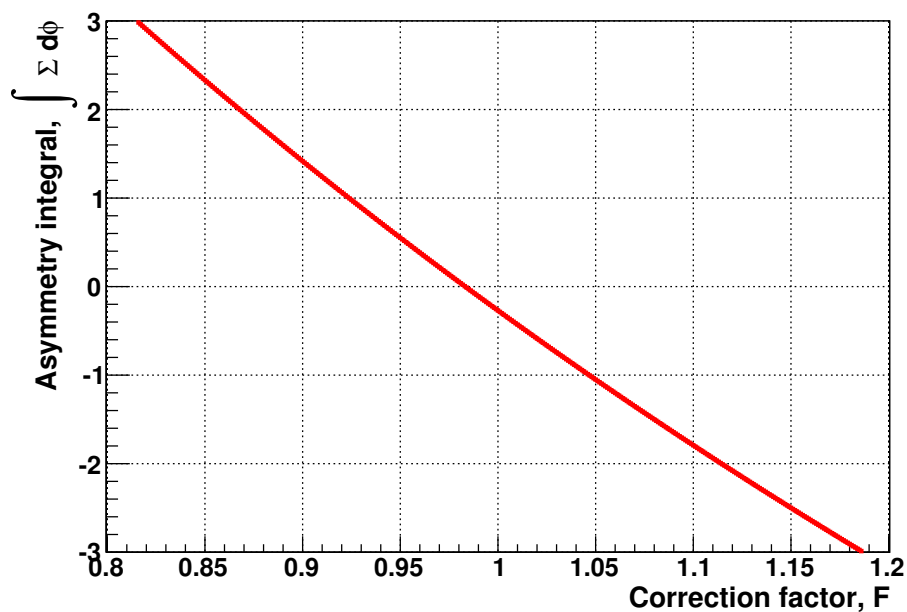


Figure 6.28: The integral of the asymmetry over all phi, $\int \Sigma$, is shown as a function of the correction factor, F , for a θ range of 80° to 90° , and an energy of 297.0 ± 10.1 MeV. The correction factor for this θ and energy range is $F = 0.983$.

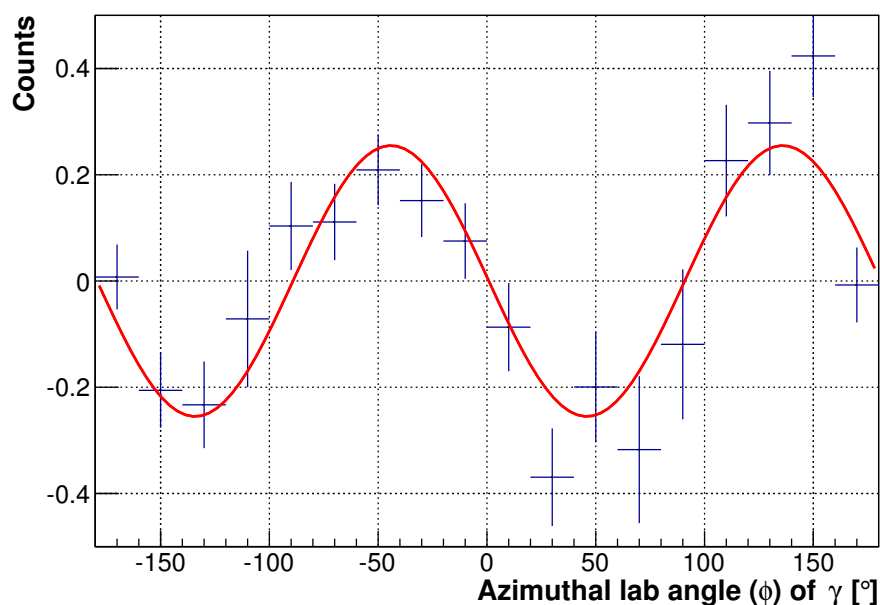


Figure 6.29: Example asymmetry distribution of Compton photons is shown for a θ range of 80° to 90° , and an energy range of 297.0 ± 10.1 MeV. A fit of the form $A * \cos(2\phi + \phi_0)$ is applied, shown in red. An extraction of the fit parameter A determines the asymmetry for this θ and energy range to be $\Sigma_3 = 0.255 \pm 0.027$.

6.3.5 Results

Asymmetry distributions are shown in Figures 6.30 and 6.31 for incident energy ranges of 277.1 ± 10.1 MeV and 297.0 ± 10.1 MeV respectively. A fit of the form $A * \cos(2\phi + \phi_o)$ was applied, where $A = \Sigma_3$, is shown in red for each distribution. The resulting asymmetries are given in Figures 6.32 and 6.33, and a table of calculation parameters, including the correction factor and χ^2 for each angular bin, are given in tables 6.2 and 6.3.

A comparison to Σ_3 results from the LEGS collaboration [4] is shown. As discussed previously, the LEGS data set shows significant discrepancies when the cross sections determined from this dataset are compared to other data sets. Although it is possible that a discrepancy exists only in cross sections, and not in asymmetries, a discrepancy so large motivates a cross check of the LEGS data set. Two theoretical models are also compared, (1) a fixed- t dispersion relation (HDPV) [15][8] provided by Pasquini, and (2) a calculation from Baryon Chiral Perturbation Theory [63] provided by Pascalutsa. For the fixed- t dispersion relation, asymmetry calculations are produced using a set of input scalar and spin polarisabilities. Nominal values for the spin polarisabilities are taken to be, $\bar{\gamma}_{E1E1} = -4.3$, $\bar{\gamma}_{M1M1} = 2.9$, $\bar{\gamma}_{E1M2} = -0.01$, and $\bar{\gamma}_{M1E2} = 2.1$. These values are given in standard spin polarisability units of 10^{-4} fm^4 , and correspond to the HDPV values given in Table 3.1 for the HDT partial wave solutions. Additionally, scalar polarisabilities $\bar{\alpha}$ and $\bar{\beta}$ are taken to be $\bar{\alpha} + \bar{\beta} = 13.82$, and $\bar{\alpha} - \bar{\beta} = 10.5$, in standard scalar polarisability units of 10^{-4} fm^3 .

6.3.6 Discussion

Within this work, Σ_3 was measured for Compton scattering for the limited angular range of 70° to 150° , and the incident photon energy range of 267 MeV up to 307 MeV (just below two-pion threshold). The Σ_3 results from the work were compared to those from the LEGS collaboration. Even though the statistical errors from both measurements are rather large, a shift in the asymmetries can be observed. This is most predominant near 90° in the higher energy region. Despite this shift, the results of this work and the LEGS dataset show a good general agreement. Finally, asymmetries determined from this work suggest that the Σ_3 asymmetry may fall off faster than predicted at backward angles within the higher energy region.

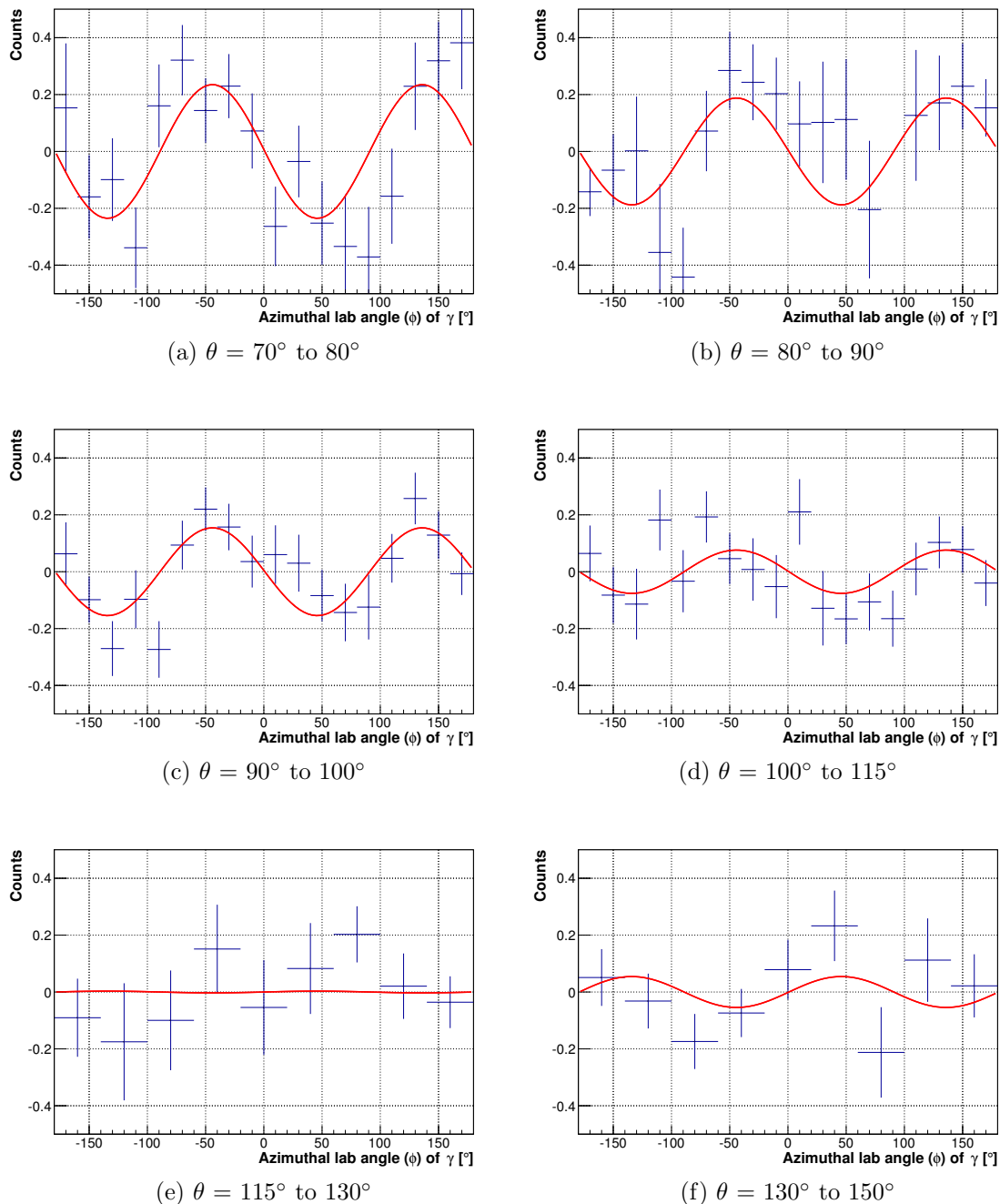


Figure 6.30: Σ_3 Asymmetry distributions for Compton scattering with an incident energy range of 277.1 ± 10.1 MeV. A fit of the form $A * \cos(2\phi + \phi_0)$ is shown in red. Fitting parameters, including a χ^2 value for each fit, are given in Table 6.2 and the final $\Sigma_3(E, \theta)$ asymmetry is shown in Figure 6.32.

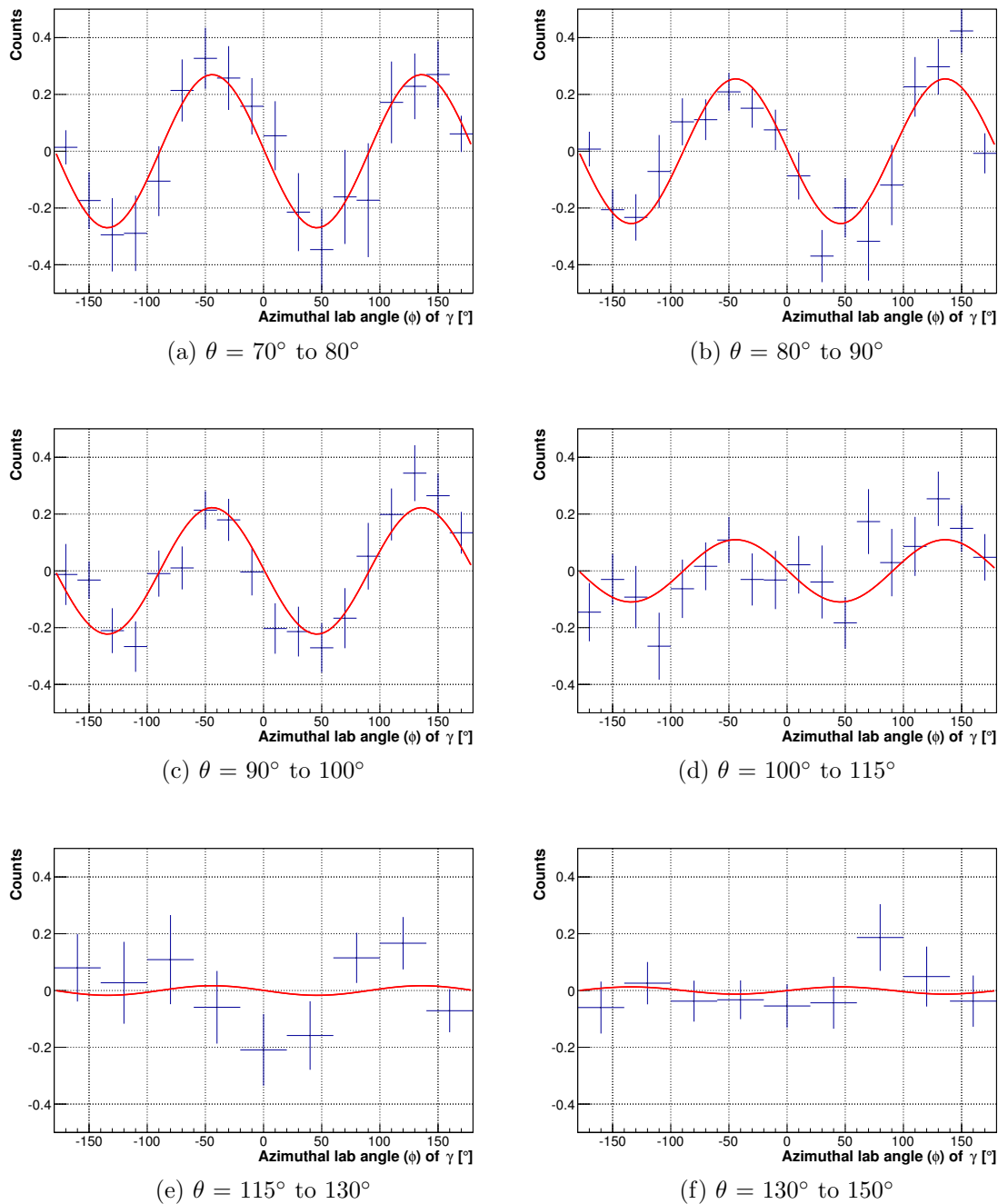


Figure 6.31: Σ_3 Asymmetry distributions for Compton scattering with an incident energy range of 297.0 ± 10.1 MeV. A fit of the form $A * \cos(2\phi + \phi_0)$ is shown in red. Fitting parameters, including a χ^2 value for each fit, are given in Table 6.3 and the final $\Sigma_3(E, \theta)$ asymmetry is shown in Figure 6.33.

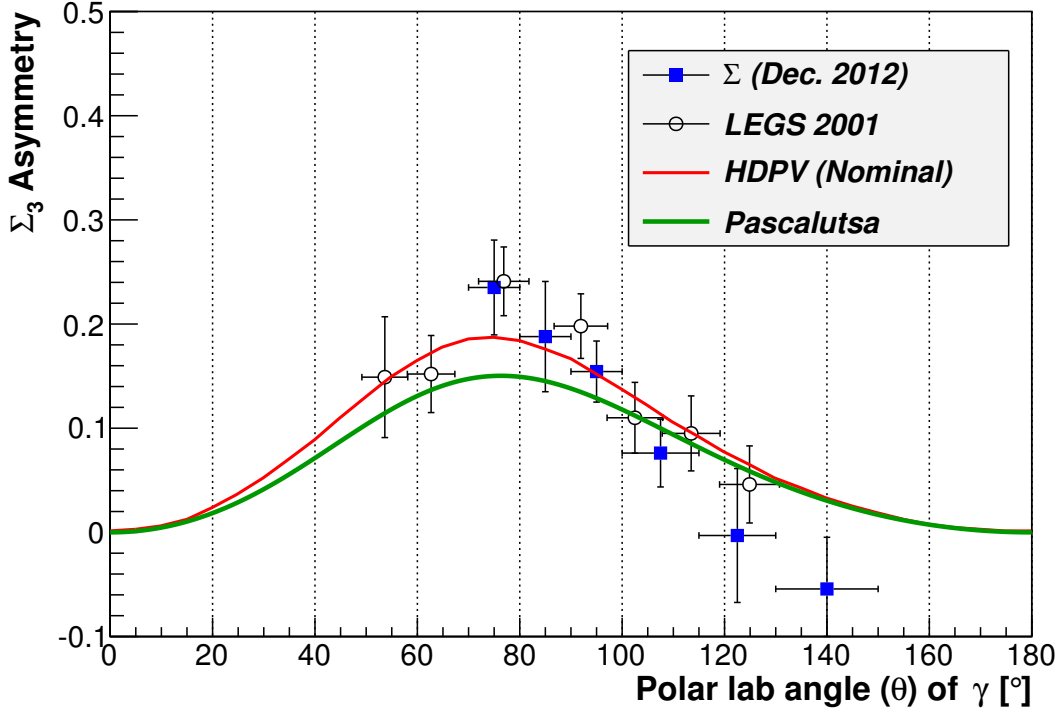


Figure 6.32: Σ_3 Asymmetry for Compton scattering with an incident energy range of $E = 277.1 \pm 10.1$ MeV. LEGS [4] data are shown for comparison. Additionally HDPV [15][8] and Pascalutsa [63] curves are shown. Only statistical errors are shown.

$E_\gamma = 277.1 \pm 10.1$ MeV					
θ_γ (lab)	Correction, F	χ^2 of fit	Σ_3	$\Delta\Sigma_3(\text{stat.})$	$\Delta\Sigma_3$ (3% pol.)
75.00 ± 5.0	1.0504	1.3844	0.2351	0.0455	0.0071
85.00 ± 5.0	1.0319	1.1856	0.1880	0.0529	0.0056
95.00 ± 5.0	0.9703	1.1118	0.1544	0.0293	0.0046
107.50 ± 7.5	0.9496	1.1001	0.0760	0.0325	0.0023
122.50 ± 7.5	1.0188	0.8993	-0.0031	0.0643	0.0001
140.00 ± 10.0	0.9595	1.2064	-0.0544	0.0496	0.0016

Table 6.2: Fitting parameters for Σ_3 determined for incident photon energies of $E = 277.1 \pm 10.1$ MeV. For each fit, a χ^2 per degree of freedom is given. Asymmetry distributions, and corresponding fits, for each angular bin are shown in Figure 6.30.

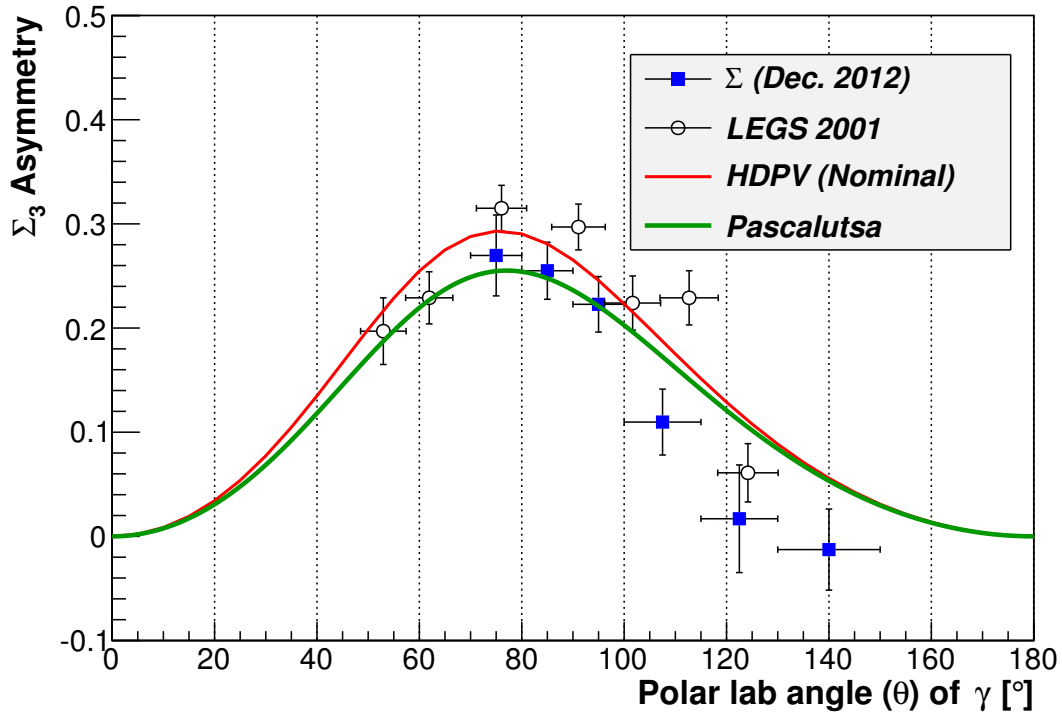


Figure 6.33: Σ_3 Asymmetry for Compton scattering with an incident energy range of $E = 297.0 \pm 10.1$ MeV. LEGS [4] data are shown for comparison. Additionally HDPV [15][8] and Pascalutsa [63] curves are shown. Only statistical errors are shown.

$E_\gamma = 297.0 \pm 10.1$ MeV					
θ_γ (lab)	Correction, F	χ^2 of fit	Σ_3	$\Delta\Sigma_3(\text{stat.})$	$\Delta\Sigma_3$ (3% pol.)
75.00 ± 5.0	1.0030	0.4775	0.2697	0.0388	0.0081
85.00 ± 5.0	0.9833	1.2144	0.2551	0.0274	0.0077
95.00 ± 5.0	0.9536	1.0637	0.2228	0.0267	0.0067
107.50 ± 7.5	0.9997	0.9507	0.1097	0.0316	0.0033
122.50 ± 7.5	0.9371	1.4233	0.0169	0.0517	0.0005
140.00 ± 10.0	0.9675	0.5725	-0.0127	0.0389	0.0004

Table 6.3: Fitting parameters for Σ_3 determined for incident photon energies of $E = 297.0 \pm 10.1$ MeV. For each fit, a χ^2 per degree of freedom is given. Asymmetry distributions, and corresponding fits, for each angular bin are shown in Figure 6.31.

Chapter 7

Discussion

The Σ_3 asymmetry is a single polarisation observable which connects the polarised and unpolarised cross sections for linearly polarised photons incident upon unpolarised protons. In chapter 6, Σ_3 results for π^0 photoproduction and Compton scattering were presented. These results were extracted from a December 2012 run period at the MAMI tagged photon facility in Mainz, Germany. The motivation of this work is largely directed towards the study of the proton's spin polarisabilities, which quantify the response of the proton's spin to an applied electromagnetic field. The spin polarisabilities, which appear in the third order effective Hamiltonian for Compton scattering, can be studied through polarised Compton scattering.

An analysis by Martel [1] studied the double polarisation observable Σ_{2x} for Compton scattering at the MAMI tagged photon facility. A recent analysis by Martel [2] determined the proton's spin polarisabilities for the first time, combining Σ_3 results from the LEGS collaboration [4] and Σ_{2x} results from the MAMI tagged photon facility. This analysis used a fixed- t dispersion relation code, provided by Barbara Pasquini [8], to fit asymmetry data. The fitting routine varies $(\bar{\alpha} + \bar{\beta})$, $(\bar{\alpha} - \bar{\beta})$, $\bar{\gamma}_{E1E1}$, and $\bar{\gamma}_{M1M1}$, γ_0 and γ_π , to fit the asymmetry data. Four constraints are applied in the analysis,

$$\begin{aligned}\bar{\alpha} + \bar{\beta} &= (13.8 \pm 0.4) \times 10^{-4} \text{ fm}^3 [27] \\ \bar{\alpha} - \bar{\beta} &= (7.6 \pm 1.7) \times 10^{-4} \text{ fm}^3 [32] \\ \gamma_0 &= (-1.00 \pm 0.18) \times 10^{-4} \text{ fm}^4 [33] \\ \gamma_\pi &= (8.0 \pm 1.8) \times 10^{-4} \text{ fm}^4 [34]\end{aligned}\tag{7.1}$$

Although only $\bar{\gamma}_{E1E1}$, and $\bar{\gamma}_{M1M1}$ are perturbed during the fitting routine, allowing γ_0 and γ_π to vary essentially allows $\bar{\gamma}_{E1M2}$, and $\bar{\gamma}_{M1E2}$ to vary as well. A global fit to all data allows the spin polarisabilities to be extracted. Through this analysis, a set of spin polarisabilities were determined to be $\bar{\gamma}_{E1E1} = -3.5 \pm 1.2$, $\bar{\gamma}_{M1M1} = 3.16 \pm 0.85$, $\bar{\gamma}_{E1M2} = -0.7 \pm 1.2$, and $\bar{\gamma}_{M1E2} = 1.99 \pm 0.29$, in standard spin polarisability units

of 10^{-4} fm^4 . Final fitting parameters for the γ_0 and γ_π constraints were determined to be $\gamma_0 = -1.03 \pm 0.18 \times 10^{-4} \text{ fm}^4$ and $\gamma_\pi = 9.3 \pm 1.6 \times 10^{-4} \text{ fm}^4$.

As discussed previously, the LEGS data set used in the fitting shows significant discrepancies when compared to other data sets. In Section 3.4, a discussion of the backward spin polarisability was presented. This backward spin polarisability, γ_π , is a linear combination of the four leading order spin polarisabilities. A value of γ_π , extracted from the LEGS data set, was determined to be $\gamma_\pi = -23.2 \times 10^{-4} \text{ fm}^4$. A value of γ_π , extracted from data from MAMI, LARA, and Saskatoon data sets, was determined to be $\gamma_\pi = -38.7 \times 10^{-4} \text{ fm}^4$. The extraction of γ_π was based upon differential cross sections measured by each collaboration. Although it is possible that a discrepancy exists only in cross sections, and not in asymmetries, a discrepancy so large motivates a cross check of the LEGS data set.

It is possible to apply the same fitting routine applied in the Martel analysis, combining Σ_{2x} results from Martel and Σ_3 results from this work, rather than LEGS. A fit to this data was performed (with the assistance of MAMI A2 collaborator, A. Rajabi [64]). Similar to the Martel analysis, the fixed- t dispersion relation code of Pasquini was used to fit asymmetry data. The fit varied $\bar{\alpha}$, $\bar{\beta}$, $\bar{\gamma}_{E1E1}$, and $\bar{\gamma}_{M1M1}$, with constraints applied on $\bar{\alpha} + \bar{\beta}$, $\bar{\alpha} - \bar{\beta}$, γ_0 and γ_π , to fit the asymmetry data. Constraints applied are the same as those given in equation 7.1. Through this most recent analysis, a set of spin polarisabilities was determined to be,

$$\begin{aligned}
 \bar{\gamma}_{E1E1} &= -5.0 \pm 1.5 \times 10^{-4} \text{ fm}^4 \\
 \bar{\gamma}_{M1M1} &= 3.13 \pm 0.88 \times 10^{-4} \text{ fm}^4 \\
 \bar{\gamma}_{E1M2} &= 1.7 \pm 1.7 \times 10^{-4} \text{ fm}^4 \\
 \bar{\gamma}_{M1E2} &= 1.26 \pm 0.43 \times 10^{-4} \text{ fm}^4
 \end{aligned} \tag{7.2}$$

which corresponds to final fitting parameters for the backward and forward spin polarisabilities of,

$$\begin{aligned}
 \gamma_0 &= -1.00 \pm 0.18 \times 10^{-4} \text{ fm}^4 \\
 \gamma_\pi &= 7.8 \pm 1.8 \times 10^{-4} \text{ fm}^4
 \end{aligned} \tag{7.3}$$

This is the first extraction of all four spin polarisabilities from data taken only at the MAMI tagged photon facility. A side by side comparison of both extractions is given in Table 7.1.

	LEGS + Martel [10^{-4} fm ⁴]	Collicott + Martel [10^{-4} fm ⁴]
$\bar{\gamma}_{E1E1}$	-3.5 ± 1.2	-5.0 ± 1.5
$\bar{\gamma}_{M1M1}$	3.16 ± 0.85	3.13 ± 0.88
$\bar{\gamma}_{E1M2}$	-0.7 ± 1.2	1.7 ± 1.7
$\bar{\gamma}_{M1E2}$	1.99 ± 0.29	1.26 ± 0.43
γ_0	-1.03 ± 0.18	-1.00 ± 0.18
γ_π	9.3 ± 1.6	7.8 ± 1.8
$\bar{\alpha} + \bar{\beta}$	14.0 ± 0.4	13.8 ± 0.4
$\bar{\alpha} - \bar{\beta}$	7.4 ± 0.9	6.6 ± 1.7
χ^2/dof	1.05	1.25

Table 7.1: Spin polarisabilities determined using either the LEGS and Martel data sets, or the Collicott (this work) and Martel data set. In both cases a fixed- t dispersion code is used to fit and extract the spin polarisabilities. Also shown are the final fitting parameters for the constraints $(\bar{\alpha} + \bar{\beta})$, $(\bar{\alpha} - \bar{\beta})$, γ_0 , and γ_π , and the χ^2 per degree of freedom for each fit.

It is important to note that the LEGS Σ_3 data set covers a wide angular and energy range, and consists of 58 data points. This work, by comparison, is only 12 data points. Comparing the spin polarisabilities determined through this new analysis, some differences are clear.

- The errors on the individual spin polarisabilities increase slightly. However, considering the reduced data set in comparison to LEGS, this could be expected.
- Although $\bar{\gamma}_{M1M1}$ remains relatively unchanged, a significant shift is seen in the other three spin polarisabilities.
- As discussed previously, the LEGS data set shows a large discrepancy from all other data sets when used to extract the backward spin polarisability. It is therefore interesting to compare the final fit parameter γ_π from each extraction. The fit for γ_π was determined to be 9.3×10^{-4} fm⁴ and 7.8×10^{-4} fm⁴ while using the LEGS data set and this work respectively. While the errors are large enough to allow these parameters to agree, the shift is noteworthy. Because $\bar{\gamma}_{E1M2}$ and $\bar{\gamma}_{M1E2}$ are determined through their linear relation to γ_0 and γ_π , a large shift in γ_π helps to explain the differing spin polarisabilities.

In Section 6.3.5, Σ_3 results from this work were compared to theoretical predictions from the fixed- t dispersion relation used in this fitting method. Curves were shown for nominal spin polarisabilities given in Table 3.1. It is possible to reproduce new dispersion relation curves, using each set of spin polarisabilities given in Table 7.1. In Figure 7.1, a new dispersion relation calculation for the Martel analysis, which combines the Σ_3 results from the LEGS collaboration and Σ_{2x} results from Martel, is shown. This calculation uses the parameters for the scalar and spin polarisabilities given in Table 7.1 under LEGS+Martel. A second dispersion relation calculation is shown for the analysis presented in this work, which combines the Σ_3 results from this work and Σ_{2x} results Martel. This second calculation uses the parameters for the scalar and spin polarisabilities given in Table 7.1 under Collicott+Martel. These new dispersion relation curves are shown along side $B\chi$ PT calculations from Pascalutsa.

7.1 Outlook

A three part experimental program was proposed at the MAMI tagged photon facility to study the proton's spin polarisability using polarised Compton scattering. The first achievement towards this program was the measurement of the double polarisation observable Σ_{2x} , measured by Martel [1]. The second achievement towards this program was the measurement of the single polarisation observable Σ_3 , presented in this work. A combination of these results allowed for a new extraction of the proton's spin polarisabilities, using only data collected at the MAMI tagged photon facility. In addition to these measurements, a final measurement is ongoing to measure the double polarisation observable Σ_{2z} . Once measured, a complete extraction of the spin polarisabilities can be completed using all three data sets. This experimental program has provided the first experimental determination of the four leading order spin polarisabilities (γ_{E1E1} , γ_{M1M1} , γ_{E1M2} , and γ_{M1E2}) of the proton for the first time.

The two extractions of the proton spin polarisabilities, first by Martel and second within this work, are in good agreement with the dispersion theory, K-matrix theory, and Heavy Baryon chiral perturbation theory calculations shown in Table 3.1. Some calculations, the fourth order (p-expansion) χ PT calculation of Ref. [40] as an example, do not agree well with the experimentally determined spin polarisabilities. It

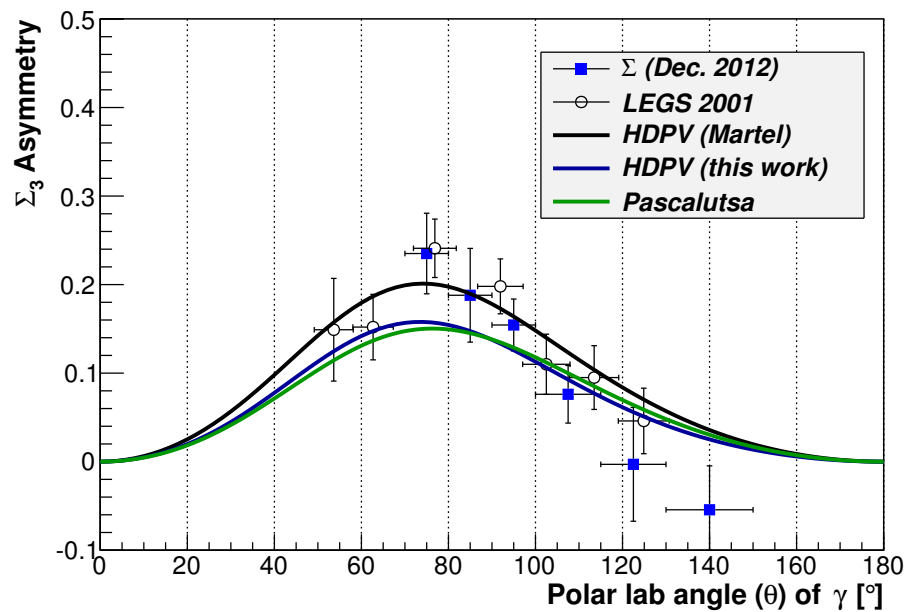
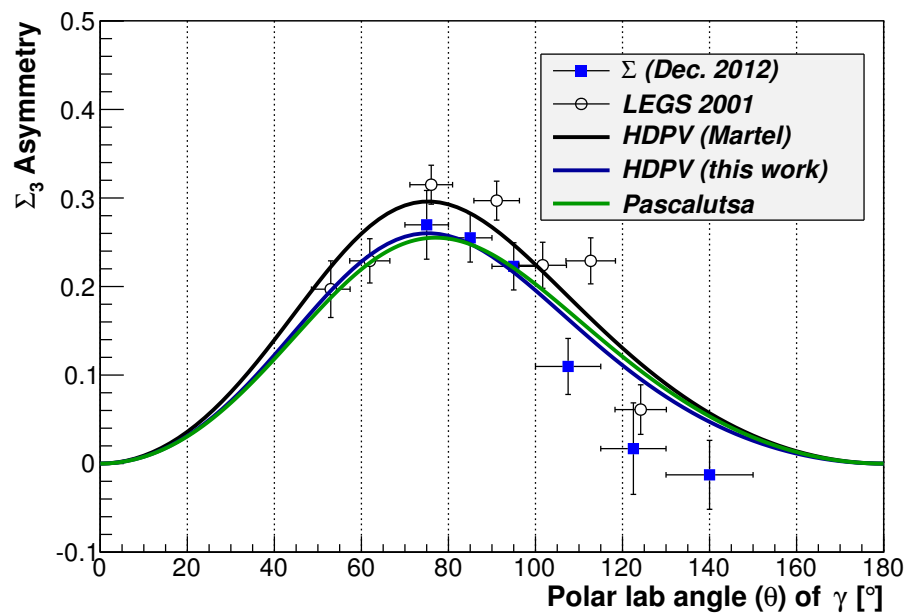
(a) $E = 277.1 \pm 10.1$ MeV(b) $E = 297.0 \pm 10.1$ MeV

Figure 7.1: Σ_3 asymmetry results are shown from this work. LEGS [4] data are shown for comparison. Additionally HDPV [15][8] and Pascalutsa [63] curves are shown. For HDPV, curves are shown for both nominal spin polarisabilities given in Table 3.1 and new spin polarisabilities determined from this analysis. Only statistical errors are shown.

is expected that results from Lattice QCD calculations [65] could provide theoretical predictions of the proton's spin polarisabilities in the near future. Lattice QCD, which uses a discretized spacetime, provides a solution to solving QCD within the non-perturbative region. These Lattice QCD calculations will provide a crucial test of our understanding of the spin-structure of nucleons as well as an extension of QCD to low energies.

Appendix A

Σ_3 results for π^0 photoproduction

$E_\gamma = 213.5 \pm 3.9$ MeV					
θ_{π^0} (Lab)	Correction, F	χ^2 of fit	Σ_3	$\Delta\Sigma_3$ (stat.)	$\Delta\Sigma_3$ (3% pol.)
12.50 \pm 2.5	1.0930	0.7281	0.3926	0.2353	0.0118
17.50 \pm 2.5	1.0200	0.6638	-0.0806	0.1792	0.0024
22.50 \pm 2.5	0.9480	0.8277	0.0566	0.1285	0.0017
27.50 \pm 2.5	0.9030	0.9576	0.2017	0.1094	0.0061
32.50 \pm 2.5	0.9200	0.9405	0.2957	0.0953	0.0089
37.50 \pm 2.5	0.8570	0.9024	0.1770	0.0830	0.0053
42.50 \pm 2.5	0.9280	1.1463	0.2931	0.0708	0.0088
47.50 \pm 2.5	0.9080	0.9229	0.1730	0.0638	0.0052
52.50 \pm 2.5	0.9380	1.0203	0.2583	0.0577	0.0077
57.50 \pm 2.5	0.9530	0.9830	0.3069	0.0526	0.0092
62.50 \pm 2.5	0.9180	0.6352	0.2426	0.0508	0.0073
67.50 \pm 2.5	0.9240	1.1079	0.1813	0.0483	0.0054
72.50 \pm 2.5	0.9230	0.8336	0.2928	0.0465	0.0088
77.50 \pm 2.5	0.9270	1.1356	0.2768	0.0463	0.0083
82.50 \pm 2.5	0.9290	0.9381	0.1952	0.0463	0.0059
87.50 \pm 2.5	0.9210	0.6561	0.2792	0.0479	0.0084
92.50 \pm 2.5	0.9200	1.0165	0.2164	0.0484	0.0065
97.50 \pm 2.5	0.9140	0.9275	0.1430	0.0493	0.0043
102.50 \pm 2.5	0.9320	0.8644	0.1593	0.0514	0.0048
107.50 \pm 2.5	0.9150	1.0076	0.1794	0.0526	0.0054
112.50 \pm 2.5	0.9200	0.8091	0.2954	0.0562	0.0089
117.50 \pm 2.5	0.9320	0.6985	0.1233	0.0594	0.0037
122.50 \pm 2.5	0.9330	1.0411	0.0884	0.0624	0.0027
127.50 \pm 2.5	0.8830	1.2548	0.1209	0.0682	0.0036
132.50 \pm 2.5	0.9110	1.0890	0.1790	0.0710	0.0054
137.50 \pm 2.5	0.9010	0.8367	0.1862	0.0793	0.0056
142.50 \pm 2.5	0.9090	1.1129	0.0489	0.0885	0.0015
147.50 \pm 2.5	0.9170	0.7941	0.0192	0.0938	0.0006
152.50 \pm 2.5	0.9250	1.3434	-0.0983	0.0999	0.0029
157.50 \pm 2.5	0.8830	0.7507	-0.0381	0.1053	0.0011
162.50 \pm 2.5	0.9090	0.8678	-0.2370	0.1376	0.0071

Table A.1: Σ_{π^0} for incident photon energies 213.52 ± 3.90 MeV. A photon flux correction factor, F , and a χ^2 (per degree of freedom) is given for each angular bin. Statistical errors are shown, along with a 3% polarisation error.

$E_\gamma = 220.9 \pm 3.9$ MeV					
θ_{π^0} (Lab)	Correction, F	χ^2 of fit	Σ_3	$\Delta\Sigma_3$ (stat.)	$\Delta\Sigma_3$ (3% pol.)
7.50 \pm 2.5	0.0000	3.6845	-0.7264	0.4625	0.0218
12.50 \pm 2.5	0.9890	1.1577	-0.2189	0.1743	0.0066
17.50 \pm 2.5	0.8970	1.0670	0.4219	0.1200	0.0127
22.50 \pm 2.5	0.9840	0.8708	-0.0146	0.0929	0.0004
27.50 \pm 2.5	0.9110	0.7681	0.1809	0.0765	0.0054
32.50 \pm 2.5	0.9870	0.9951	0.2781	0.0648	0.0083
37.50 \pm 2.5	0.9370	1.3139	0.3023	0.0559	0.0091
42.50 \pm 2.5	0.9070	1.2817	0.3280	0.0500	0.0098
47.50 \pm 2.5	0.9040	1.2932	0.2166	0.0452	0.0065
52.50 \pm 2.5	0.9130	1.0843	0.3045	0.0409	0.0091
57.50 \pm 2.5	0.9230	1.0652	0.3304	0.0385	0.0099
62.50 \pm 2.5	0.9020	1.3545	0.2858	0.0367	0.0086
67.50 \pm 2.5	0.9160	1.4727	0.2688	0.0357	0.0081
72.50 \pm 2.5	0.9180	1.0528	0.3062	0.0341	0.0092
77.50 \pm 2.5	0.9410	0.9797	0.2351	0.0337	0.0071
82.50 \pm 2.5	0.9110	0.7196	0.3387	0.0346	0.0102
87.50 \pm 2.5	0.9400	1.1658	0.3008	0.0352	0.0090
92.50 \pm 2.5	0.9060	1.0733	0.2672	0.0356	0.0080
97.50 \pm 2.5	0.9290	1.5332	0.2226	0.0364	0.0067
102.50 \pm 2.5	0.9320	1.0170	0.3078	0.0383	0.0092
107.50 \pm 2.5	0.9330	0.7036	0.2256	0.0389	0.0068
112.50 \pm 2.5	0.9170	1.1346	0.2342	0.0425	0.0070
117.50 \pm 2.5	0.9230	0.9171	0.1504	0.0441	0.0045
122.50 \pm 2.5	0.9050	1.0305	0.1401	0.0472	0.0042
127.50 \pm 2.5	0.9420	1.9763	0.2097	0.0498	0.0063
132.50 \pm 2.5	0.9290	0.7825	0.2030	0.0526	0.0061
137.50 \pm 2.5	0.9440	0.8659	0.1639	0.0563	0.0049
142.50 \pm 2.5	0.9220	0.6812	0.1394	0.0627	0.0042
147.50 \pm 2.5	0.9110	0.9861	0.0604	0.0683	0.0018
152.50 \pm 2.5	0.8330	1.1314	0.0923	0.0805	0.0028
157.50 \pm 2.5	0.9220	1.1510	0.0553	0.0888	0.0017
162.50 \pm 2.5	0.9170	0.8151	-0.1258	0.1011	0.0038

Table A.2: Σ_{π_0} for incident photon energies 220.95 ± 3.92 MeV. A photon flux correction factor, F , and a χ^2 (per degree of freedom) is given for each angular bin. Statistical errors are shown, along with a 3% polarisation error.

$E_\gamma = 225.9 \pm 3.9$ MeV					
θ_{π^0} (Lab)	Correction, F	χ^2 of fit	Σ_3	$\Delta\Sigma_3(\text{stat.})$	$\Delta\Sigma_3$ (3% pol.)
7.50 \pm 2.5	0.9300	0.8325	0.3379	0.2439	0.0101
12.50 \pm 2.5	0.9350	0.9183	0.0168	0.1384	0.0005
17.50 \pm 2.5	0.9770	1.3324	0.3063	0.0954	0.0092
22.50 \pm 2.5	0.9440	1.1268	0.1396	0.0732	0.0042
27.50 \pm 2.5	0.9440	0.8276	0.3044	0.0585	0.0091
32.50 \pm 2.5	0.9480	1.4698	0.2554	0.0519	0.0077
37.50 \pm 2.5	0.9000	0.9552	0.2847	0.0456	0.0085
42.50 \pm 2.5	0.9110	0.8396	0.3213	0.0389	0.0096
47.50 \pm 2.5	0.9290	1.2962	0.2583	0.0350	0.0077
52.50 \pm 2.5	0.9310	1.1687	0.2884	0.0325	0.0087
57.50 \pm 2.5	0.9140	0.9719	0.3502	0.0299	0.0105
62.50 \pm 2.5	0.9210	1.4915	0.3600	0.0291	0.0108
67.50 \pm 2.5	0.9500	1.1372	0.2787	0.0278	0.0084
72.50 \pm 2.5	0.8990	0.7839	0.3128	0.0272	0.0094
77.50 \pm 2.5	0.9200	1.0820	0.3248	0.0268	0.0097
82.50 \pm 2.5	0.9070	1.1912	0.3009	0.0273	0.0090
87.50 \pm 2.5	0.9530	0.7118	0.2725	0.0278	0.0082
92.50 \pm 2.5	0.9480	1.2284	0.2411	0.0279	0.0072
97.50 \pm 2.5	0.9260	1.2124	0.2891	0.0283	0.0087
102.50 \pm 2.5	0.9140	1.3564	0.2179	0.0316	0.0065
107.50 \pm 2.5	0.9400	1.4233	0.1966	0.0312	0.0059
112.50 \pm 2.5	0.9240	0.8786	0.2348	0.0332	0.0070
117.50 \pm 2.5	0.9390	1.2145	0.1832	0.0352	0.0055
122.50 \pm 2.5	0.9040	1.0466	0.2041	0.0380	0.0061
127.50 \pm 2.5	0.9230	0.9384	0.1422	0.0410	0.0043
132.50 \pm 2.5	0.9260	1.1077	0.1893	0.0425	0.0057
137.50 \pm 2.5	0.9440	1.0836	0.1524	0.0457	0.0046
142.50 \pm 2.5	0.9100	0.8732	0.0914	0.0519	0.0027
147.50 \pm 2.5	0.9210	1.1044	0.0960	0.0557	0.0029
152.50 \pm 2.5	0.8410	1.4936	-0.0301	0.0644	0.0009
157.50 \pm 2.5	0.9030	1.4375	-0.0108	0.0713	0.0003
162.50 \pm 2.5	0.8820	0.8152	-0.0482	0.0859	0.0014

Table A.3: Σ_{π_0} for incident photon energies 225.92 ± 3.91 MeV. A photon flux correction factor, F , and a χ^2 (per degree of freedom) is given for each angular bin. Statistical errors are shown, along with a 3% polarisation error.

$E_\gamma = 235.9 \pm 3.9$ MeV					
θ_{π^0} (Lab)	Correction, F	χ^2 of fit	Σ_3	$\Delta\Sigma_3$ (stat.)	$\Delta\Sigma_3$ (3% pol.)
7.50 \pm 2.5	0.9710	0.8455	-0.1691	0.1782	0.0051
12.50 \pm 2.5	0.9570	1.3786	0.1249	0.1053	0.0037
17.50 \pm 2.5	0.9110	1.1815	0.0813	0.0723	0.0024
22.50 \pm 2.5	0.8650	1.1336	0.2001	0.0546	0.0060
27.50 \pm 2.5	0.9310	1.0432	0.2992	0.0416	0.0090
32.50 \pm 2.5	0.9430	0.9712	0.2353	0.0350	0.0071
37.50 \pm 2.5	0.9100	1.3333	0.3012	0.0312	0.0090
42.50 \pm 2.5	0.9140	1.4306	0.3381	0.0280	0.0101
47.50 \pm 2.5	0.9100	0.8931	0.3612	0.0252	0.0108
52.50 \pm 2.5	0.8900	0.8017	0.3527	0.0233	0.0106
57.50 \pm 2.5	0.9090	0.6738	0.3594	0.0218	0.0108
62.50 \pm 2.5	0.9140	1.2442	0.3234	0.0207	0.0097
67.50 \pm 2.5	0.9210	1.1619	0.3938	0.0202	0.0118
72.50 \pm 2.5	0.9210	0.7284	0.3643	0.0198	0.0109
77.50 \pm 2.5	0.9050	1.1680	0.3689	0.0201	0.0111
82.50 \pm 2.5	0.9170	0.5643	0.3380	0.0204	0.0101
87.50 \pm 2.5	0.9150	1.3118	0.3103	0.0209	0.0093
92.50 \pm 2.5	0.9160	1.1006	0.3526	0.0224	0.0106
97.50 \pm 2.5	0.9180	1.0606	0.3229	0.0227	0.0097
102.50 \pm 2.5	0.9160	1.1506	0.2183	0.0237	0.0065
107.50 \pm 2.5	0.9320	0.8071	0.2249	0.0248	0.0067
112.50 \pm 2.5	0.9320	1.2721	0.2872	0.0263	0.0086
117.50 \pm 2.5	0.9030	0.8352	0.2571	0.0277	0.0077
122.50 \pm 2.5	0.9050	1.0072	0.2297	0.0299	0.0069
127.50 \pm 2.5	0.9040	1.0940	0.1504	0.0317	0.0045
132.50 \pm 2.5	0.8910	0.8960	0.1942	0.0335	0.0058
137.50 \pm 2.5	0.9100	1.2680	0.0686	0.0362	0.0021
142.50 \pm 2.5	0.9330	1.6209	0.1153	0.0396	0.0035
147.50 \pm 2.5	0.9200	1.4295	0.0770	0.0457	0.0023
152.50 \pm 2.5	0.9060	1.3079	0.1196	0.0510	0.0036
157.50 \pm 2.5	0.9100	0.9958	0.0486	0.0557	0.0015
162.50 \pm 2.5	0.9160	1.4647	0.0385	0.0627	0.0012

Table A.4: Σ_{π_0} for incident photon energies 235.89 ± 3.89 MeV. A photon flux correction factor, F , and a χ^2 (per degree of freedom) is given for each angular bin. Statistical errors are shown, along with a 3% polarisation error.

$E_\gamma = 243.4 \pm 3.9$ MeV					
θ_{π_0} (Lab)	Correction, F	χ^2 of fit	Σ_3	$\Delta\Sigma_3$ (stat.)	$\Delta\Sigma_3$ (3% pol.)
7.50 \pm 2.5	0.8000	0.7191	0.0733	0.1653	0.0022
12.50 \pm 2.5	0.8480	0.9942	0.1343	0.0900	0.0040
17.50 \pm 2.5	0.9160	1.4063	0.2800	0.0622	0.0084
22.50 \pm 2.5	0.8970	1.0930	0.1644	0.0461	0.0049
27.50 \pm 2.5	0.9310	1.2530	0.2545	0.0360	0.0076
32.50 \pm 2.5	0.9140	0.6833	0.3380	0.0300	0.0101
37.50 \pm 2.5	0.9040	0.8714	0.3367	0.0260	0.0101
42.50 \pm 2.5	0.9100	1.0862	0.3452	0.0236	0.0104
47.50 \pm 2.5	0.9150	1.2010	0.4033	0.0220	0.0121
52.50 \pm 2.5	0.8970	0.6475	0.3753	0.0202	0.0113
57.50 \pm 2.5	0.9140	0.7760	0.3921	0.0194	0.0118
62.50 \pm 2.5	0.9090	1.5435	0.3838	0.0182	0.0115
67.50 \pm 2.5	0.8940	1.5955	0.4085	0.0178	0.0123
72.50 \pm 2.5	0.8980	0.8201	0.3534	0.0179	0.0106
77.50 \pm 2.5	0.9060	0.6361	0.3818	0.0183	0.0115
82.50 \pm 2.5	0.9080	0.9615	0.3536	0.0184	0.0106
87.50 \pm 2.5	0.9260	0.6627	0.3344	0.0190	0.0100
92.50 \pm 2.5	0.9160	0.9864	0.3020	0.0201	0.0091
97.50 \pm 2.5	0.9090	0.9743	0.3395	0.0218	0.0102
102.50 \pm 2.5	0.9090	1.3830	0.2756	0.0231	0.0083
107.50 \pm 2.5	0.8980	0.9143	0.3272	0.0245	0.0098
112.50 \pm 2.5	0.9030	1.1224	0.2631	0.0270	0.0079
117.50 \pm 2.5	0.9000	0.8594	0.2977	0.0281	0.0089
122.50 \pm 2.5	0.9130	1.2060	0.2001	0.0297	0.0060
127.50 \pm 2.5	0.8950	1.0398	0.2162	0.0303	0.0065
132.50 \pm 2.5	0.9060	1.4110	0.1303	0.0312	0.0039
137.50 \pm 2.5	0.8870	1.0714	0.0777	0.0343	0.0023
142.50 \pm 2.5	0.9120	1.2858	0.1196	0.0371	0.0036
147.50 \pm 2.5	0.9200	1.0117	0.0437	0.0425	0.0013
152.50 \pm 2.5	0.8940	0.7359	0.1329	0.0464	0.0040
157.50 \pm 2.5	0.9330	1.6744	0.0480	0.0540	0.0014
162.50 \pm 2.5	0.8940	1.0715	0.0302	0.0637	0.0009

Table A.5: Σ_{π_0} for incident photon energies 243.40 ± 3.90 MeV. A photon flux correction factor, F , and a χ^2 (per degree of freedom) is given for each angular bin. Statistical errors are shown, along with a 3% polarisation error.

$E_\gamma = 250.8 \pm 3.9$ MeV					
θ_{π^0} (Lab)	Correction, F	χ^2 of fit	Σ_3	$\Delta\Sigma_3$ (stat.)	$\Delta\Sigma_3$ (3% pol.)
7.50 \pm 2.5	0.8620	0.8250	-0.2128	0.1304	0.0064
12.50 \pm 2.5	0.9510	1.2276	0.1588	0.0713	0.0048
17.50 \pm 2.5	0.9100	0.7774	0.1515	0.0458	0.0045
22.50 \pm 2.5	0.9470	1.0267	0.2284	0.0358	0.0069
27.50 \pm 2.5	0.8950	1.3935	0.2766	0.0282	0.0083
32.50 \pm 2.5	0.9260	0.9906	0.3218	0.0233	0.0097
37.50 \pm 2.5	0.9300	1.1336	0.3684	0.0200	0.0111
42.50 \pm 2.5	0.9040	0.9896	0.3598	0.0179	0.0108
47.50 \pm 2.5	0.9200	1.2001	0.4069	0.0167	0.0122
52.50 \pm 2.5	0.9070	1.0131	0.4070	0.0158	0.0122
57.50 \pm 2.5	0.8960	0.6774	0.4067	0.0147	0.0122
62.50 \pm 2.5	0.9100	1.1410	0.4144	0.0143	0.0124
67.50 \pm 2.5	0.9280	0.9501	0.3838	0.0140	0.0115
72.50 \pm 2.5	0.9140	0.7989	0.3967	0.0139	0.0119
77.50 \pm 2.5	0.9150	1.2966	0.4019	0.0144	0.0121
82.50 \pm 2.5	0.9060	1.3502	0.3790	0.0150	0.0114
87.50 \pm 2.5	0.8990	0.6407	0.3953	0.0160	0.0119
92.50 \pm 2.5	0.9200	1.0608	0.3182	0.0170	0.0095
97.50 \pm 2.5	0.8910	1.1560	0.3455	0.0191	0.0104
102.50 \pm 2.5	0.9370	0.6564	0.3183	0.0219	0.0095
107.50 \pm 2.5	0.9240	1.1728	0.3371	0.0241	0.0101
112.50 \pm 2.5	0.9100	1.0762	0.2944	0.0266	0.0088
117.50 \pm 2.5	0.9300	1.1816	0.2692	0.0275	0.0081
122.50 \pm 2.5	0.9310	1.1670	0.1695	0.0284	0.0051
127.50 \pm 2.5	0.8890	1.1927	0.1457	0.0278	0.0044
132.50 \pm 2.5	0.9380	1.2786	0.2055	0.0278	0.0062
137.50 \pm 2.5	0.9250	1.1630	0.1157	0.0291	0.0035
142.50 \pm 2.5	0.9250	1.2367	0.2031	0.0301	0.0061
147.50 \pm 2.5	0.9430	0.9270	0.1348	0.0333	0.0040
152.50 \pm 2.5	0.8870	0.6253	0.0495	0.0378	0.0015
157.50 \pm 2.5	0.9070	0.4725	0.0733	0.0438	0.0022
162.50 \pm 2.5	0.8370	0.8945	0.0587	0.0529	0.0018

Table A.6: Σ_{π_0} for incident photon energies 250.85 ± 3.92 MeV. A photon flux correction factor, F , and a χ^2 (per degree of freedom) is given for each angular bin. Statistical errors are shown, along with a 3% polarisation error.

$E_\gamma = 257.1 \pm 2.7$ MeV					
θ_{π^0} (Lab)	Correction, F	χ^2 of fit	Σ_3	$\Delta\Sigma_3$ (stat.)	$\Delta\Sigma_3$ (3% pol.)
7.50 \pm 2.5	0.8770	0.8731	0.0372	0.1402	0.0011
12.50 \pm 2.5	0.8480	0.9294	0.1169	0.0737	0.0035
17.50 \pm 2.5	0.8900	1.0960	0.1672	0.0439	0.0050
22.50 \pm 2.5	0.9190	1.1084	0.2027	0.0344	0.0061
27.50 \pm 2.5	0.9220	1.2172	0.2840	0.0275	0.0085
32.50 \pm 2.5	0.9060	0.8874	0.3411	0.0225	0.0102
37.50 \pm 2.5	0.9190	0.8491	0.3195	0.0189	0.0096
42.50 \pm 2.5	0.9200	0.4604	0.3560	0.0170	0.0107
47.50 \pm 2.5	0.9190	0.8908	0.3867	0.0158	0.0116
52.50 \pm 2.5	0.9120	1.3025	0.4259	0.0147	0.0128
57.50 \pm 2.5	0.9000	1.0527	0.4048	0.0141	0.0121
62.50 \pm 2.5	0.9050	0.8950	0.4153	0.0139	0.0125
67.50 \pm 2.5	0.9230	0.9080	0.4190	0.0136	0.0126
72.50 \pm 2.5	0.9180	0.8413	0.4222	0.0138	0.0127
77.50 \pm 2.5	0.9150	0.6112	0.4130	0.0141	0.0124
82.50 \pm 2.5	0.9070	1.0428	0.3844	0.0148	0.0115
87.50 \pm 2.5	0.9280	0.8990	0.4073	0.0167	0.0122
92.50 \pm 2.5	0.9110	0.8876	0.3640	0.0184	0.0109
97.50 \pm 2.5	0.8830	1.1951	0.3902	0.0214	0.0117
102.50 \pm 2.5	0.9260	1.3115	0.3328	0.0232	0.0100
107.50 \pm 2.5	0.8910	1.5651	0.3092	0.0259	0.0093
112.50 \pm 2.5	0.9160	0.8831	0.3534	0.0273	0.0106
117.50 \pm 2.5	0.8950	0.9724	0.2663	0.0290	0.0080
122.50 \pm 2.5	0.9360	0.9577	0.2235	0.0296	0.0067
127.50 \pm 2.5	0.9320	1.5244	0.1796	0.0307	0.0054
132.50 \pm 2.5	0.9430	1.1697	0.1778	0.0310	0.0053
137.50 \pm 2.5	0.9060	1.2386	0.1242	0.0309	0.0037
142.50 \pm 2.5	0.9420	0.7404	0.1325	0.0311	0.0040
147.50 \pm 2.5	0.8940	0.8008	0.1013	0.0348	0.0030
152.50 \pm 2.5	0.9160	1.2327	0.0561	0.0380	0.0017
157.50 \pm 2.5	0.9320	1.1504	0.0291	0.0461	0.0009
162.50 \pm 2.5	0.9390	0.8104	0.0725	0.0508	0.0022

Table A.7: Σ_{π^0} for incident photon energies 257.09 ± 2.66 MeV. A photon flux correction factor, F , and a χ^2 (per degree of freedom) is given for each angular bin. Statistical errors are shown, along with a 3% polarisation error.

$E_\gamma = 272.1 \pm 5.2$ MeV					
θ_{π_0} (Lab)	Correction, F	χ^2 of fit	Σ_3	$\Delta\Sigma_3$ (stat.)	$\Delta\Sigma_3$ (3% pol.)
7.50 \pm 2.5	0.9670	0.7334	0.0277	0.0544	0.0008
12.50 \pm 2.5	0.9000	1.1986	0.1456	0.0304	0.0044
17.50 \pm 2.5	0.9110	0.8462	0.1340	0.0199	0.0040
22.50 \pm 2.5	0.8930	1.1910	0.2514	0.0144	0.0075
27.50 \pm 2.5	0.9120	1.0684	0.3127	0.0113	0.0094
32.50 \pm 2.5	0.9030	1.1765	0.3488	0.0094	0.0105
37.50 \pm 2.5	0.9170	0.9189	0.3607	0.0081	0.0108
42.50 \pm 2.5	0.9090	1.0913	0.4107	0.0074	0.0123
47.50 \pm 2.5	0.9060	0.7933	0.4181	0.0068	0.0125
52.50 \pm 2.5	0.9030	0.8097	0.4345	0.0065	0.0130
57.50 \pm 2.5	0.9070	1.0257	0.4390	0.0062	0.0132
62.50 \pm 2.5	0.9030	1.3875	0.4472	0.0061	0.0134
67.50 \pm 2.5	0.9090	1.3471	0.4368	0.0062	0.0131
72.50 \pm 2.5	0.9130	1.2718	0.4459	0.0064	0.0134
77.50 \pm 2.5	0.9080	1.1727	0.4359	0.0068	0.0131
82.50 \pm 2.5	0.9080	0.8820	0.4345	0.0073	0.0130
87.50 \pm 2.5	0.9060	1.5141	0.4207	0.0077	0.0126
92.50 \pm 2.5	0.8940	0.9873	0.4095	0.0085	0.0123
97.50 \pm 2.5	0.9100	1.0117	0.3961	0.0094	0.0119
102.50 \pm 2.5	0.9040	1.0957	0.3865	0.0104	0.0116
107.50 \pm 2.5	0.9070	1.1760	0.3473	0.0114	0.0104
112.50 \pm 2.5	0.8940	0.7787	0.3572	0.0120	0.0107
117.50 \pm 2.5	0.9110	1.0982	0.2972	0.0126	0.0089
122.50 \pm 2.5	0.8890	0.8921	0.2805	0.0130	0.0084
127.50 \pm 2.5	0.9050	1.2580	0.2436	0.0138	0.0073
132.50 \pm 2.5	0.9160	1.2607	0.2204	0.0142	0.0066
137.50 \pm 2.5	0.8950	0.9357	0.1994	0.0150	0.0060
142.50 \pm 2.5	0.9010	0.8519	0.1482	0.0157	0.0044
147.50 \pm 2.5	0.8920	0.7340	0.1392	0.0166	0.0042
152.50 \pm 2.5	0.9170	0.7990	0.0981	0.0183	0.0029
157.50 \pm 2.5	0.9170	1.1817	0.0734	0.0214	0.0022
162.50 \pm 2.5	0.9240	1.1853	0.0138	0.0243	0.0004

Table A.8: Σ_{π_0} for incident photon energies 272.09 ± 5.15 MeV. A photon flux correction factor, F , and a χ^2 (per degree of freedom) is given for each angular bin. Statistical errors are shown, along with a 3% polarisation error.

$E_\gamma = 280.8 \pm 3.9$ MeV					
θ_{π_0} (Lab)	Correction, F	χ^2 of fit	Σ_3	$\Delta\Sigma_3$ (stat.)	$\Delta\Sigma_3$ (3% pol.)
7.50 \pm 2.5	0.9850	1.2157	0.0398	0.0481	0.0012
12.50 \pm 2.5	0.8990	0.7496	0.1221	0.0262	0.0037
17.50 \pm 2.5	0.9380	1.3221	0.1930	0.0165	0.0058
22.50 \pm 2.5	0.9150	1.1224	0.2347	0.0120	0.0070
27.50 \pm 2.5	0.8990	1.2152	0.2827	0.0093	0.0085
32.50 \pm 2.5	0.9120	1.1778	0.3450	0.0077	0.0103
37.50 \pm 2.5	0.9200	1.5956	0.3709	0.0068	0.0111
42.50 \pm 2.5	0.9170	0.7389	0.4055	0.0061	0.0122
47.50 \pm 2.5	0.9100	1.6094	0.4283	0.0057	0.0129
52.50 \pm 2.5	0.9200	1.0141	0.4350	0.0054	0.0130
57.50 \pm 2.5	0.9120	1.4891	0.4441	0.0053	0.0133
62.50 \pm 2.5	0.9140	1.2059	0.4619	0.0052	0.0139
67.50 \pm 2.5	0.9190	0.9681	0.4594	0.0053	0.0138
72.50 \pm 2.5	0.9240	1.4503	0.4633	0.0056	0.0139
77.50 \pm 2.5	0.9170	1.9813	0.4514	0.0059	0.0135
82.50 \pm 2.5	0.9220	1.0920	0.4401	0.0060	0.0132
87.50 \pm 2.5	0.9210	1.6159	0.4254	0.0064	0.0128
92.50 \pm 2.5	0.9180	1.1365	0.4234	0.0071	0.0127
97.50 \pm 2.5	0.9200	1.4862	0.4244	0.0081	0.0127
102.50 \pm 2.5	0.9220	1.8767	0.4001	0.0091	0.0120
107.50 \pm 2.5	0.9180	1.2270	0.3576	0.0098	0.0107
112.50 \pm 2.5	0.9290	1.1575	0.3589	0.0104	0.0108
117.50 \pm 2.5	0.9190	0.8720	0.3305	0.0109	0.0099
122.50 \pm 2.5	0.9160	0.8976	0.2958	0.0110	0.0089
127.50 \pm 2.5	0.9250	1.3682	0.2933	0.0116	0.0088
132.50 \pm 2.5	0.9290	0.7492	0.2622	0.0121	0.0079
137.50 \pm 2.5	0.9410	1.0029	0.2099	0.0128	0.0063
142.50 \pm 2.5	0.9180	1.2271	0.1644	0.0135	0.0049
147.50 \pm 2.5	0.9210	0.7715	0.1390	0.0145	0.0042
152.50 \pm 2.5	0.8990	1.1756	0.1200	0.0160	0.0036
157.50 \pm 2.5	0.9270	1.0992	0.0882	0.0185	0.0026
162.50 \pm 2.5	0.9420	0.8445	0.0832	0.0218	0.0025

Table A.9: Σ_{π_0} for incident photon energies 280.80 ± 3.92 MeV. A photon flux correction factor, F , and a χ^2 (per degree of freedom) is given for each angular bin. Statistical errors are shown, along with a 3% polarisation error.

$E_\gamma = 288.3 \pm 3.9$ MeV					
θ_{π_0} (Lab)	Correction, F	χ^2 of fit	Σ_3	$\Delta\Sigma_3$ (stat.)	$\Delta\Sigma_3$ (3% pol.)
7.50 ± 2.5	0.9080	0.7178	0.0656	0.0418	0.0020
12.50 ± 2.5	0.9240	1.0012	0.1614	0.0237	0.0048
17.50 ± 2.5	0.9170	1.2924	0.2194	0.0155	0.0066
22.50 ± 2.5	0.9270	1.1812	0.2220	0.0111	0.0067
27.50 ± 2.5	0.9150	1.0848	0.3053	0.0086	0.0092
32.50 ± 2.5	0.9210	1.5869	0.3524	0.0070	0.0106
37.50 ± 2.5	0.9180	0.9830	0.3975	0.0061	0.0119
42.50 ± 2.5	0.9220	1.1955	0.4284	0.0057	0.0129
47.50 ± 2.5	0.9160	1.8780	0.4375	0.0053	0.0131
52.50 ± 2.5	0.9130	1.0587	0.4543	0.0051	0.0136
57.50 ± 2.5	0.9200	1.4262	0.4699	0.0049	0.0141
62.50 ± 2.5	0.9160	1.7415	0.4733	0.0050	0.0142
67.50 ± 2.5	0.9230	1.0836	0.4733	0.0051	0.0142
72.50 ± 2.5	0.9190	1.0739	0.4732	0.0053	0.0142
77.50 ± 2.5	0.9160	1.0833	0.4847	0.0054	0.0145
82.50 ± 2.5	0.9210	1.0899	0.4686	0.0057	0.0141
87.50 ± 2.5	0.9200	0.8749	0.4611	0.0061	0.0138
92.50 ± 2.5	0.9130	0.8970	0.4431	0.0068	0.0133
97.50 ± 2.5	0.9270	0.9137	0.4281	0.0078	0.0128
102.50 ± 2.5	0.9140	0.9464	0.4189	0.0089	0.0126
107.50 ± 2.5	0.9140	1.0165	0.4081	0.0095	0.0122
112.50 ± 2.5	0.9160	1.1854	0.3704	0.0099	0.0111
117.50 ± 2.5	0.9310	1.0015	0.3518	0.0103	0.0106
122.50 ± 2.5	0.9190	0.6966	0.3122	0.0105	0.0094
127.50 ± 2.5	0.9210	1.1858	0.2876	0.0109	0.0086
132.50 ± 2.5	0.9220	0.7391	0.2668	0.0118	0.0080
137.50 ± 2.5	0.9320	0.9759	0.2089	0.0121	0.0063
142.50 ± 2.5	0.9200	0.8969	0.1945	0.0133	0.0058
147.50 ± 2.5	0.9270	1.6095	0.1504	0.0142	0.0045
152.50 ± 2.5	0.9180	0.6588	0.1213	0.0154	0.0036
157.50 ± 2.5	0.9260	0.9900	0.0870	0.0180	0.0026
162.50 ± 2.5	0.8970	0.9495	0.0195	0.0215	0.0006

Table A.10: Σ_{π_0} for incident photon energies 288.29 ± 3.90 MeV. A photon flux correction factor, F , and a χ^2 (per degree of freedom) is given for each angular bin. Statistical errors are shown, along with a 3% polarisation error.

$E_\gamma = 295.8 \pm 3.9$ MeV					
θ_{π_0} (Lab)	Correction, F	χ^2 of fit	Σ_3	$\Delta\Sigma_3$ (stat.)	$\Delta\Sigma_3$ (3% pol.)
7.50 \pm 2.5	0.8930	0.8082	0.0767	0.0411	0.0023
12.50 \pm 2.5	0.9200	0.7248	0.1343	0.0231	0.0040
17.50 \pm 2.5	0.9350	1.2911	0.1660	0.0152	0.0050
22.50 \pm 2.5	0.9130	0.9945	0.2515	0.0107	0.0075
27.50 \pm 2.5	0.9270	0.9740	0.3112	0.0083	0.0093
32.50 \pm 2.5	0.9280	0.9669	0.3702	0.0068	0.0111
37.50 \pm 2.5	0.9160	1.1275	0.4075	0.0060	0.0122
42.50 \pm 2.5	0.9180	0.6804	0.4239	0.0054	0.0127
47.50 \pm 2.5	0.9180	1.4386	0.4571	0.0051	0.0137
52.50 \pm 2.5	0.9290	1.2027	0.4734	0.0049	0.0142
57.50 \pm 2.5	0.9190	1.5618	0.4816	0.0048	0.0144
62.50 \pm 2.5	0.9220	1.0909	0.4926	0.0049	0.0148
67.50 \pm 2.5	0.9200	1.3978	0.4987	0.0051	0.0150
72.50 \pm 2.5	0.9220	1.4887	0.5016	0.0052	0.0150
77.50 \pm 2.5	0.9220	1.4989	0.5003	0.0053	0.0150
82.50 \pm 2.5	0.9180	1.2295	0.5040	0.0056	0.0151
87.50 \pm 2.5	0.9170	0.9781	0.4878	0.0061	0.0146
92.50 \pm 2.5	0.9250	1.2831	0.4705	0.0069	0.0141
97.50 \pm 2.5	0.9210	0.7010	0.4603	0.0078	0.0138
102.50 \pm 2.5	0.9210	1.1353	0.4521	0.0087	0.0136
107.50 \pm 2.5	0.9100	1.4135	0.4148	0.0093	0.0124
112.50 \pm 2.5	0.9220	0.9478	0.3965	0.0096	0.0119
117.50 \pm 2.5	0.9180	1.2133	0.3888	0.0100	0.0117
122.50 \pm 2.5	0.9240	0.8232	0.3580	0.0104	0.0107
127.50 \pm 2.5	0.9250	1.1631	0.3279	0.0108	0.0098
132.50 \pm 2.5	0.9130	0.6543	0.2852	0.0114	0.0086
137.50 \pm 2.5	0.9140	1.3329	0.2053	0.0120	0.0062
142.50 \pm 2.5	0.9060	0.8252	0.2358	0.0133	0.0071
147.50 \pm 2.5	0.9110	0.9184	0.1734	0.0140	0.0052
152.50 \pm 2.5	0.9010	1.3922	0.1534	0.0157	0.0046
157.50 \pm 2.5	0.9290	1.1104	0.1182	0.0180	0.0035
162.50 \pm 2.5	0.9530	1.3146	0.0938	0.0220	0.0028

Table A.11: Σ_{π_0} for incident photon energies 295.78 ± 3.88 MeV. A photon flux correction factor, F , and a χ^2 (per degree of freedom) is given for each angular bin. Statistical errors are shown, along with a 3% polarisation error.

$E_\gamma = 303.3 \pm 3.9$ MeV					
θ_{π_0} (Lab)	Correction, F	χ^2 of fit	Σ_3	$\Delta\Sigma_3$ (stat.)	$\Delta\Sigma_3$ (3% pol.)
7.50 \pm 2.5	0.9690	0.7517	0.0112	0.0438	0.0003
12.50 \pm 2.5	0.9250	1.1165	0.1206	0.0271	0.0036
17.50 \pm 2.5	0.9560	1.2117	0.2066	0.0172	0.0062
22.50 \pm 2.5	0.9690	1.1551	0.2738	0.0119	0.0082
27.50 \pm 2.5	0.9710	1.1665	0.3424	0.0094	0.0103
32.50 \pm 2.5	0.9610	1.0463	0.3794	0.0076	0.0114
37.50 \pm 2.5	0.9670	1.4494	0.4356	0.0067	0.0131
42.50 \pm 2.5	0.9680	1.4200	0.4677	0.0061	0.0140
47.50 \pm 2.5	0.9560	1.3778	0.4996	0.0058	0.0150
52.50 \pm 2.5	0.9640	2.0887	0.5057	0.0055	0.0152
57.50 \pm 2.5	0.9620	1.2455	0.5124	0.0055	0.0154
62.50 \pm 2.5	0.9700	0.9873	0.5387	0.0057	0.0162
67.50 \pm 2.5	0.9620	0.5227	0.5397	0.0058	0.0162
72.50 \pm 2.5	0.9660	1.2097	0.5358	0.0058	0.0161
77.50 \pm 2.5	0.9770	1.2609	0.5428	0.0060	0.0163
82.50 \pm 2.5	0.9680	1.2848	0.5445	0.0065	0.0163
87.50 \pm 2.5	0.9660	0.7551	0.5291	0.0071	0.0159
92.50 \pm 2.5	0.9600	0.7855	0.5288	0.0079	0.0159
97.50 \pm 2.5	0.9690	1.0955	0.5070	0.0089	0.0152
102.50 \pm 2.5	0.9710	0.9399	0.4810	0.0097	0.0144
107.50 \pm 2.5	0.9750	1.4109	0.4574	0.0104	0.0137
112.50 \pm 2.5	0.9610	0.6621	0.4341	0.0110	0.0130
117.50 \pm 2.5	0.9710	0.6934	0.4014	0.0115	0.0120
122.50 \pm 2.5	0.9640	0.8647	0.3860	0.0118	0.0116
127.50 \pm 2.5	0.9610	0.9083	0.3630	0.0125	0.0109
132.50 \pm 2.5	0.9510	0.9029	0.3039	0.0133	0.0091
137.50 \pm 2.5	0.9510	1.0898	0.2847	0.0144	0.0085
142.50 \pm 2.5	0.9700	0.7832	0.2171	0.0149	0.0065
147.50 \pm 2.5	0.9520	0.8061	0.1886	0.0164	0.0057
152.50 \pm 2.5	0.9600	1.2569	0.1717	0.0181	0.0052
157.50 \pm 2.5	0.9880	1.1359	0.1216	0.0209	0.0036
162.50 \pm 2.5	0.9800	1.0355	0.0718	0.0244	0.0022

Table A.12: Σ_{π_0} for incident photon energies 303.30 ± 3.89 MeV. A photon flux correction factor, F , and a χ^2 (per degree of freedom) is given for each angular bin. Statistical errors are shown, along with a 3% polarisation error.

Bibliography

- [1] P. Martel, “Measuring proton spin polarizabilities with polarized compton scattering,” *Ph.D dissertation, University of Massachusetts Amherst*, 2013.
- [2] P. Martel *et al.* , “Measurements of the proton spin polarizabilities with double-polarized compton scattering,” *Phys. Rev. Lett.*, 2014.
- [3] G. Blanpied *et al.* , “ $N \rightarrow \Delta$ transition from simultaneous measurements of $p(\gamma, \pi^0)$ and $p(\gamma, \gamma)$,” *Phys. Rev. Lett.*, vol. 79, 1997.
- [4] G. Blanpied *et al.* , “ $N \rightarrow \Delta$ transition and proton polarizabilities from measurements of $p(\gamma, \gamma)$, $p(\gamma, \pi^0)$, and $p(\gamma, \pi^+)$,” *Phys. Rev. C.*, vol. 64, 2001.
- [5] M. Levchuk and A. Lvov, “Deuteron compton scattering below pion photoproduction threshold,” *Nucl. Phys. A*, vol. 674, pp. (449–492), 2000.
- [6] M. Schumacher, “Polarizability of the nucleon and compton scattering,” *Progress in Particle and Nuclear Physics*, vol. 55, pp. (567–646), 2005.
- [7] D. Babusci, G. Giordano, A. Lvov, G. Matone, and A. Nathan, “Low-energy compton scattering of polarized photons on polarized nucleons,” *Phys. Rev. C*, vol. 58, pp. 1013–1041, 1998.
- [8] B. Holstein, D. Drechsel, B. Pasquini, and M. Vanderhaeghen, “Higher order polarizabilities of the proton,” *Phys. Rev. C.*, vol. 61, 2000.
- [9] V. Petrun’kin, “Scattering of low-energy photons on a system with spin 1/2,” *Sov. Phys. JETP.*, vol. 13, 1961.
- [10] V. Petrun’kin, “Scattering of low-energy photons on a zero-spin particle,” *Nucl. Phys.*, vol. 55, 1964.
- [11] I. Guiasu, C. Pomponiu, and E. Radescu, “Elastic γ -proton scattering at low and intermediate energies,” *Annals of Physics*, vol. 114, pp. 296–331, 1978.
- [12] B. MacGibbon *et al.* , “Measurement of the electric and magnetic polarizabilities of the proton,” *Phys. Rev. C.*, vol. 52, 1995.
- [13] A. Lvov, V. Petrun’kin, and M. Schumacher, “Dispersion theory of proton compton scattering in the first and second resonance regions,” *Phys. Rev. C.*, vol. 55, 1997.
- [14] B. Pasquini, D. Drechsel, and M. Vanderhaeghen, “Proton spin polarizabilities from polarized compton scattering,” *Phys. Rev. C.*, vol. 76, 2007.

- [15] D. Drechsel, B. Pasquini, and M. Vanderhaeghen, “Dispersion relations in real and virtual compton scattering,” *Phys. Rept.*, vol. 378, 2003.
- [16] A. Baldin, “Polarizability of nucleons,” *Nucl. Phys.*, vol. 18, pp. (310–317), 1960.
- [17] J. Bernabeu, T. Ericson, and C. Ferro Fontan, “The nucleon electromagnetic polarizabilities,” *Phys. Lett. B*, vol. 49, 1974.
- [18] M. Schumacher, “Electromagnetic polarizabilities of the nucleon and properties of the σ -meson pole contribution,” *Eur. Phys. J.*, vol. 30, 2006.
- [19] J. Ahrens *et al.* , “First measurement of the gerasimov-drell-hearn integral for ^1h from 200 to 800 MeV,” *Phys. Rev. Lett.*, vol. 87, 2001.
- [20] S. Drell and A. Hearn, “Exact sum rule for nucleon magnetic moments,” *Phys. Rev. Lett.*, vol. 16, p. 908, 1966.
- [21] S. Gerasimov, “A sum rule for magnetic moments and the damping of the nucleon magnetic moment in nuclei,” *Sov. J. Nucl. Phys.*, vol. 2, p. 403, 1966.
- [22] M. Damashek and F. Gilman, “Forward compton scattering,” *Phys. Rev. D*, vol. 1, 1970.
- [23] T. Armstrong *et al.* , “Total hadronic cross section of γ rays in Hydrogen in the energy range 0.265–4.215 GeV,” *Phys. Rev. D*, vol. 5, 1972.
- [24] M. MacCormick *et al.* , “Total photoabsorption cross sections for ^1H , ^2H , and ^3He from 200 to 800 MeV,” *Phys. Rev. C*, vol. 53, 1996.
- [25] D. Babusci, G. Giordano, and G. Matone, “New evaluation of the baldin sum rule,” *Phys. Rev. C*, vol. 57, 1998.
- [26] R. Workman, W. Briscoe, M. Paris, and I. Strakovsky, “Updated SAID analysis of pion photoproduction data,” *Phys. Rev. C*, vol. 85, 2012.
- [27] O. de Leòn *et al.* , “Low-energy compton scattering and the polarizabilities of the proton,” *Eur. Phys. J.*, vol. 10, 2001.
- [28] R. Arndt, I. Strakovsky, and R. Workman, “Updated resonance photodecay amplitudes to 2 GeV,” *Phys. Rev. C*, vol. 53, 1996.
- [29] F. Federspiel *et al.* , “Proton compton effect: A measurement of the electric and magnetic polarizabilities of the proton,” *Phys. Rev. Lett.*, vol. 67, 1991.
- [30] A. Zieger, R. Van de Vyver, D. Christmann, A. De Graeve, C. Van den Abeele, and B. Ziegler, “180-degrees compton scattering by the proton below the pion threshold,” *Phys. Lett. B*, vol. 278, 1992.
- [31] V. Lensky and V. Pascalutsa, “Predictive powers of chiral perturbation theory in compton scattering off protons,” *Eur. Phys. J. C*, vol. 65, 2010.

- [32] J. McGovern, D. Phillips, and H. Griebhammer, “Compton scattering from the proton in an effective field theory with explicit delta degrees of freedom,” *Eur. Phys. J. A*, vol. 49, 2013.
- [33] H. Dutz *et al.* , “First measurement of the Gerasimov-Drell-Hearn Sum Rule for ^1H from 0.7 to 1.8 GeV at ELSA,” *Phys. Rev. Lett.*, vol. 91, 2003.
- [34] M. Camen *et al.* , “Backward spin polarizability γ_π of the proton,” *Phys. Rev. C*, vol. 65, 2002.
- [35] E. Hallin *et al.* , “Compton scattering from the proton,” *Phys. Rev. C*, vol. 48, 1993.
- [36] G. Galler *et al.* , “Compton scattering by the proton,” *Phys. Lett. B*, vol. 503, 2001.
- [37] S. Wolf *et al.* , “Compton scattering by the proton using a large acceptance arrangement,” *Eur. Phys. J.*, vol. 12, 2001.
- [38] S. Weinberg, “Phenomenological lagrangians,” *Physica A*, vol. 96, 1979.
- [39] K. Vijaya Kumar, J. McGovern, and M. Birse, “Spin polarisabilities of the nucleon at NLO in the chiral expansion,” *Phys. Lett. B*, vol. 479, 2000.
- [40] G. Gellas, T. Hemmert, and U.-G. Meiner, “Complete one loop analysis of the nucleon’s spin polarizabilities,” *Phys. Rev. Lett.*, vol. 85, 2001.
- [41] T. Hemmert, B. Holstein, J. Kambor, and G. Knochlein, “Compton scattering and the spin structure of the nucleon at low energies,” *Phys. Rev. D*, vol. 57, 1998.
- [42] V. Lensky and J. McGovern, “Proton polarizabilities from compton data using covariant chiral effective field theory,” *Phys. Rev. C*, vol. 89, 2014.
- [43] S. Chung *et al.* , “Partial wave analysis in k-matrix formalism,” *Annalen Phys.*, vol. 4, 1995.
- [44] S. Kondratyuk and O. Scholten, “Compton scattering on the nucleon at intermediate energies and polarizabilities in a microscopic model,” *Phys. Rev. C*, vol. 64, 2001.
- [45] T. Hemmert *in Proceedings of the Symposium on the Gerasimov-Drell-Hearn Sum rule and the Nucleon Spin Structure in the Resonance Region (GDH2000)*. Eds. D. Drechsel and L. Tiator, World Scientific, Singapore, 2001.
- [46] K. Livingston, “The Stonehenge Technique. a new method of aligning crystals for linearly polarized photon production from coherent bremsstrahlung,” *Nucl. Inst. and Meth. A*, vol. 603, 2009.

- [47] A. Jankowiak, “The mainz microtron mami — past and future,” *Eur. Phys. J.*, vol. 28, 2006.
- [48] M. Dehn *et al.* , “The MAMI C accelerator: The beauty of normal conduction multi-turn recirculators,” *Eur. Phys. J. Special Topics*, vol. 198, 2011.
- [49] F. Rambo *et al.* , “Enhancement of the linear polarization of coherent bremsstrahlung by collimation of the photon beam,” *Phys. Rev. C*, vol. 58, 1998.
- [50] P. Yu and M. Cardona, *Fundamentals of Semiconductors: Physics and Materials Properties*. Springerlink Fourth Edition, 2010.
- [51] R. Tilley, *Crystals and Crystal Structure*. John Wiley & Sons, 2006.
- [52] R. T. Jones, “Intense beams of polarized and nearly monochromatic photons from coherent bremsstrahlung.” Indiana University, 1997.
- [53] F. Natter *et al.* , “Enhancement of the linear polarization of coherent bremsstrahlung by collimation of the photon beam,” *Nucl. Inst. and Meth. B.*, vol. 211, 2003.
- [54] R. Fernow, *Introduction to Experimental Particle Physics*. Cambridge University Press, 1986.
- [55] A. Thomas, *Crystal Ball Hydrogen (Deuterium) Target manual*. A2 Collaboration, 5 2013.
- [56] K. Livingston, *Polarization from Coherent Bremsstrahlung Enhancement*. A2 Collaboration, 2014.
- [57] R. Leukel, “Photoproduktion neutraler pionen am proton mit linear polarisierten photonen in bereich der $\delta(1232)$ -resonanz,” *Ph.D dissertation, Johannes Gutenberg-Universitaet*, 2001.
- [58] S. Kamalov and S. Yang *Phys. Rev. Lett.*, vol. 83, 1999.
- [59] D. Drechsel, O. Hanstein, S. Kamalov, and L. Tiator, “A unitary isobar model for pion photo- and electroproduction on the proton up to 1 GeV,” *Nucl. Phys. A.*, vol. 65, 1999.
- [60] D. Drechsel, S. Kamalov, and L. Tiator, “Unitary isobar model - MAID2007,” *Eur. Phys. J. A.*, vol. 34, 2007.
- [61] S. Kamalov, D. Drechsel, L. Tiator, and S. Yang, “Multipole analysis for pion photoproduction with MAID and a dynamical models,” 2001.
- [62] Geant4 Collaboration, “Geant4 - a simulation toolkit,” *Nucl. Instrum. Methods A*, vol. 506, 2003.

- [63] V. Lensky and V. Pascalutsa, “Predictive powers of chiral perturbation theory in compton scattering off protons,” *Eur. Phys. J. C.*, vol. 65, 2010.
- [64] A. Rajabi, “Private communication,” 2015.
- [65] W. Detmold, B. Tiburzi, and A. Walker-Loud, “Electromagnetic and spin polarizabilities in lattice qcd,” *Phys. Rev. D*, vol. 73, 2006.